UNIVERSITÀ
DEGLI STUDI
DI PADOVA

Università degli Studi di Padova

Dipartimento di Tecnica e Gestione dei sistemi industriali

CORSO DI DOTTORATO DI RICERCA IN INGEGNERIA MECCATRONICA E DELL'INNOVAZIONE MECCANICA DEL PRODOTTO

Meccanica dei materiali

CICLO XXX

TOWARDS THE DEVELOPMENT OF DESIGN TOOLS FOR FATIGUE LIFE ASSESSMENT OF COMPOSITE STRUCTURES

Coordinatore: Ch.mo Prof. Roberto Caracciolo

Supervisore: Ch.mo Prof. Marino Quaresimin

Dottorando: Elisa Novello

Summary

The threat of delaminations arising during in-service loading conditions is one of the key factors limiting the use of composite materials in large volume for main structures. Delamination occurrence is primarily caused by the interlaminar tension and shear stresses that develop due to different factors. These include geometric or materials discontinuities (e.g. edges, holes, dropped ply), but are also linked to internal mechanism failure, such as matrix cracks. The present thesis focuses on the investigation of the correlation existing between different damage mechanisms occurring in composite laminates.

The problem of delamination initiation from transverse cracks in cross-ply laminates under quasi-static loading is thoroughly studied in Chapter 2. An analytical solution is presented for the local mode I, II and III stress fields arising in the close neighbourhoods of a transverse crack, stresses being written as a function of Generalised Stress Intensity Factors (GSIFs). Moreover, a fracture criterion for the delamination onset in cross-ply laminates under tension, based on a critical value for the mode 1 GSIF, is proposed and validated taking advantage of the results from an experimental campaign.

The analytical solution describing the stress fields in the adjacencies of a transverse crack, found for cross-ply laminates, was then extended to be suitable to describe the stress fields for laminates with generic orientation (Chapter 3).

The results of the research activity focused on the investigation of delamination evolution for composite laminates subjected to cyclic loads are presented in the following chapters.

In particular, the outcomes of the experimental tests carried out on glass/epoxy cross ply laminates are presented in Chapter 4.

Numerical analyses were performed to characterize the evolution of delamination area during fatigue life. Energy release rates (ERR) associated with delamination growth was calculated by using the virtual crack closure technique (VCCT) and a Paris-like curve was derived (Chapter 5). Furthermore, the reduction of Young's modulus and Poisson's ratio were modelled. Theoretical predictions were found to be consistent with collected experimental data.

The process of delamination growth may be affected by different parameters. The presence of the friction sliding between the delaminated interfaces is one of these. The friction effects on ERR values are discussed in the Appendix. Different conditions of damage were numerically simulated, varying the value of the coefficient of friction and the length of delaminations. It was found that the presence of friction was not so influent for the purposes of delamination growth assessment.

Then, with the aim of investigating damage evolution for laminates characterized by different orientations, fatigue tests were carried out on $[0/45_2/-45_2]_s$ and $[0/45_2]_s$ laminates.

The different phases of the damage process were documented by collecting a detailed series of images, showing the accumulation of the observed failure modes. During the tests, the Young's modulus and the Poisson's ratio evolution were determined and their correlation with the damage evolution was investigated (Chapter 6).

Following the approach used for cross-ply laminates, a correlation between the growth rate of delamination and ERR was investigated. Furthermore, a series of numerical investigations in response to the free edge delamination problem was performed. In fact, delamination initiation and growth was observed to occur more extensively near the free edges, both for balanced and unbalanced configuration of laminates. The results of these FE analyses are presented in Chapter 7.

Finally, a model based on a probabilistic approach for the prediction of fibre failure of 0° laminae in cross ply laminates subjected to tensile-tensile fatigue loading will be described in Chapter 8.

Sommario

Il problema delle delaminazioni formatesi durante le condizioni di servizio, è uno dei fattori che maggiormente limitano l'utilizzo di materiali compositi nelle applicazioni strutturali. La formazione delle delaminazioni è causata principalmente dalle elevate tensioni interlaminari che si sviluppano in corrispondenza di discontinuità geometriche o dei materiali. Inoltre, queste possono essere indotte anche dalla presenza di altri meccanismi di danneggiamento, come la formazione di cricche. Obiettivo di questa tesi è studiare le relazioni esistenti tra i diversi meccanismi di danneggiamento che si manifestano nei laminati compositi, ponendo particolare attenzione alla formazione e allo sviluppo delle delaminazioni.

Il problema dell'innesco delle delaminazioni, indotte dalla formazione delle cricche trasversali nei laminati cross-ply soggetti a trazione, è presentato nel capitolo 2. Dapprima viene ricavata una soluzione analitica per descrivere i campi di tensione associati ai modi I, II e III di deformazione, espressi in funzione dei fattori di intensificazione di tensione. La soluzione trovata quindi è stata elaborata e generalizzata, al fine di poter essere applicata a laminati caratterizzati da una orientazione generica (capitolo 3).

I capitoli successivi sono invece dedicati allo studio dell'evoluzione delle delaminazioni in laminati soggetti a fatica.

In particolare, i risultati dei test sperimentali condotti su laminati cross-ply sono presentati nel capitolo 4. L'evoluzione dell'area di delaminazione è stata caratterizzata mediante apposite analisi numeriche; il tasso di rilascio dell'energia di deformazione (ERR) è stato calcolato con l'utilizzo della tecnica di chiusura virtuale (VCCT) e i valori sono stati correlati alla velocità di propagazione della cricca mediante curva di Paris (Capitolo 5). Un modello di previsione della perdita di

rigidezza, causata dal processo di danneggiamento, è presentato nello stesso capitolo, validato mediante confronto con dati sperimentali.

La crescita delle delaminazioni risente dell'influenza di diversi fattori, tra cui la presenza di attrito in corrispondenza dell'interfaccia delaminata 0°/90°. L'influenza che questa esercita sui valori di ERR è argomento dell'Appendice. Diverse condizioni di danneggiamento sono state simulate, variando sia il coefficiente di attrito, sia la lunghezza di delaminazione, ma i risultati ottenuti hanno evidenziato una scarsa influenza dell'attrito ai fini della stima della crescita delle delaminazioni.

Successivamente, con l'obiettivo di investigare l'evoluzione del danneggiamento per laminati caratterizzati da una orientazione generica, dei test a fatica sono stati condotti su laminati $[0/45_2]_s$ e $[0/45_2/-45_2]_s$. Le fasi caratterizzanti il progressivo processo di danneggiamento sono state determinate e documentate tramite una serie di immagini. Durante i test si è studiata l'evoluzione del modulo di rigidezza e del modulo di Poisson e si è correlato il loro andamento con la formazione dei meccanismi di danneggiamento. In analogia con quanto visto per i cross-ply, si è studiata l'applicabilità della curva di Paris per descrivere in maniera efficace la crescita delle delaminazioni. Successivamente, delle simulazioni numeriche sono state condotte per studiare il problema delle delaminazioni innescate dai bordi liberi, particolarmente sviluppate sia nel caso dei laminati con configurazione bilanciata e non bilanciata (Capitolo 7). In conclusione, un modello basato su un approccio probabilistico per la previsione della rottura delle fibre delle lamine orientate a 0° in laminati cross-ply viene presentato nel Capitolo 8.

List of contents

1. Introduction

1.1. Composite materials

The increasing request of enhanced performance from structural engineering, such as improved strength, stiffness and, at the same time, lowered weight and costs, have led scientists to stress the characteristics of the traditional materials or, when these prove to be inadequate, develop innovative materials. Composites represent a promising class of materials, providing new prospects to the demand of high-performance engineering materials.

A composite material can be generally defined as a combination of various components characterized by distinct boundaries and properties different from those of the individual components. The constituents are usually denominated as matrix and reinforcement. The first surrounds and supports the reinforcement materials, distributing the load between the different phases, while the latter imparts its special mechanical properties.

The concept of composite materials is present in the nature. Bones consist of organic fibres, collagen with high elastic modulus, surrounded by an organic matrix, with a low elastic modulus, permeated with pores filled with liquids. Similarly, wood can be regarded as a natural composite, since it is composed of varying shapes of cellulose fibres embedded in a lignin and hemicellulose matrix.

Moreover, the practice of manufacturing tools by combining different materials was already known in the history. Persian bows were made of horn for the part subjected to compression, while the stretched ones were made of wood and ligaments laminated together. Japanese swords are made of two types of steel: the high-carbon outer steel (kawagane) and the softer lower carbon core (shingane steel), combining good resistance for flexure and impact.

The main reasons that promoted the use of composite materials in place of traditional materials, are listed as follows:

- Higher values of Young's modulus per unit mass (specific stiffness) and tensile strength per unit mass (specific strength).
- A weight reduction, which results in fuel saving and increasing payload, or in a general improvement of performances, e.g. the increase of range.
- A worthy corrosion resistance, leading to maintenance cost saving.
- A lowered sensitivity to the chemicals used in engines, like grease, oils, hydraulic liquids and solvents.
- Superior fire resistance with respect to the light alloys.

To the benefits above listed, the flexibility of design has to be added, since a composite material can be effectively tailored to suit a particular functional requirement. Further advantages include increased toughness, mechanical damping.

These advantages have determined the success of composites, which have found applications in technological advanced field, such as military markets, recreational marine, wind energy and aerospace or in consumer sports goods. Table 1.1 reports the principal applications:

Table 1.1 Applications of composites (Adapted from [1])

Industrial sector	Examples
Aerospace	Wings, fuselage, radomes, antennae, tail-planes, helicopter blades, landing gears, seats, floors, interior panels, fuel tanks, rocket motor cases, nose cones, launch tubes
Automotive	Body panels, cabs, spoilers, consoles, instrument panels, lamp-housings, bumpers,

	leaf springs, drive shafts, gears, bearing
Boats	Hulls, decks, masts, engine shrouds, interior panels
Chemical	Pipes, tanks, pressure vessels, hoppers, valves, pumps, impellers
Domestic	Interior and exterior panels, baths, shower units, ladders
Electrical	Panes, housings, switchgear, insulator, connectors
Leisure	Motor homes, trailers, golf clubs, racquets, protective helmets, skis, archery bows, surfboards, fishing rod, canoes.

Composite materials now occupy an established position in different industrial applications, but there are clear signals that their importance will increase in the future

In the next paragraph, the results of a recent market report are summarized, justifying the interest that nowadays many scientists are devoting to study the behavior of these materials.

1.2. Carbon market report

CceV (Carbon Composites e.V., association of companies and research institutes which covers the entire value chain of high performance fiber reinforced composites) published a market report in 2016 [2], reporting a positive assessment of the economic situation for the global carbon composites market.

Figure 1.1 shows how the demand for carbon fiber has been steadily growing since 2010, indicating the produced amount in tons.

The global demand of 91000 tons recorded in 2015 represented a growth of 10% respect than the previous year, while when compared with the request of the 2009, year of the economic recession, the requirement has more than doubled.

It was estimated that the annual growth rate from 2010 to 2015 was about 12%, and, assuming that will keep stable for the future developments, in 2022 the demand of carbon reinforced polymers (CRP) can be estimated equal to 191000 tons.

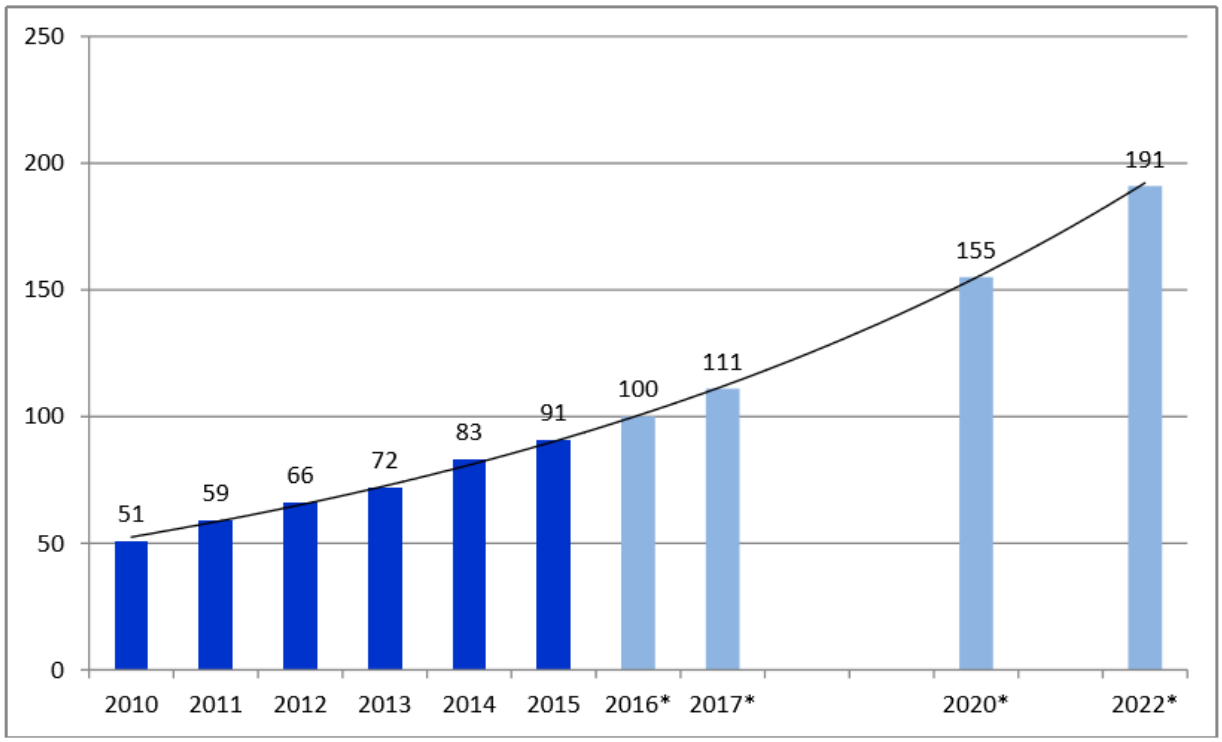

Figure 1.1 Global demand for CRP in 1000 tons (*estimates)

The major driver for the growth of composites demand in the next years is the increasing use of CRP in the aerospace structure and in automobile construction.

Figure 1.2 shows the request for carbon composites by region. The biggest share belongs to the North America (38%), driven by the aerospace and defence sector and Europe (35%), driven by aerospace, wind turbine and automotive sectors.

Furthermore, new market areas are emerging in Asian regions, including the Pacific region, as a consequence of state sponsored funding programs.

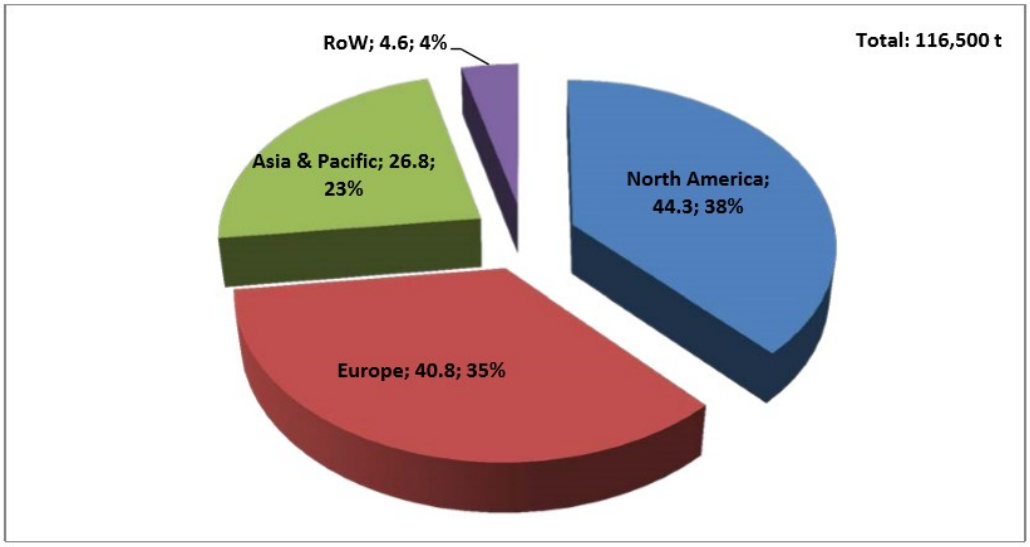

Figure 1.2 CC demand in 1000 tons divided by regions (2015)

Conversely, Figure 1.3 illustrates the demand for carbon composites according to applications. It is evident that the most important market sector is the aerospace (30% of the global demand), where commercial aviation showed a growth rate of 7% over the past years in supplied units.

This is followed by the automotive sector (22%), wind turbines, sport and leisure (12%), construction industry (5%) and ship building (1%).

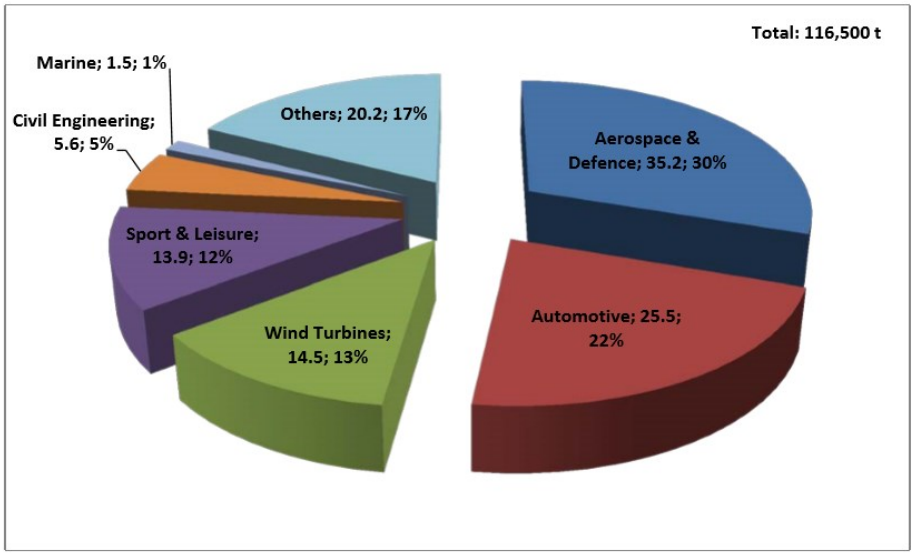

Figure 1.3 CC demand in 1000 tons divided by applications (2015)

The prediction of CC request divided by application, is shown in Figure 1.4. It is expected that a higher share will be used in the automotive construction than in aerospace, followed by the other applications: wind turbines, sport and leisure, construction and marine.

As concerns aerospace sector, current projects are the A350 and the B787, where more than 50 % the structure is made of CC, or the new projects of Boeing 777X with CC wings.

The potential for savings in material and production costs is an important factor for growing share in future applications. The automotive sector is investing on automated efficient production of CC components that can result in cheaper prices for wider application in middle class cars and not only in the luxury and sport cars segment. The application in civil engineering presents an actual low demand for CC and a reduced expected growth for the future. Carbon reinforced concrete is becoming more common, used in the repair of bridges or other constructions that are aging. The higher price than the steel reinforced concrete is balanced by the cheaper and reduced assembly together with easier transportation. Some factors that can determine an increase use for the future applications are the reduction of the costs of carbon concrete and the development of standards and regulations.

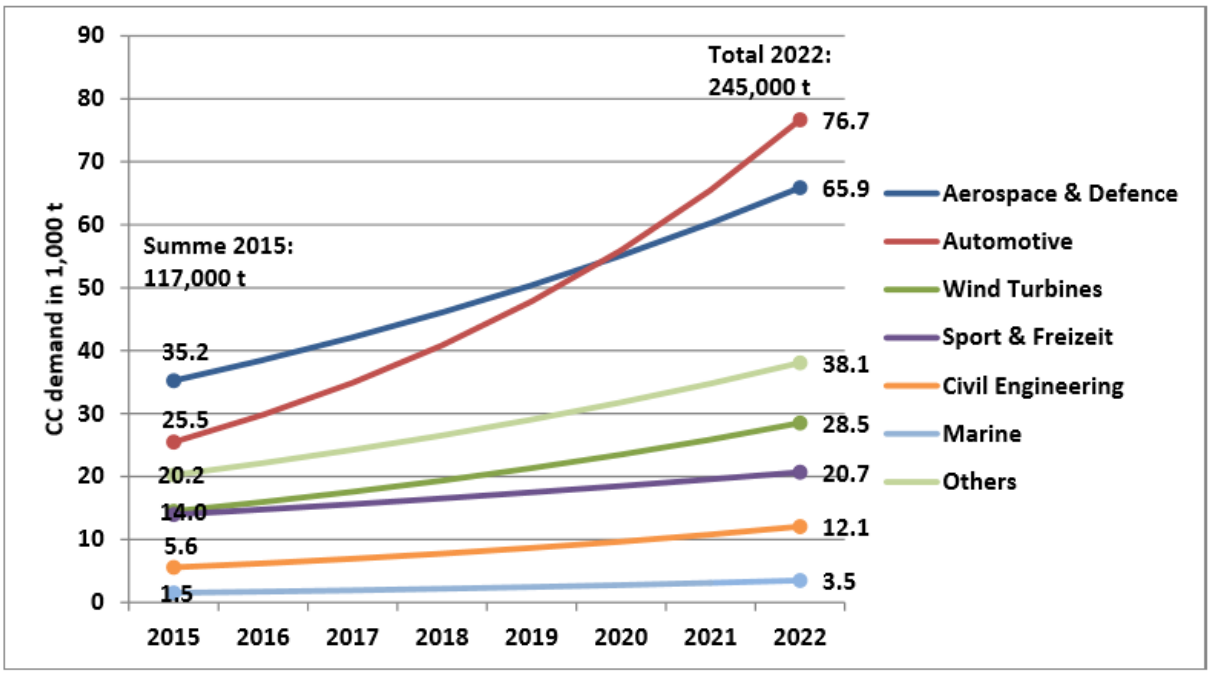

Figure 1.4 Predicted CC demand in 1000 tonnes according to application until 2022.

1.3. Fatigue of composite materials

The increased use of composite materials, especially in structural components, has not always gone together with the knowledge of the response of the material during in-service loading conditions.

An example is the American Airlines 587 plane accident, November 2001, when an Airbus A300 crashed due to the fall of the tail fin after the take-off. Successive investigations, conducted by ultrasonic tests, revealed the presence of a flaw in correspondence of the tail connection with the fuselage, grown due to the prolonged and repeated excessive maneuvers of the driver in response to a turbulence.

It is now well known that composites are prone to fatigue failure.

Research into this field has a long history. The first works appeared in the 1950s and 60s, by Boller [3], who studied the fatigue behaviour of glass-reinforced plastics, Owen and collaborators [4], who studied carbon-fibre reinforced plastics while Baker and co-workers [5], focused on metal matrix composites.

The research focused soon on the understanding of the damage mechanisms that occur during fatigue life, which was a prerequisite for the enhancement of the performance of composites. Remarkable were the contributions given by the authors Reifsnider [6] and Talreja [7].

The tendency to generalize *a priori* the consolidated methodologies of design for metals subjected to fatigue loading to composite materials is an erroneous practice.

The heterogeneity and anisotropy intrinsic to the nature of composite materials are the factors that differ the composite materials from the monolithic materials, such as metals or ceramics.

These generally fail due to unstable growth of a crack while the heterogeneous internal structure of a composite leads to the formation of multiple damage mechanisms.

The complexities of damage observed under quasi-static loading increase when the loading applied is cyclic. The variety of parameters affecting the governing mechanisms (e.g. constituent properties, ply orientation, architecture of the reinforcement) may lead to the risk of a fatigue design empirically based, while a mechanism based modeling should be adopted.

From the early 1970s, important progresses in understanding damage mechanisms have been made, thanks to the advance of non-destructive observation techniques. This has made possible the development of tools and methodologies for the prediction of the fracture and fatigue of composite materials. However, fatigue damage modeling and life prediction still need a great deal of further work.

Design against fatigue, which is essential to improve the reliability of composite structural parts, can have different goals, as follows:

i) against crack onset (no damage);

When design focuses on the prevention of any damage, the prediction of the portion of fatigue life spent for the onset of the first damage mechanisms is necessary.

ii) against stiffness loss;

There are some applications, where the safety requirements are less demanding, for which a damage tolerant approach can be accepted. The functionality of the component in service is linked with its stiffness, i.e. the component can be considered perfectly functioning until it has lost a certain amount of stiffness. In this case, the key factor for a safe design is the prediction of the stiffness loss of a component under fatigue loading.

iii) slow growth philosophy

In a slow growth philosophy, borrowed from the experience in metals, a controlled growth of damage is accepted, avoiding an overdesign and resulting in a weight saving and cheaper structures.

In this way, by planning a regular maintenance, timely repair is ensured and the safety of the structure is guaranteed.

This is possible only if designers can rely on models that accurately describe damage mechanisms formation and growth during fatigue loading. In this way, inspections can be scheduled in order to monitor the damage before its critical condition.

iv) design against failure.

The aim is to avoid the failure of the structure before a certain number of cycles. Even in this case, the designers need models that describe the entire damage evolution, taking into account the multiscale nature of the composites, as will be explained in the following paragraph.

1.4.Multiscale nature of composite materials

The heterogeneous composition of materials suggests the use of an approach multi-scale for modeling, which is based on the notion that phenomena occurring at lower length scales determine the response of the material at higher levels (see Figure 1.5).

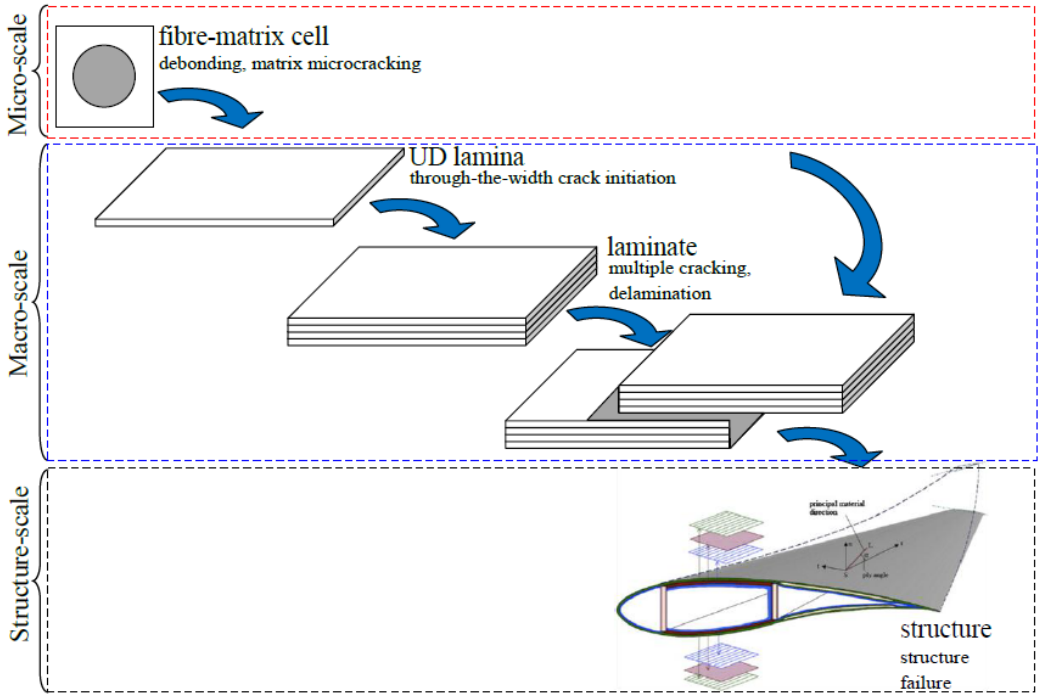

Figure 1.5 The multiscale nature of composite materials: length scales and related constituents and damage mechanisms.

The lowest level that can be identified (micro-scale level) corresponds to the fibre-matrix unit cell. At this scale, the damage mechanisms are represented by the formation of debonds and matrix microcracking.

The intermediate level (macro-scale level) corresponds to the unidirectional lamina. The damage mechanism consists of formation of macro cracks, due to the coalescence of debonds and microcracks.

Multidirectional laminates are made of the UD laminae stacked with different orientations. The damage present in the laminae affects the distribution of stress, which is redistributed in the adjacent layers, and this causes the formation of multiple off-axis cracks. These may lead to the onset of delaminations and act as stress concentration for load bearing plies, causing the final failure of the laminate.

The higher level is represented by the structures, made of unidirectional or multidirectional laminates. Their failure or degradation is due to the hierarchical failure of the constituents that belong to the smaller length scales

It is clear that the prediction of failure of structures should be based on the prediction of damage initiation and evolution at the smaller length scales.

1.5.Summary of previous results

The DTG research group has dedicated many years to the study of damage evolution under fatigue and definition of procedure for its prediction [8], [9]. It is important to clarify the achievements obtained for understanding the contents and aims of the present work.

In the following paragraph, the results obtained will be briefly described, for further details the reader is referred to the references.

A criterion for the initiation of matrix cracks for UD laminae subjected to fatigue loading was proposed, based on the calculation of the Local Maximum Principal Stress (LMPS) in the matrix and the Local Hydrostatic Stress (LHS). Depending on the entity of the shear stress component, the maximum value of the LHS (when the shear stress is negligible) or LMPS (when the shear stress is significant). The criterion was validated by recalculating the fatigue curves relative to different multiaxial loading conditions and the results confirmed that the curves collapsed in a single scatter band.

Then a model based on the shear lag approach was developed, in order to determine the elastic properties of Young's modulus and Poisson's ratio of symmetric laminates in the presence of cracks, taking into account the mutual interaction.

Finally, the weighted crack density evolution was predicted through an iterative procedure. Given a step of cycles ΔN:

i) Calculation of the stresses in each lamina;

ii) Calculation of local stresses modelling a fibre matrix unit cell;

iii) Determination of LHS and LMPS;

iv) Calculation of the total density of nucleated cracks, using the LMPS and LHS master curves;

v) Determination of the weighted crack density by analyzing the propagation of nucleated cracks;

Then the ΔN is increased and, considering the updated crack density, the procedure is repeated.

Many efforts have been spent on studying the initial phase of damage, consisting on the formation of matrix cracks. However, these lead to the formation of further damage mechanisms, such as the initiation and growth of delaminations between adjacent layers. Delaminations have an important role, since affect the stress distribution, cause further stiffness loss and may lead to the final failure of the laminate.

In the following section, the issue of delamination will be briefly discussed.

1.6. Delamination

Laminate structures are one of the most common forms in which composite materials are used, based on the stacking at different orientations of layers of unidirectional fibers.

One of the main mode of failure of laminates consists of delamination, i.e. the separation along the interface of adjacent laminae. These are due to the high values of interlaminar stresses caused by different factors, such as free edge effects, structural discontinuities, moisture and temperature

variations, or may be caused by other internal damage mechanisms, such as matrix cracks, as above mentioned.

A schematic representation of the configurations adopted that can lead to the occurrence of delaminations is reported in Figure 1.6, taken from [10]. These can be divided into two categories:

i) Curved sections: e.g. rings, hollow cylinders, pressurized vessels;

ii) Tapers and transitions: e.g. ply drop-offs, doublers, stiffener termination.

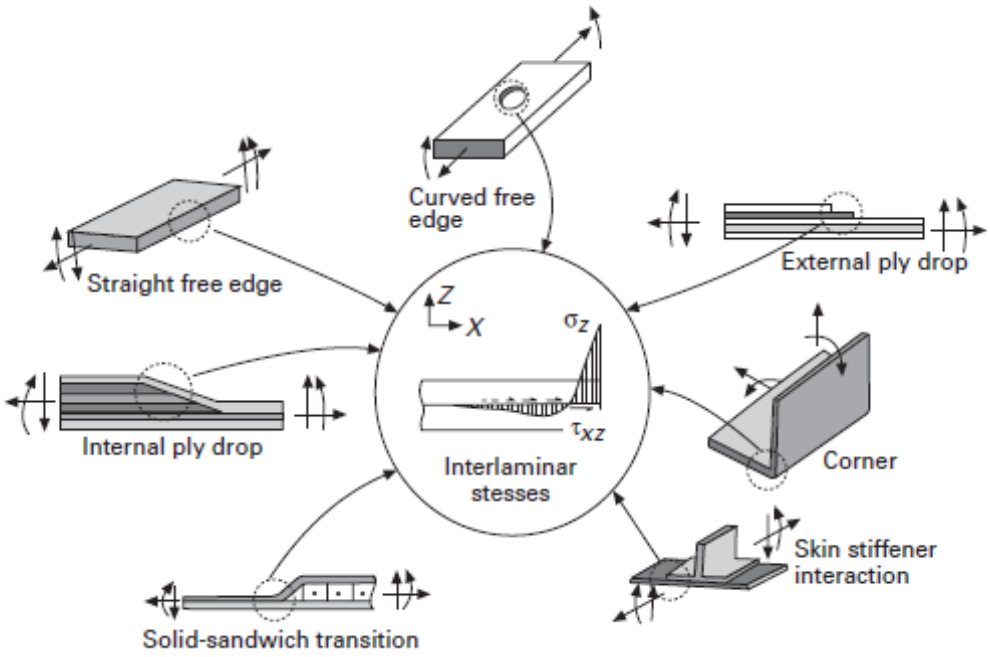

Figure 1.6 Sources of delamination: generic delamination sources; sources arising in torque box assembly (from [10] *).*

Delamination can be dangerous for the integrity and the functionality of the structure, since, hidden from the superficial visual inspection, can propagate, resulting in a reduction of the stiffness and leading to the final failure. Furthermore, the interfacial separation may lead to early buckling, vibration, intrusion of moisture.

When the aim of the design is the damage-resistance, the formation of delaminations is minimized by trying to reduce the interlaminar stresses. This is achieved by an accurate choice of the stacking

sequence, the incorporation of wrapping plies in regions with containing ply drops, avoiding the use of small radii for curved sections and the use of interleaves, i.e. a thin layer tough, ductile, fibre-free resin layer to reduce the interlaminar stresses. Conversely, when the aim is the damage tolerance, transverse reinforcements are incorporated into the microstructure of the composite, such as Z-pins and stitching. However, the addition of the transverse reinforcement decreases the growth of delaminations, but it facilitates its initiation.

The criticality of delamination allowable depends on the different structural applications.

Consider the example of a fixed wing aircraft. Delamination has low criticality for the inboard wing skin, which is usually designed in-plane strength, while the outboard skin is designed by minimizing the gage. Differently, the mid region of the wing skin is usually designed by taking into account delamination damage tolerance criterion.

Another example is the composite rotor blades, for which the main mode of failure during qualification testing is delamination. This may lead to a reduction of the stiffness below the limits imposed by design, compromising the functionality of the blades. Usually, delaminations occur in correspondence of internal ply drop-offs. In order to avoid the modelling of all the plies of the entire rotor blade, which is computationally onerous, the common design approach aims at calculating the effective laminate strains by means of global finite element models, assuming homogenized properties for the laminate. Then, interlaminar stresses are estimated using analytical models. Delaminations are prevented using interleaves, or by opportunely modifying the local geometry or local taper angle.

It is worth to mention that in practice, damage tolerance considerations are treated empirically using expensive tests on structural subcomponents and delamination failures are not well understood, such as test programs allow to achieve adequate conservative design solutions, but not optimum.

This justifies the attention devoted to the argument since the late 1960s, when Hayashi [11], Puppo and Evensen [12] and Pipes and Pagano [13] investigated the effect of free edges. However, these studies were just theoretical and did not take into account the characterization of the phenomena.

A comprehensive study of the delamination problem should take into account different aspects:

i) an investigation on the principles that govern the formation of delamination and their interaction with other damage mechanisms;
ii) definition of factors affecting the onset and propagation of delaminations;
iii) development of strategies and tools for the assessment of delamination initiation and growth under typical loading scenarios.

1.7.Objective of the present thesis

The present work is focused on the investigation of delamination initiation and growth, both under quasi-static and fatigue tensile loading.

As regards quasi-static loading, the results of an experimental campaign, conducted on cross-ply laminates with the aim of investigating the initiation of delaminations induced by transverse cracks, are presented in Chapter 2. Here, a criterion based on the fracture mechanics is proposed and then validated, with the aid of FE analyses. The comparison of the theoretical predictions with data, both collected from the experimental campaign and the literature, confirmed the validity of the approach.

Then, the analytical method proposed for calculating the stress fields in the closeness of transverse cracks, based on the Lekhitskii's formulation, is developed for being suitable to be applied also to generic stacking sequences, different from the cross-plies (Chapter 3).

The problem of delamination formation under fatigue loading is addressed in the following chapters. The results of experimental tests, carried out on cross-ply laminates, aimed at understanding damage evolution are presented in Chapter 4.

Energy Release Rate (ERR) was identified as the driving force for delamination propagation. FE analyses were carried out to calculate the ERR through the Virtual Crack Closure Technique (VCCT). Then, the delamination growth rate was described by means of a power-law equation, obtaining a Paris like curve in terms of ERR. Since the data fitted with the power law equation presented a wide scatter band, the curve was recalculated, relating the growth rate with the average value of the first principal stresses, determined in a process zone located in front of the delamination tips (Chapter 5).

Delamination evolution investigation was generalized to laminates characterized by interfaces different from 0°/90°. Both balanced and unbalanced laminates were manufactured and fatigue tested, monitoring and documenting damage evolution (Chapter 6).

Furthermore, the outcomes of the numerical analyses, performed in order to calculate ERR are reported in Chapter 7, where delaminations formed in the proximity of free edges are treated separately with respect to those developed in the interior part of the specimens.

Finally, Chapter 8 presents a draft of a procedure for predicting the failure of cross-ply laminates due to the fibre failure.

References of chapter 1

[1] Matthews, Frank L., and Rees D. Rawlings. Composite materials: engineering and science. Elsevier, 1999.

[2] Kraus, T., Kuhnel M. (CCeV). Market report: “The global CRP market”, 2016.

[3] Boller, K. "Fatigue fundamentals for composite materials." Composite Materials: Testing and Design. ASTM International, 1969.

[4] Owen, M. Y. "Fatigue of carbon-fiber-reinforced plastics." Composite materials 5 (2016): 341-369.

[5] Baker, A. A. "The fatigue of fibre-reinforced aluminium." Journal of Materials Science 3.4 (1968): 412-423.

[6] Reifsnider, K. L., ed. Fatigue of composite materials. Vol. 4. Elsevier, 2012.

[7] Talreja, R. Fatigue of composite materials. Technomic, 1987.

[8] Carraro P.A., Quaresimin M.. "A damage based model for crack initiation in unidirectional composites under multiaxial cyclic loading", Compos Sci Technol 2014, 99, 154–163

[9] Carraro P.A., Quaresimin M.. "A stiffness degradation model for cracked multidirectional laminates with cracks in multiple layers". Int J Solids Struct 2015, 58, 34–51.

[10] Sridharan, Srinivasan, ed. Delamination behaviour of composites. Elsevier, 2008.

[11] Hayashi, T. "On the law of mixture of creep strength of fiber reinforced composite materials (Law of mixture governing creep strength of composite materials reinforced unidirectionally by continuous filaments, taking into account fibers and matrix viscoelastic properties)." japan society for aeronautical and space sciences, transactions 10.17 (1967): 54-58.

[12] Puppo, A. H., and H. A. Evensen. "Interlaminar shear in laminated composites under generalized plane stress." Journal of composite materials 4.2 (1970): 204-220.

[13] Pipes, R. Byron, and N. J. Pagano. "Interlaminar stresses in composite laminates under uniform axial extension." Journal of Composite Materials 4.4 (1970): 538-548.

2. Delamination onset in symmetric cross-ply laminates under static loads: theory, numerics and experiments

2.1 Introduction

The initiation and growth of delaminations, often preceded and triggered by matrix cracking, is one of the dominant failure mechanisms in composite laminates, both under static and fatigue loadings. The presence of off-axis cracks and delaminations typically causes a more or less pronounced stiffness loss and contributes to the complete failure of structural components made of composite materials. For this reason, understanding the formation and growth of delaminations is a matter of primary concerns in the design of composite parts, justifying the large attention devoted by several authors to this subject, either by the experimental or theoretical point of view.

In the following, without the ambition to provide a comprehensive literature review, a brief summary of the past and recent investigations on this topic is presented, focusing the attention on the papers that are more strictly related to the analysis carried out in the present chapter.

One of the pioneering experimental studies on this topic is that of Rodini and Eisenmann [1], who carried out quasi-static tensile tests on different laminates and tried to provide insights on the main variables influencing such a phenomenon.

Some years later, Crossman et al. [2] and Wang [3] performed an extensive experimental campaign on $[\pm 25/90_n]_s$ graphite/epoxy laminates, discussing the effect of the thickness of the 90° plies.

Independently, O' Brien [4] studied the delamination onset and growth in $[\pm 30/\pm 30/90/90]_s$ laminates tested under quasi-static and tension-tension fatigue loadings and concluded that an Energy Release Rate (ERR) based approach was effective to predict the initiation of delaminations.

The delamination onset on $[0_n/\pm 15_n]_s$ laminates under quasi-static loadings was studied by Brewer and Lagace [5] whereas the propagation of delaminations under mode I, II and mixed mode was extensively studied by Hojo and co-workers [6]-[8] and Anderson and co-authors [9]-[10], who

proved the suitability of the ERR or the stress intensity factor as the driving force for the static and fatigue propagation.

More recently, Takeda and Ogihara [11]-[12] carried out quasi-static tests at different temperatures and studied the delamination onset from transverse cracks in $[0/90_n/0]$ laminates, also developing a shear lag stress analysis to predict the stiffness loss including the contribution of delaminations.

Differently, Zubillaga et al. [13], carried out tensile tests on carbon-epoxy laminates with five different lay-ups, namely $[45_3/-45_3]_s$, $[60_3/-60_3]_s$, $[60_4/-60_4]_s$, $[45_2/-45_2/-60_4/45_2/-45_2/60_4]_s$ and $[45_2/-45_2/90_4/45_2/-45_2/90_4]_s$, and provided a detailed analysis of the damage mechanisms and their interaction.

On parallel tracks, over the years, several modelling activities, either analytical or numerical, have been carried out, with the main aim to predict the initiation and growth of delaminations (see Refs. [14]-[18] , among the others, or Refs. [19]-[20] for a more comprehensive literature review).

Stress values, as computed by a shear lag analysis, were used to formulated predictive criteria by Dharani and Tang [21], Kashtalyan and Soutis [22] and Berthelot and Corre [23].

Differently, Nairn and Hu [24] and Rebière and Gamby [26] extended the variational analysis proposed by Hashin [25] in order to account for the presence of delaminations and determined the Energy Release Rate associated to the delamination process, whilst Zhang and Minnetyan [27] adopted a displacement-based variational approach to predict the longitudinal Young's modulus degradation as a function of crack density and the delamination length.

It is worth mentioning that the shear lag and the variational analyses provide approximated solutions, which are not reliable for calculating the local stress fields in the neighbourhood of crack tips. In addition, the ERR associated to a delamination, calculated with those approaches, does not contain any information about the mode mixity, which is an essential parameter to account for when predicting the initiation and growth of delaminations [8]. This represents two major drawbacks of this kind of approaches.

Based on a micromechanical framework, Farrokhabadi et al. [28] devised a model to calculate stress

and displacement distributions in laminate with delaminations, valid for different lay-ups and loading conditions, whereas Johnson and Chang [29] and Zubillaga et al. [30] compared the Energy Release Rate with the fracture toughness of the interface to predict the onset of delaminations.

A modified Tsai-Wu failure criterion was proposed by Zou et al. [31] to predict delaminations initiation, whilst, to the same end, Maimí et al. [32] used a plastic-damage model in combination with a fracture mechanics based approach.

As an alternative to analytical methods, a numerical technique that has emerged in the last decades, also for the assessment of the formation and propagation of delaminations, is that based on the use of Cohesive Zone Models (CZMs) in FE analyses (see [33]-[40] and references reported therein).

The effective application of CZMs requires the definition of the cohesive law that governs the element separation, both from the qualitative (law type) and quantitative point of view, to be calibrated through a dedicated experimental procedure, as well as sophisticated non-linear FE analyses.

As highlighted in this brief literature review on the problem of initiation of delaminations, the models available so far in the literature are characterised by more or less pronounced drawbacks.

The main aim of the present work is to overcome these limitations by proposing an initiation criterion based on fracture mechanics concepts. Such a criterion is able to account for the scale effect (i.e. the influence of the ply thickness on the delamination resistance [1], [11], [12]) and easy to apply, since it does not require complicated non-linear FE analyses.

To this end, the problem related to the initiation of delaminations from the tips of existing transverse cracks in cross-ply laminates under static loadings is reconsidered, providing a comprehensive stress analysis of the problem, taking advantage of analytical and numerical tools, together with a detailed experimental study.

After some preliminary remarks, based on experimental evidences reported in the previous literature, needed to clarify the damage scenario under investigation, an explicit closed form solution for mode I, II and III stress fields near the tip of transverse cracks in cross-ply laminates is

presented, and stresses written as a function of Generalized Stress Intensity Factors (GSIFs), meant as an extension of Irwin's Stress Intensity Factor (SIF). According to Gross and Mendelson [41], the word "Generalized" is used here to specify that the singularity degree of the stress field is different from 0.5.

An extensive numerical investigation is later carried out on carbon fibre and glass fibre-epoxy laminates with the aim to verify the accuracy of the analytical solutions and to identify the effect of the material elastic properties, lay-up and crack density on the mode 1 GSIF.

Then, inspired by previous works, where the GSIFs were successfully used to predict the fracture behaviour for different fields of application [42]-[60], a fracture criterion based on a critical value for the mode 1 GSIF is proposed to assess the delamination onset in cross-ply laminates under tension.

Moving to the experimental activity, a number of quasi static tests is carried out on glass fiber-epoxy $[0/90_2]_s$ and $[0_2/90_4]_s$ specimens with the twofold aim to study experimentally the delamination initiation at the 0°/90° interface and to produce some data to validate the criterion proposed for the delamination initiation.

Eventually, a bulk of experimental data taken from the literature is reconsidered and used to further validate the fracture criterion proposed.

2.2 Damage scenario under investigation

In this work the attention is focused on symmetric cross-ply $[0_m/90_n]_s$ laminates under static loads, for which it is acknowledged in the literature [11], [12], [61], [62] that the first event of damage is the formation of transverse cracks in the 90° plies, growing across the whole ligament. Increasing the applied load results in multiple cracking phenomena and in the onset of delaminations at the 0/90 layer interfaces, close to the tip of transverse cracks. Such a damage evolution is schematically represented in Figure 2.1.

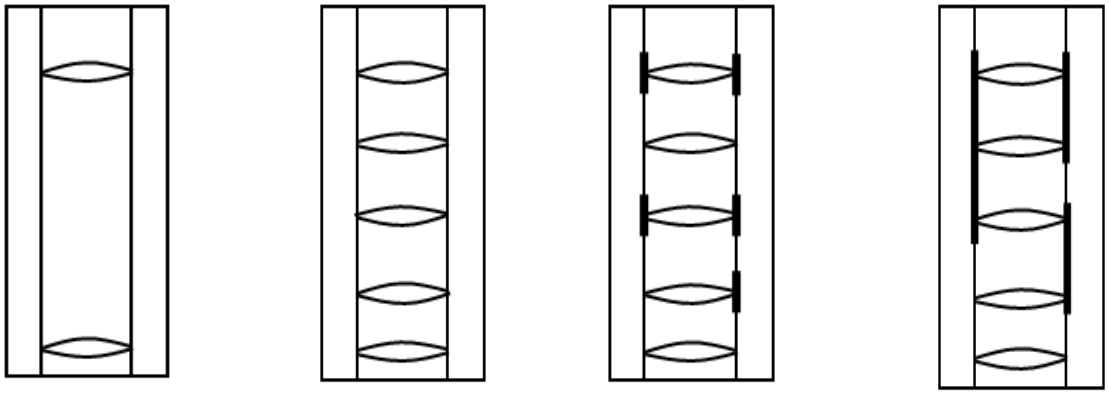

Figure 2.1 Schematic of the damage evolution in a cross ply laminate under a quasi-static load.

With the aim to develop a damage-based model to predict the initiation of delaminations from transverse cracks the schematic shown in Figure 2.2 is considered.

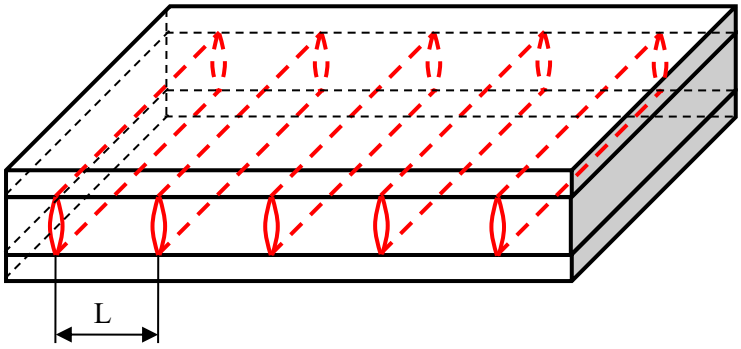

Figure 2.2 Schematic of the damaged cross-ply laminate $[0/90_n]_s$.

In particular, a regular pattern of uniformly distributed cracks in the 90° plies is thought of as representative of the phenomenon of matrix cracking. In this way, the distance from two adjacent cracks, L, can be used to quantify the crack density, $\rho=1/L$. This allows the analysis of the singular stress field at the tip of transverse cracks to be significantly simplified by considering a laminate segment of length L, only (see Figure 2.3).

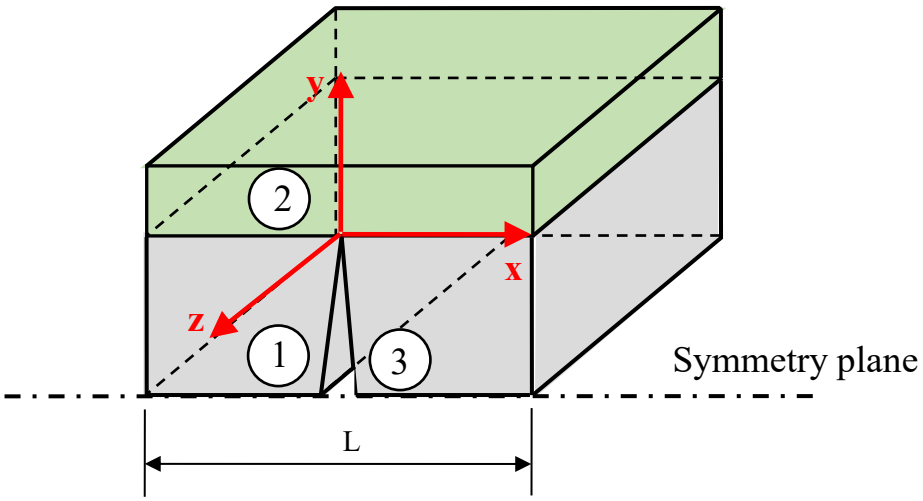

Figure 2.3 Schematic of the laminate segment of length L comprised between two transverse cracks.

2.3 Stress analysis

2.3.1 Preliminary remarks

Stress distributions around a crack normal to and terminating at an interface of two joined isotropic, orthotropic and anisotropic materials were already studied in the literature by several authors (see for example Refs. [63], [64] and references quoted therein). The problem of a composite laminate containing a layer with a crack that does not terminate at the interface was also addressed in the past [65], [66]. However, despite such an intense scrutiny, explicit expressions for the asymptotic stress field for such a problem are still missing in the literature, thus motivating the following sections where a comprehensive analytical study is carried out on the cracked geometry sketched in Figure 2.3. As evident, the domain under investigation is a multi-material one, where three different zones do exist. In particular, the 90° ply is divided into two regions (1 and 3) at each side of the crack, whilst the 0° ply is fully included in region 2. Taking advantage of a Cartesian coordinate system centred at the crack tip, an orthotropic material behaviour can be used to describe the stress-strain relation in all regions, according to the following expressions:

$$\begin{Bmatrix} \varepsilon_{xx} \\ \varepsilon_{yy} \\ \varepsilon_{zz} \\ \gamma_{yz} \\ \gamma_{xz} \\ \gamma_{xy} \end{Bmatrix} = \begin{bmatrix} \frac{1}{E_x} & -\frac{\nu_{yx}}{E_y} & -\frac{\nu_{zx}}{E_z} & 0 & 0 & 0 \\ -\frac{\nu_{xy}}{E_x} & \frac{1}{E_y} & -\frac{\nu_{zy}}{E_z} & 0 & 0 & 0 \\ -\frac{\nu_{xz}}{E_x} & -\frac{\nu_{yz}}{E_y} & \frac{1}{E_z} & 0 & 0 & 0 \\ 0 & 0 & 0 & \frac{1}{G_{yz}} & 0 & 0 \\ 0 & 0 & 0 & 0 & \frac{1}{G_{xz}} & 0 \\ 0 & 0 & 0 & 0 & 0 & \frac{1}{G_{xy}} \end{bmatrix} \begin{Bmatrix} \sigma_{xx} \\ \sigma_{yy} \\ \sigma_{zz} \\ \sigma_{yz} \\ \sigma_{xz} \\ \sigma_{xy} \end{Bmatrix} \qquad (1)$$

where E_x, E_y and E_z, are the longitudinal elastic moduli, G_{xy}, G_{yz} and G_{xz} are the shear moduli and ν_{xy}, ν_{xz} and ν_{yz} the Poisson's ratios.

Generally speaking, due to the superposition of the possible loads applied to a laminate, the crack tip can be subjected to all the three principal loading modes (I, II and III).

In the following, the three-dimensional problem under investigation is simplified by the adoption of two-dimensional analyses. In particular, the plane strain assumption is used to study mode I and II stress distributions, whereas the mechanical model of antiplane shear is adopted for the mode III problem.

This choice is also supported by recent findings in the three-dimensional analysis of orthotropic solids, according to which a general 3D problem with stress singularities can be simplified by solving, separately, the plane strain and the antiplane strain problems ([67], [68]).

2.3.2 Mode I and II stress fields

For each of the considered sub-domains (1,2,3) the following complex variables can be defined:

$$z_{1,k} = x + \mu_{1,k} y = r \rho_{1,k} e^{i\theta_{1,k}} \qquad z_{2,k} = x + \mu_{2,k} y = r \rho_{2,k} e^{i\theta_{2,k}} \qquad (2)$$

The subscript (k) allows one to make distinction between the three regions (k=1,2,3).

The following relationships hold also valid:

$$\rho_{j,k} = \sqrt{\cos\theta^2 + \left(\beta_{j,k}\sin\theta\right)^2} \qquad \theta_{j,k} = \mathrm{Arg}\left(\cos\theta + i\beta_{j,k}\sin\theta\right) \tag{3}$$

where $\mu_{1,k} = i\beta_{1,k}$, $\mu_{2,k} = i\beta_{2,k}$ ($\beta_{1,k}, \beta_{2,k} > 0$) are the conjugate roots of the following equation [69]:

$$B_{11,k}\mu^4 + (2B_{12,k} + B_{66,k})\mu^2 + B_{22,k} = 0 \tag{4}$$

In Eq. (4) B_{ij} are the coefficients of the reduced compliance matrix:

$$B_{ij,k} = S_{ij,k} - \frac{S_{i3,k}S_{j3,k}}{S_{33,k}} \tag{5}$$

Stress and displacement fields can be written in terms of two complex functions as follows [69]:

$$\begin{aligned}
\sigma_{rr,k} &= 2\,\mathrm{Re}\left\{\sum_{j=1}^{2}\left(m_{j1rr,k} + i m_{j2rr,k}\right)\phi'_{j,k}(z_{j,k})\right\} \\
\sigma_{\theta\theta,k} &= 2\,\mathrm{Re}\left\{\sum_{j=1}^{2}\left(m_{j1\theta\theta,k} + i m_{j2\theta\theta,k}\right)\phi'_{j,k}(z_{j,k})\right\} \\
\sigma_{r\theta,k} &= 2\,\mathrm{Re}\left\{\sum_{j=1}^{2}\left(m_{j1r\theta,k} + i m_{j2r\theta,k}\right)\phi'_{j,k}(z_{j,k})\right\}
\end{aligned} \qquad
\begin{aligned}
u_{r,k} &= 2\,\mathrm{Re}\left\{\sum_{j=1}^{2}\left(p_{j1r,k} + i\,p_{j2r,k}\right)\phi_{j,k}(z_{j,k})\right\} \\
u_{\theta,k} &= 2\,\mathrm{Re}\left\{\sum_{j=1}^{2}\left(p_{j1\theta,k} + i\,p_{j2\theta,k}\right)\phi_{j,k}(z_{j,k})\right\}
\end{aligned} \tag{6}$$

where [68]:

$$m_{j1rr,k} = \sin\theta^2 - \left(\beta_{j,k}\cos\theta\right)^2 \qquad m_{j2rr,k} = -2\beta_{j,k}\sin\theta\cos\theta \tag{7}$$

$$m_{j1\theta\theta,k} = \cos\theta^2 - \left(\beta_{j,k}\sin\theta\right)^2 \qquad m_{j2\theta\theta,k} = 2\beta_{j,k}\sin\theta\cos\theta \tag{8}$$

$$m_{j1r\theta,k} = \frac{1}{2}\sin 2\theta\left[1 + \left(\beta_{j,k}\right)^2\right] \qquad m_{j2r\theta,k} = -\beta_{j,k}\cos 2\theta \tag{9}$$

$$p_{j1r,k} = \left[-\beta_{j,k}^2 B_{11,k} + B_{12,k}\right]\cos\theta \qquad p_{j2r,k} = \left[B_{12,k}\beta_{j,k} - \frac{B_{22,k}}{\beta_{j,k}}\right]\sin\theta \tag{10}$$

$$p_{j1\theta,k} = \left[\left(\beta_{j,k}\right)^2 B_{11,k} - B_{12,k}\right]\sin\theta \qquad p_{j2\theta,k} = \left[B_{12,k}\beta_{j,k} - \frac{B_{22,k}}{\beta_{j,k}}\right]\cos\theta \tag{11}$$

Accurate predictions of the stress fields close to the crack tip can be obtained using the following complex functions [63, 67, 68]:

$$\phi_{1,k}(z_{1,k}) = \left(A_{11,k} + iA_{12,k}\right)\left(z_{1,k}\right)^{\lambda} \qquad \phi_{2,k}(z_{2,k}) = \left(C_{11,k} + iC_{12,k}\right)\left(z_{2,k}\right)^{\lambda} \tag{12}$$

The resulting stress and displacement fields can be written in the following form:

$$\begin{aligned}
\sigma_{ts,k}^{(j)} &= \frac{K_j}{\sqrt{2\pi}} r^{\lambda_j - 1}\left(\rho_{1,k}\right)^{\lambda_j - 1}\{\chi_{1,k}^{(j)}[m_{11ts,k}\cos\left(1-\lambda_j\right)\theta_{1,k} + m_{12ts,k}\sin(1-\lambda_j)\theta_{1,k}] \\
&+ \chi_{2,k}^{(j)}[m_{11ts,k}\mathrm{sen}\left(1-\lambda_j\right)\theta_{1,k} - m_{12ts,k}\cos(1-\lambda_j)\theta_{1,k}]\} \\
&+ \frac{K_j}{\sqrt{2\pi}} r^{\lambda_j - 1}\left(\rho_{2,k}\right)^{\lambda_j - 1}\{\chi_{3,k}^{(j)}[m_{21ts,k}\cos\left(1-\lambda_j\right)\theta_{2,k} + m_{22ts,k}\sin(1-\lambda_j)\theta_{2,k}] \\
&+ \chi_{4,k}^{(j)}[m_{21ts,k}\mathrm{sen}\left(1-\lambda_j\right)\theta_{2,k} - m_{22ts,k}\cos(1-\lambda_j)\theta_{2,k}]\}
\end{aligned} \qquad t,s=r,\theta \tag{13}$$

$$\begin{aligned}
u_t^{(j)} &= \frac{K_j r^{\lambda^{(j)}}\left(\rho_1^{(k)}\right)^{\lambda^{(j)}}}{\sqrt{2\pi}\lambda^{(j)}} \times \\
&\left\{\chi_{1,k}^{(j)}\left[p_{11t,k}\cos\lambda^{(j)}\theta_{1,k} - p_{12t,k}\sin\lambda^{(j)}\theta_{1,k}\right] - \chi_{2,k}^{(j)}\left[p_{12t,k}\cos\lambda^{(j)}\theta_{1,k} + p_{11t,k}\sin\lambda^{(j)}\theta_{1,k}\right]\right\} \\
&+ \frac{K_j r^{\lambda^{(j)}}\left(\rho_{2,k}\right)^{\lambda^{(j)}}}{\sqrt{2\pi}\left(\lambda^{(j)}\right)^2} \\
&\left\{\chi_{3,k}^{(j)}\left[p_{21t,k}\cos\lambda^{(j)}\theta_{2,k} - p_{22t,k}\sin\lambda^{(j)}\theta_{2,k}\right] - \chi_{4,k}^{(j)}\left[p_{22t,k}\cos\lambda^{(j)}\theta_{2,k} + p_{21t,k}\sin\lambda^{(j)}\theta_{2,k}\right]\right\}
\end{aligned} \qquad t=r,\theta \tag{14}$$

respectively, where the subscript j denotes the loading mode, symmetric (1) or skew-symmetric (2), Different, λ_j and coefficients $\chi_{i,k}^{(j)}$ (i=1,2) come from the solution to the eigenvalue problem resulting from the traction free conditions on the crack faces and equilibrium and compatibility conditions at the interface, namely:

$$\sigma_{\theta\theta,1}\big|_{\theta=\pi} = 0 \qquad \sigma_{r\theta,1}\big|_{\theta=\pi} = 0 \tag{15a}$$

$$\sigma_{\theta\theta,3}\big|_{\theta=-\pi} = 0 \qquad \sigma_{r\theta,3}\big|_{\theta=-\pi} = 0 \tag{15b}$$

$$\sigma_{\theta\theta,1}\big|_{\theta=\pi/2} = \sigma_{\theta\theta,2}\big|_{\theta=\pi/2} \qquad \sigma_{r\theta,1}\big|_{\theta=\pi/2} = \sigma_{r\theta,2}\big|_{\theta=\pi/2} \tag{15c}$$

$$\sigma_{\theta\theta,3}\big|_{\theta=-\pi/2} = \sigma_{\theta\theta,2}\big|_{\theta=-\pi/2} \qquad \sigma_{r\theta,3}\big|_{\theta=-\pi/2} = \sigma_{r\theta,2}\big|_{\theta=-\pi/2} \tag{15d}$$

$$u_{r,1}\big|_{\theta=\pi/2} = u_{r,2}\big|_{\theta=\pi/2} \qquad u_{\theta,1}\big|_{\theta=\pi/2} = u_{\theta,2}\big|_{\theta=\pi/2} \tag{15e}$$

$$u_{r,2}\big|_{\theta=-\pi/2} = u_{r,3}\big|_{\theta=-\pi/2} \qquad u_{\theta,2}\big|_{\theta=-\pi/2} = u_{\theta,3}\big|_{\theta=-\pi/2} \tag{15f}$$

In addition to Eqs. (15) it was imposed that:

$$\chi_{1,2}^{(1)} + \chi_{3,2}^{(1)} = 1 \tag{16}$$

and:

$$\chi_{2,2}^{(2)} \cdot \beta_{1,2} + \chi_{4,2}^{(2)} \cdot \beta_{2,2} = 1 \tag{17}$$

Eq. (16) and (17) guarantee that along the crack bisector (θ=0), Eq. (13) simplifies to give:

$$\sigma_{\theta\theta,2}(\theta = 0, r) = \frac{K_1}{\sqrt{2\pi}} r^{\lambda_1 - 1} \tag{18}$$

$$\sigma_{r\theta,2}(\theta = 0, r) = \frac{K_2}{\sqrt{2\pi}} r^{\lambda_2 - 1} \tag{19}$$

In Eqs. (13) and (14), K_j are the Generalized Stress Intensity Factors (GSIFs), which quantify the intensity of the asymptotic stress distribution close to the crack tip, and they are defined as [41]:

$$K_1 = \lim_{r \to 0} \sqrt{2\pi} \cdot \sigma_{\theta\theta}\big|_{\theta=0} \cdot r^{1-\lambda_1} \tag{20}$$

$$K_2 = \lim_{r \to 0} \sqrt{2\pi} \cdot \sigma_{r\theta}\big|_{\theta=0} \cdot r^{1-\lambda_2} \tag{21}$$

3.3 Mode III stress fields

Following the same approach used in the foregoing section, for each of the considered sub-domains (1,2,3) the following complex variable can be defined:

$$z_{3,k} = x + \mu_3 y = r\rho_{3,k} e^{i\theta_{3,k}} \qquad k=1,2,3 \tag{22}$$

where:

$$\rho_{3,k} = \sqrt{\cos^2\theta + (\beta_{3,k} \sin\theta)^2} \qquad \theta_{3,k} = \mathrm{Arg}(\cos\theta + i\beta_{3,k} \sin\theta) \tag{23}$$

and

$$\beta_{3,k} = \sqrt{S_{44,k} / S_{55,k}} \tag{24}$$

Out of plane stress and displacement fields can be written as [69]:

$$\sigma_{z\theta,k} = -2\,\mathrm{Re}\{(\cos\theta + i\beta_{3,k} \sin\theta)\phi'_{3,k}(z_{3,k})\} \tag{25}$$

$$\sigma_{zr,k} = -2\,\mathrm{Re}\{(\sin\theta - i\beta_{3,k} \cos\theta)\phi'_{3,k}(z_{3,k})\} \tag{26}$$

$$w_k = 2\,\mathrm{Re}\{i\frac{S_{44,k}}{\beta_{3,k}}\phi_{3,k}(z_{3,k})\} \tag{27}$$

Accurate predictions of the stress fields close to the crack tip can be obtained using the following complex function [67]:

$$\phi_{3,k} = (D_{1,k} + iD_{2,k}){z_{3,k}}^{\lambda_3} \tag{28}$$

The resulting stress and displacement fields can be written as follows:

$$\begin{aligned}
&\sigma_{z\theta,k} = \frac{K_3}{\sqrt{2\pi}} r^{\lambda_3-1}\left(\rho_{3,k}\right)^{\lambda_3-1}\{-\chi_{5,k}[\beta_{3,k}\sin\theta\cdot\sin(1-\lambda_3)\theta_{3,k} + \cos\theta\cdot\cos(1-\lambda_3)\theta_{3,k}] + \\
&-\chi_{6,k}[\cos\theta\cdot\sin(1-\lambda_3)\theta_{3,k} - \beta_{3,k}\sin\theta\cdot\cos(1-\lambda_3)\theta_{3,k}]\} \\
&\sigma_{zr,k} = \frac{K_3}{\sqrt{2\pi}} r^{\lambda_3-1}\left(\rho_{3,k}\right)^{\lambda_3-1}\{\chi_{5,k}[\beta_{3,k}\cos\theta\cdot\sin(1-\lambda_3)\theta_{3,k} - \sin\theta\cdot\cos(1-\lambda_3)\theta_{3,k}] \\
&+\chi_{6,k}[\sin\theta\cdot\sin(1-\lambda_3)\theta_{3,k} + \beta_{3,k}\cos\theta\cdot\cos(1-\lambda_3)\theta_{3,k}]\}
\end{aligned} \tag{29}$$

$$w = \frac{K_3}{\sqrt{2\pi}}\frac{r^{\lambda_3}\rho_{3,k}^{\lambda_3}}{\lambda_3}\frac{S_{44,k}}{\beta_{3,k}}\left\{-\chi_{5,k}\sin\lambda_3\ \theta_{3,k} - \chi_{6,k}\cos\lambda_3\theta_{3,k}\right\} \tag{30}$$

respectively, where λ_3 and $\chi_{i,k}^{(j)}$ (i=5,6) come from the solution to the eigenvalue problem resulting from the following free-of-stress, equilibrium and compatibility conditions:

$$\sigma_{z\theta,1}\big|_{\theta=\pi} = \sigma_{z\theta,3}\big|_{\theta=-\pi} = 0 \quad \sigma_{z\theta,2}\big|_{\theta=-\pi/2} = \sigma_{z\theta,3}\big|_{\theta=-\pi/2} \quad \sigma_{z\theta,2}\big|_{\theta=\pi/2} = \sigma_{z\theta,1}\big|_{\theta=\pi/2} \tag{31}$$

$$w_2\big|_{\theta=-\pi/2} = w_3\big|_{\theta=-\pi/2} \qquad w_2\big|_{\theta=\pi/2} = w_1\big|_{\theta=\pi/2} \tag{32}$$

In addition to Eqs. (31) it was imposed that $\chi_{5,2} = -1$.

In Eqs. (29) and (30), K_3 is the mode III Generalized Stress Intensity Factor (GSIF) defined according to the following expression ([70], [71]):

$$K_3 = \lim_{r\to 0}\sqrt{2\pi}\,\sigma_{z\theta}\big|_{\theta=0}\cdot r^{1-\lambda_3} \tag{33}$$

2.4 Numerical analyses

In this section, a comprehensive numerical study is carried out on cross-ply laminates with transverse cracks with a two-fold aim:

- First, to verify the accuracy of the analytical solutions derived in the previous section by comparing theoretical predictions and numerical results on carbon fibre-epoxy laminates;
- Secondly, to identify the effect of the material elastic properties, lay-up and crack density on the mode 1 GSIF.

The material properties used in the numerical analyses are summarised in Table 2.1 and the corresponding values of $\beta_{i,k}$, λ_j and $\chi_{ij,k}$ are listed in Table 2.2, Table 2.3 and Table 2.4, respectively.

Table 2.1 Material properties used in the numerical analyses

	Carbon/Epoxy	Glass/Epoxy
E_1 [GPa]	128	41.4
E_2 [GPa]	7.2	13.1
E_3 [GPa]	7.2	13.1
G_{12} [GPa]	4	4
G_{13} [GPa]	4	4
G_{23} [GPa]	2.4	4.3
ν_{12}	0.3	0.3
ν_{23}	0.5	0.4

Table 2.2 Value of parameters β_I associated to the material properties listed in Table 2.1.

Carbon/epoxy	Glass/epoxy
$\beta_{1,1}= \beta_{1,3}=0.9974$	$\beta_{1,1}= \beta_{1,3}=0.9981$
$\beta_{2,1}= \beta_{2,3}=1.0026$	$\beta_{2,1}= \beta_{2,3}=1.0019$
$\beta_{1,2}=0.1801$	$\beta_{1,2}=0.3244$
$\beta_{2,2}=1.5166$	$\beta_{2,2}=1.8647$
$\beta_{3,1}=\beta_{3,3}=1$	$\beta_{3,1}=1$

$\beta_{3,2}$= 0.7746	$\beta_{3,2}$= 1.0408

Table 2.3 Linear elastic eigenvalues for the material properties listed in Table 2.1.

Carbon epoxy	Glass epoxy
λ_1=0.65094	λ_1=0.56831
λ_2=0.52049	λ_2=0.49462
λ_3=0.45946	λ_3=0.50636

Table 2.4 Stress field parameters to be used in Eq. (13) and Eq. (29). Material properties listed in Table 2.1.

	Carbon epoxy	Glass epoxy		Carbon epoxy	Glass epoxy
$\chi_{1,1}(\lambda_1)$	45.8267	150.9396	$\chi_{1,1}(\lambda_2)$	-59.8876	-18.1264
$\chi_{2,1}(\lambda_1)$	-6.5595	-16.5396	$\chi_{2,1}(\lambda_2)$	-145.7372	-264.7065
$\chi_{1,2}(\lambda_1)$	1.1463	1.2111	$\chi_{1,2}(\lambda_2)$	0.0000	0.0000
$\chi_{2,2}(\lambda_1)$	0.0000	0.0000	$\chi_{2,2}(\lambda_2)$	-1.1659	-0.5557
$\chi_{1,3}(\lambda_1)$	45.8267	150.9396	$\chi_{1,3}(\lambda_2)$	59.8876	18.1237
$\chi_{2,3}(\lambda_1)$	6.5595	16.5396	$\chi_{2,3}(\lambda_2)$	-145.7372	-264.7068
$\chi_{3,1}(\lambda_1)$	-45.6215	-150.3858	$\chi_{3,1}(\lambda_2)$	59.6273	18.0416
$\chi_{4,1}(\lambda_1)$	6.4542	16.4189	$\chi_{4,1}(\lambda_2)$	145.7476	264.7050
$\chi_{3,2}(\lambda_1)$	-0.1463	-0.2111	$\chi_{3,2}(\lambda_2)$	0.0000	0.0000
$\chi_{4,2}(\lambda_1)$	0.0000	0.0000	$\chi_{4,2}(\lambda_2)$	0.8016	0.6330
$\chi_{3,3}(\lambda_1)$	-45.6215	-150.3858	$\chi_{3,3}(\lambda_2)$	-59.6273	-18.0389
$\chi_{4,3}(\lambda_1)$	-6.4542	-16.4189	$\chi_{4,3}(\lambda_2)$	145.7476	264.7054
$\chi_{5,1}(\lambda_3)$	-1.0023	-1.0001	$\chi_{5,2}(\lambda_3)$	-1.0000	-1.0000
$\chi_{5,3}(\lambda_3)$	-1.0023	-1.0001	$\chi_{6,1}(\lambda_3)$	-0.1284	0.0200
$\chi_{6,2}(\lambda_3)$	0.0000	0.0000	$\chi_{6,3}(\lambda_3)$	0.1284	-0.0200

FE analysis were carried out with Ansys® 13 software package, using a very fine mesh pattern close to the singularity point, in order to get the desired degree of accuracy.

Initially the attention was focused on mode 1 stress fields. To this end one, a quarter of a carbon/epoxy laminate segment of size L=20 mm, h_{90}=2 mm and h_0=3 mm was modelled (see the schematic in Figure 2.4) and a uniform displacement along the y-direction was applied on the right-hand side of the laminate segment such to obtain a resulting average tensile stress σ=100 MPa. 8 nodes isoparametric elements (PLANE 183) were used, with the plane strain option.

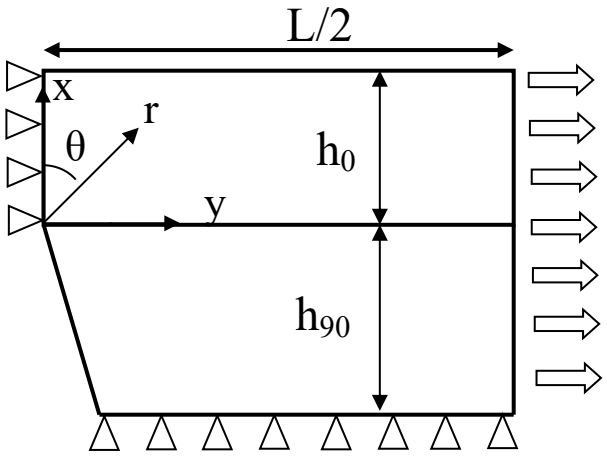

Figure 2.4. Boundary conditions in the mechanical FE model

Stresses were evaluated along a circular path of radius $r=3\cdot10^{-5}$ mm embracing the crack tip as well as along the interface of 0°and 90° plies. Numerical results are compared with the theoretical predictions given by Eqs. (13) in Figure 2.5 and Figure 2.6, where a very satisfactory agreement can be noted.

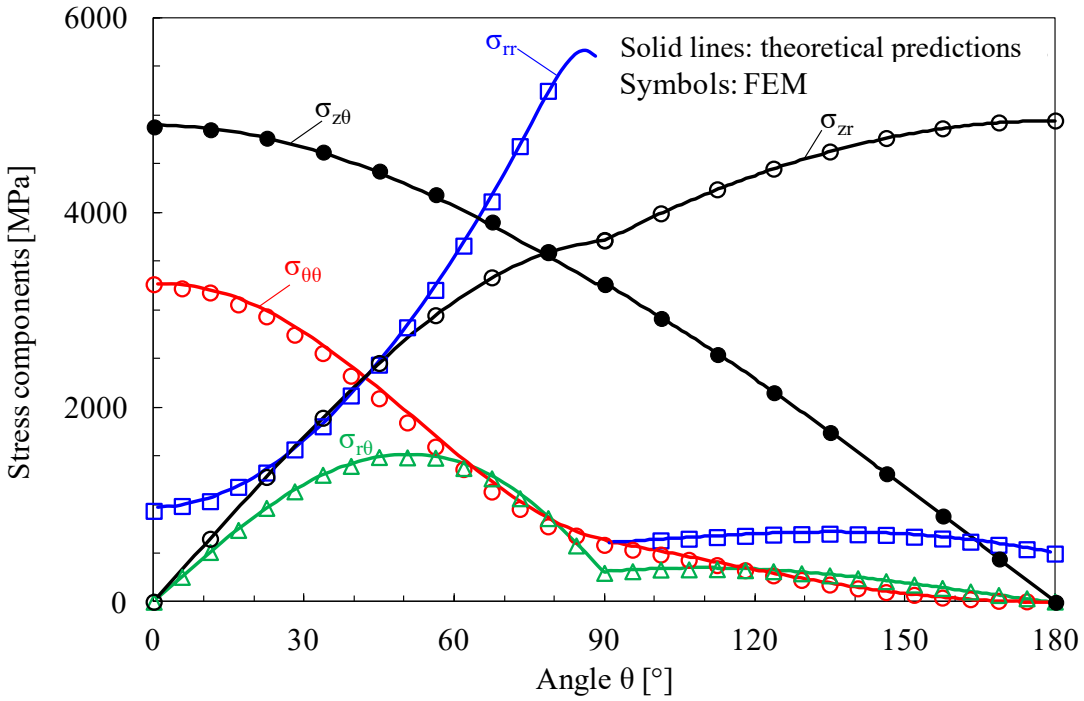

Figure 2.5 Comparison between stress fields values calculated theoretically and by FE analysis. The in-plane stress components refer to the case of a laminate subjected to a tensile stress of σ=100 MPa, while antiplane stress components are referred to the case of the laminate subjected to a τ_{yz}=5 MPa.

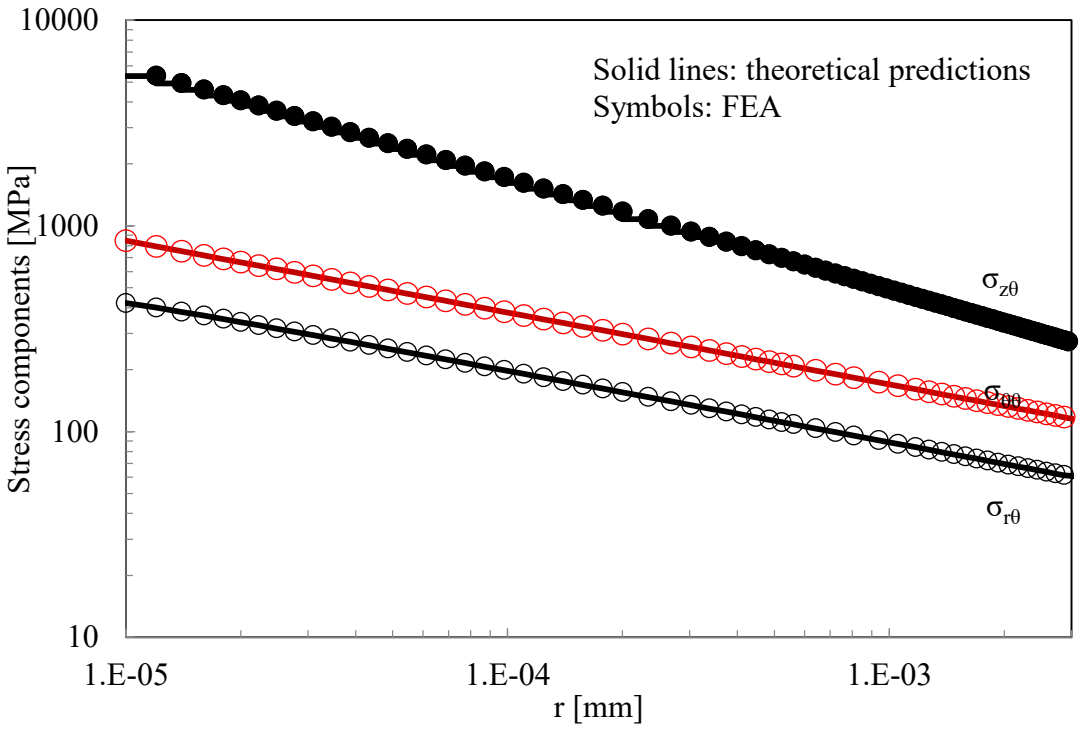

Figure 2.6 Comparison between theoretical and FE stress values, calculated at the interface of 0° and 90° plies. In-plane $\sigma_{r\theta}$, $\sigma_{\theta\theta}$ and antiplane$\sigma_{z\theta}$ components were calculated for a laminate subjected to a tensile stress of σ=100 MPa, while antiplane stress components are referred to the case of the laminate subjected to τ_{yz}=5 MPa.

In order to avoid time consuming three-dimensional FE analyses, the stress field under antiplane shear loadings were carried out invoking the analogies existing between the in-plane electrical conduction problem and the mechanical anti-plane shear problem (see Appendix for further details). Accordingly, electrical 8 nodes elements (Plane 230) were used to carry out 2D electrically conductive FE analyses on the same carbon/epoxy laminate segment described before. To this end, the conductivity values were set to equate the shear moduli of the C/E plies and an electric potential difference was applied to the FE model (see again Figure 2.7).

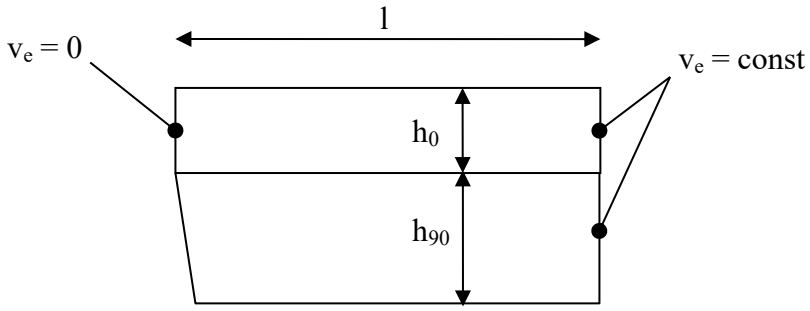

Figure 2.7 Boundary conditions in the electrical FE model

Reversing the sign to the values of the current densities so determined gives the shear stresses σ_{zr} and $\sigma_{z\theta}$, which are compared with the theoretical predictions given by Eqs. (29) in Figure 2.5 and Figure 2.6, where a very satisfactory agreement can be noted.

As mentioned before, another important aspect to be tackled is the analysis of the several parameters influencing the Generalized Stress Intensity Factor. Limiting the attention to mode 1 loadings, K_1 can be written as:

$$K_1 = \sigma \cdot k_1 \cdot h_{90}^{1-\lambda_1} \tag{34}$$

where σ is the nominal tensile stress and k_1 is a non-dimensional parameter depending on the elastic properties of the plies, the ply thicknesses and the crack density. With the aim of investigating the dependency of k_1 from these factors, a large bulk of numerical analyses was carried out. The material properties listed in Table 2.1 were used, and the h_{90}/h_0 and the $L/2h_{90}$ ratios were varied from 0.5 to 2 and from 1 to 12.5, respectively. Numerical results, shown in Figure 2.8, allow the

following conclusions to be drawn:

- increasing $L/2h_{90}$ results in a monotonic increase of k_1, till a plateau value representative of the non-interactive regime is reached, i.e. cracks are far enough to guarantee the absence of mutual stress perturbation;
- increasing h_{90}/h_0 results in an increase of k_1, independently of the considered material and the crack density;
- k_1 is greater for E-glass /epoxy laminates than for carbon /epoxy laminates.

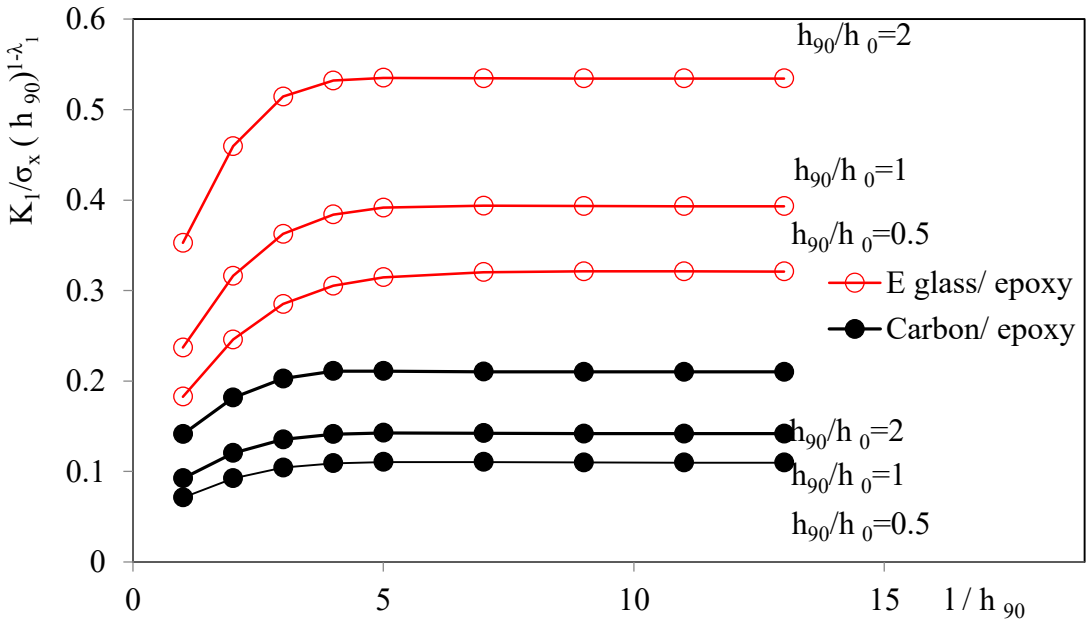

Figure 2.8 Generalized stress intensity factor normalized to the angular function and the thickness h_{90} elevated to the singularity $1-\lambda_1$ for glass/epoxy and carbon/epoxy laminates.

2.5 A criterion for the delamination onset in cross-ply laminates under tension

As mentioned in section 2.2, the first event of damage in a cross-ply laminate under static loads is the formation of matrix cracks. Increasing the applied load results in a multiplication of transverse cracks and, at the same time, in the onset of micro-delaminations, at the layers interface, reasonably promoted by the singular stress field arising close to the tip of transverse cracks. Such a kind of damage scenario corroborates the idea that the onset of delaminations is driven by the singular stress components $\sigma_{\theta\theta}$, $\sigma_{r\theta}$ and $\sigma_{\theta z}$ in the close neighbourhood of a transverse crack tip along the

interface between the plies ($\theta = \pi/2$ in Figure 2.3). Their intensity can be directly quantified using the Generalized Stress Intensity Factors, K_1, K_2 and K_3. Accordingly, any parameter to be used to predict the initiation of delaminations should be based on the GSIFs. This idea is also supported by the several successful applications of the GSIF for predicting damage onset, as discussed in the introduction.

For the simple case of a laminate under a tensile load N_y transverse to the crack faces, K_2 and K_3 are zero, and K_1 suffices to quantify the intensity of the local stress fields. Accordingly, under these circumstances, the following criterion can be formulated to predict the onset of delaminations:

$$K_1 = K_{1c} \tag{36}$$

where K_{1c} is the critical value for the GSIF, expected to depend on the interface toughness and the materials involved. As a consequence, K_{1c} must be first determined for the particular material system under analysis, and then used to predict the initiation of delaminations for different geometries (ply thickness and geometrical ratios), as usually done for conventional fracture mechanics problems.

Differently, if a general combination of external loads is applied to the laminate, inducing a mixed mode loading condition at the transverse crack tip, a more general failure criterion must be defined combining K_1, K_2 and K_3, in order to account for the multiaxial stress state at the interface. However, the formulation of such a more general approach is not within the aims of the present work and will be addressed in future works.

2.6 Experimental investigation

2.6.1 Materials and testing procedure

300x300 mm cross-ply laminates were manufactured by liquid resin infusion, using dry unidirectional glass fibres UT-E500 (500 g/m^2, Gurit) and the epoxy system Epikote RIMR235-Epikure RIMH235. The laminates were cured for three days at room temperature and then post-cured in an oven at 60°C for 12 hours. The thickness of each ply was measured to be equal to 0.34

mm.

To analyse the influence of the 90° plies thickness on the delamination onset, laminates with two different lay-ups were manufactured, namely $[0/90_2]_s$ and $[0_2/90_4]_s$. Then, 25x200 mm specimens were cut, polished on the edges and tabbed, with a final gage length of 140 mm.

Quasi-static tensile tests were later carried out on a Mini-bionix MTS 858 servo-hydraulic machine equipped with a 25 kN load cell, under displacement control, with a rate of 2mm/min. In particular, a series of load ramps were applied to the specimens. Each ramp was interrupted whenever new transverse cracks were noted, and specimens were analysed by visual inspection, taking advantage of a front-back lighting system. An optical microscope was also used to analyse the damage mechanisms with a higher degree of detail. To avoid the potential influence of the end tabs on the damage process, the observation region was restricted to a length of 60 mm across the specimen mid-length. Two tests were carried out for each laminate configuration.

2.6.2 Damage analysis and experimental results

The first visible damage event in all specimens was the onset of transverse cracks in the 90° plies, propagating unstably in the width direction.

As already discussed in the introduction, the presence of a transverse crack possibly triggers the initiation of a delamination at the 0°/90° interface. In general, this phenomenon can occur according to three different scenarios, as schematically shown in Figure 2.9.

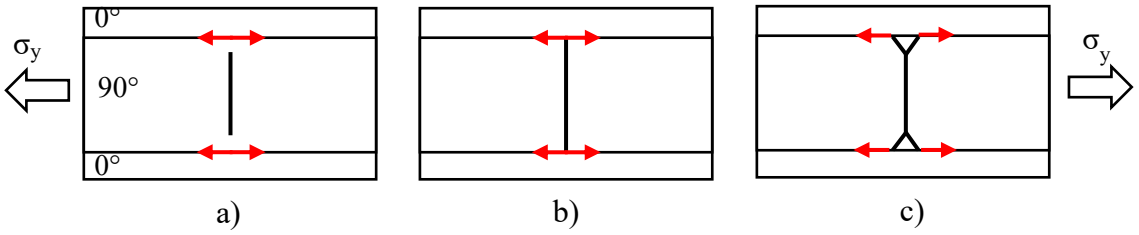

Figure 2.9 Possible delamination initiation mechanisms: a) Cook-Gordon mechanism, initiation from the tips of a b) straight and c) branched transverse crack.

The first possibility is that the delamination initiates before the transverse crack reaches the

interface, as suggested by Cook and Gordon [72] (Figure 2.9a). These authors showed that, when a crack propagates towards a bi-material interface, the peak value of the radial stress along the crack bisector is located at a certain distance from the crack tip. Therefore, as a crack approaches an interface, this peak value can be at the interface itself and its intensity is about 1/5 of that of the tangential stress in the bulk material. As this represents a peel stress for the interface, a delamination can initiate before the crack reaches the interface, provided that it is at least five times weaker that the bulk material in which the crack is propagating [73]. This scenario, known in the literature as the "Cook-Gordon mechanism", is also supported by the numerical results given by Blasquez et al. [74], Paris et al. [75]-[76] and Garcia et al. [77], suggesting that the crack should arrest at about 95% of the 90° ply thickness.

However, in the authors' opinion, the inter-laminar and the intra-laminar strength and toughness of composite laminates are, reasonably, similar, as both are controlled by the matrix and the fibre-matrix interface. Therefore, the initiation of a delamination is not expected to occur according to the Cook-Gordon mechanism.

To clarify this issue, a FE analysis was carried out on a cross-ply laminate, with a transverse crack with a length equal to the 95% of the transverse ply thickness, assuming a crack spacing of 10 mm. The thickness of the 0° and 90° plies were equal to 0.5 and 1 mm, respectively. In Figure 2.10 the stress fields along the crack bisector and the interface ahead of the crack tip are shown. It can be seen that the intensity of the tangential stress at the crack tip is one order of magnitude higher with respect to the peel stress at the interface, suggesting that the crack should not arrest. In fact, the scenario depicted in Figure 2.9a was never observed in the specimens tested during the present experimental campaign.

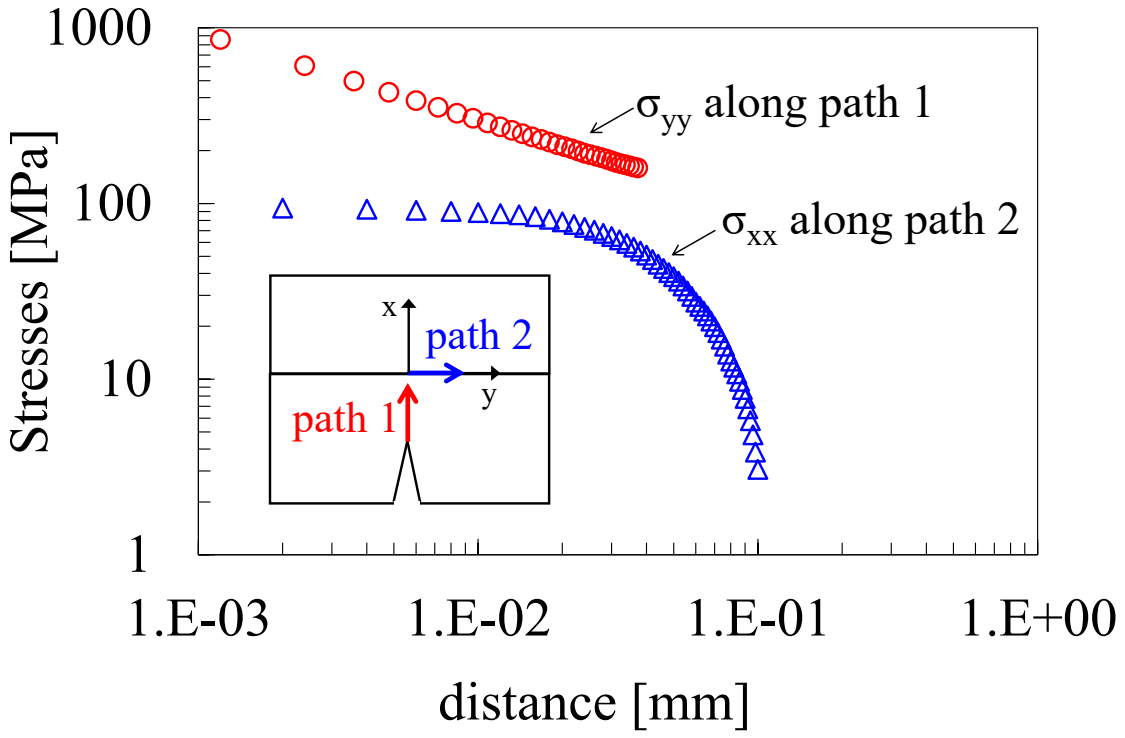

Figure 2.10 Stress fields along the crack bisector and the interface for a crack length equal to 95% of the 90° ply thickness (crack spacing = 10 mm, applied global stress σ_y = 100 MPa).

From the micrographic images taken on the edges of the specimens it can be seen, instead, that the mechanisms of crack initiation are those depicted in Figure 2.9 b and Figure 2.9 c. As shown in the examples of Figure 2.11, transverse cracks reach the interface, in a straight or branched configuration, and then delaminations initiate from their tips.

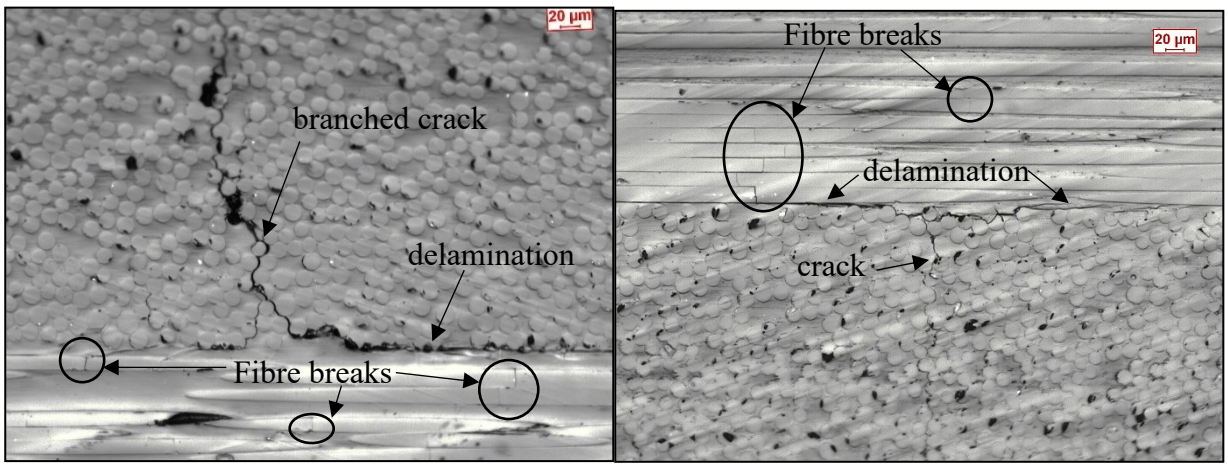

Figure 2.11 Examples of delaminations initiating from the tips of a transverse crack (branched or straight) terminating at the interface

Even if, by a strictly theoretical point of view, the analytical framework for the stress analysis presented in section 3 is relevant only to the scenario depicted in Figure 2.9 b, in which the transverse crack is straight, by a practical point of view it can be extended also to the branched configuration, whenever the branching length is limited when compared to the ply thickness. In order to support this idea, FE analyses were carried out on the same lay-up described above, modelling the geometries shown in Figure 2.9 b and Figure 2.9 c. In particular, the branched cracks were modelled with a branching angle equal to 30° and with a length of 55 μm, according to experimental observations. The stress fields at the interface for the straight and branched configurations are plotted, as a function of the distance from the crack tip, in Figure 2.12. As evident, the results are very similar, thus suggesting that the analytical framework developed in section 3 and the criterion proposed in section 5 can be reasonably used even if the crack geometry is slightly different from that of a straight crack.

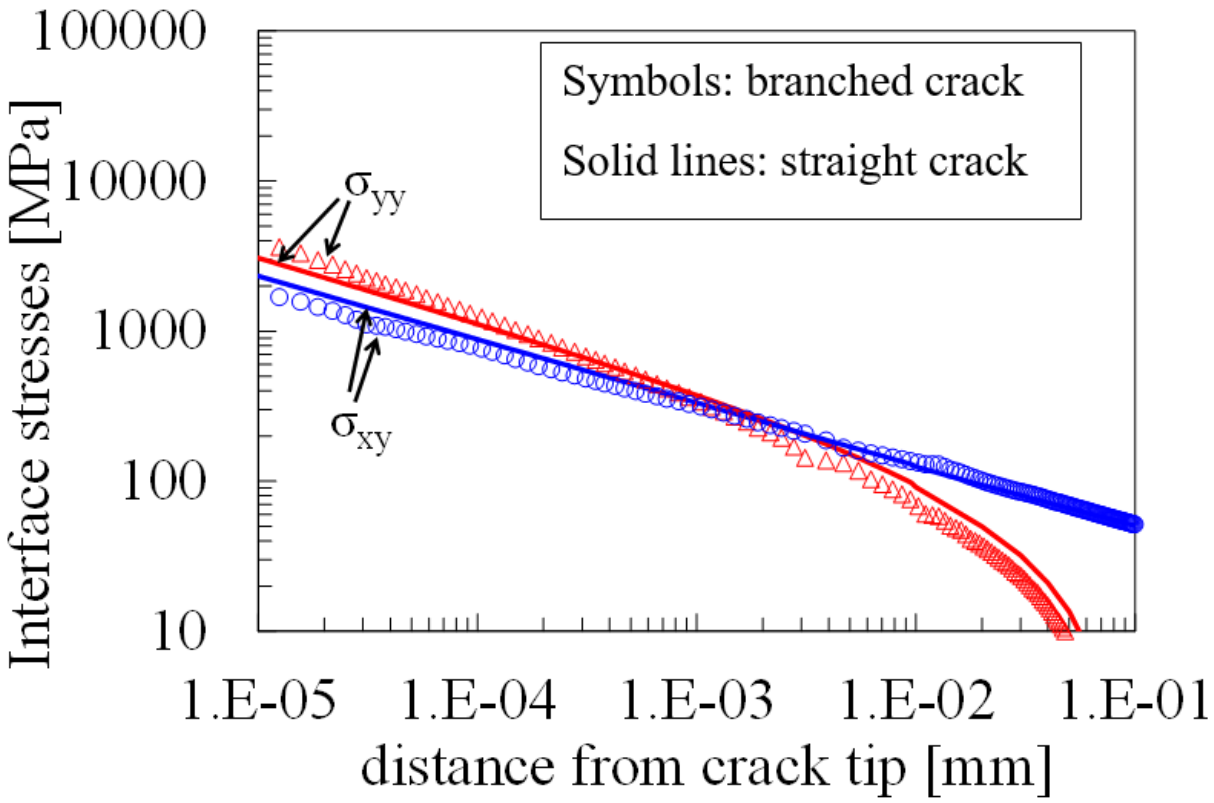

Figure 2.12 Interface stress fields in the case of straight and branched crack (crack spacing = 10 mm, global applied stress σ_y = 100 MPa).

As already discussed, the transverse cracks involved the entire 90° layer thickness and stopped at the 0°/90° interface. This lead to two main consequences (see Figure 2.11):

- the initiation of delaminations, mainly from the laminate edges (see Figure 2.13);
- the failure of the 0° fibres in the neighbourhood of the crack tips (as found also by Takeda and Ogihara [0]).

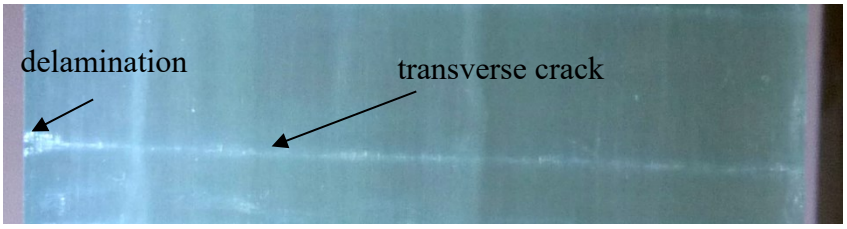

Figure 2.13 Example of delamination initiated at the edge in correspondence of a transverse crack for a $[0_2/90_4]_s$ laminate (loading direction is vertical).

The fact that delaminations were seen to initiate at the edges raised the issue about the importance of the edge effects on this phenomenon. To clarify this point, a 3D FE analysis was carried out on a cross-ply laminate with the same lay-up described above and a transverse crack terminating at the plies interface. The width of the laminate, w, was equal to 23 mm. The interface stress fields were evaluated at a distance of 0.001 mm from the crack tip, along the width of the specimen, from one edge to the mid-width. The results are shown in Figure 2.14, as a function of the distance from the edge normalised to the total specimen thickness. At the edge, the shear stress σ_{xz} is different from zero and then decreases rapidly when moving inside the specimen. However, its intensity is one order of magnitude lower than that of the peel stress σ_{xx} and the shear stress σ_{xy}. In addition, the value of these two stress components at the edge is only slightly higher with respect to the inner part of the laminate. These evidences lead to the conclusion that the stress intensification due to the edge effect is much less pronounced than that due to the presence of the transverse crack, which can therefore be considered as the main cause for the initiation of a delamination. Accordingly, the fact that delaminations were seen to initiate mainly, but not only, at the edges, may be due to the possible presence of irregularities on the edge surfaces, though the specimens were accurately

polished.

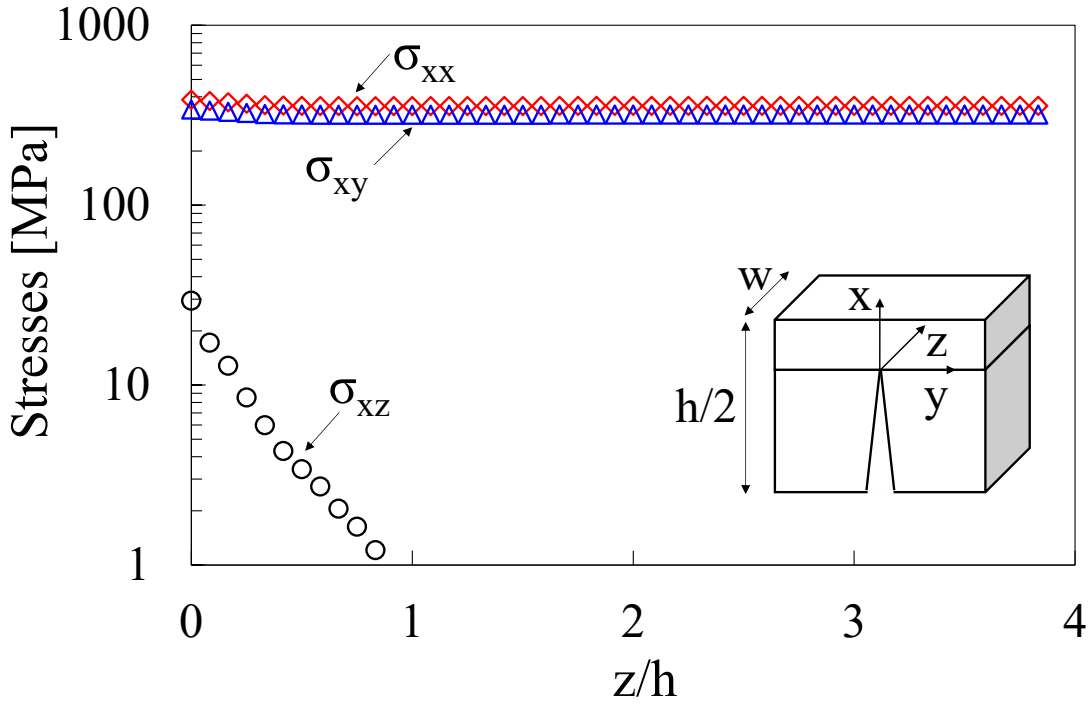

Figure 2.14 Interface stress fields at a distance of 0.001 mm from the crack tip in the 3D FE model (crack spacing = 10 mm, global applied stress σ_y = 100 MPa).

During the tests, the values of the stress and strain for the initiation of each crack and delamination were recorded. Initiations at the two edges of each specimen were considered as independent events, as there is no interaction between delaminations at opposite edges.

A summary of the measured values for the stress applied to the specimens associated to the initiation of the first transverse crack and the onset of the first delamination is reported in Figure 2.15, from which the following conclusions can be drawn:

- For the lay-ups under investigation, the number of 90° layers does negligibly influence the stress required for the initiation of the first detectable transverse crack;
- Conversely, a strong reduction of the critical stress for the first delamination initiation can be observed when the laminate thickness is increased.

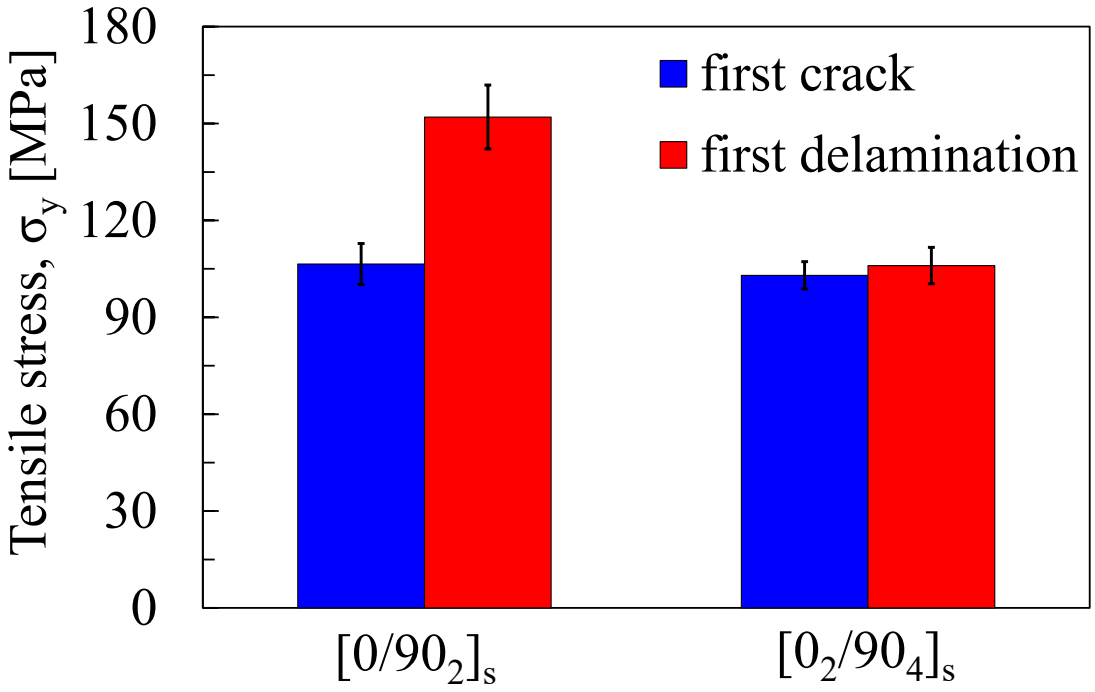

Figure 2.15 Laminate stress for the first crack and first delamination initiation

The evolution of the total transverse crack density as a function of the tensile stress applied to the specimen, σ_y, is plotted in Figure 2.16 where the stress for the initiation of the first delamination is reported as well (vertical lines). It is noteworthy that in the $[0/90_2]_s$ specimens the onset of the first delamination does occur at a much higher value of stress and crack density than for the $[0_2/90_4]_s$ samples.

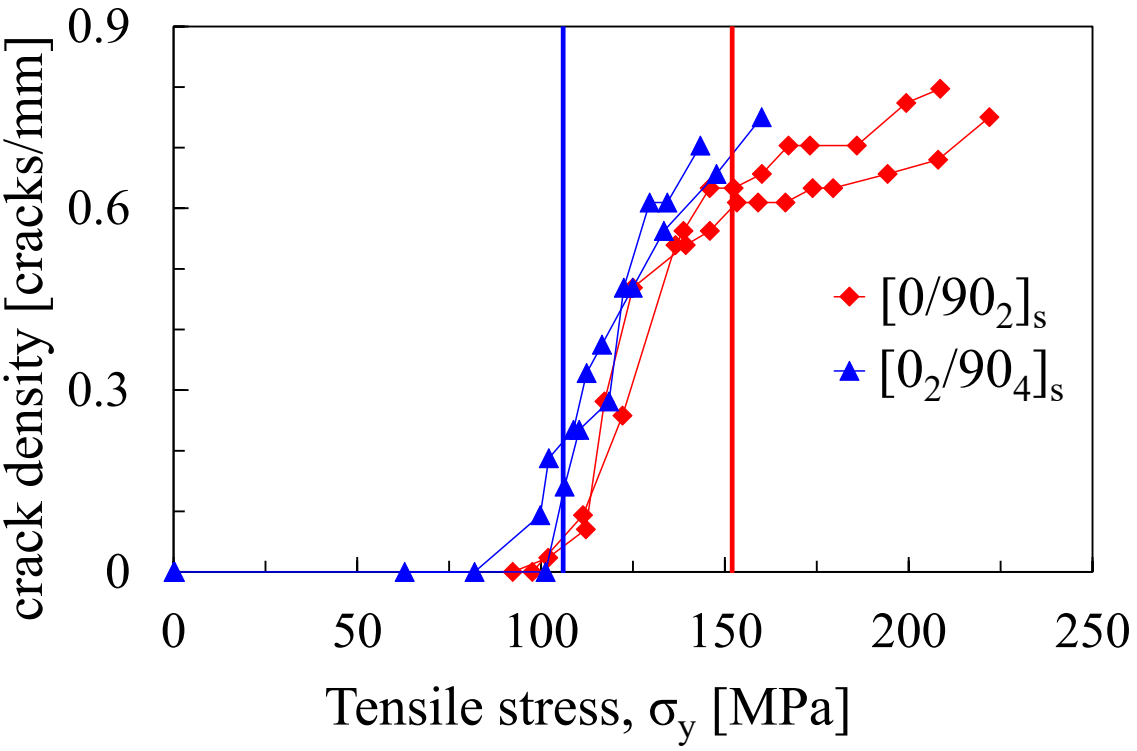

Figure 2.16 Crack density evolution and delamination initiation (vertical lines).

2.6.3 Application of the criterion for the initiation of delaminations

With the aim of validating the criterion for the delamination onset proposed in section 2.5, several FE analyses were carried out, considering the crack density and the laminate stress relevant to the initiation of each delamination. The K_I values were calculated according to Eq. (20) for all the delaminations initiated during the quasi-static tests.

The in-plane elastic properties to be used in the numerical analyses were measured by means of static tests on UD laminates with off-axis angles 0°, 45° and 90° and were found to be:

$E_1 = 48830$ MPa $E_2 = 14070$ MPa $G_{12} = 5200$ MPa $\nu_{12} = 0.308$

corresponding to

$\beta_{1,1}=0.9982$ $\beta_{1,1}=0.9982$ $\beta_{1,2}=0.3482$ $\beta_{2,2}=1.6687$ $\lambda_1=0.57769318$.

A transversely isotropic behaviour was assumed to estimate the out-of-plane elastic properties, resulting in:

$E_3 = 14070$ MPa $G_{13} = 5200$ MPa $G_{23} = 5000$ MPa $\nu_{23} = 0.4$ $\nu_{13} = 0.308$.

To enhance the statistical significance of the reported data, the stress values related to the initiation of the first ten delaminations at each edge, σ_c, were measured and reported in Figure 2.17. The figure makes it evident the presence of a scale effect on σ_c. This corroborates the idea that the initiation of delaminations at the interface of 0/90 plies is mainly driven by the local stress fields at the tip of transverse cracks, whose intensity is quantified by the mode 1 GSIF. Namely, a delamination initiates at the tips of transverse cracks when a critical value of K_1 is reached.

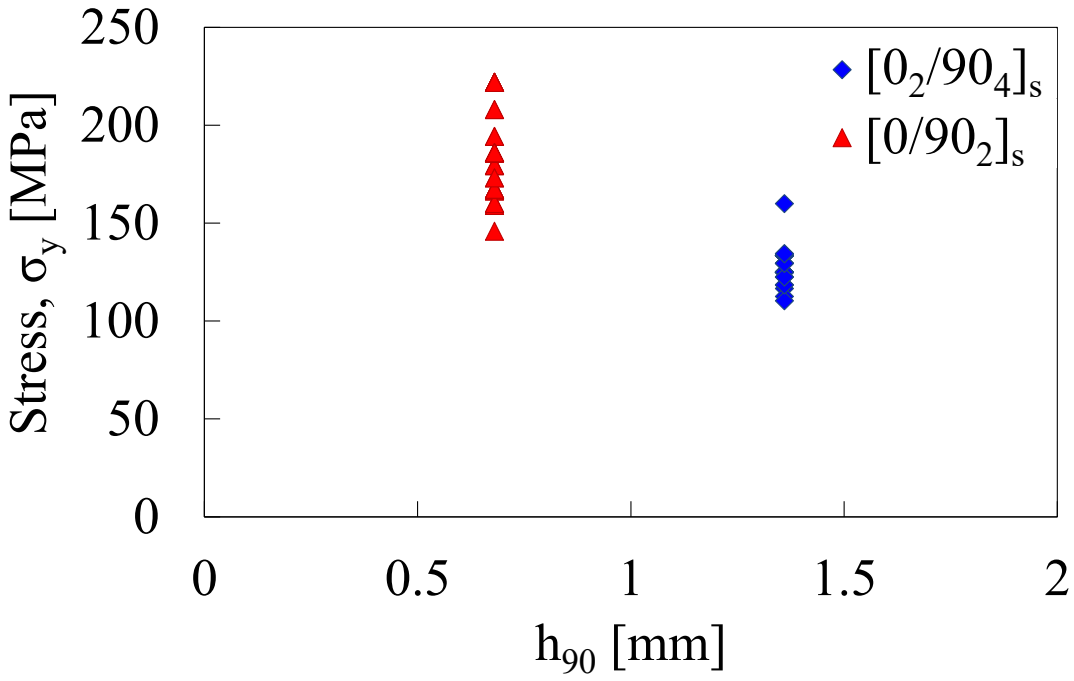

Figure 2.17 Laminate stress for the initiation of the first five delaminations at each edge.

The validity of such a conclusion is confirmed by the results shown in Figure 2.18, where the K_1 values associated to the initiation of the first ten delaminations of each edge are shown: all the data fall inside a single horizontal scatter band (mean value plus/minus two standard deviations), with an average value K_{1c} = 79.5 MPa·mm$^{0.423}$ and a limited scatter index ($T_{K1c}=K_{1c,\text{upper bound}}/K_{1c,\text{lower bound}}=1.45$).

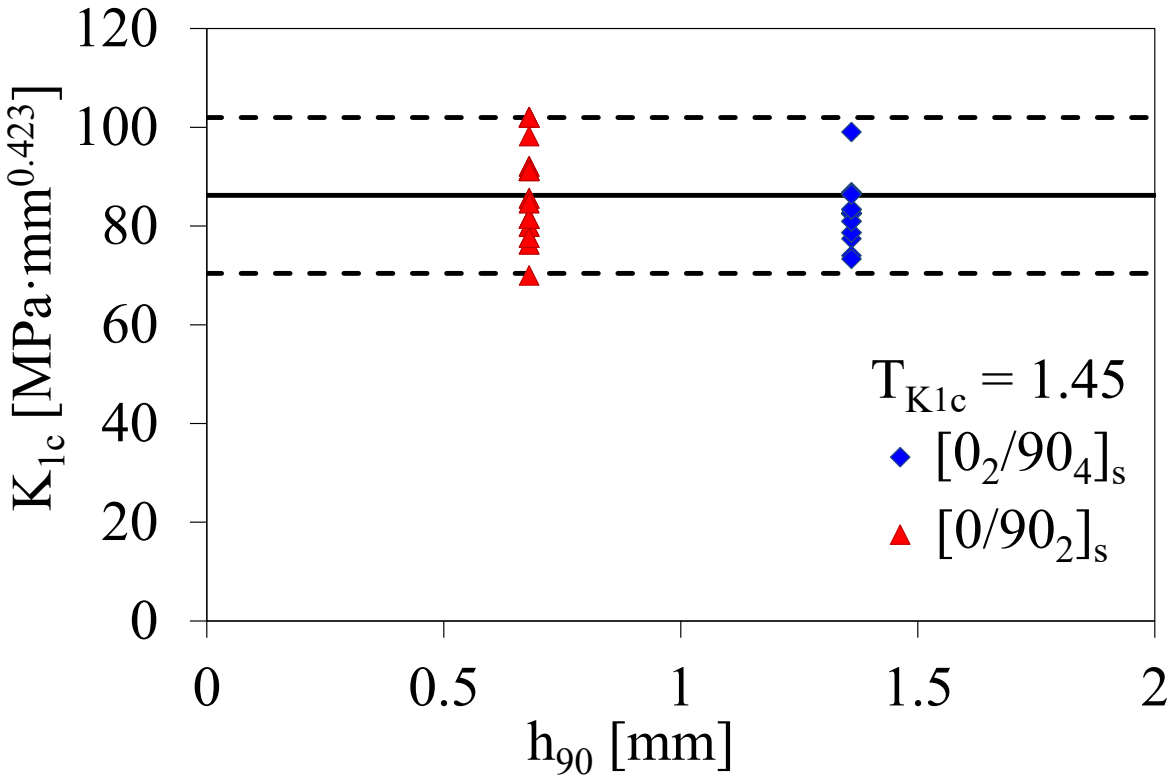

Figure 2.18 Critical GSIF for the initiation of delaminations in $[0/90_2]_s$ and $[0_2/90_4]_s$ laminates.

2.7 Analysis of data taken from the literature

In this section, experimental results taken from the literature are re-analyzed in terms of Generalized Stress Intensity Factors, in order to further verify the reliability of the GSIF-based onset criterion presented in the section 2.5.

2.7.1 Analysis of the data reported by Takeda and Ogihara

Takeda and Ogihara [11], [12] reported a set of experimental data on CFRP T800H/3631 $[0/90_n/0]$ laminates characterised by the following elastic properties:

E_1= 152.2 GPa	E_2= 9.57 GPa	E_3= 9.57 GPa
G_{12}=4.8 GPa	G_{13}=4.8 GPa	G_{23}=4.8 GPa
ν_{12}=0.31	ν_{13}=0.31	ν_{23}=0.5

The associated mode I eigenvalue is λ_1 =0.6466. The number of 90° plies was n=4, 8 and 12 and the

ply thickness was 0.132 mm. For this set of data K_1 was determined using the crack density values reported in the original work, including in the FE analyses thermal residual stresses ($\alpha_1=0.1\cdot10^{-6}$ K^{-1} and $\alpha_2=35.5\cdot10^{-6}$ K^{-1}([11]-[12])).

Experimental results are reported in terms of stress to delamination onset, σ_c (Figure 2.19a), and the associated value of K_{1c} (Figure 2.19b). The reliability of the K-based criterion for the delamination onset is clearly confirmed. Indeed, varying the number of 90° plies result in a remarkable variation of the nominal stress to delamination onset, whereas the K_{1c} is almost the same for all the series.

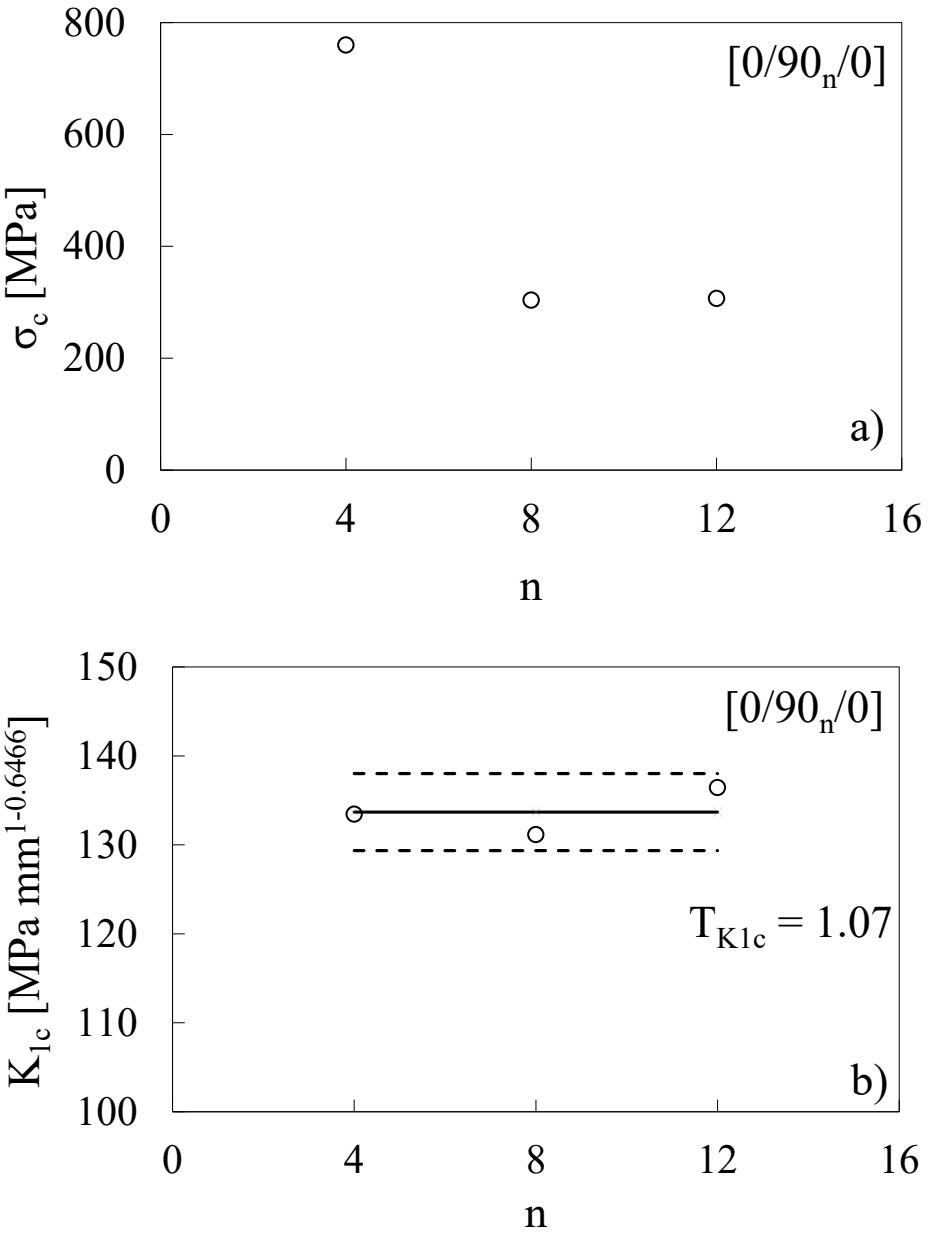

Figure 2.19 Experimental data from [11], [12] in terms of a) stress and b) GSIF for the delamination initiation.

2.7.2 Analysis of the data reported by Rodini and Eisenmann

In principle, the fracture criterion proposed in the previous section is not necessarily limited to cross-ply laminates, but can be used also to predict delamination onset on 0/90 interfaces in multidirectional laminates. In order to support this statement the experimental data from tensile tests on $[+45_n/ -45_n/0_n/90_n]_s$ (n=1,2,3) graphite epoxy laminates reported by Rodini and Eisenmann [1] were reconsidered. The elastic properties, as given in the original work [1], are:

E_1= 138 GPa E_2= 15 GPa E_3= 15 GPa G_{12}=5.9 GPa G_{13}=5.9 GPa

G_{23}=5.35 GPa ν_{12}=0.21 ν_{13}=0.21 ν_{23}=0.4

The mode I eigenvalue associated to this case is λ_1 =0.63270 and the thickness of each ply was equal to 0.15 mm.

In the original paper, the authors mentioned that delaminations occurred after some transverse cracks had initiated, without specifying the actual crack density. Accordingly, K_1 was evaluated for a low value for the crack density, implicitly assuming a non-interactive regime.

The experimental data are shown in Figure 2.20 both in terms of the stress for the delamination initiation (Figure 2.20 a) and the relevant values of K_{1c} (Figure 2.20 b). It is evident that the stress to the delamination onset, σ_c, is remarkably affected by the number of 90° plies. Notwithstanding this, when plotting the experimental data in terms of GSIF, the scatter is considerably reduced, thus validating, again, the proposed K-based criterion for the onset of delaminations.

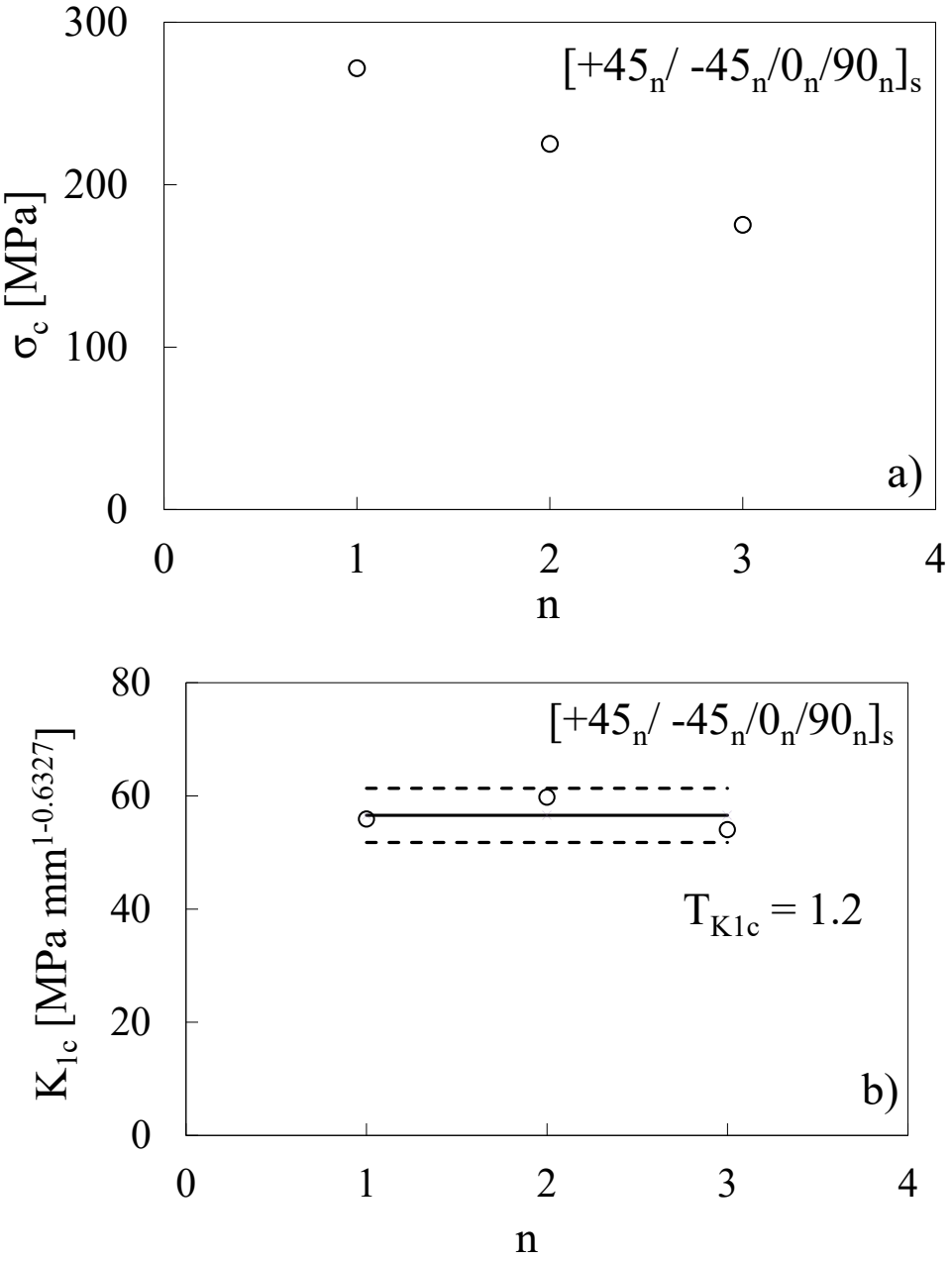

Figure 2.20 Experimental data from [1] in terms of a) stress and b) GSIF for the delamination initiation.

2.8 Conclusions

In this chapter, a comprehensive study on the phenomenon of delamination onset from transverse cracks in composite cross-ply laminates under static loadings was presented.

The work stems from the idea, corroborated by several experimental evidences available in the literature, that the onset of delaminations is driven by the singular stress field arising in the close

neighbourhood of transverse cracks, along the interface between the 0 and 90 plies.

According to this idea, in the first part of the chapter, great efforts were devoted to deriving explicit formulations for the local mode I, II and III stress fields in the close neighbourhoods of the tip of transverse cracks. Taking advantage of an asymptotical analysis based on Lekhnitskii formalism, stresses were given in closed form and their intensity quantified by Generalized Stress Intensity Factors (GSIFs). The effect of the elastic properties of the plies, the ply thicknesses and the crack density on the mode I GSIF was also discussed, taking advantage of the results from a number of FE analyses.

Subsequently, a fracture criterion for the delamination onset in cross-ply laminates under tension, based on a critical value for the mode 1 GSIF, was proposed and validated by comparison with the results from an experimental campaign carried out in the present work, as well as rearranging a bulk of data taken from the literature. In all cases, a satisfactory efficacy of a K-based criterion for the delamination onset was found.

References of chapter 2

[1] Rodini BT Jr, Eisenman JR. An analytical and experimental investigation of edge delamination in composite laminates. In: Lenoe EM, Oplinger DW, Burke J, editors. Fibrous composites in structural design. New York:Plenum, 1980. p. 441-457

[2] Crossman FW, Warren WJ, Wang ASD, Law GE. Initiation and Growth of Transverse Cracks and Edge Delamination in Composite Laminates Part 2. Experimental Correlation. J Compos Mater 1980;14:88–108, 1980.

[3] Wang ASD. Initiation and growth of transverse cracks and edge delamination in composite laminates. Part 1. An Energy Method. J Compos Mater 1980; 14: 71–87.

[4] O'Brien TK. Characterization of delamination onset and growth in a composite laminate. In: Reifsnider KL, editor. Damage in composite materials, ASTM STP 775. Philadelphia: American Society for Testing and Materials: 1982, p.140-167.

[5] Brewer JC, Lagace PA. Quadratic Stress Criterion for Initiation of Delamination. J Compos Mater 1988; 22:1141–1155.

[6] Hojo M, Tanaka K, Gustafson CG, Hayashi R. Effect of stress ratio on near-threshold propagation of delamination fatigue cracks in unidirectional CFRP. Compos Sci Technol 1987;29(4):273-292.

[7] Hojo M, Ochiai S, Gustafson CG, Tanaka K. Effect of matrix resin on delamination fatigue crack growth in cfrp laminates, Eng Fract Mech 1994;49(1):35-47.

[8] Hojo M, Ando T, Tanaka M, Adachi T, Ochiai S, Endo Y. Modes I and II interlaminar fracture toughness and fatigue delamination of CF/epoxy laminates with self-same epoxy interleaf. Int J Fatigue 2006;28:1154–1165.

[9] Andersons J, Hojo M, Ochiai S. Empirical model for stress ratio effect on fatigue delamination growth rate in composite laminates, Int J Fatigue 2004;26:597–604.

[10] Andersons J, Hojo M, Ochiai S. Model of delamination propagation in brittle-matrix composites under cyclic loading. J Reinf Plast Compos 2001;20(05):431-450.

[11] Takeda N, Ogihara S. Initiation and growth of delamination from the tips of transverse cracks in cfrp cross-ply laminates. Compos Sci Technol 1994;52:309–318.

[12] Takeda N, Ogihara S. In situ observation and probabilistic prediction of microscopic failure processes in cfrp cross-ply laminates. Compos Sci Technol 1994;94:183–195.

[13] Zubillaga L, Turon A, Renart J, Costa J, Linde P. An experimental study on matrix crack induced delamination in composite laminates. Compos Struct 2015;127:10–17.

[14] Akshantala NV, Talreja R. A mechanistic model for fatigue damage evolution in composite laminates. Mech. Mater. 1998,29:123–140.

[15] Akshantala NV, Talreja R. A micromechanics based model for predicting fatigue life of composite laminates. Mater Sci Eng A 2000;285:303–313.

[16] Allegri G and Wisnom MR. A non-linear damage evolution model for mode II fatigue

delamination onset and growth. Int J Fatigue 2012;43:226–234.

[17] Zhang J, Fan J, Herrmann KP. Delaminations induced by constrained transverse cracking in symmetric composite laminates. Int J Solids Struct 1999;36:813–846.

[18] O'Brien TK. Analysis of local delamination and their influence on composite laminate behaviour. Delamination and Debonding of Materials, ASTM STP 876. Philadelphia: American Society for Testing and Materials, 1985, p. 282–297.

[19] Pagano NJ, Schoeppner GA. Delamination of polymer matrix composites: problems and assessment. In: Kelly A, Zweben C, editors. Comprehensive composite materials, vol.2. Oxford: Elsevier Science Ltd, 2000 p.433-528.

[20] Berthelot JM. Transverse cracking and delamination in cross-ply glass-fiber and carbon-fiber reinforced plastic laminates: Static and fatigue loading. Appl Mech Rev 2003. 56 (1):111–147.

[21] Dharani LR, Tang H. Micromechanics characterization of sublaminate damage. Int J Fract 1990,46:123–140.

[22] Kashtalyan M and Soutis C. Effect of delaminations induced by transverse cracks and splits on stiffness properties of composite laminates. Compos Part A Appl Sci Manuf 2000;31:107–119.

[23] Berthelot J, Le Corre J. A model for transverse cracking and delamination in cross-ply laminates 2000;60:1055–1066.

[24] Nairn J, Hu S. The initiation and growth of delaminations induced by matrix microcracks in laminated composites. Int J Fract 1992;57:1–24.

[25] Hashin Z. Analysis of cracked laminates: a variational approach. Mech Mater 1985;4 (2):121–136.

[26] Rebière JL, Gamby D. A criterion for modelling initiation and propagation of matrix cracking and delamination in cross-ply laminates. Compos Sci Technol 2004;64: 2239–2250.

[27] Zhang H, Minnetyan L. Variational analysis of transverse cracking and local delamination in $[\theta_m/90_n]_s$ laminates. Int J Solids Struct 2006;43:7061–7081.

[28] Farrokhabadi A, Hosseini-Toudeshky H, Mohammadi B. A generalized micromechanical approach for the analysis of transverse crack and induced delamination in composite laminates. Compos Struct 2011;93: 443–455.

[29] Johnson P, Chang FK. Characterization of Matrix Crack-Induced Laminate Failure - Part II: Analysis and Verifications. J Compos Mater 2001;35:2037–2074.

[30] Zubillaga L, Turon A, Maimí P, Costa J, Mahdi S, Linde P. An energy based failure criterion for matrix crack induced delamination in laminated composite structures. Compos Struct 2014;112: 339–344.

[31] Zou Z, Reid SR, Li S, Soden PD. Application of a delamination model to laminated composite structures. Compos Struct 2002;56:375–389.

[32] Maimí P, Camanho PP, Mayugo JA, Turon A. Matrix cracking and delamination in laminated composites. Part I: Ply constitutive law, first ply failure and onset of delamination. Mech Mater

2011;43:169–185.

[33] Camanho PP, C. G. Dávila, D. R. Ambur, Numerical Simulation of Delamination Growth in Composite Materials, NASA Technical publication, 2001.

[34] Bui VQ, Iannucci L, Robinson P, Pinho ST. A coupled mixed-mode delamination model for laminated composites. J. Compos Materials 45(16):1717–1729

[35] Turon A, Camanho PP, Costa J, Dávila CG. A damage model for the simulation of delamination in advanced composites under variable-mode loading. Mech Mater 2006;38:1072–1089.

[36] Turon A, Costa J, Camanho PP, Dávila CG.Simulation of delamination in composites under high-cycle fatigue. Compos Part A Appl Sci Manuf 2007;38:2270–2282.

[37] Jalalvand M, Hosseini-Toudeshky H, Mohammadi B. Numerical modeling of diffuse transverse cracks and induced delamination using cohesive elements. Proc. Inst. Mech. Eng. Part C J. Mech. Eng. Sci. 2013;227:1392–1405.

[38] Liu PF, Islam MM. A nonlinear cohesive model for mixed-mode delamination of composite laminates. Compos Struct 2013;106:47–56.

[39] Zhao L, Gong Y, Zhang J, Chen Y, Fei B. Simulation of delamination growth in multidirectional laminates under mode I and mixed mode I/II loadings using cohesive elements. Compos. Struct. 2014;116:509–522.

[40] Chen BY, Tay TE, Pinho ST, Tan VBC. Modelling the tensile failure of composites with the floating node method. Comput. Methods Appl. Mech. Eng.2016;308:414–442

[41] Gross R, Mendelson A. Plane elastostatic analisys of V-notched plates. Int J Fract Mech 1972;8:267-276.

[42] Nui LS, Chehimi C, Pluvinage G. Stress field near a large blunted tip V-notch and application of the concept of the critical notch stress intensity factor (NSIF) to the fracture toughness of very brittle materials. Engng Fract Mech 1994;49:325–35.

[43] Dunn ML, Suwito W, Cunningham S. Fracture initiation at sharp notches: correlation using critical stress intensities. Int J Solids Struct 1997;34:3873-3883.

[44] Dunn ML, Suwito W, Cunningham S and May CW. Fracture initiation at sharp notches under mode I, mode II, and mild mixed mode loading. Int J Fract 1997;84:367–381.

[45] Gómez FJ, Elices M. Fracture of components with V-shaped notches. Eng Fract Mech 2003;70:1913-1927.

[46] Gómez FJ and Elices M. A fracture criterion for sharp V-notched samples. Int J Fract 2003;123:163-175.

[47] Boukharouba T, Tamine T, Nui L, Chehimi C and Pluvinage G. The use of notch stress intensity factor as a fatigue crack initiation parameter. Eng Fract Mech 1995;52:503-512.

[48] Verreman Y, Nie B. Early development of fatigue cracking at manual fillet welds. Fatigue Fract Eng Mater Struct 1996;19:669–81.

[49] Lazzarin P, Tovo R. A Notch Intensity Approach to the Stress Analysis of Welds. Fatigue Fract Eng Mater Struct 1998;21:1089-1104.

[50] Lazzarin P, Livieri P. Notch Stress Intensity Factors and fatigue strength of aluminium and steel welded joints. Int J Fatigue 2001;23:225-232.

[51] Gradin PA. A fracture criterion for edge-bonded bi-material bodies. J Compos Mater 1982;16:448–456.

[52] Adams RD, Harris JA. The influence of local geometry on the strength of adhesive joints. Int J Adhes Adhes 1987;7:69–80.

[53] Groth HL. Stress singularities and fracture at interface corners in bonded joints. Int J Adhes Adhes 1988;8:107–113.

[54] Hattory T, Sakata S, Hatsuda T, Murakami G. A stress singularity parameter approach for evaluating adhesives strength. JSME Int J Series I, 1988;31:718–723

[55] Reedy Jr ED. Asymptotic interface-corner solutions for butt tensile joints. Int J Solids Struct 1993;30:767-777.

[56] Reedy Jr ED, Guess TR. Comparison of butt tensile strength data with interface corner stress intensity factor prediction. Int J Solids Struct 1993;30:2929-2936.

[57] Lefebvre DR, Dillard DA. A stress singularity approach for the prediction of fatigue crack initiation in adhesive bonds. Part I: theory. J Adhes 1999;70:119–138.

[58] Quaresimin M, Ricotta M. Fatigue behaviour and damage evolution of single lap bonded joints in composite material. Compos Sci Technol 2006;66:176-87

[59] Quaresimin M, Ricotta M. Stress intensity factors and strain energy release rates in single lap bonded joints in composite materials. Compos Sci Technol 2006;66:647–656.

[60] Quaresimin M, Ricotta M. Life prediction of bonded joints in composite materials. Int J Fatigue 2006;28(10):1166-1176

[61] Garrett KW, Bailey JE. Multiple transverse fracture in 90° cross-ply laminates of a glass fibre-reinforced polyester. J of Mater Sci 1977;12:157-168.

[62] Berthelot JM. Transverse cracking and delamination in cross-ply glass-fiber and carbon-fiber reinforced plastic laminates: Static and fatigue loading, Appl Mech Rev 2003;56(1):111-147.

[63] Chen DH, Harada K. Stress Singularities for Crack Normal to and Terminating at Bimaterial Interface of Anisotropic Half-Planes. Int J Fract 1996;81(2):147-162.

[64] Im S. Asymptotic stress field around a crack normal to the ply-interface of an anisotropic composite laminate. Int J Solids .Struct 1990;26(1):111-127.

[65] Arin K. An orthotropic laminate composite containing a layer with a crack. Int J Eng Sci 1977;15:545-559.

[66] Gupta GD. A layered composite with a broken laminate. Int J Solids Struct 1973;9:1141-1154.

[67] Zappalorto M, Carraro PA. Stress fields at sharp angular corners in thick anisotropic composite

plates. Compos Struct 2014;117:346-353

[68] Zappalorto M, Carraro PA, Quaresimin M. Analytical solution for the three-dimensional stress fields in anisotropic composite bimaterial corners. Compos Struct 2015;122:127-138.

[69] Lekhnitskii SG. Theory of elasticity of an anisotropic body. Moskow: Mir Publishers; 1984.

[70] Dunn ML, Suwito W and Cunningham S. Stress intensities at notch singularities. Eng Fract Mech 1997;57:417-430

[71] Zappalorto M., Lazzarin P., Berto F. (2009). Elastic Notch Stress Intensity Factors for sharply V-notched rounded bars under torsion. Engineering Fracture Mechanics, Vol. 76, pp. 439-453.

[72] Cook J, Gordon JE. A mechanism for the control of crack propagation in all-brittle systems, Proc. R. Soc. A 1964;282:508-520.

[73] Raab M, Shulz E, Sova M. The Cook-Gordon Mechanism in Polymeric Materials. Polymer Eng Sci 1993;33:1438-1443.

[74] Blazquez A, Mantic V, Paris F, McCartney NL. BEM analysis of damage progress in 0/90 laminates. Eng Anal Bound Elem 2009;33:762–769.

[75] París F, Blázquez A, McCartney L, Mantič V. Characterization and evolution of matrix and interface related damage in [0/90]s laminates under tension. Part I: numerical predictions. Compos Sci Technol 2010;70 (7):1168–1175.

[76] París F, Blázquez A, McCartney L, Barroso A. Characterization and evolution of matrix and interface related damage in [0/90]s laminates under tension. Part II: experimental evidence. Compos. Sci. Technol 2010;70(7):1176–1183.

[77] García IG, Mantic V, Blázquez A, París F. Transverse crack onset and growth in cross-ply $[0/90]_s$ laminates under tension. Application of a coupled stress and energy criterion. Int J Solids Struct 2014;51:3844–3856.

Appendix

As mentioned in section 4, electrically conductive FE analyses were carried out, instead of 3D analyses under anti-plane shear loadings. This allowed 2D models to be adopted, thus saving computational time and allowing the number of elements in the crack tip region to be increased, therefore increasing the accuracy of the analyses. This was possible in virtue of the formal analogy between the anti-plane shear and the in-plane electric conduction problems. This concept is explained in this appendix. Consider a conductive material with an orthotropic behaviour in the xy plane, so that the current densities j_x and j_y in the x and y direction respectively can be written as:

$$\begin{aligned} j_x &= S_x \cdot e_x \\ j_y &= S_y \cdot e_y \end{aligned} \tag{A1}$$

where S_x and S_y are the conductivities along x and y and e_x and e_y are the electric fields defined as:

$$\begin{aligned} e_x &= -\frac{\partial v_e}{\partial x} \\ e_y &= -\frac{\partial v_e}{\partial y} \end{aligned} \tag{A2}$$

Eventually, v_e is the electric potential. The principle of conservation of the electric charge reads as:

$$\frac{\partial j_x}{\partial x} + \frac{\partial j_y}{\partial y} = 0 \tag{A3}$$

and substituting (A1) and (A2) into (A3) gives:

$$S_x \frac{\partial^2 v_e}{\partial x^2} + S_y \frac{\partial^2 v_e}{\partial y^2} = 0 \tag{A4}$$

The last equation is formally identical to the equation governing the mechanical anti-plane shear problem [41], and therefore the following analogies can be made between electrical and mechanical variables.

$$\begin{aligned} &S_x \equiv G_{xz}, S_y \equiv G_{yz} \\ &e_x \equiv -\gamma_{xz}, e_y \equiv -\gamma_{yz} \\ &j_x \equiv -\sigma_{xz}, j_y \equiv -\sigma_{yz} \end{aligned} \tag{A5}$$

Eventually, for the solution of the electrical conduction problem for the same geometry shown in

Figure (1b), the following boundary conditions must be imposed on the crack faces, where no current flow is admitted, and at the plies interface:

$$j_{y,1}\big|_{\theta=\pi} = j_{y,3}\big|_{\theta=-\pi} = 0 \qquad j_{x,2}\big|_{\theta=-\pi/2} = j_{x,3}\big|_{\theta=-\pi/2} \qquad j_{x,2}\big|_{\theta=\pi/2} = j_{x,1}\big|_{\theta=\pi/2}$$

$$v_{e,2}\big|_{\theta=\pi/2} = v_{e,1}\big|_{\theta=\pi/2} \qquad v_{e,2}\big|_{\theta=\pi/2} = v_{e,3}\big|_{\theta=\pi/2} \tag{A6}$$

These conditions are formally identical to those written in Eq. (31) for the mechanical problem.

As a consequence, it can be concluded that the anti-plane shear loading condition can be simulated by means of 2D electrically conductive FE analyses where the conductivity values are equal to the shear moduli and the boundary conditions shown in Figure 7 are applied to the FE model.

3. Extension of the delamination onset model to the case of generic laminates

3.1 Introduction

Over the past years, efforts have been devoted to analyzing and describing the stress analysis of composite laminates in the proximity of singularity points, in order to formulate reliable engineering strength criteria. The high stress gradients reached in correspondence of these points, in fact, may limit the load carrying capability of the components, thus leading to premature failure.

Typical causes of stress singularities for composite materials are wedges, notches or the presence of defects within the material, such as cracks.

In the literature, many studies focused on the problem of wedges can be found. Some of the pioneer studies were conducted by Reissner [1], Bogy [2], Hein and Erdogan [3] and Kuo and Bogy [4]. With the advent of composite materials, even the description of stress fields for anisotropic wedges became important; examples can be found in [5]-[8]

As regards notches, Williams [9] analysed the stress fields for V-sharped notches and found out that singular stresses were proportional to the term $r^{1-\lambda}$. Other remarkable studies were carried out by Creager and Paris [10] and Glinka [11], who obtained closed-form expression for the generalized stress intensity factor in the case of parabolic notches. More recently, Lazzarin and Tovo [12] determined a solution capable of addressing any combination of notch tip radius and opening angle.

However, the presence of a matrix crack causes the formation of singular stress fields in the closeness of its tip, that may lead to the formation of other damage mechanisms. One of the causes leading to delamination formation is the presence of matrix cracks. In fact, cracks in the proximity of the interface, shared between adjacent layers, causes the formation of singular stress fields that may induce the initiation of delaminations.

The problem of a crack in a bimaterial plate has been widely studied over the years. First the research focused on the case of isotropic materials [13]-[15], and then extended to the case of anisotropic materials [16]-[22]. In particular, Delale and Erdogan [19], Delale [20] and Chen and Harada [22] analyzed the problem of the orthotropic material, which can be considered as a peculiar case of the complete anisotropy. Singular stress field associated with mode I and mode II could be treated separately, with different order of singularities.

A similar approach has already been adopted for describing the stress field in the adjacencies of a matrix crack in cross-ply laminates.

In this section, the analytical model based on the Lekhninstkii's formulation, already presented in the previous chapter, will be opportunely modified and extended, in order that can be used for the case of laminates characterized by generic orientation of plies.

3.2 Statement of the problem and formulation

The problem of a crack terminating at an interface of two adjacent layers is considered in this section.

An analytical study is carried out on the cracked geometry sketched in Figure 3.1.

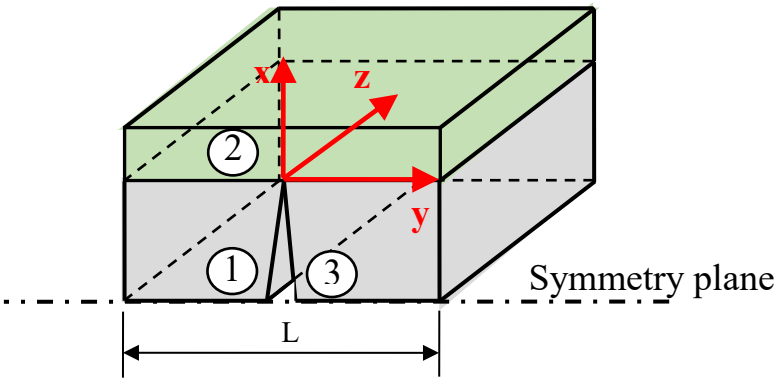

Figure 3.1 Schematic of the laminate segment

It evident that the domain under investigation is a multi-material one, where three different zones do exist. In particular, the cracked ply is divided into two regions (1 and 3) at each side of the crack, whilst the undamaged layer is fully included in region 2. The materials are supposed to obey to an

anisotropic elastic behaviour. Taking advantage of a Cartesian coordinate system centred at the crack tip, the stress-strain relation for each of the zones individuated can be described as follows:

$$\begin{Bmatrix} \varepsilon_{xx} \\ \varepsilon_{yy} \\ \varepsilon_{zz} \\ \varepsilon_{yz} \\ \varepsilon_{xz} \\ \varepsilon_{xy} \end{Bmatrix} = \begin{bmatrix} S_{33} & S_{31} & S_{32} & S_{36} & 0 & 0 \\ S_{13} & S_{11} & S_{12} & S_{16} & 0 & 0 \\ S_{23} & S_{21} & S_{22} & S_{26} & 0 & 0 \\ S_{63} & S_{61} & S_{62} & S_{66} & 0 & 0 \\ 0 & 0 & 0 & 0 & S_{44} & S_{45} \\ 0 & 0 & 0 & 0 & S_{54} & S_{55} \end{bmatrix} \quad (1)$$

The coefficients of the reduced compliance matrix were determined according to the following:

$$B_{ij} = S_{ij} - \frac{S_{i3}{}^2}{S_{33}} \text{ if } i=j \quad B_{ij} = S_{ij} - \frac{S_{i3}S_{j3}}{S_{33}} \text{ if } i \neq j \quad (2)$$

For the case of generalized plane strain, Lekhnitskii developed a formulation in terms of the complex variables $\Phi_1(z_1)$, $\Phi_2(z_2)$ and $\Phi_3(z_3)$ to express the stress components in the form:

$$\begin{aligned} \sigma_x &= 2\,\mathrm{Re}\left[\mu_1^2\phi_1'(z_1) + \mu_2^2\phi_2'(z_2) + \mu_3^2\phi_3'(z_3)\Lambda_3\right] \\ \sigma_y &= 2\,\mathrm{Re}\left[\phi_1'(z_1) + \phi_2'(z_2) + \phi_3'(z_3)\Lambda_3\right] \\ \tau_{xy} &= -2\,\mathrm{Re}\left[\mu_1\phi_1'(z_1) + \mu_2\phi_2'(z_2) + \mu_2\phi_3'(z_3)\Lambda_3\right] \\ \tau_{xz} &= 2\,\mathrm{Re}\left[\mu_1\Lambda_1\phi_1'(z_1) + \mu_2\Lambda_2\phi_2'(z_2) + \mu_2\phi_3'(z_3)\right] \\ \tau_{yz} &= -2\,\mathrm{Re}\left[\Lambda_1\phi_1'(z_1) + \Lambda_2\phi_2'(z_2) + \phi_3'(z_3)\right] \end{aligned} \quad (3)$$

With:

$$z_{i,k} = x + \mu_{i,k}y = r\rho_{i,k}e^{i\theta_{1,k}} \quad i=1,2,3\ k=1,2,3 \quad (4)$$

$$\begin{aligned} \rho_{j,k} &= \sqrt{(\cos\theta + \alpha_{j,k}\sin\theta)^2 + (\beta_{j,k}\sin\theta)^2} \\ \theta &= Arg(\cos\theta + \alpha_{j,k}\sin\theta + i\beta_{j,k}\sin\theta) \end{aligned} \quad (5)$$

Where μ_i are the roots of the following characteristic equation:

$$l_4(\mu)l_2(\mu) - l_3^2(\mu) = 0 \qquad (6)$$

Lekhnitkii proved that for anisotropic materials the Eq. 5 does not have real roots, and μ_i occur in three pairs of complex conjugate numbers.

The parameters Λ_1, Λ_2 and Λ_3 are defined as follows:

$$\Lambda_1 = -\frac{l_3(\mu_1)}{l_2(\mu_1)} \quad \Lambda_2 = -\frac{l_3(\mu_2)}{l_2(\mu_2)} \quad \Lambda_3 = -\frac{l_3(\mu_3)}{l_4(\mu_3)} \qquad (7)$$

Where the l_2, l_3 and l_4 are determined according to:

$$\begin{aligned} l_{2,k}(\mu_k) &= B_{55,k}\mu^2 - 2B_{45,k}\mu + B_{44,k} \\ l_{3,k}(\mu_k) &= B_{15,k}\mu^3 - (B_{14,k} + B_{56,k})\mu^2 + (B_{25,k} + B_{46,k})\mu - B_{24,k} \\ l_{4,k}(\mu_k) &= B_{11,k}\mu^4 - 2B_{16,k}\mu^3 + (2B_{12,k} + B_{66,k})\mu^2 - 2B_{26,k}\mu + B_{22,k} \end{aligned} \qquad (8)$$

The stresses and displacements can be expressed using the cylindrical coordinates, in order to express the boundaries conditions more conveniently:

$$\sigma_{rr,k} = 2\,\mathrm{Re}\left\{\sum_{j=1}^{2}(m_{j1rr,k} + im_{j2rr,k})\phi'_{j,k}(z_{j,k}) + (m_{31rr,k} + im_{32rr,k})\phi'_{3,k}(z_{3,k})\lambda_{3,k}\right\} \qquad (9)$$

$$\sigma_{r\theta,k} = 2\,\mathrm{Re}\left\{\sum_{j=1}^{2}(m_{j1rr,k} + im_{j2rr,k})\phi'_{j,k}(z_{1,k}) + (m_{31rr,k} + im_{32rr,k})\phi'_{3,k}(z_{3,k})\lambda_{3,k}\right\}$$

$$\begin{aligned} \sigma_{\theta\theta,k} = 2\,\mathrm{Re}\{&(\cos\theta + \mu_{1,k}\sin\theta)^2\phi'_{1,k}(z_{1,k}) + (\cos\theta + \mu_{2,k}\sin\theta)^2\phi'_{2,k}(z_{2,k}) \\ &+ (\cos\theta + \mu_{3,k}\sin\theta)^2\phi'_{3,k}(z_{3,k})\lambda_{3,k}\} \end{aligned}$$

$$\sigma_{rz,k} = 2\,\mathrm{Re}\{\sum_{j=1}^{2}(m_{j1rr,k} + im_{j2rr,k})\phi'_{1,k}(z_{1,k})\lambda_{1,k} + \left(-\sin\theta + \mu_{2,k}\cos\theta\right)^2\phi'_{2,k}(z_{2,k})\lambda_{2,k} + \left(-\sin\theta + \mu_{2,k}\cos\theta\right)^2\phi'_{3,k}(z_{3,k})\}$$

$$\sigma_{\theta z,k} = 2\,\mathrm{Re}\{\left(-\cos\theta - \mu_{1,k}\sin\theta\right)^2\phi'_{1,k}(z_{1,k})\lambda_{1,k} + \left(-\cos\theta - \mu_{2,k}\sin\theta\right)^2\phi'_{2,k}(z_{2,k})\lambda_{2,k} + \left(-\cos\theta - \mu_{3,k}\sin\theta\right)^2\phi'_{3,k}(z_{3,k})\}$$

$$u_{\theta,k} = 2\,\mathrm{Re}\{\left(q_{1,k}\cos\theta - p_{1,k}\sin\theta\right)\phi_{1,k}(z_{1,k}) + \left(q_{2,k}\cos\theta - p_{2,k}\sin\theta\right)\phi_{2,k}(z_{2,k}) + \left(q_{3,k}\cos\theta - p_{3,k}\sin\theta\right)\phi_{3,k}(z_{3,k})\}$$

$$u_{r,k} = 2\,\mathrm{Re}\{\left(q_{1,k}\sin\theta + p_{1,k}\cos\theta\right)\phi_{1,k}(z_{1,k}) + \left(q_{2,k}\sin\theta + p_{2,k}\cos\theta\right)\phi_{2,k}(z_{2,k}) + \left(q_{3,k}\cos\theta + p_{3,k}\sin\theta\right)\phi_{3,k}(z_{3,k})\}$$

$$w_k = 2\,\mathrm{Re}\left\{\left(s_{1,k}\phi_{1,k}(z_{1,k}) + s_{2,k}\phi_{2,k}(z_{2,k}) + s_{3,k}\phi_{3,k}(z_{3,k})\right)\right\}$$

With:

$$\begin{aligned}
m_{j1rr,k} &= (\sin\theta - \alpha_{j,k}\cos\theta)^2 - (\beta_{j,k}\cos\theta)^2 \\
m_{j2rr,k} &= 2\beta_{j,k}\cos\theta(\alpha_{j,k}\cos\theta - \sin\theta) \\
m_{j1\theta\theta,k} &= (\cos\theta + \alpha_{j,k}\sin\theta)^2 - (\beta_{j,k}\sin\theta)^2 \\
m_{j2\theta\theta,k} &= 2\beta_{j,k}\sin\theta(\cos\theta + \alpha_{j,k}\sin\theta) \\
m_{j1r\theta,k} &= \frac{1}{2}\sin(2\theta)(1 - \alpha_{j,k}{}^2 + \beta_{j,k}{}^2) - \alpha_{j,k}\cos(2\theta) \\
m_{j2r\theta,k} &= -\beta_{j,k}\cos(2\theta) - \alpha_{j,k}\beta_{j,k}\sin(2\theta) \\
p_{j,k} &= B_{11,k}\mu^2{}_{j,k} + B_{12,k} - B_{16,k}\mu_{j,k} + \lambda_{j,k}(B_{15,k}\mu_{j,k} - B_{14,k}) \quad j = 1,2 \\
p_{3,k} &= \lambda_{3,k}(B_{11,k}\mu^2{}_{3,k} + B_{12,k} - B_{16}\mu_{3,k}) + B_{15,k}\mu_{3,k} - B_{14,k} \\
q_{j,k} &= B_{12,k}\mu_{j,k} + \frac{B_{22,k}}{\mu_{j,k}} - B_{26,k} + \lambda_{j,k}(B_{25,k} - \frac{B_{24,k}}{\mu_{j,k}}) \quad j = 1,2 \\
q_{3,k} &= \lambda_{3,k}(B_{12,k}\mu_{3,k} + \frac{B_{22,k}}{\mu_{3,k}} - B_{26,k}) + B_{25,k} - \frac{B_{24,k}}{\mu_{3,k}} \\
s_{j,k} &= B_{14,k}\mu_{j,k} + \frac{B_{24,k}}{\mu_{j,k}} - B_{46,k} + \lambda_{j,k}(B_{45,k} - \frac{B_{44,k}}{\mu_{j,k}}) \quad j = 1,2 \\
s_{3,k} &= \lambda_{3,k}(B_{14,k}\mu_{3,k} + \frac{B_{24,k}}{\mu_{3,k}} - B_{46,k}) + B_{45,k} - \frac{B_{44,k}}{\mu_{3,k}}
\end{aligned} \tag{10}$$

Extension of the model to the case of generic laminates

In order to obtain accurate predictions of the stress fields in the proximity of the transverse crack tip, the first singular terms of the asymptotic expansion were used. The complex functions can be chosen as:

$$\begin{aligned}\phi_{1,k}(z_{1,k}) &= (A_{1,k} + iA_{2,k}) z_{1,k}^{\lambda} \\ \phi_{2,k}(z_{2,k}) &= (C_{1,k} + iC_{2,k}) z_{2,k}^{\lambda} \\ \phi_{3,k}(z_{3,k}) &= (D_{1,k} + iD_{2,k}) z_{3,k}^{\lambda}\end{aligned} \tag{11}$$

Boundary conditions are given by the free of stress conditions on the crack faces, the equilibrium and compatibility conditions at the interface.

$$\sigma_{\theta\theta,1}(\pi) = 0 \tag{12}$$
$$\sigma_{r\theta}(\pi) = 0$$
$$\sigma_{\theta\theta,3}(-\pi) = 0$$
$$\sigma_{r\theta,3}(-\pi) = 0$$
$$\sigma_{\theta\theta,1}(\frac{\pi}{2}) = \sigma_{\theta\theta,2}(\frac{\pi}{2})$$
$$\sigma_{r\theta,1}(\frac{\pi}{2}) = \sigma_{r\theta,2}(\frac{\pi}{2})$$
$$u_{r,1}(\frac{\pi}{2}) = u_{r,2}(\frac{\pi}{2})$$
$$u_{\theta,1}(\frac{\pi}{2}) = u_{\theta,2}(\frac{\pi}{2})$$
$$\sigma_{\theta\theta,3}(-\frac{\pi}{2}) = \sigma_{\theta\theta,2}(-\frac{\pi}{2})$$
$$\sigma_{r\theta,3}(-\frac{\pi}{2}) = \sigma_{r\theta,2}(-\frac{\pi}{2})$$
$$u_{r,3}(-\frac{\pi}{2}) = u_{r,2}(-\frac{\pi}{2})$$
$$u_{\theta,3}(-\frac{\pi}{2}) = u_{\theta,2}(-\frac{\pi}{2})$$
$$\sigma_{\theta z,1}(\pi) = 0$$
$$\sigma_{\theta z,3}(-\pi) = 0$$
$$w_1(\frac{\pi}{2}) = w_2(\frac{\pi}{2})$$
$$w_2(-\frac{\pi}{2}) = w_3(-\frac{\pi}{2})$$
$$\sigma_{\theta z,1}(\frac{\pi}{2}) = \sigma_{\theta z,2}(\frac{\pi}{2})$$
$$\sigma_{\theta z,3}(-\frac{\pi}{2}) = \sigma_{\theta z,2}(-\frac{\pi}{2})$$

These equations can be written in matrix form as reported in the following:

(13)

$$[b(\lambda)]\begin{Bmatrix} A_{11,1} \\ A_{12,1} \\ A_{11,2} \\ A_{12,2} \\ A_{11,3} \\ A_{12,3} \\ C_{11,1} \\ C_{12,1} \\ C_{11,2} \\ C_{12,2} \\ C_{11,3} \\ C_{12,3} \\ D_{11,1} \\ D_{12,1} \\ D_{11,2} \\ D_{12,2} \\ D_{11,3} \\ D_{12,3} \end{Bmatrix} = \overline{0}$$

In order to obtain non-trivial solutions, the determinant of the matrix b must be zero:

$$\det[b(\lambda)] = 0$$

The solution of the characteristic polynomial gives infinite solutions for the eigenvalues λ. However, only those real component is included between 0 and 1 $0 < \mathrm{Re}[\lambda] < 1$ are selected, since these will result in a singular stress field in the proximity of the crack tip.

Once numerically determined the stress singularities and the angular functions, stresses can be written in terms of the three Generalized Stress Intensity Factors (GSIF):

$$\sigma_{ij}(\vartheta) = f_{ij}^{(1)}(\vartheta)\frac{K_1}{r^{1-\lambda_1}} + f_{ij}^{(2)}(\vartheta)\frac{K_2}{r^{1-\lambda_2}} + f_{ij}^{(3)}(\vartheta)\frac{K_3}{r^{1-\lambda_3}} \quad (14)$$

where the GSIF are determined by 3D finite element analyses.

3.3 Conclusion

In this chapter, the analytical model developed for the description of the stress fields in the closeness of matrix cracks, valid for cross-ply laminates, has been extended to generic laminates.

The eigenvalue problem for a crack terminating normal to the interface was developed.

The eigenequation obtained, which can be numerically solved, gives three values for the stress singularity 1- λ_1, 1- λ_2 and 1- λ_3. However, differently from the case of cross-ply laminates, these singularities are not associated with the respective mode I, mode II and mode III of deformation, and the singular stress fields cannot be separated and analyzed independently.

References

[1] Reissner, Eric. "On the theory of bending of elastic plates." *Studies in Applied Mathematics* 23.1-4 (1944): 184-191.

[2] Bogy, David B. "Edge-bonded dissimilar orthogonal elastic wedges under normal and shear loading." *Journal of Applied Mechanics* 35.3 (1968): 460-466.

[3] Hein, V. L., and F. Erdogan. "Stress singularities in a two-material wedge." *International Journal of Fracture Mechanics* 7.3 (1971): 317-330.

[4] Kuo, M. C., and D. B. Bogy. "Plane solutions for the displacement and traction-displacement problems for anisotropic elastic wedges." *Journal of Applied Mechanics* 41.1 (1974): 197-202

[5] Delale, F. "Stress singularities in bonded anisotropic materials." *International journal of solids and structures* 20.1 (1984): 31-40.

[6] Lin, Y. Y., and J. C. Sung. "Stress singularities at the apex of a dissimilar anisotropic wedge." *Journal of applied mechanics* 65.2 (1998): 454-463.

[7] Chen, Hua-Peng. "Stress singularities in anisotropic multi-material wedges and junctions." *International Journal of Solids and Structures* 35.11 (1998): 1057-1073.

[8] Chue, Ching-Hwei, and Chuan-I. Liu. "Stress singularities in a bimaterial anisotropic wedge with arbitrary fiber orientation." *Composite structures* 58.1 (2002): 49-56.

[9] Williams, M. L. "Stress singularities resulting from various boundary conditions in angular corners of plates in extension." *Journal of applied mechanics* 19.4 (1952): 526-528.

[10] Creager, Matthew, and Paul C. Paris. "Elastic field equations for blunt cracks with reference to stress corrosion cracking." *International Journal of Fracture* 3.4 (1967): 247-252.

[11] Glinka, Grzegorz. "Calculation of inelastic notch-tip strain-stress histories under cyclic loading." *Engineering Fracture Mechanics* 22.5 (1985): 839-854.

[12] Lazzarin, P., and R. Tovo. "A notch intensity factor approach to the stress analysis of welds." *Fatigue & fracture of engineering materials & structures* 21.9 (1998): 1089-1103

[13] Zak, A. R., and Max L. Williams. "Crack point stress singularities at a bi-material interface." (1962).

[14] Bogy, David. "On the plane elastostatic problem of a loaded crack terminating at a material interface." ASME, 1971.

[15] Cook, T. S., and F. Erdogan. "Stresses in bonded materials with a crack perpendicular to the interface." *International Journal of Engineering Science* 10.8 (1972): 677-697.

[16] Gupta, G. D. "A layered composite with a broken laminate." *International Journal of Solids and Structures* 9.10 (1973): 1141-1154.

[17] Dai-Heng, Chen. "A crack normal to and terminating at a bimaterial interface." *Engineering Fracture Mechanics* 49.4 (1994): 517-532.

[18] Ting, T. C. T., and P. H. Hoang. "Singularities at the tip of a crack normal to the interface of an anisotropic layered composite." *International Journal of Solids and Structures* 20.5 (1984): 439-454.

[19] Delale, F., and F. Erdogan. "Bonded orthotropic strips with cracks." *International Journal of Fracture* 15.4 (1979): 343-364.

[20] Delale, F. "Fracture of composite orthotropic plates for materials type 2." Technical Report NASA (1976).

[21] Gupta, V., A. S. Argon, and Z. Suo. "Crack deflection at an interface between two orthotropic media." *J. Appl. Mech* 59.2S (1992): S79-S87.

[22] Chen, Dai-Heng, and Kazunori Harada. "Stress singularities for crack normal to and terminating at bimaterial interface on orthotropic half-plates." *International Journal of Fracture* 81.2 (1996): 147-162.

4. Experimental investigation on delamination initiation and growth for cross-ply laminates subjected to cyclic loading

4.1 Introduction

Fatigue damage evolution of composite structures has been extensively investigated in the literature. In particular, much effort has been devoted to characterizing the behaviour of cross-ply laminates. These, in fact, is a basic laminate configuration and can be extended to more complex stacking sequences of plies. An extensive review of experimental investigations and modelling activities performed for the case of damaged cross-ply laminates can be found in [1].

It is well known that damage process of cross-ply laminates, subjected to tensile loading, is characterized by a sequence of mechanisms, interacting one with each other. Early fatigue damage consists of the formation of transverse matrix cracks in the 90° plies, which leads to the formation of delaminations in correspondence of the interface 0°/90° (see Refs. [2]–[9]). These may lead to the degradation of both strength and stiffness, compromising the functionality of the components in service.

The research group of DTG is working since several years in the characterization and modelling of the fatigue damage evolution of composite laminates, mainly focusing on the first stages of crack initation, propagation and connected stiffness loss [10]–[13].

The problem of delaminations has been widely addressed in the literature, both by means of experimental investigations and theoretical approaches.

Most of the models aims at describing the stress fields in damaged laminates, due to the combined presence of matrix cracks and induced delaminations.

These can be divided into two broad categories, based on the procedure adopted to obtain stress fields in the damaged laminate: shear lag and variational approaches.

Some of the studies based on a shear lag methodology were conducted by [14], [15] and [16].

Conversely, [17], [18], [19] and [20] proposed models based on a variational procedure.

Akshantala and Talreja [21],[22] included the effects of frictional sliding, existing between adjacent plies delaminated, by modelling a super-imposed shear stress on the interface, assumed as a linear and cubic polynomial distribution.

Differently, Armanios et al. [23] developed a shear deformation model based on the laminate plate theory, including the hygrothermal effects.

Most of the studies individuated the energy release rate or the stress intensity factor range as reliable parameters able to predict the delamination initation and growth.

Among these, O'Brien [24] put efforts into defining a methodology describing both the initiation and development of delaminations. Delamination growth rate was expressed as a power function of the energy release rate.

Alternatively, Andersons, Hojo, and Ochiai [25] developed an empirical model to provide a way of describing the effects of stress ratio on the fatigue delamination growth rate. The authors assumed that a power law based on the stress intensity factor range was representative of the delamination growth rate.

In [26], the authors defined a scalar damage variable, represented by the ratio of the number of cycles to the total number fatigue cycles and then a law that described the evolution of this during the fatigue life. Based on these, they proposed a criterion to predict the initiation and growth of delaminations under pure mode II.

Moreover, Wang et al. [27] developed a 3D finite element model which simulates the process of delamination growth. Nodes were gradually released, and the delamination area and the corresponding energy release rate were determined after each step for the assumed delamination growth.

Further studies based on 3D finite analyses can be found in [28] and [29]. In particular, the latter investigated the effects of the free edges on the development of local delaminations, initiated from the tips of transverse cracks.

Although delaminations have been widely addressed, to the best of author's knowledge, there is no study in the literature analyzing the evolution of delaminations and, in particular, the influence that matrix cracks have on this process.

The research on the evolution of delaminations, under fatigue loading, is divided into two parts. The first presents the results of an experimental investigations, aimed at studying the development of delaminations in cross-ply laminates. Tests were carried out on glass/epoxy laminates, as the transparency of the material eases the monitoring of damage. Furthermore, the evolution of material properties, was characterized and the phases of damage scenario were determined, by observing specimen edges using the optical microscope and comparing the micrographs with the photographs taken to the frontal side of the specimen during the test.

The second part is devoted to the characterization of the growth of delamination areas with the number of cycles and, by means of a campaign of Finite Element analyses, the determination of energy release rates values (ERR) linked with the delamination growth. Following a similar

approach to the one adopted by Quaresimin et al. for bonded joints [30]–

[32], a Paris-like curve was derived to correlate the fatigue delamination growth rate to the ERR. Finally, the reduction of Young's modulus was modeled. Predictions were then compared with experimental data of stiffness loss, finding a good agreement between the two data sets.

4.2 Materials and testing

Laminates of 300x300 mm characterized by two different lay-up $[0_2/90_4]_s$ and $[0/90_2]_s$ were manufactured by liquid resin infusion. Materials used were dry unidirectional glass fibres UT-E500 (500 g/m^2, Gurit) and the epoxy system EC157-W152LR (Elantas). Laminates were cured for three days at room temperature and then post-cured in an oven at 60°C for 12 hours.

From these, specimens of 25mm x 250mm were cut and polished at the edges to ease microscopic observations. Finally, tabs were applied at the ends of the specimens, reducing the gage length to 140 mm.

Quasi-static tensile tests conducted on unidirectional laminates at 0°, 45° and 90° allowed to determine the in-plane elastic properties of the plies, which are:

$E_1 = 48800$ MPa $\quad E_2 = 14000$ MPa

$G_{12} = 5200$ MPa $\quad \nu_{12} = 0.308$

Fatigue tests were carried out with a stress ratio R=0.05 and a frequency of 10 Hz on a servo-hydraulic machine MTS 858 machine equipped with a 100 kN load cell.

Tests were performed under load-control, keeping a constant amplitude of the sinusoidal wave. A wide range of maximum values of stress was applied, as reported in Table 4.1. These were chosen in order to ease experimental observations of the onset and development of delaminations.

Table 4.1 Stress levels and stacking sequence of performed fatigue tests

Stacking sequence	**Maximum stress [MPa]**
$[0_2/90_4]s$	σ_{max}=140, 120, 100, 90,80, 70
$[0/90_2]s$	σ_{max}=120, 100, 90

To detect the evolution of both axial and transverse strain during the tests, a biaxial extensometer with a gauge length of 25 mm was mounted on the specimens.

During the tests, damage development was investigated and documented by means of pictures taken at the backlit specimens. These were additionally illuminated with a LED light, located frontally respect to the specimens, allowing the enhancement of delaminated areas. The camera used was a Canon EOS equipped with a 60mm macro lens. The area observed of the specimens was reduced to a length of 60 mm in the central region, in order to avoid the influence of the end tabs on the damage process.

The images were then processed through an image analysis tool developed in Matlab®. This allowed to calculate the area of delaminations, by binarizing and filtering the images to enhance the contours of the delaminations. An example of the image processing is represented in Figure 4.1.

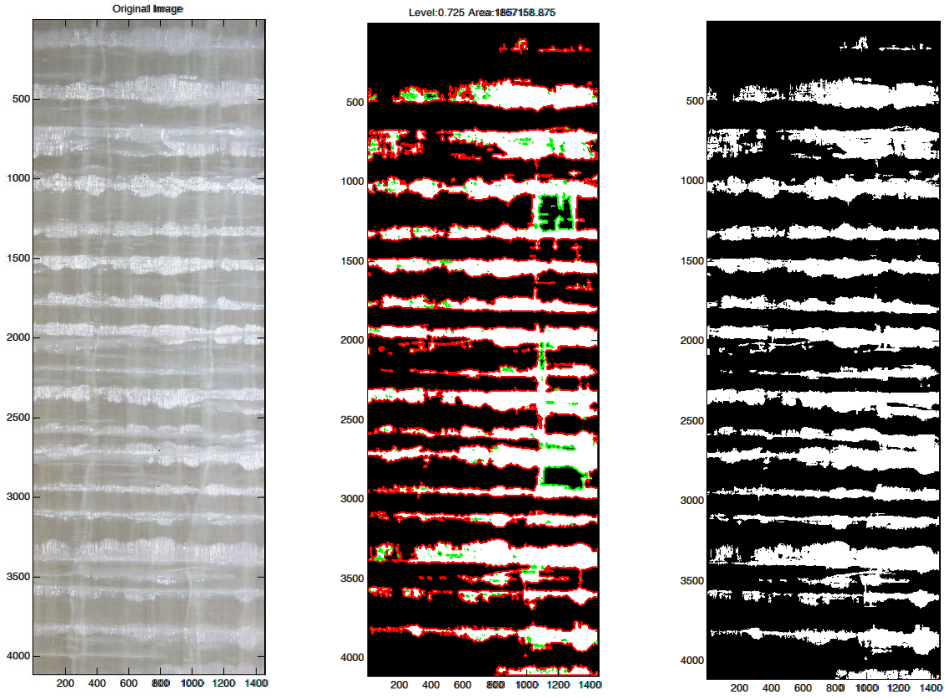

Figure 4.1 Example of image processing to quantify the delaminated areas. In particular: a) Original image, b) filtered image where areas have been enclosed by a red lines, C) filtered images where areas that are not attributable to delaminations have been removed.

4.2.1 Stiffness, Poisson's ratio

During the tests, the Young's modulus and the Poisson's ratio were continuously monitored, since these have been taken as indicators of damage development occurring into specimens. Stiffness was calculated by determining the slope of the secant of the hysteresis cycles monitored during fatigue life. Both parameters were then normalized to their initial values.

4.2.2 Crack density evolution

A meaningful parameter consists of the crack density, which correlates with the stiffness loss in a laminate. This can be computed in different ways, by considering each transverse crack with the same relevance (total crack density), or by weighting this by its length (*weighted* crack density), to account for those cracks that do not extend along the entire width of the specimen. The weighted crack density is defined as:

$$\rho_w = \frac{\sum_{i=1}^{n} c_i}{wL} \tag{1}$$

where n is the number of cracks, L the length of the observation area, c_i the length of the i-th crack and w the specimen width.

For the $[0_2/90_4]_s$ laminates, the total crack density was equal to the weighted crack density, since all the cracks were extended through the whole width of the specimens. Differently, for $[0/90_2]_s$ laminates, many cracks did not extend through the whole width and therefore it was decided to calculate the weighted crack density.

4.2.3 Delamination ratio

As already mentioned, the growth of the delaminated areas was monitored by regularly capturing images of the specimens. The average delaminated area, induced by each matrix, crack was determined dividing the sum of the delaminated areas by the number of transverse cracks. The parameter *delamination ratio* was then introduced, accordingly to [7], in order to describe the delamination growth, defined as the delaminated area divided by the entire area of the interface 0°/90°.

4.3 Experimental results for $[0_2/90_4]_s$ laminates

Figure 4.2-Figure 4.13 show the curves of crack density, delamination ratio, Young's modulus and Poisson's ratio obtained for the maximum stress values respectively of 140 MPa, 120 MPa, 100 MPa 90 MPa, 80 MPa and 70 MPa. For each stress level, two tests were carried out and, as it can be seen, the trend of the curves is the same for all the tests.

Stiffness reduction is characterized by two distinct phases. In the first stage, axial stiffness drastically decreases after the first cycles, due to the formation and development of matrix cracks. After that, the value of normalized stiffness decreases constantly, at a lower rate, mainly as a consequence of the propagation of delaminations. The relation between the stiffness reduction and damage evolution will be better clarified in the section 4.5.1, where damage development sequence will be presented.

A similar trend was observed for the Poisson's ratio during the fatigue life, characterized by a substantial decrease in the first stage, followed by a continuous but minor loss for the rest of fatigue life.

As regards the crack density, this has a trend opposite to the stiffness curve, rapidly increasing in the first part of fatigue life until reaching a saturation condition.

From the figures, the trend of delamination ratio can be observed. Delaminations initiate in the first stage of fatigue life, from the tips of transverse cracks uniformly distributed across the width of the specimens. As the number of cycles increases, these rapidly develop, parallel to the direction of the load applied. However, when the delamination ratio reaches a critical value, these grow with a decreased rate, which will be kept for the rest of the fatigue life. The decrease in growth rate can be explained as the consequence of the mutual shielding effect for which adjacent delaminations influence each other.

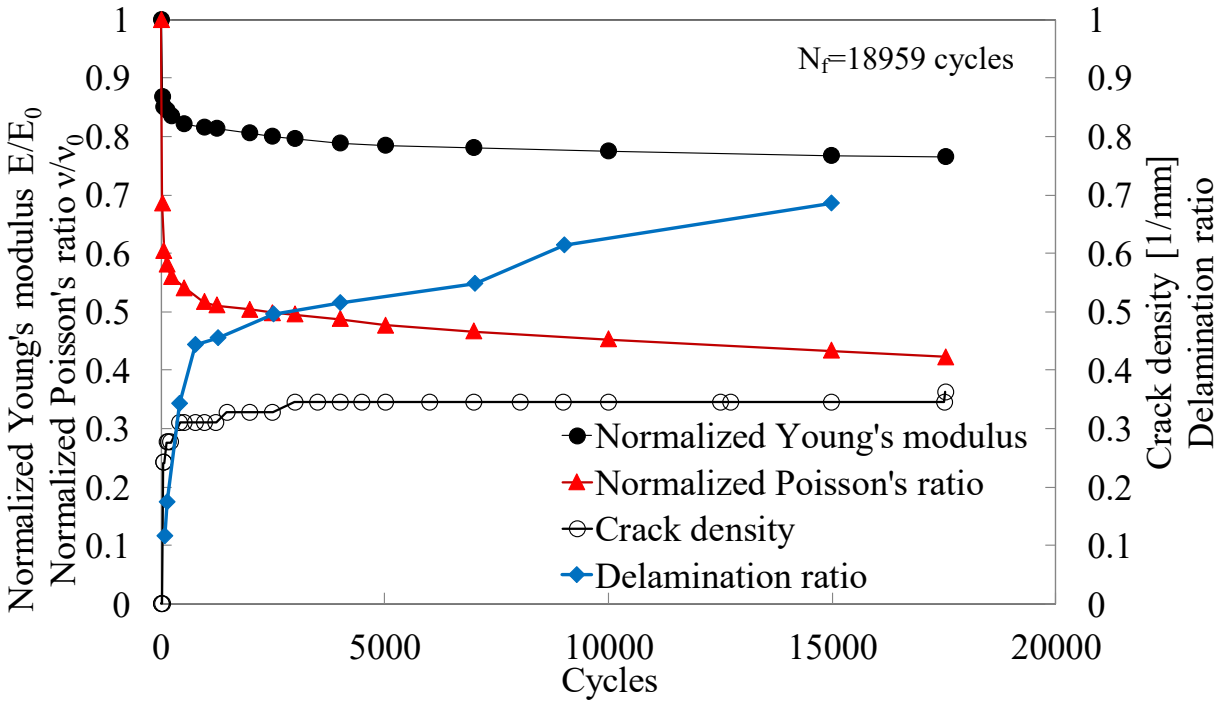

Figure 4.2. Normalized stiffness, Poisson's ratio, crack density and delamination ratio evolution for the fatigue test carried out with a σ_{max}= 140 MPa, test n° 1.

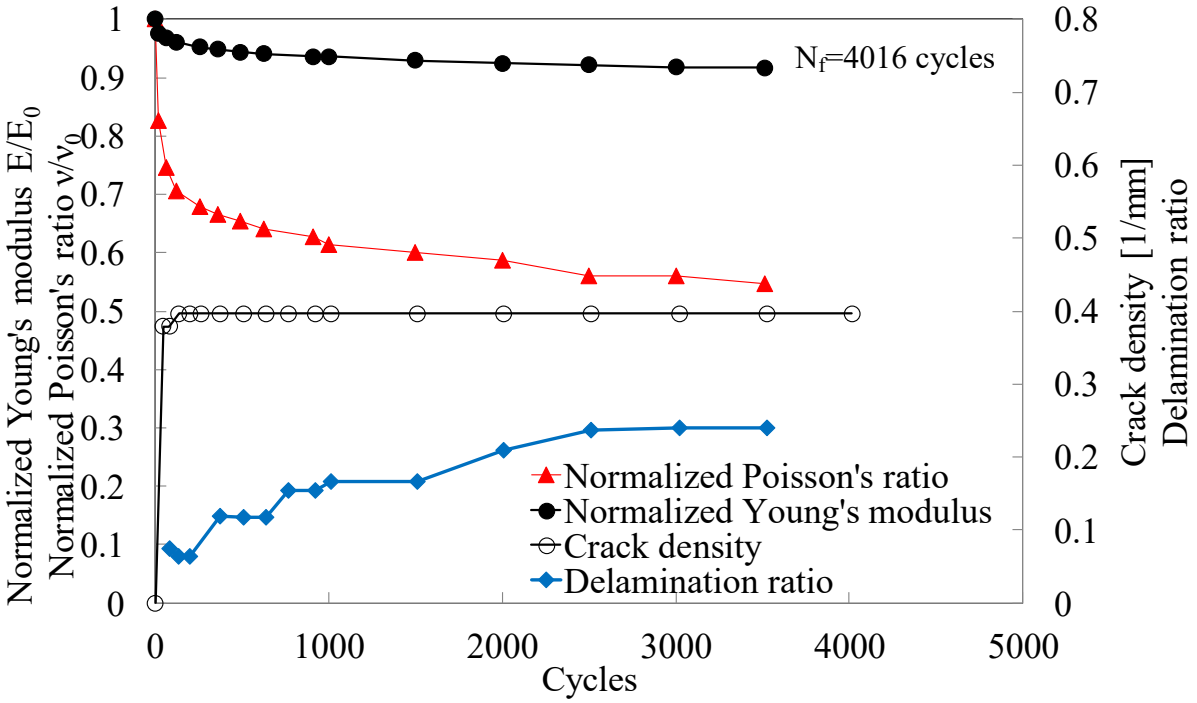

Figure 4.3. Normalized stiffness, Poisson's ratio, crack density and delamination ratio evolution for a fatigue test carried out with a σ_{max}= 140 MPa, test n° 2.

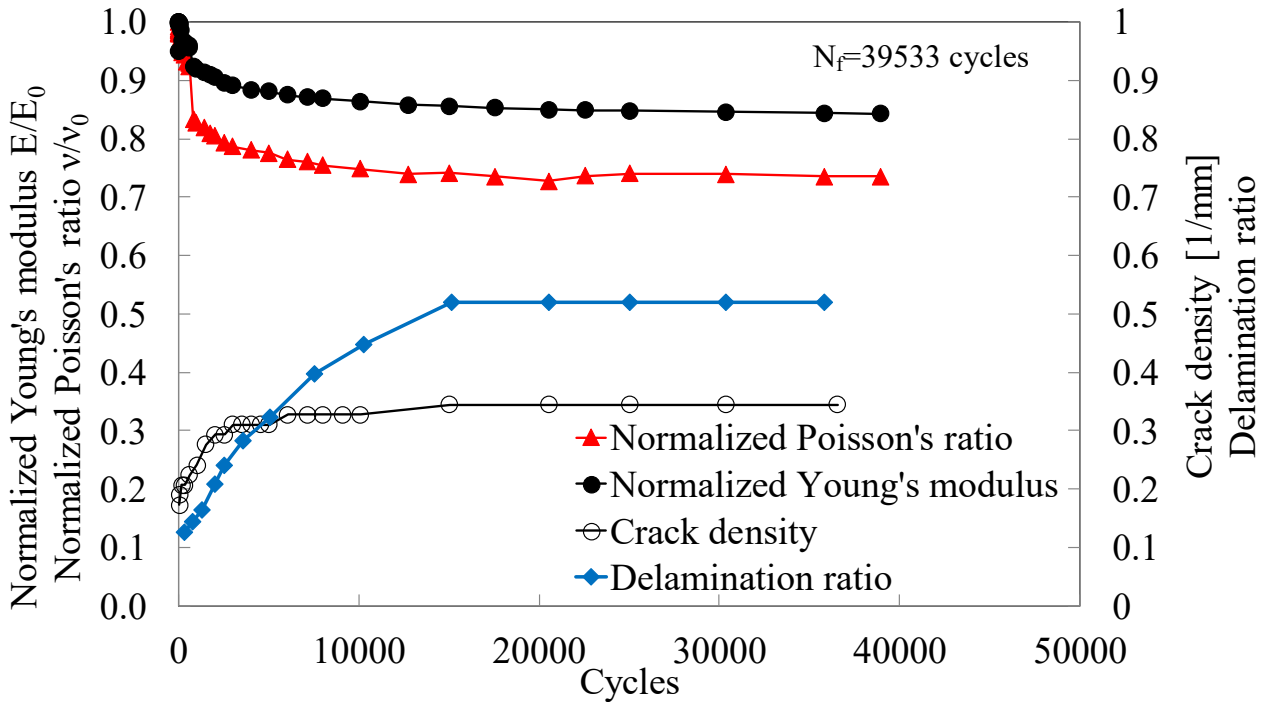

Figure 4.4. Normalized stiffness, Poisson's ratio, crack density and delamination ratio evolution for a fatigue test carried out with a σ_{max}= 120 MPa, test n° 1.

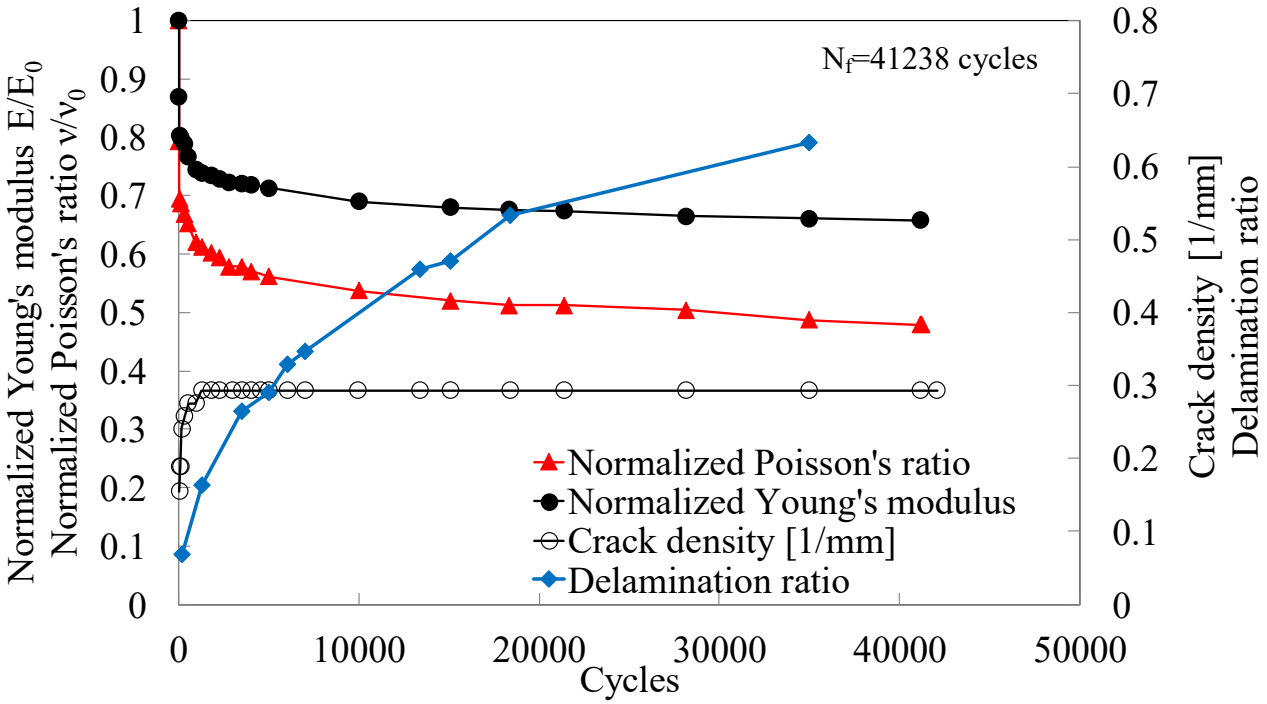

Figure 4.5. Normalized stiffness, Poisson's ratio, crack density and delamination ratio evolution for a fatigue test carried out with a σ_{max}= 120 MPa, test n° 2.

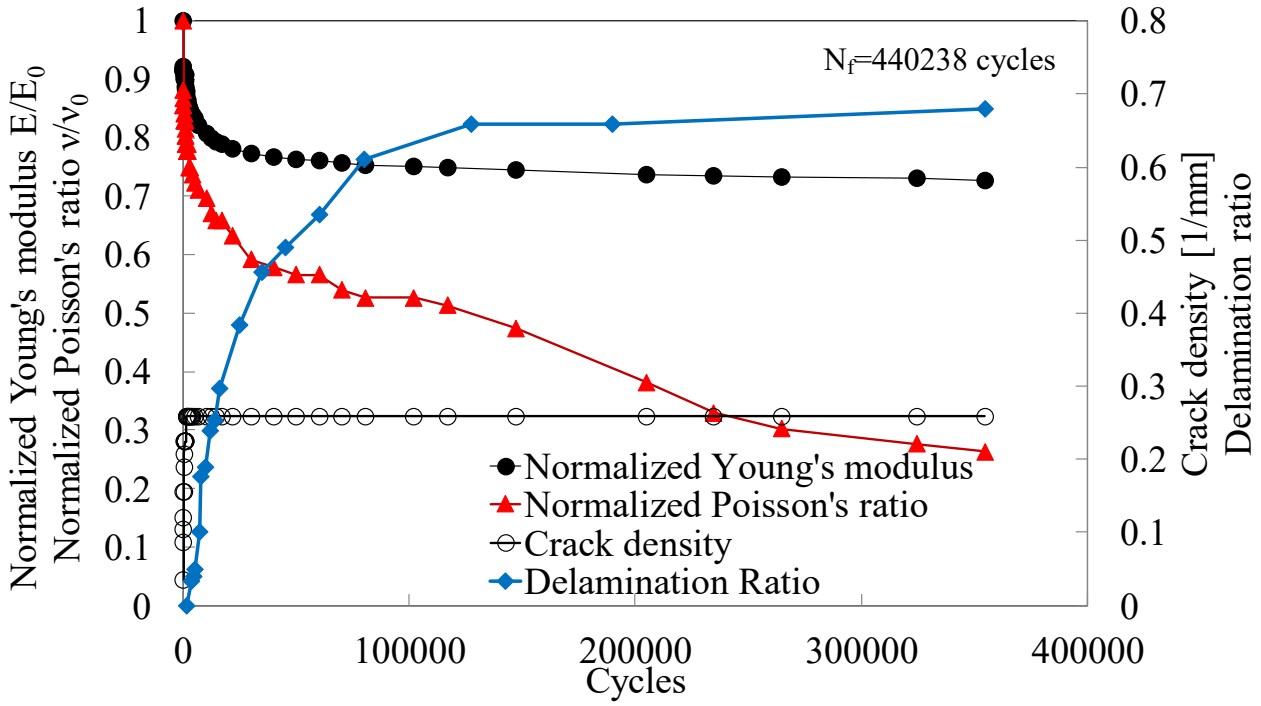

Figure 4.6. Normalized stiffness, Poisson's ratio, crack density and delamination ratio evolution for a fatigue test carried out with a σ_{max}= 100 MPa, test n° 1.

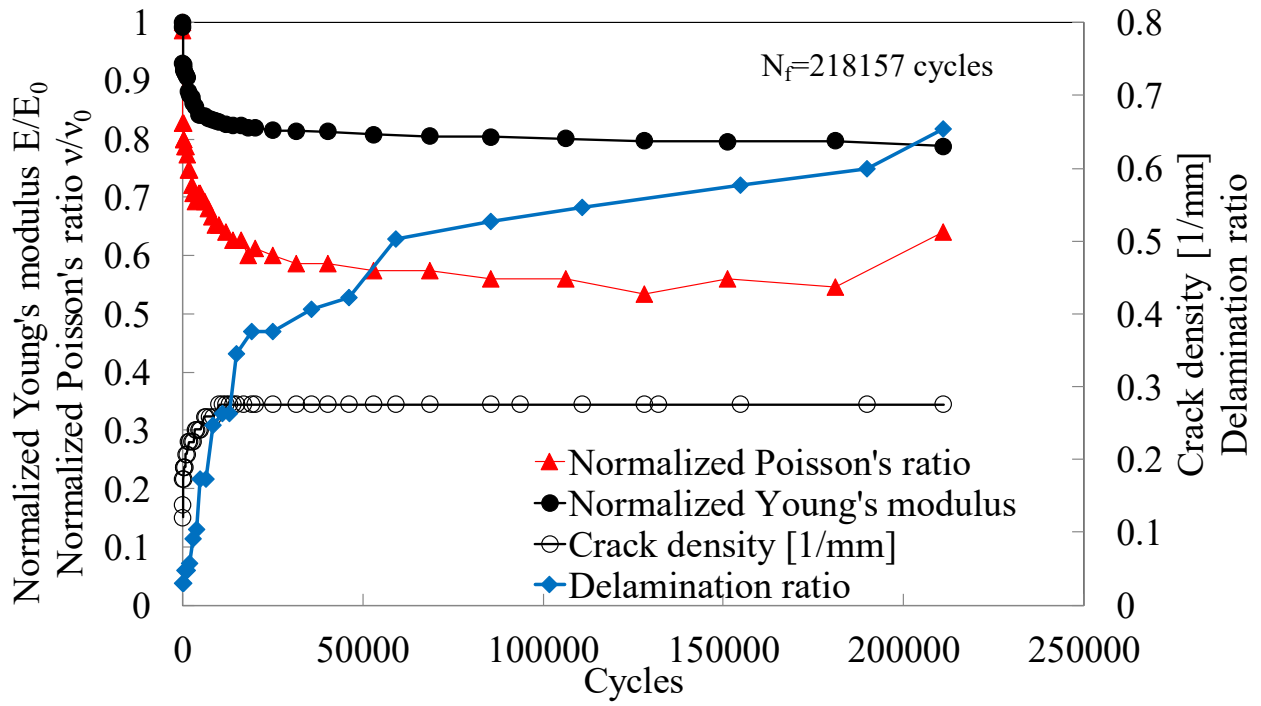

Figure 4.7. Normalized stiffness, Poisson's ratio and crack density evolution for a fatigue test carried out with a σ_{max}= 100 MPa, test n° 2.

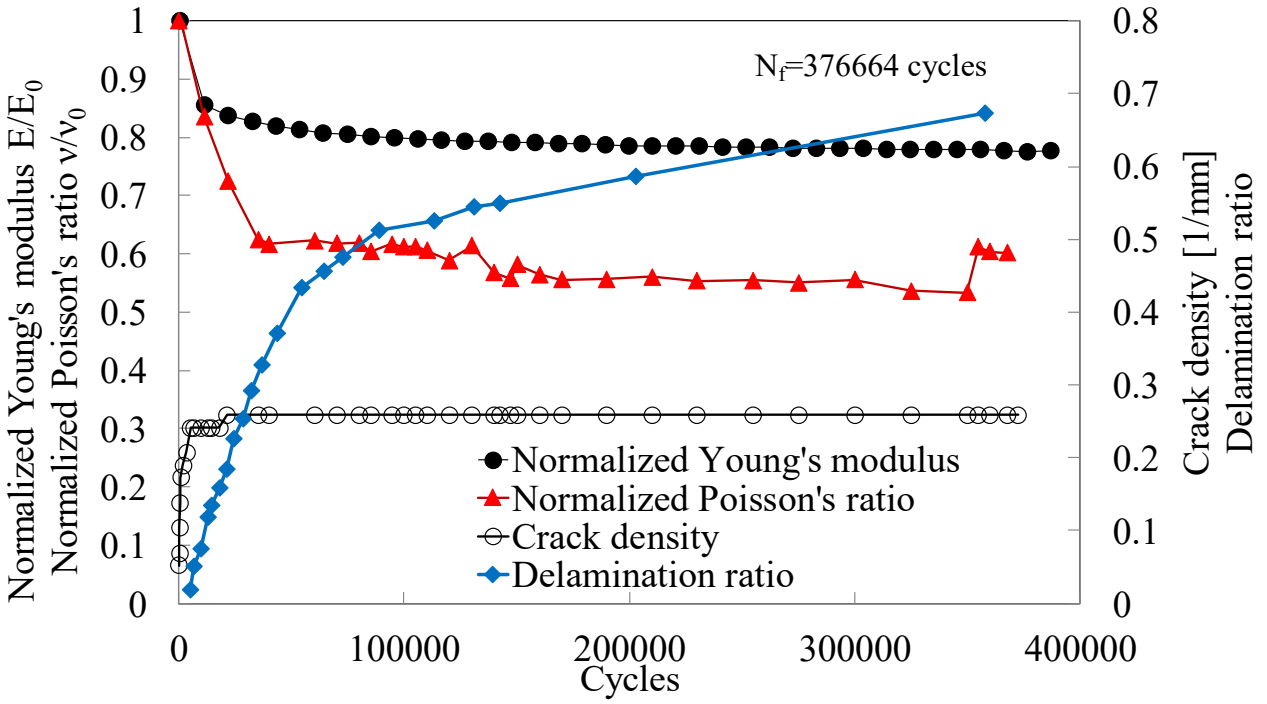

Figure 4.8. Normalized stiffness, Poisson's ratio evolution for a fatigue test carried out with a σ_{max}=90 MPa, test n° 1.

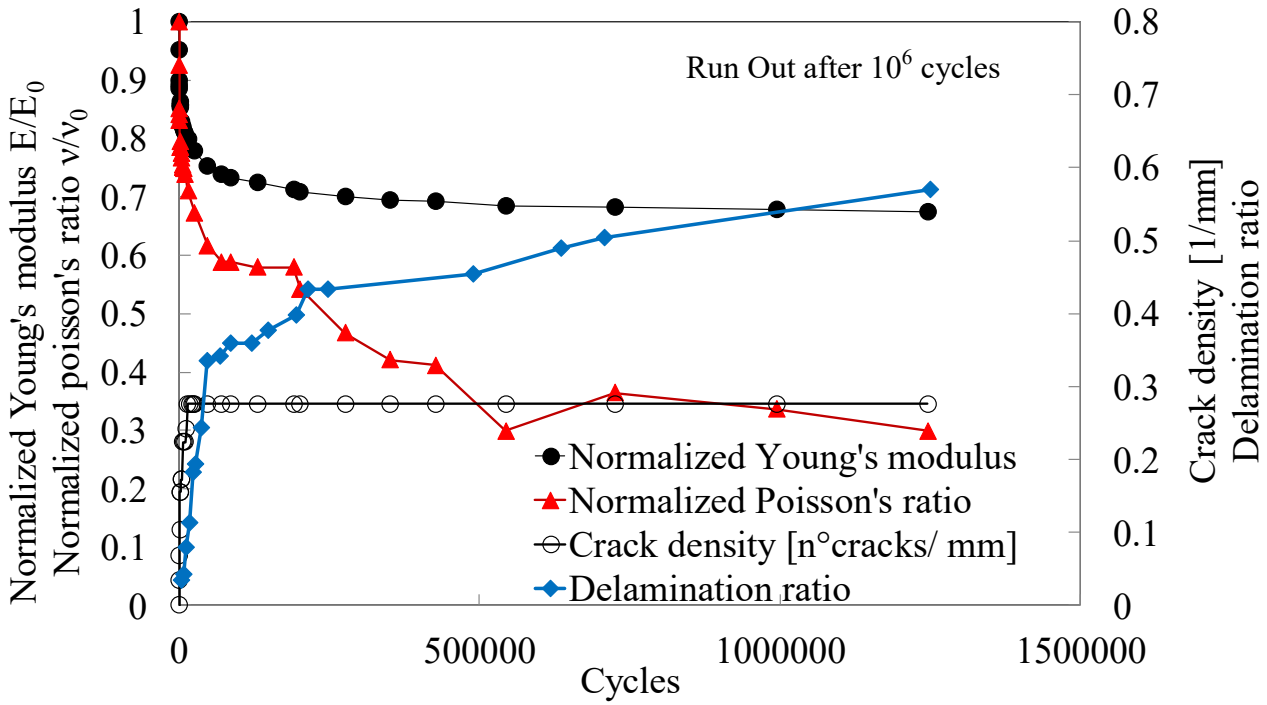

Figure 4.9. Normalized stiffness, Poisson's ratio evolution for a fatigue test carried out with a σ_{max}=90 MPa, test n°2.

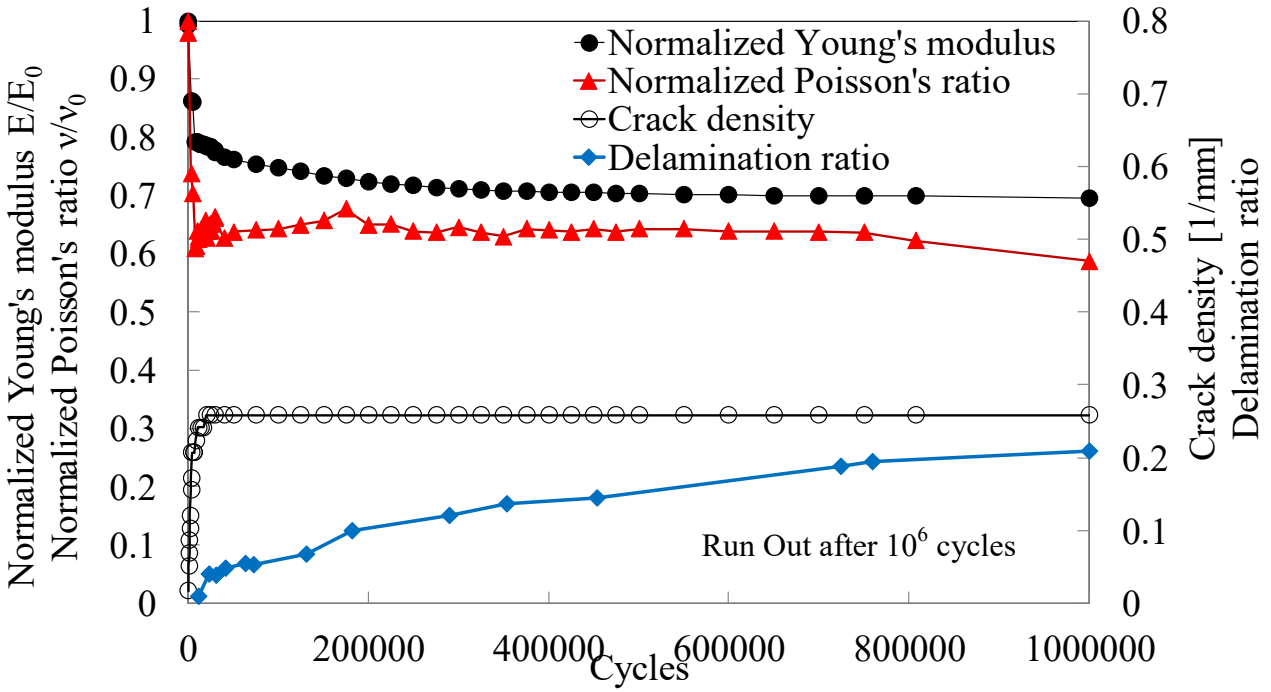

Figure 4.10. Normalized stiffness, Poisson's ratio evolution for a fatigue test carried out with a σ_{max}=80 MPa, test n°1.

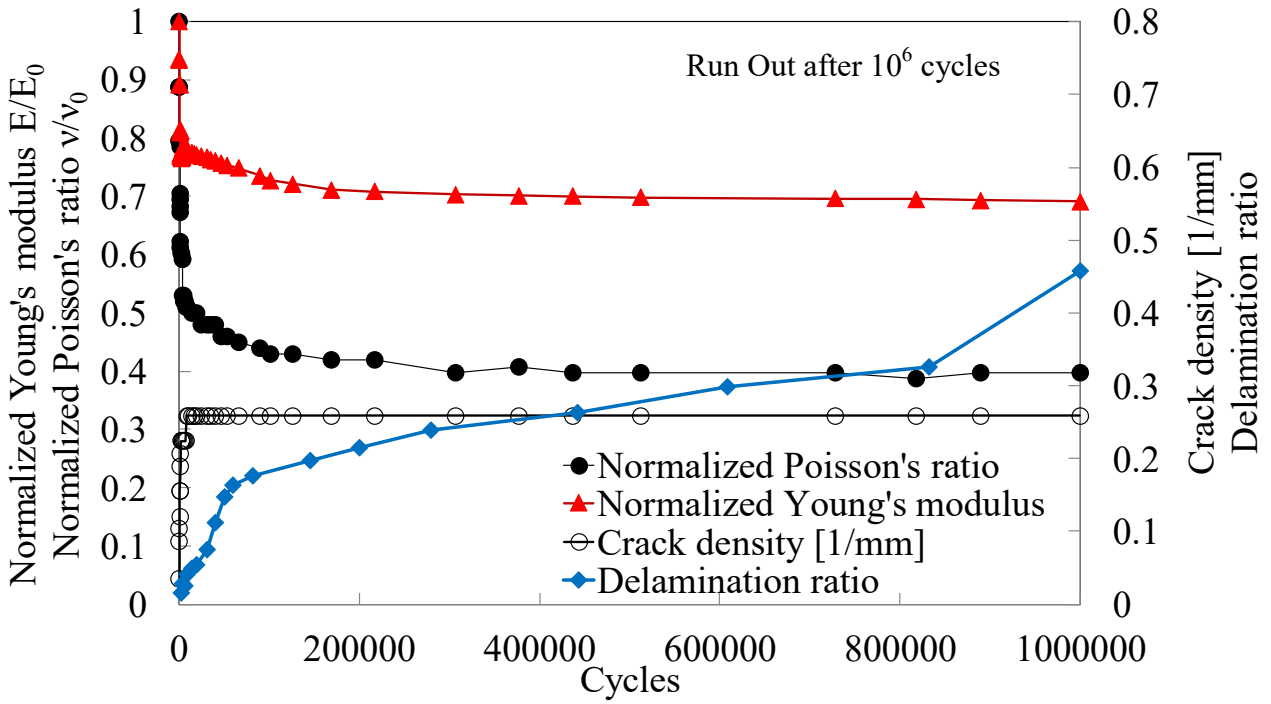

Figure 4.11. Normalized stiffness, Poisson's ratio evolution for a fatigue test carried out with a σ_{max}=80 MPa, test n°2.

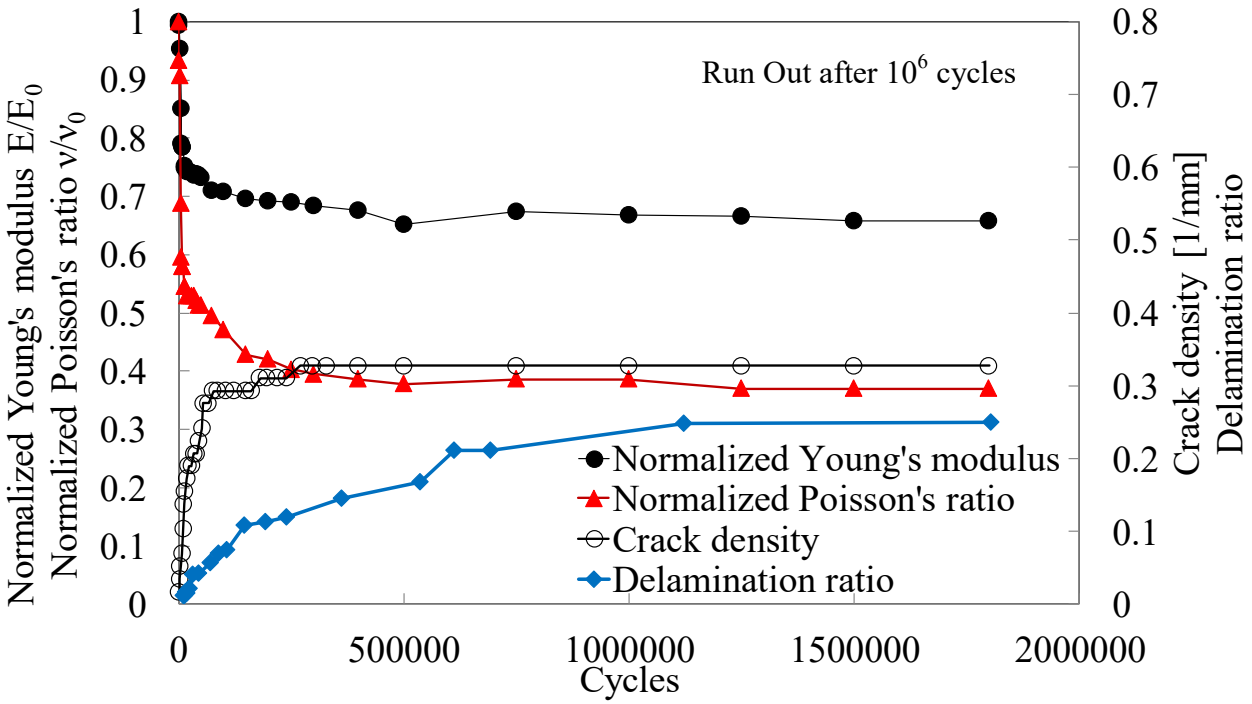

Figure 4.12. Normalized stiffness, Poisson's ratio evolution for a fatigue test carried out with a σ_{max}=70 MPa, test n°1.

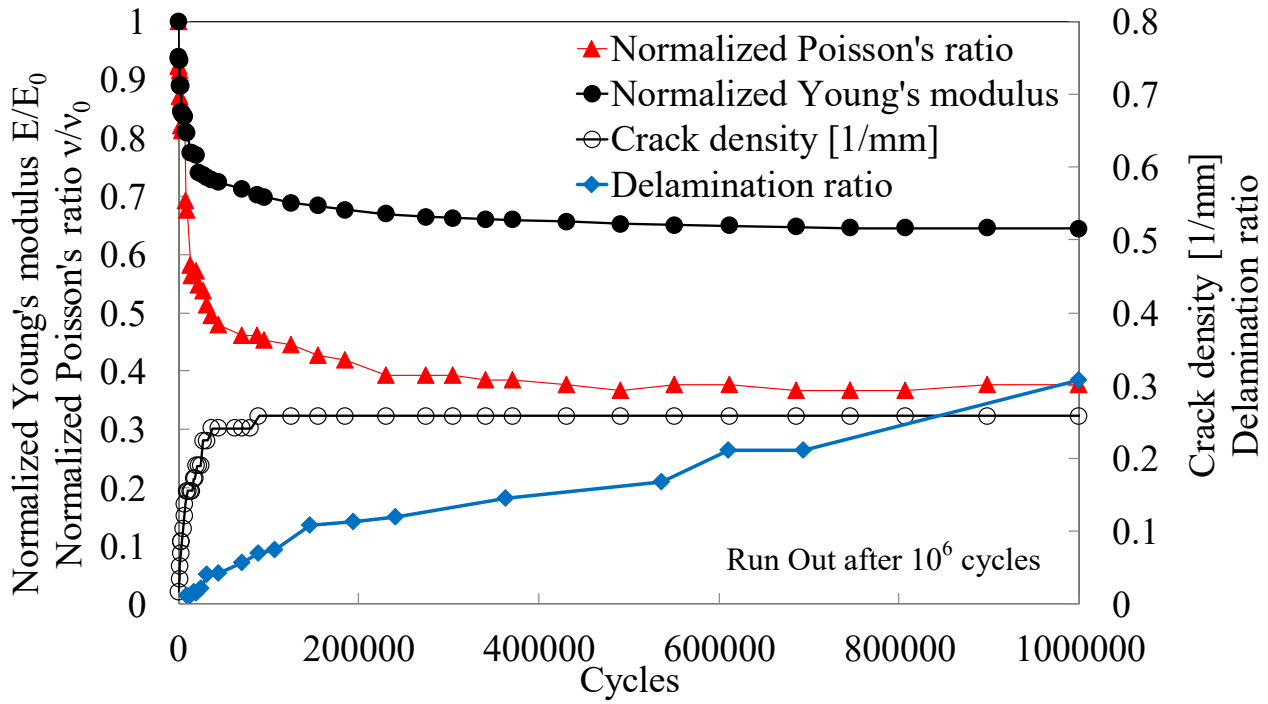

Figure 4.13. Normalized stiffness, Poisson's ratio evolution for a fatigue test carried out with a σ_{max}=70 MPa, test n°2.

Data referred to number of cycles at which delaminations occurred, crack density saturated and the number of cycles spent for final failure, are reported in Table 4.2. Furthermore, the amount of stiffness loss due to the formation and accumulation of transverse cracks and due to the delamination propagation are reported in the table.

Table 4.2 Data obtained from experimental tests performed on $[0_2/90_4]_s$ specimens

Maximum stress σ_{max} [MPa]	Number of cycles for delamination onset	Number of cycles for crack density saturation	Number of cycles for final failure	Stiffness drop due to transverse cracks [%]	Stiffness drop due to delaminations [%]
140 MPa 01	43	2984	18'959	15.20	3.20
140 MPa 02	47	135	4'016	4.80	3.50
120 MPa 01	71	7154	39'533	6.90	4.40
120 MPa 02	70	1279	41'238	26.10	8.11
100 MPa 01	120	1’500	440’238	13.00	14.00
100 MPa 02	160	6’018	218’157	16.00	5.30
90 MPa 01	3’483	17’938	376’664	28.90	4.38
90 MPa 02	1’400	10’079	Not failed	18.62	13.90
80 MPa 01	6’534	16’726	Not failed	21.44	9.47
80 MPa 02	3’772	10’576	Not failed	21.90	9.10
70 MPa 01	7’872	54’699	Not failed	28.90	5.10
70 MPa 02	7’614	37’380	Not failed	28.80	7.20

4.4 Experimental results for $[0/90_2]_s$ laminates

As abovementioned, with the aim of verifying if the evolution of delamination was influenced by the thickness of the 90° layer, glass epoxy laminates characterized by $[0/90_2]_s$ lay-up were manufactured.

Even during these tests, the Young's modulus and the Poisson's ratio were monitored. The trend of the curves is similar to the one obtained for the scaled stacking sequence $[0_2/90_4]_s$. Stiffness drastically decreases after the first cycles, and then keep decreasing during the fatigue life with a minor rate.

The Poisson's ratio presented a similar trend to the Young's modulus, as can be seen in Figure 4.14-Figure 4.19. In the first part of fatigue life, the normalized Poisson's ratio drastically decreases until reaching a value comprised between 0.4 and 0.6. Then, it continues decreasing but with a rate that can be considered almost negligible.

The crack density curve, similarly to what already observed for $[0_2/90_4]_s$ laminates, increases in the first part of fatigue life and then soon reaches a saturation condition.

As regards delamination ratio, even in this case delaminations were observed to form in the first part of fatigue life, quickly develop and then slow down the growth.

The data referred to the fatigue life consumed for the delamination onset, crack density saturation and the number of cycles for final failure are reported in Table 4.3, together with the amount of stiffness loss due to respectively to the formation of matrix cracks (recorded until the crack density saturation level) and to the delamination initiation and propagation.

4.5 Discussion

By comparing the data collected in Table 4.2 and Table 4.3, it can be observed that delamination onset occurs in the first stage, consuming a low percentage of fatigue life (<1% of total fatigue life).

Therefore, if the aim of a model is the assessment of the fatigue life of a component, the number of cycles spent for the initiation of delaminations can be assumed negligible.

A further conclusion that can be drawn from the results obtained is that the initial stiffness loss is due prevalently to the formation and growth of transverse cracks. However, with the perspective of developing a model aimed at predicting stiffness degradation, also delaminations need to be included in the model, since their contribution to the total stiffness loss is significant.

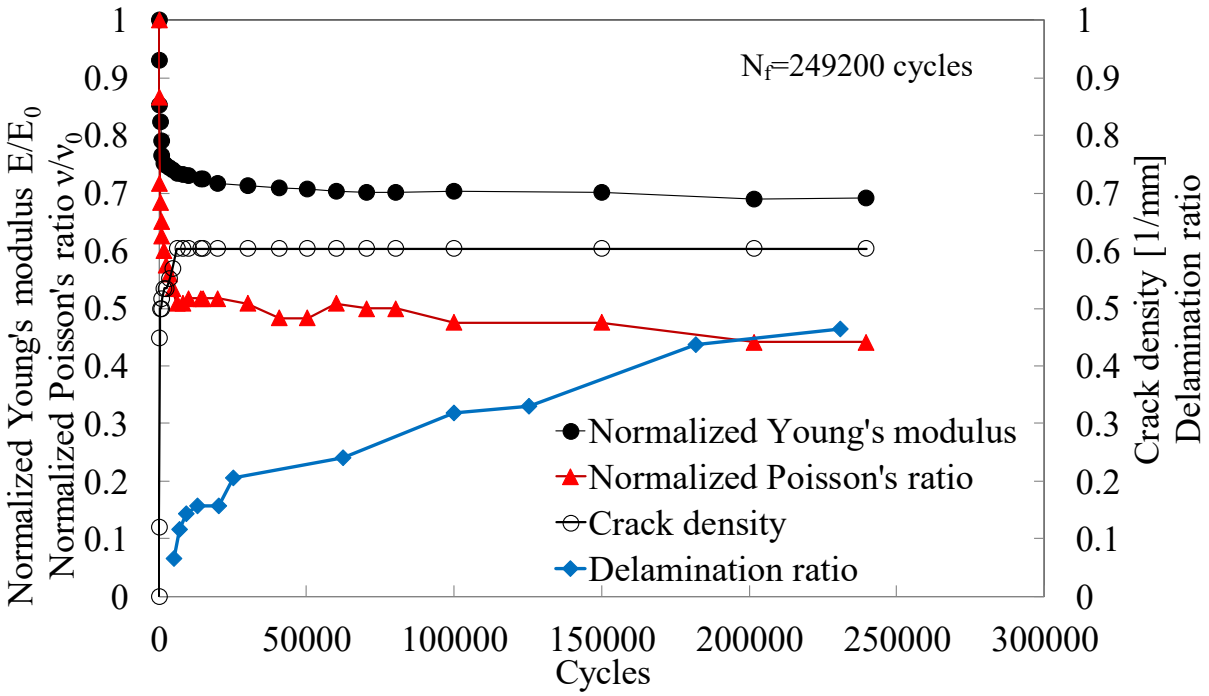

Figure 4.14 Normalized stiffness, Poisson's ratio evolution for a fatigue test carried out with a σ_{max}=120 MPa, test n°1. In the secondary axis the delamination ratio and crack density are reported.

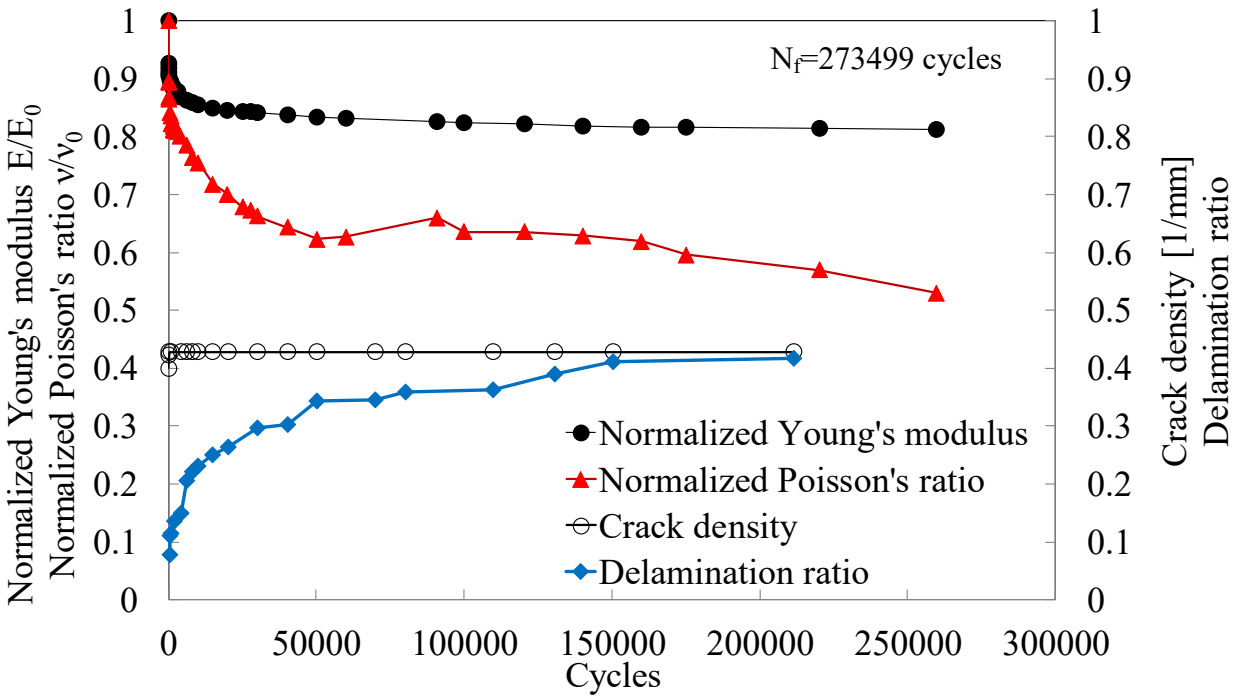

Figure 4.15 Normalized stiffness, Poisson's ratio evolution for a fatigue test carried out with a σ_{max}=120 MPa, test n°2. In the secondary axis the delamination ratio and crack density are reported.

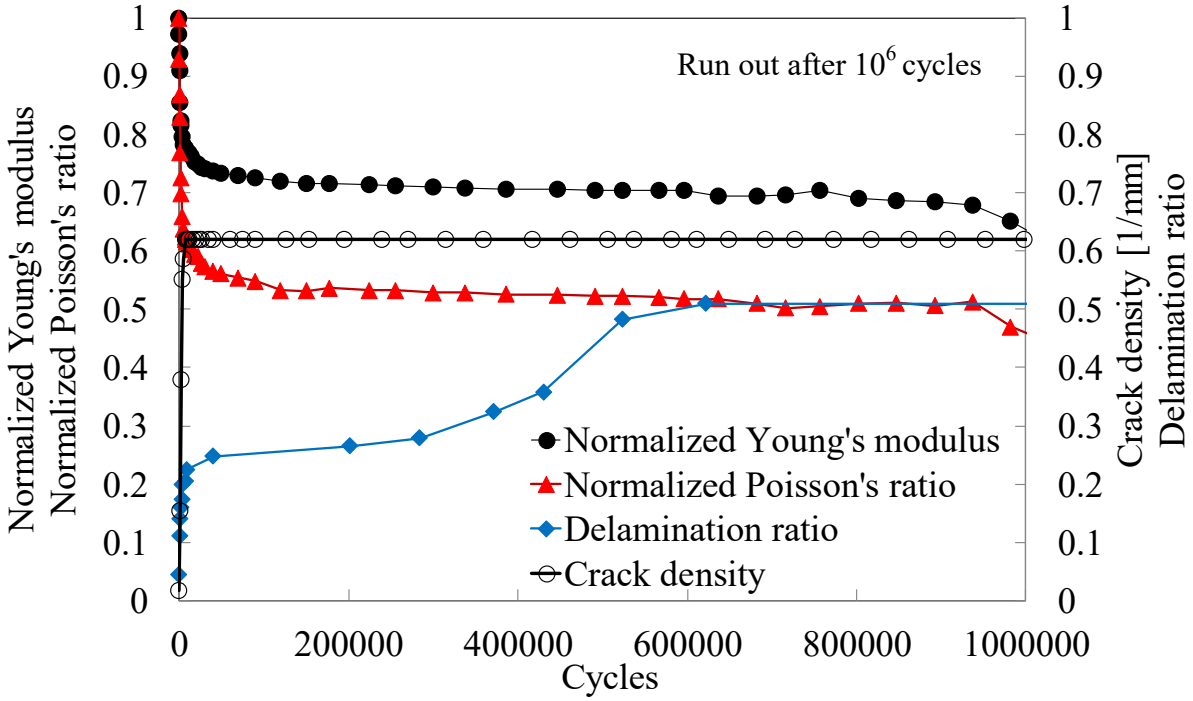

Figure 4.16 Normalized stiffness, Poisson's ratio evolution for a fatigue test carried out with a σ_{max}=100 MPa, test n°1. In the secondary axis the delamination ratio and crack density are reported.

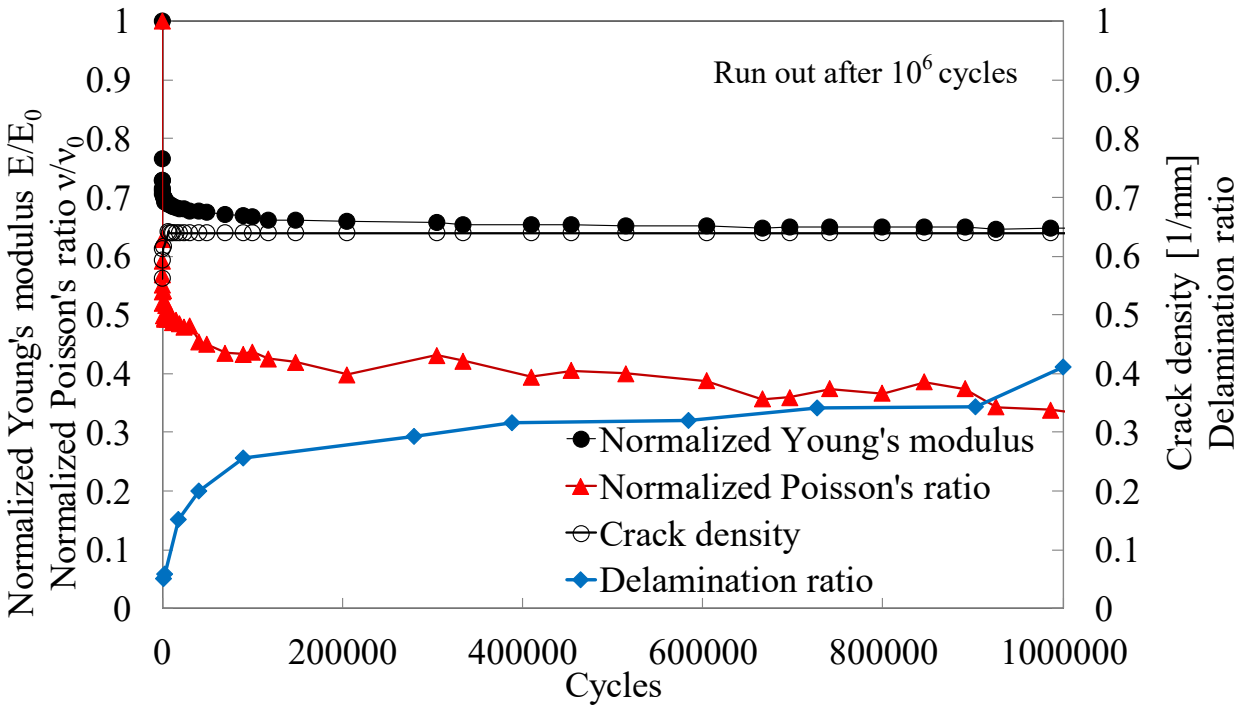

Figure 4.17 Normalized stiffness, Poisson's ratio evolution for a fatigue test carried out with a σ_{max}=100 MPa, test n°2. In the secondary axis the delamination ratio and crack density are reported.

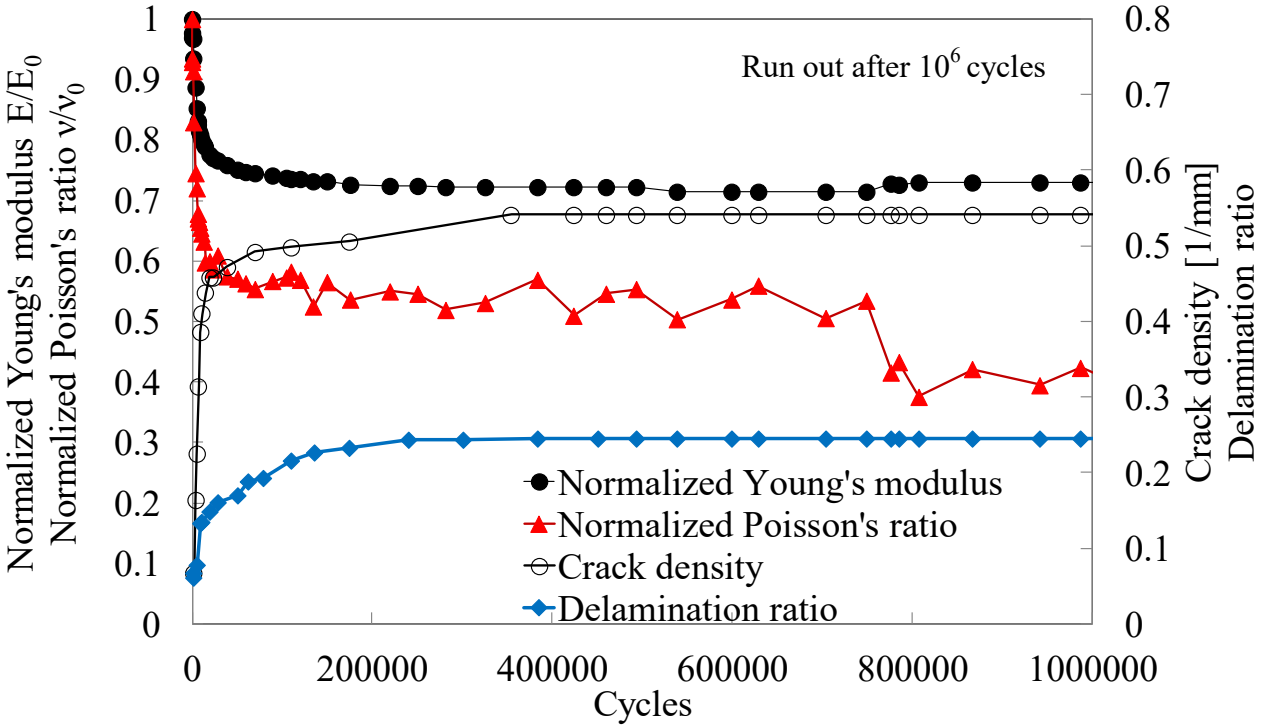

Figure 4.18 Normalized stiffness, Poisson's ratio evolution for a fatigue test carried out with a σ_{max}=90 MPa, test n°1. In the secondary axis the delamination ratio and crack density are reported.

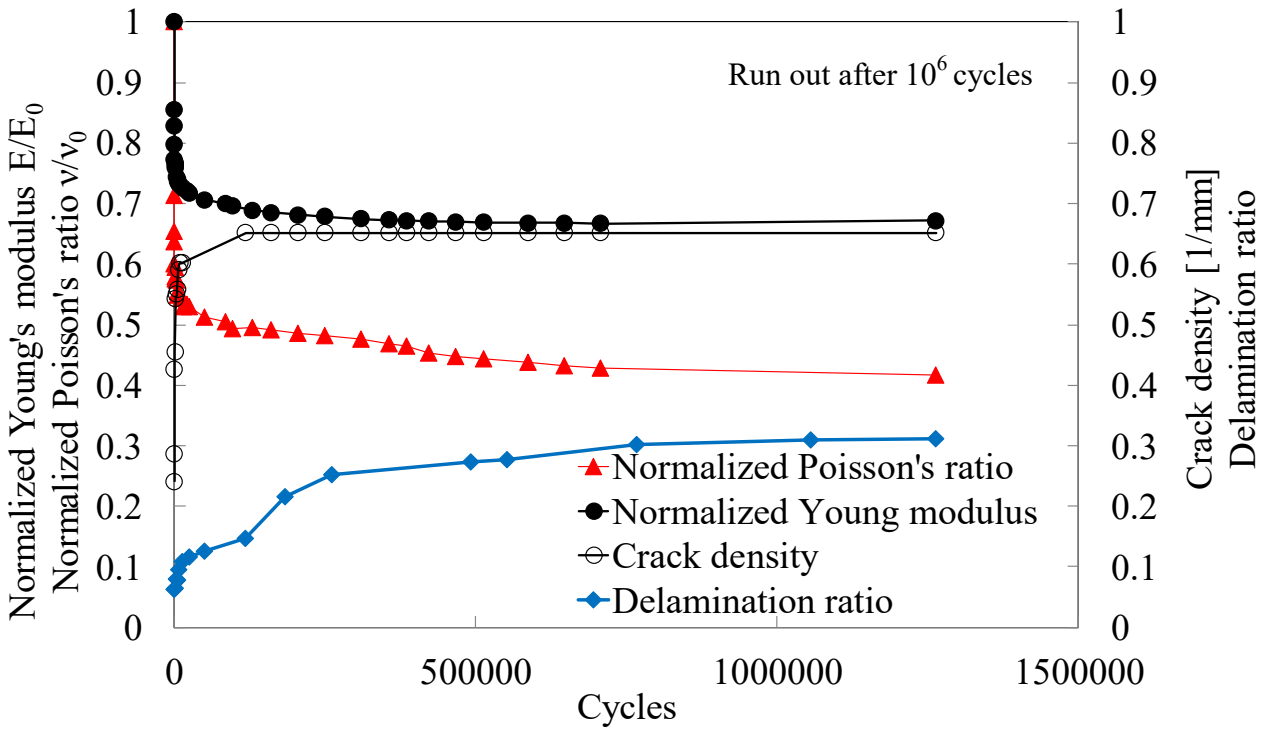

Figure 4.19 Normalized stiffness, Poisson's ratio evolution for a fatigue test carried out with a σ_{max}=90 MPa, test n°2. In the secondary axis the delamination ratio and crack density are reported.

Table 4.3 Data obtained from experimental tests performed on $[0/90_2]_s$ specimens.

Maximum stress σ_{max} [MPa]	**Number of cycles for delamination onset**	**Number of cycles for crack density saturation**	**Number of cycles for delamination propagation**	**Number of cycles for final failure**	**Stiffness drop due to transverse cracks [%]**	**Stiffness drop due to delaminations [%]**
120 MPa 01	934	6041	249200	255241	27.00	4.00
120 MPa 02	731	185	273499	274230	14.00	33.00
100 MPa 01	1519	5519	998481	Not failed	18.40	14.90
100 MPa 02	2094	8028	997906	Not failed	31.13	4.00
90 MPa 01	11293	110119	988707	Not failed	26.40	0.60
90 MPa 02	6103	118720	993897	Not failed	31.00	2.00

4.5.1 Damage development

In order to study the evolution of damage, some $[0_2/90_4]_s$ specimens were subjected to dedicated fatigue tests. As soon as transverse cracks were seen to form and reach the edges, tests were interrupted and specimen edges were analyzed using an optical microscope, in order to analyze the damage as soon as it occurred. Then, damaged specimens were subjected to further loading cycles until new damage mechanisms were seen to occur and tests were interrupted again to realize new microscopic investigations. By adopting this method, it was possible to document the different phases characterizing the damage process, by collecting a detailed series of images showing the accumulation of the observed failure modes.

Figure 4.20 and

Figure 4.21 illustrate the stages of the damage development observed for a $[0_2/90_4]$s and a $[0/90_2]$s laminate.

The specimens were fatigue tested with a stress level of σ_{max}= 90 MPa (R=0.05, υ=10 Hz), which was definitively interrupted after 10^6 cycles.

From the figures, it is evident that, as soon as the matrix crack reaches the interface 0°/90°, there induces the formation of a delamination that will continue propagate along the interface. Then, as the delamination grows, some fibres of the 0° layers break in the proximity of the transverse crack and delamination tips. This scenario was common to all the transverse cracks and delaminations observed. Therefore, damage evolution can be summarized in three stages: the formation of transverse cracks, the onset and propagation of delaminations followed by the breakage of the fibres of 0° layers.

It is worth noticing that the fatigue damage evolution, observed for this lay-up, seems to be different from the damage evolution observed for the same specimens tested under quasi-static loading. In

fact, in the latter case, first the matrix crack reached the interface and, only after that, the delamination was seen to form, as documented in [33].

a)

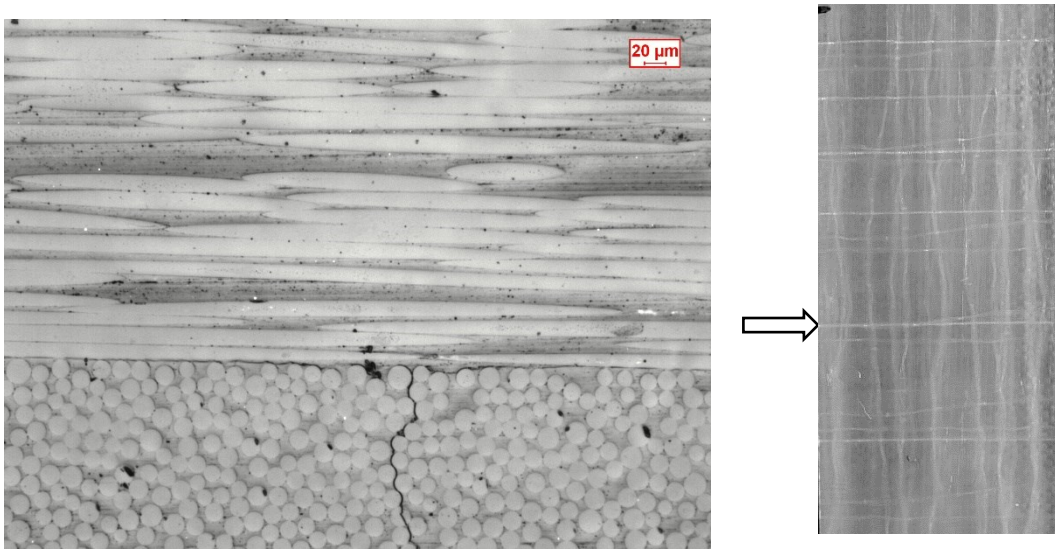

b)

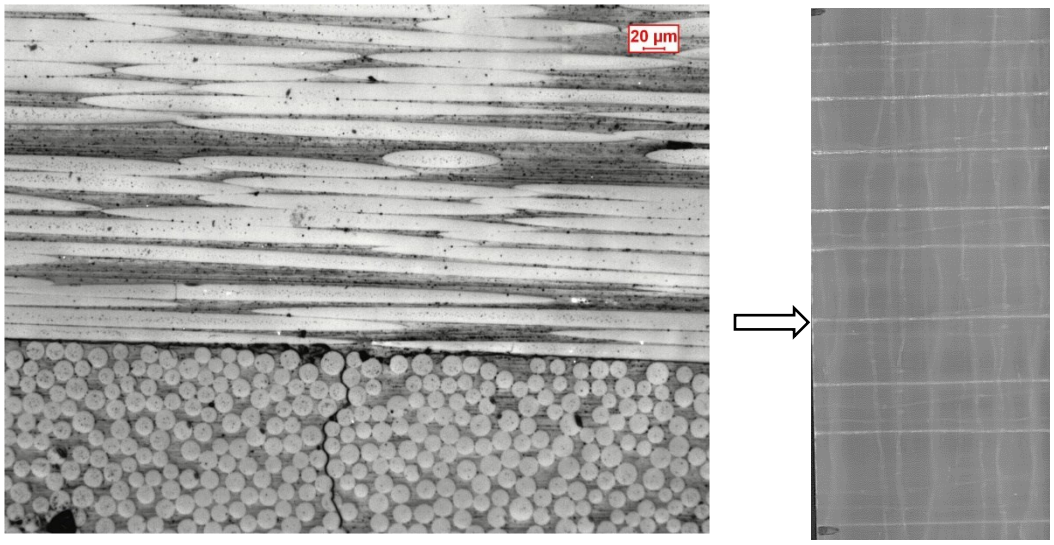

c)

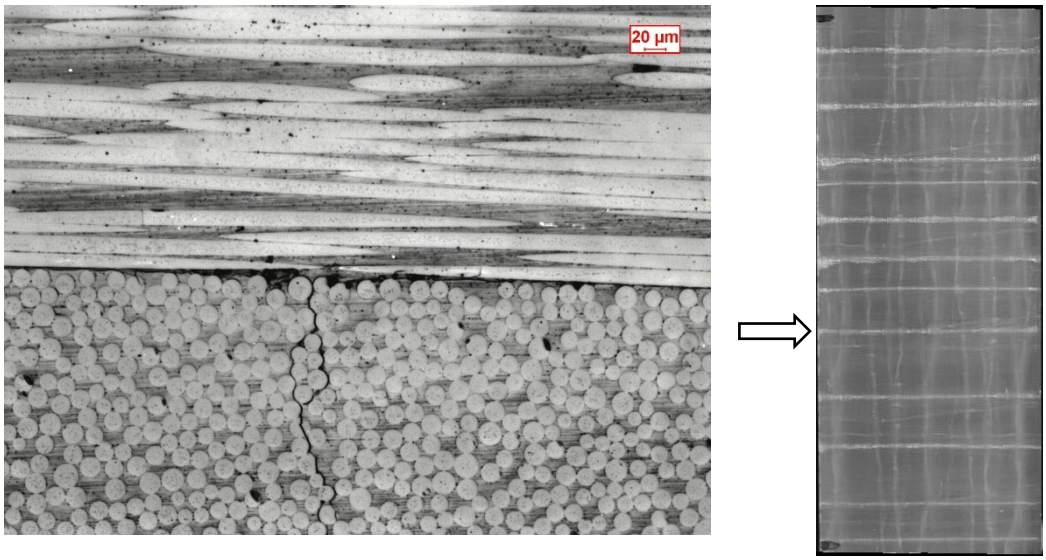

d)

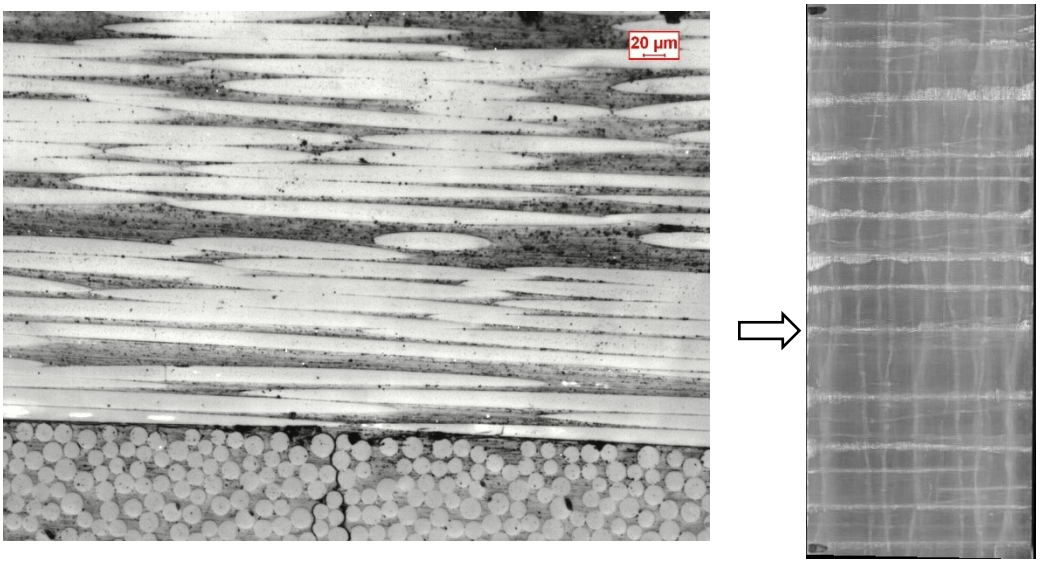

e)

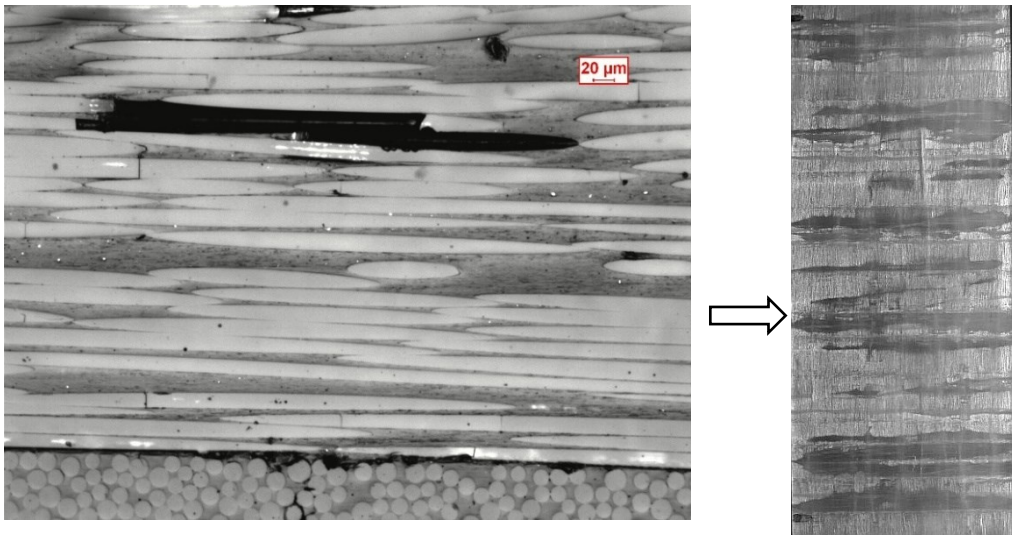

f)

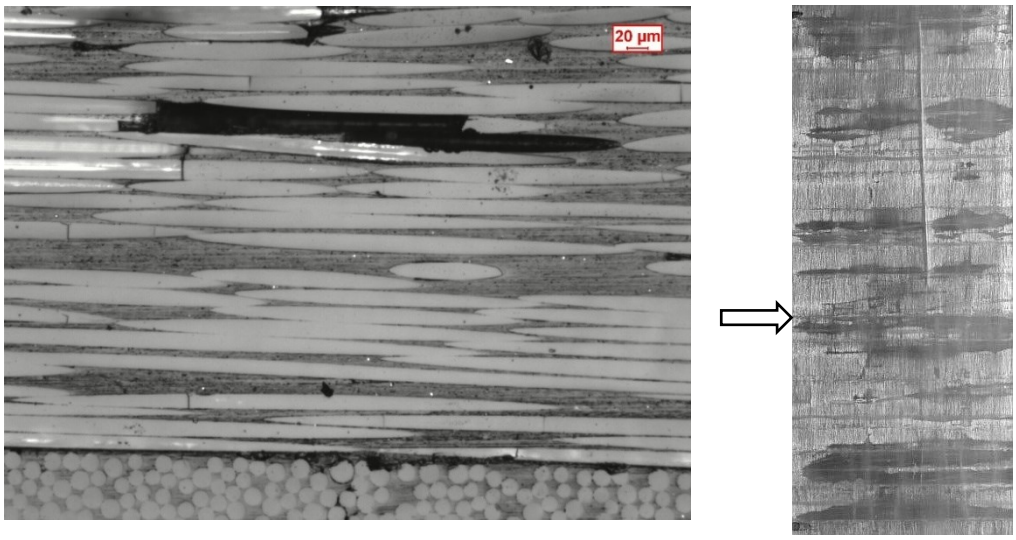

g)

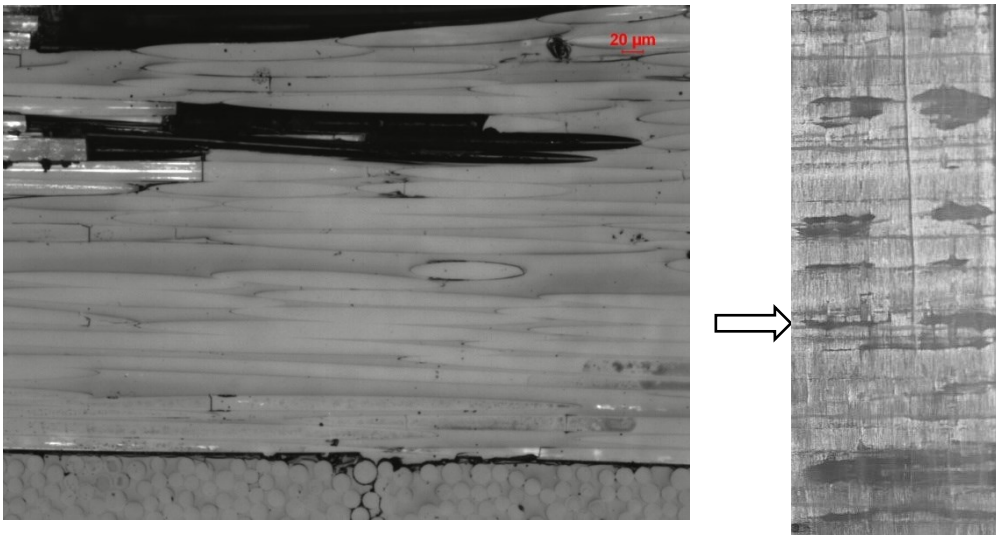

Figure 4.20. Damage evolution: the right-hand side column reports the photographs of the frontal surface of the specimen where delaminated areas appear as white areas. The left-hand side column reports the microscopic images of the area indicated with an arrow. Images are referred to the damage scenario observed after a) 111 cycles b) 421 cycles c) 1567 cycles d) 3934 cycles e) 165155 cycles f) 657740 and g) 1034225 cycles.

a)

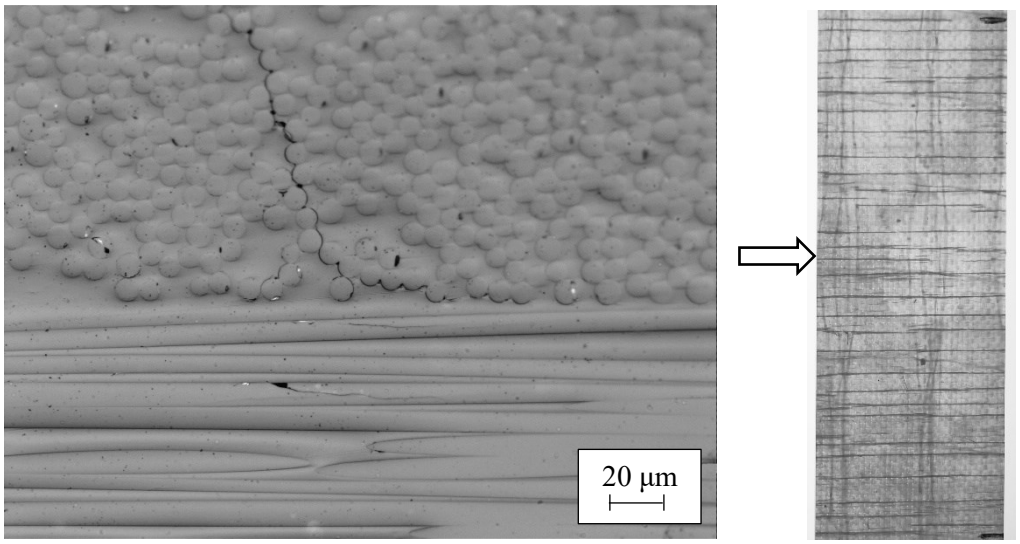

b)

c)

d)

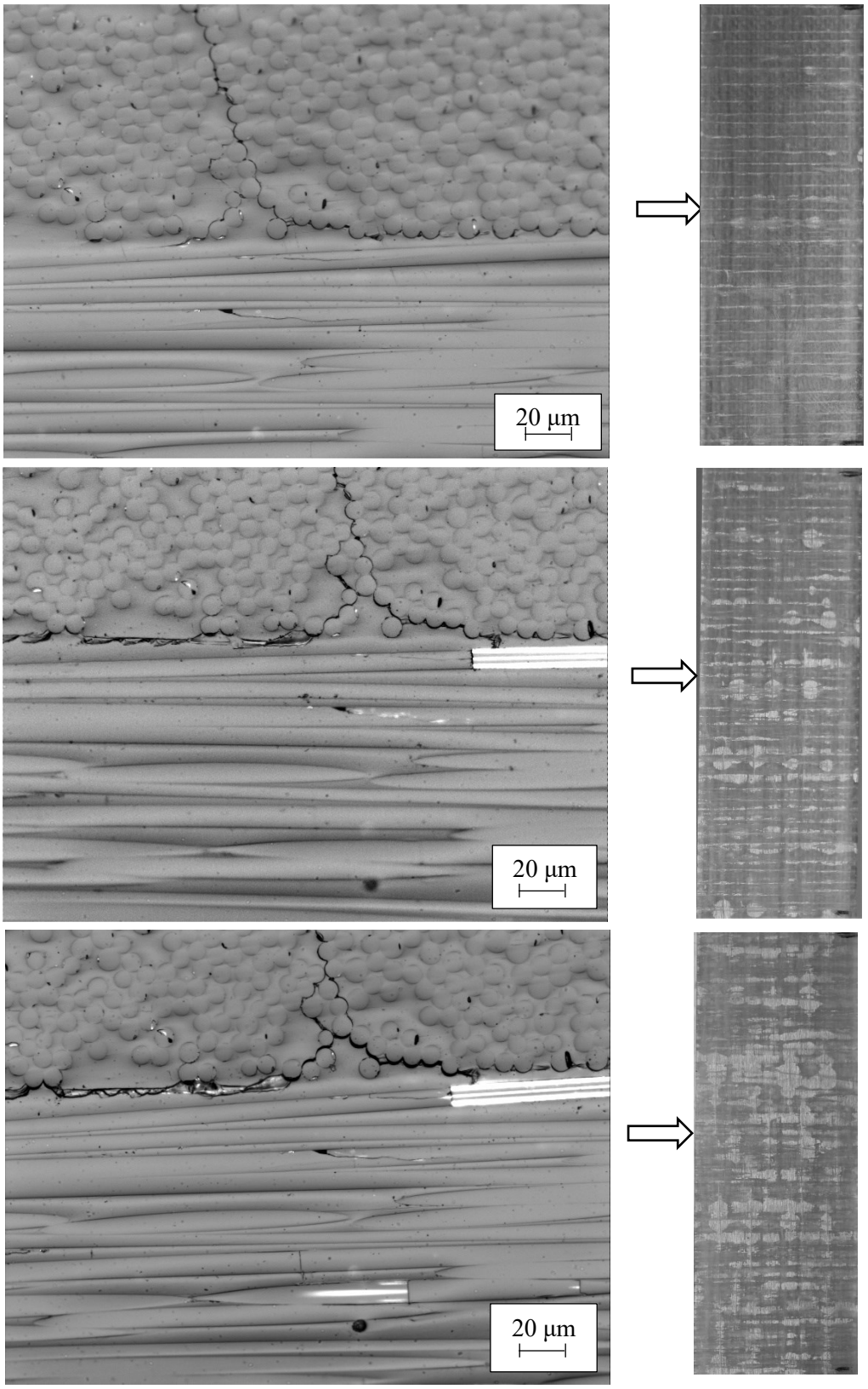

Figure 4.21 Micrographs of damage evolution for a $[0/90_2]_s$ laminate fatigue tested with a σ_{max}=90 MPa. Images are referred to the scenario observed after a) 500 cycles b) 10001 cycles c) 152707 cycles and d) 10^6 cycles.

4.6 Statistical analysis

From the micrographs collected it was noticed that, in some cases, delaminations grew symmetrically in both directions from the tips of the transverse cracks, whereas in others developed predominantly in one direction. A similar damage scenario has already been presented by Gamstedt et al.[34]. In this paper, the authors explained the unsymmetrical growth as due to local variations in microstructure or to the arresting effect of adjacent matrix cracks on delamination growth.

A further distinction that can be made consists of the presence or less of a branching of transverse cracks in the proximity of the interface 0°/90°.

The edges of fatigue tested specimens were observed by using an optical microscope, in order to quantify how many delaminations were formed symmetrically respect to the plane of the transverse crack (H-shaped) and asymmetrically (Z-shaped). In addition to the configurations of delaminations already mentioned, some of these were seen to form only along an interface, either symmetrically or asymmetrically respect to the plane of the transverse crack, while no delamination was observed at the opposite end of the transverse crack. These cases were referred to as incomplete H-shaped or Z-shaped delaminations. For the sake of clarity, the possible configurations of delaminations are schematically illustrated in Figure 4.22. The data collected are reported in Table 4.4.

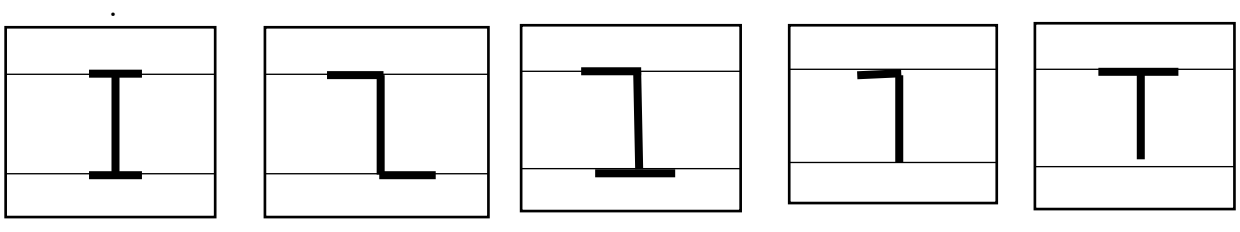

H- shaped delaminations | *Z- shaped delaminations* | *Mixed configuration* | *Incomplete Z-shaped delamination* | *Incomplete H-shaped delamination*

Figure 4.22. Configurations of delaminations.

Table 4.4 Data of the configurations of delaminations.

Specimen code	**H- shaped delaminations**		**Z- shaped delaminations**	**Mixed configuration**		**Incomplete Z-shaped delamination**	**Incomplete H-shaped delamination**
		Branched			Branched		
$[0_2/90_4]_s$ 70 MPa 01	4	2	1	0		3	0
$[0_2/90_4]_s$ 70 MPa 02	2	3	4	7		0	0
$[0_2/90_4]_s$ 80 MPa 01	4		1	4	1	1	1
$[0_2/90_4]_s$ 80 MPa 02	4	1	4	3		0	0
$[0_2/90_4]_s$ 90 MPa 01	4	5	0	4		4	1
$[0_2/90_4]_s$ 90 MPa 02	11	2	3	0	2	3	0
$[0_2/90_4]_s$ 100 MPa 01	6	1	1	1	1	0	0
$[0/90_2]_s$ 90 MPa 01	3	5	6	5		2	0
$[0/90_2]_s$ 100 MPa 01	3		2	3	3	1	0
Total	41	19	22	27	7	14	2
%	31.06	14.39	16.67	20.45	5.30	10.61	1.52

From the table, it is evident that delaminations propagate prevalently symmetric to the plane of matrix cracks, following the schematic denominated H-shaped.

In the following figures, some representative micrographs are illustrated. In particular, Figure 4.23 (a-b) represent the Z-shaped delaminations, while Figure 4.23 (c-d) the H-shaped delaminations. Further micrographs are reported in the Appendix.

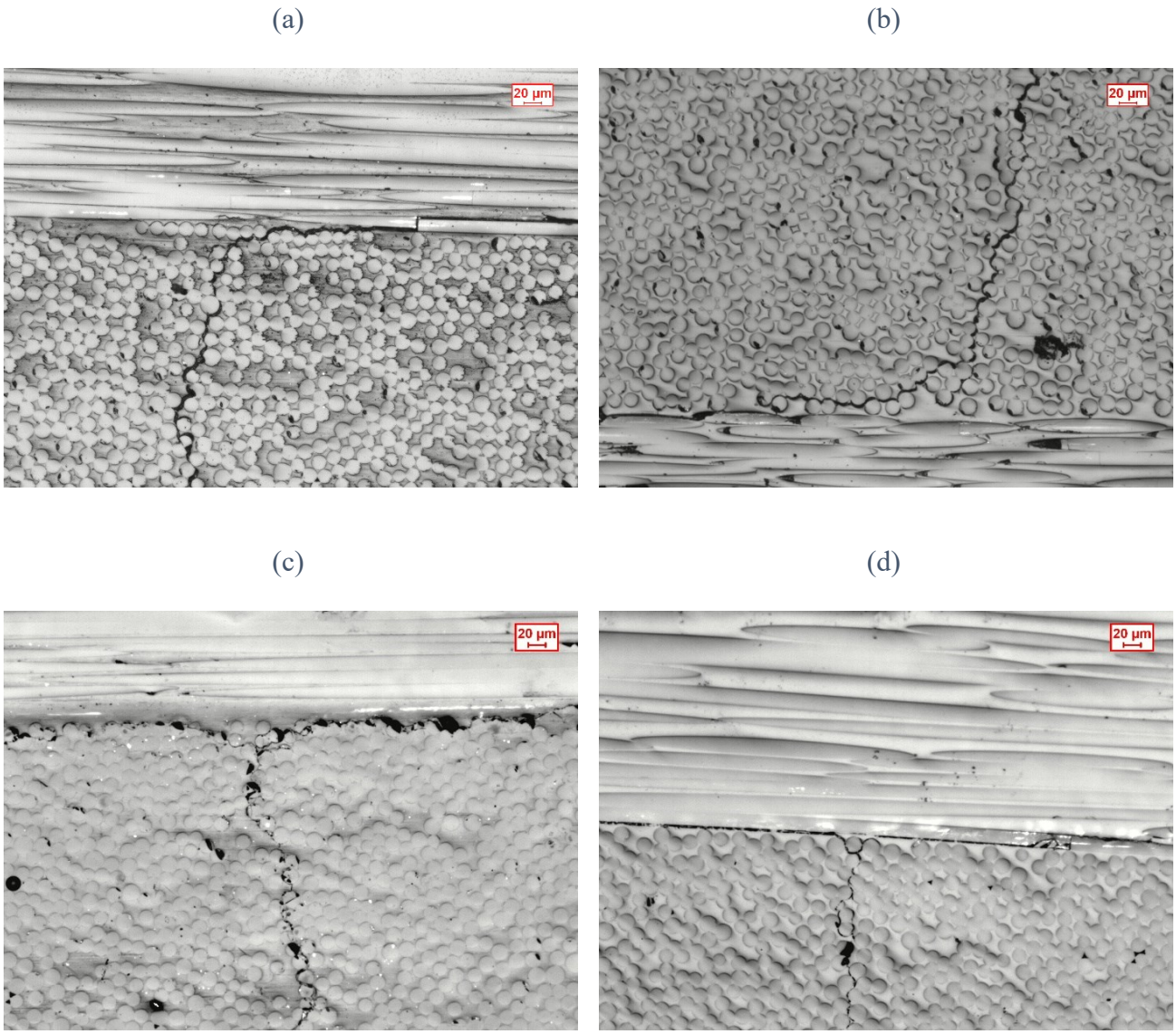

Figure 4.23. Examples of Z-shaped delaminations (a-b) and H-shaped delaminations (c-d).

4.7 Conclusions

In this work, the results of an experimental investigation focused on the progression of delaminations induced by transverse cracks were illustrated. The research was aimed at analyzing the occurrence and growth of damage.

Glass-epoxy laminates characterized by two different lay-ups were manufactured and fatigue tested. Evidences collected showed that the number of cycles needed for delamination onset to occur can be considered negligible in terms of fatigue life if compared to the number of cycles spent for the delamination growth.

Furthermore, by means of microscopy observations, the sequence of damage mechanisms and the effects of these on the mechanical properties were determined. Froom the micrographs collected, it was verified that the majority of delaminations developed symmetrically to the transverse crack plane.

Appendix

Further microscopic observations are reported in the following images, which are referred to the case of the fatigue test carried out with a σ_{max}=90 MPa (R=0.05 and v=10 Hz) on a $[0_2/90_4]_s$ laminate.

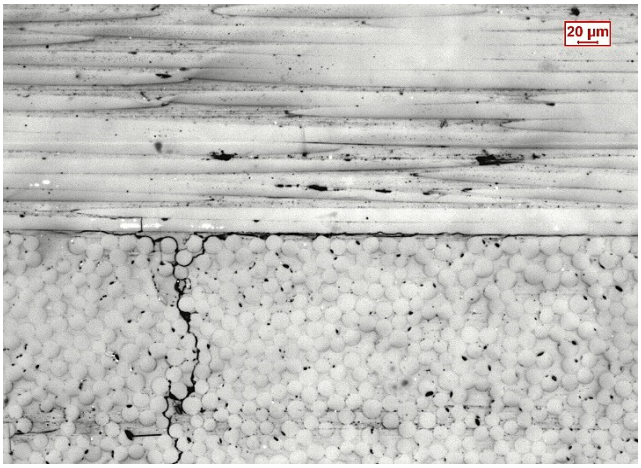

a)

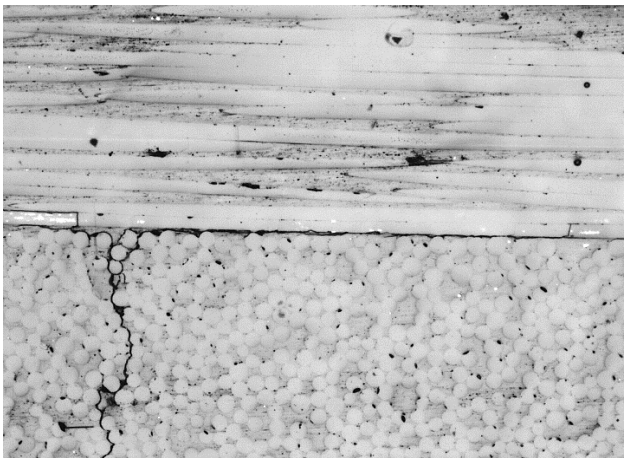

b)

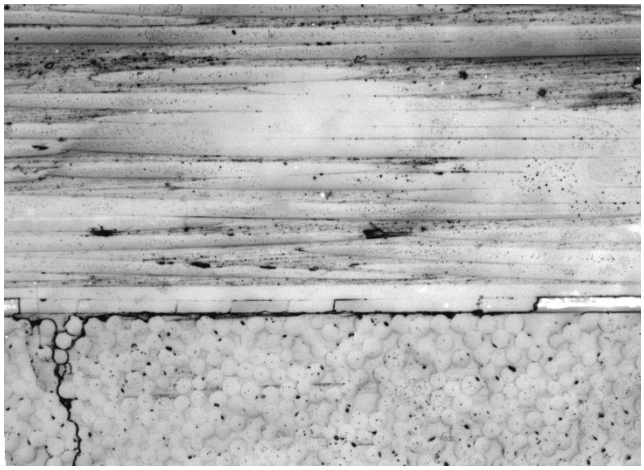

c)

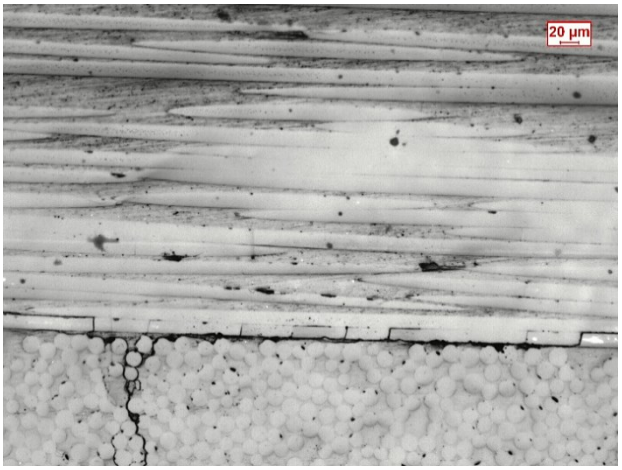

d)

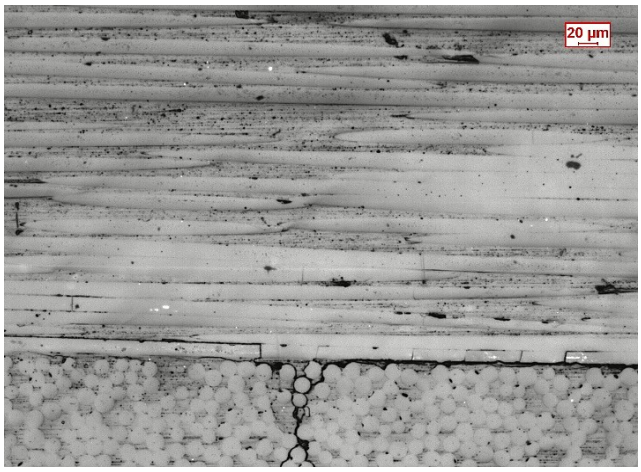

e)

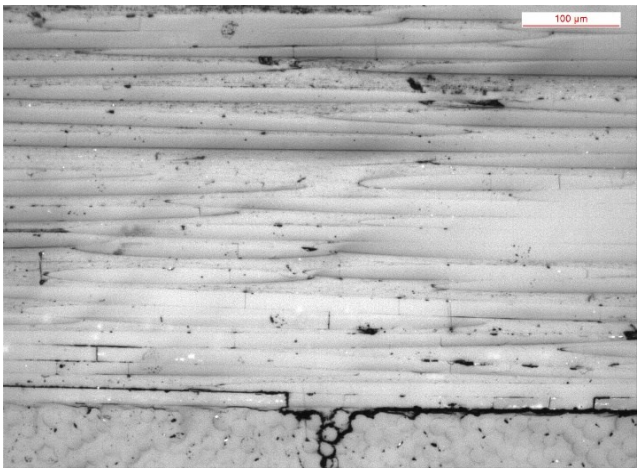

f)

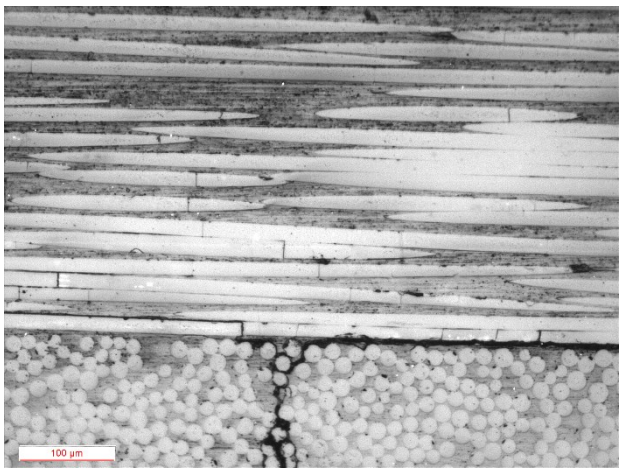

g)

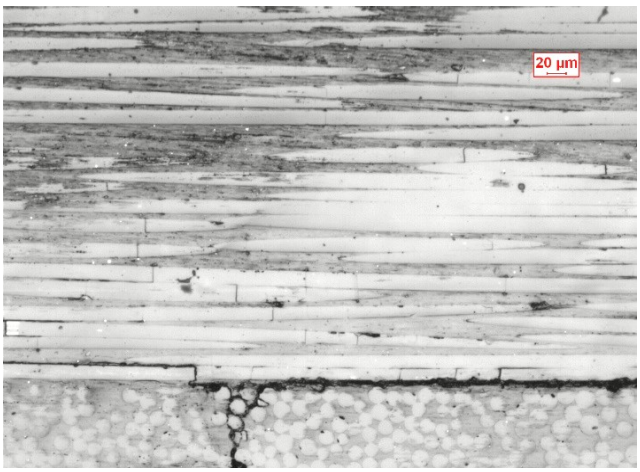

h)

i)

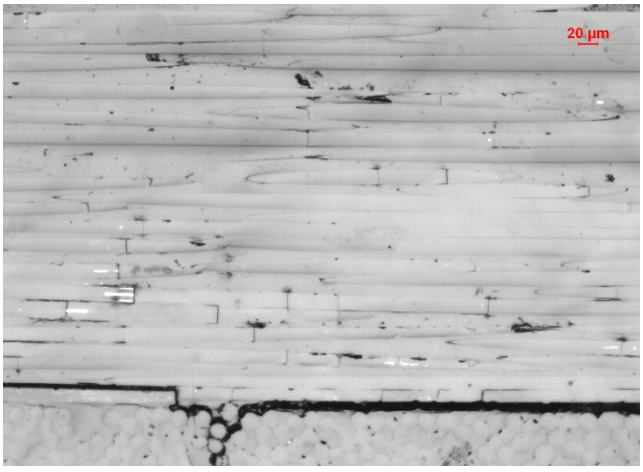

j)

Figure 4.24 Delamination evolution and formation of fibre breakage Stop after a) 54, b) 111, c) 421, d) 1567, e) 3934, f) 22390, g) 83936, h) 165155, i) 657740 and j) 1034225 cycles.

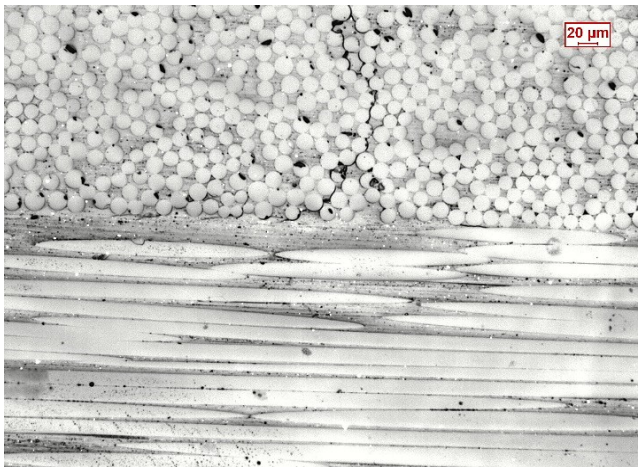

a)

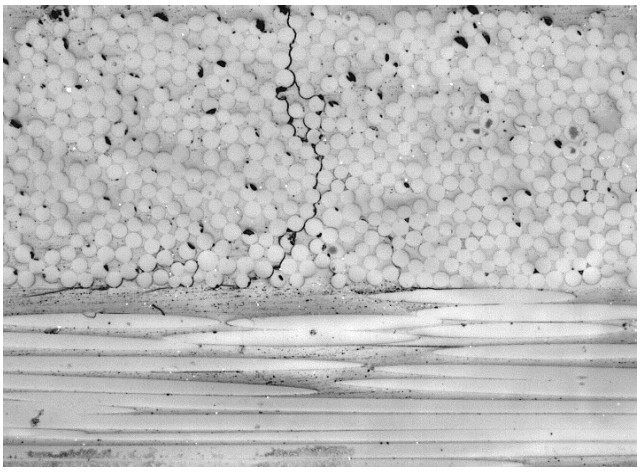

b)

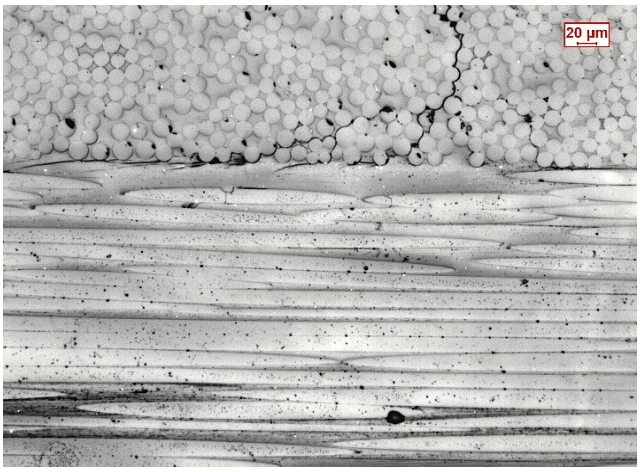

c)

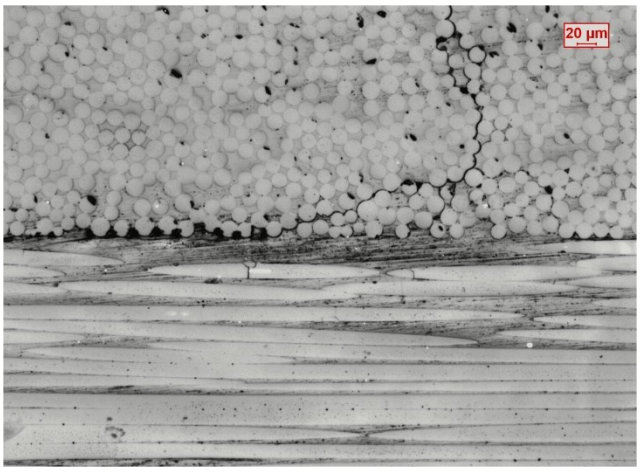

d)

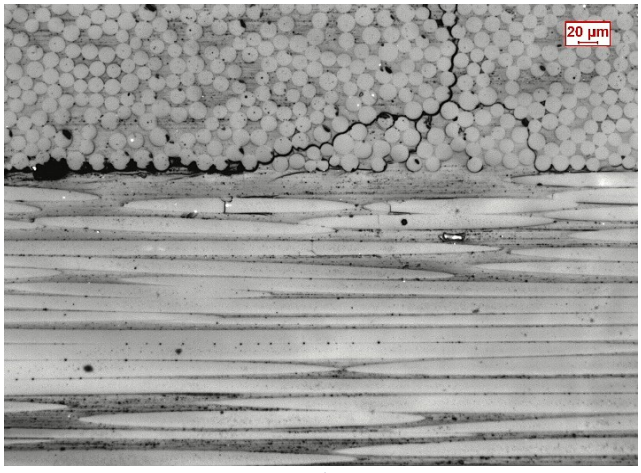

e)

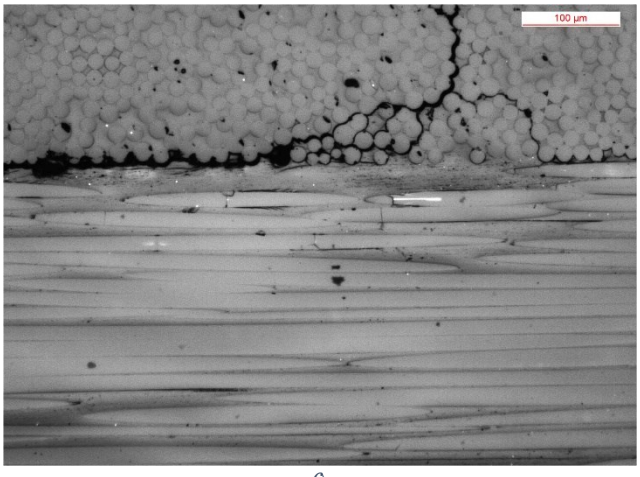

f)

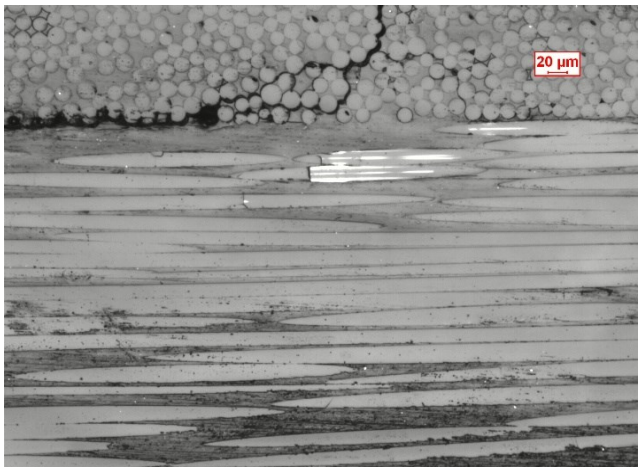

g)

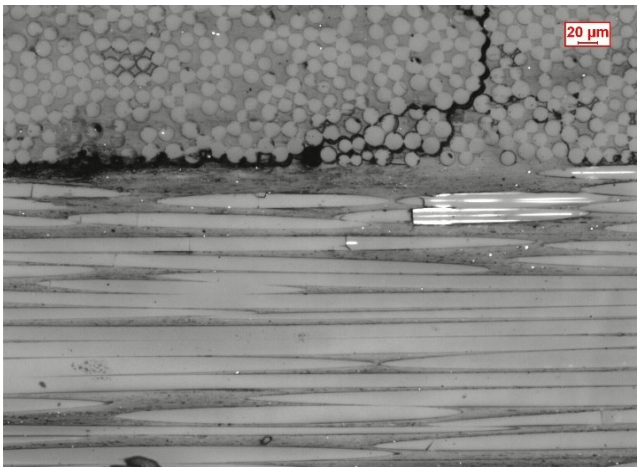

h)

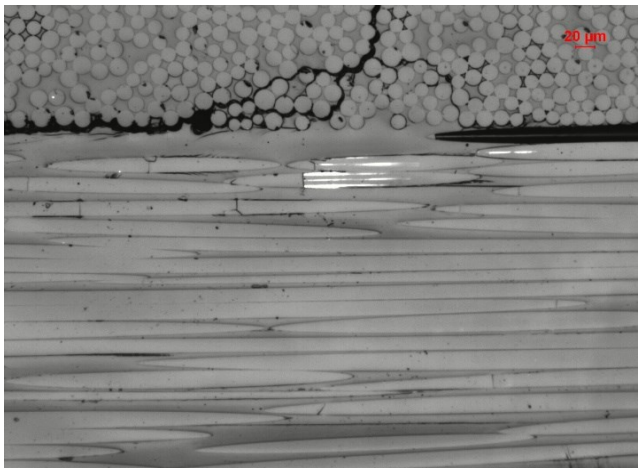

i)

Figure 4.25 Delamination evolution and formation of fibre breakage. Stop after a) 54, b) 111, c) 421, d) 1567, e) 3934, f) 22390, g) 165155, h) 657740 and i) 1034225 cycles.

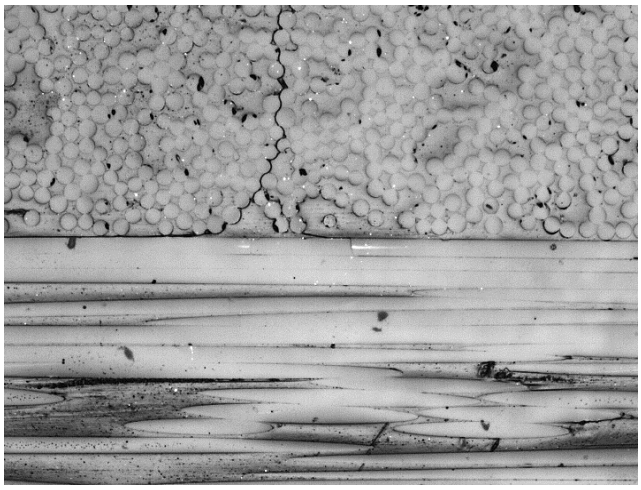

a)

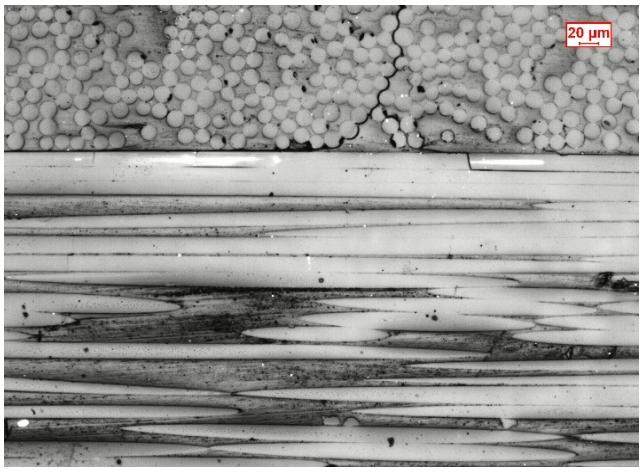

b)

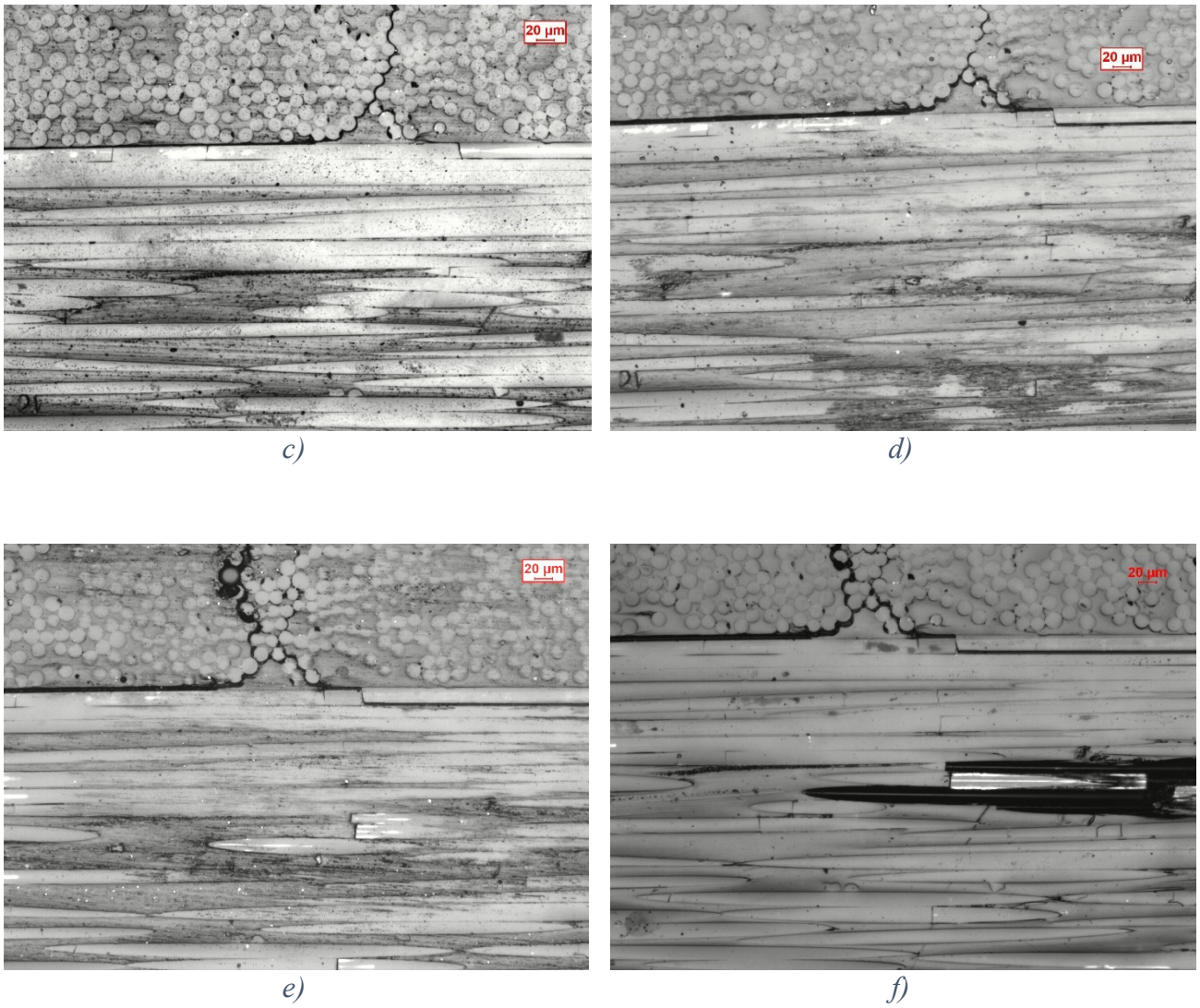

c) d)

e) f)

Figure 4.26. Delamination evolution and formation of fibre breakage. Stop after a) 111, b) 1567, c) 3934, d) 165155, e) 657740 and f) 1034225 cycles.

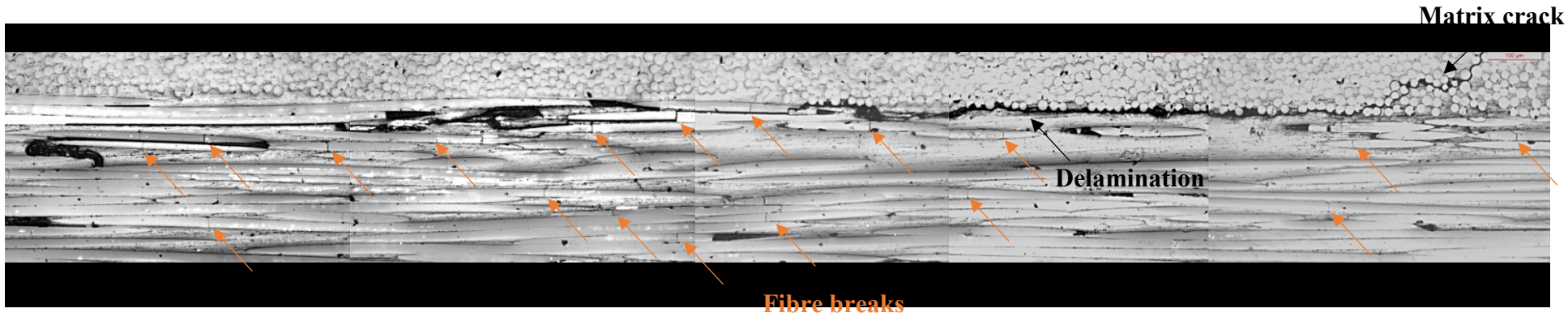

Figure 4.27. Panoramic image of damage mechanisms. The matrix crack and the delamination are indicated with black arrows, while fibre breaks are indicated with orange arrows.

References of chapter 4

[1] Berthelot J-M. Transverse cracking and delamination in cross-ply glass-fiber and carbon-fiber reinforced plastic laminates: Static and fatigue loading. Appl Mech Rev 2003;56:111–47.

[2] Lenoe EM, Oplinger DW, Burke JJ. Fibrous Composites in Structural Design.

[3] Crossman FW, Warren WJ, Wang a. SD, Law GE. Initiation and Growth of Transverse Cracks and Edge Delamination in Composite Laminates Part 2. Experimental Correlation. J Compos Mater 1980;14:88–108.

[4] Wang SD. Initiation and growth of transverse cracks and edge delamination in composite laminates. Part 1. An Energy Method. J Compos Mater 1980;14:71–87.

[5] O'Brien TK. Characterization of delamination onset and growth in a composite laminate. Damage Compos Mater ASTM STP 755 1982:140–67.

[6] O'Brien TK. Analysis of local delamination and their influence on composite laminate behaviour. In: Johnson W, editor. Delamination Debonding Mater., vol. ASTM STP 8, ASTM STP 876; 1985, p. 282–97.

[7] Takeda N, Ogihara S. Initiation and growth of delamination from the tips of transverse cracks in cfrp cross-ply laminates 1994;52:309–18.

[8] Takeda N, Ogihara S. in situ observation and probabilistic prediction of microscopic failure processes in cfrp cross-ply laminates 1994;3538:183–95.

[9] Ogihara S, Takeda N. Interaction between transverse cracks and delamination during damage progress in CFRP cross-ply laminates. Compos Sci Technol 1995;54:395–404.

[10] Quaresimin M, Carraro PA. Composites : Part B On the investigation of the biaxial fatigue behaviour of unidirectional composites. Compos Part B 2013;54:200–8.

[11] Carraro PA, Quaresimin M. A damage based model for crack initiation in unidirectional composites under multiaxial cyclic loading. Compos Sci Technol 2014;99:154–63.

[12] Quaresimin M, Carraro PA, Maragoni L. Early stage damage in off-axis plies under fatigue loading. Compos Sci Technol 2016;128:147–54. doi:10.1016/j.compscitech.2016.03.015.

[13] Carraro PA, Quaresimin M. International Journal of Solids and Structures A stiffness degradation model for cracked multidirectional laminates with cracks in multiple layers. Int J Solids Struct 2015;58:34–51.

[14] Dharani LR, Tang H. Micromechanics characterization of sublaminate damage. Int J Fract 1990;46:123–40.

[15] Kashtalyan M, Soutis C. Effect of delaminations induced by transverse cracks and splits on stiffness properties of composite laminates. Compos Part A Appl Sci Manuf 2000;31:107–19.

[16] Berthelot J, Corre J Le. A model for transverse cracking and delamination in cross-ply laminates 2000;60:1055–66.

[17] Hashin Z. Analysis of cracked laminates: a variational approach. Mech Mater 1985;4:121–36.

[18] Nairn J a., Hu S. The initiation and growth of delaminations induced by matrix microcracks in laminated composites. Int J Fract 1992;57:1–24.

[19] Rebière JL, Gamby D. A criterion for modelling initiation and propagation of matrix cracking and delamination in cross-ply laminates. Compos Sci Technol 2004;64:2239–50.

[20] Zhang H, Minnetyan L. Variational analysis of transverse cracking and local delamination in [??m/90n]s laminates. Int J Solids Struct 2006;43:7061–81. doi:10.1016/j.ijsolstr.2006.03.004.

[21] Akshantala N V, Talreja R. A mechanistic model for fatigue damage evolution in composite laminates. Mech Mater 1998;29:123–40.

[22] Akshantala N V, Talreja R. A micromechanics based model for predicting fatigue life of composite laminates. Mater Sci Eng A (Structural Mater Prop Microstruct Process 2000;285:303–13.

[23] Armanios, Erian A., P. Sriram, and Ashraf M. Badir. "Fracture analysis of transverse crack-tip and free-edge delamination in laminated composites." *Composite Materials: Fatigue and Fracture (Third Volume)*. ASTM International, 1991

[24] O'Brien TK. Towards a Delamination Fatigue Methodology for Composite Materials. 16th Int Conf Compos Mater 2007:1–5.

[25] Andersons J, Hojo M, Ochiai S. Empirical model for stress ratio effect on fatigue delamination growth rate in composite laminates. Int J Fatigue 2004;26:597–604. doi:10.1016/j.ijfatigue.2003.10.016.

[26] Allegri G, Wisnom MR. A non-linear damage evolution model for mode II fatigue delamination onset and growth. Int J Fatigue 2012;43:226–34.

[27] Wang ASD, Kishore NN, Li CA. Crack development in graphite—epoxy cross-ply laminates under uniaxial tension. Compos Sci Technol 1985;24:1–31.

[28] Fish J, Lee S. Three-Dimensional Analysis of Combined Free-Edge and Transverse-Crack-Tip Delamination. Compos. Mater. Test. Des. (Ninth Vol., 100 Barr Harbor Drive, PO Box C700, West Conshohocken, PA 19428-2959: ASTM International; n.d., p. 271–271 – 16.

[29] Salpekar SA, O'Brien TK. Combined effect of matrix crackins and stress-free edge on delamination. NASA Tech Memo 1990;1.

[30] Quaresimin M, Ricotta M. Stress intensity factors and strain energy release rates in single lap bonded joints in composite materials. Compos Sci Technol 2006;66:647–56.

[31] Quaresimin M, Ricotta M. Fatigue behaviour and damage evolution of single lap bonded joints in composite material. Compos Sci Technol 2006;66:176–87.

[32] Quaresimin M, Ricotta M. Life prediction of bonded joints in composite materials. Int J Fatigue 2006;28:1166–76.

[33] Carraro PA, Novello E, Quaresimin M, Zappalorto M. Delamination onset in symmetric cross-ply laminates under static loads : theory , numerics and experiments n.d.:1–38.

[34] Gamstedt EK, Sjogren B a. An experimental investigation of the sequence effect in block amplitude loading of cross-ply composite laminates. Int J Fatigue 2002;24:437–46

5. Numerical investigation of delamination growth in cross-ply laminates subjected to cyclic loading.

5.1 Introduction

One of the main modes of failure of laminated composite materials consists of delamination between adjacent layers. This can be caused by different factors, such as material and structural discontinuities, where interlaminar stresses reach high values. Typical examples of regions, which are inclined to the formation of delaminations, include stress-free edges and ply drops regions subjected to out-of plane bending. Conversely, delaminations may be induced also by other internal failure mechanisms, such as matrix cracking, and then interact with these. This type of damage is detrimental for the structure, since may grow during in-loading service, hidden from the superficial inspections, reducing the stiffness of the structure and leading to the final failure.

A complete investigation concerning delamination growth should have two different aims:

1. To understand the mechanisms involved in the delamination growth process, and clarify how the mechanisms interact each other;
2. To define the driving force that governs the delamination growth and develop numerical procedures to assess the possibility of delamination occurrence under in-service loadings.

Since no standard exists for the characterization of delamination growth, often a no-growth threshold approach has been proposed in the literature. However, if a controlled and limited growth of damage due to fatigue loading is accepted, i.e. if a slow growth philosophy is adopted, the design of lighter structures can be achieved.

In order to adopt this approach, the underlying physics of the damage growth must be fully understood. At the same time, procedures should be developed to plan scheduled inspection, enabling the detection of damage before it becomes critical. A brief excursus through the different

types of fatigue damage models helps understanding the primary role of fracture mechanics on the modelling of delamination growth problems.

In the literature, many models to predict damage evolution and failure of composites subjected to fatigue loadings can be found. A classification of these was proposed by Degrieck and Van Paepegem [1], who identified fatigue life phenomenological, and progressive damage models.

The adoption of the slow growth philosophy requires a model that belongs to the category of progressive damage models.

In fact, fatigue life models cannot be related to the actual degradation mechanisms, phenomenological models describe the gradual reduction of mechanical properties, (such as strength or stiffness) while progressive damage are the only category of models that predicts the evolution of actual damage features.

As regards the progressive damage models, in particular focused on the delamination growth prediction, Pascoe, Alderliesten and Benedictus [2] subdivided these into four macro categories:

1. **Stress/strain based methods**, which relate the delamination growth to the stress or strain;
2. **Fracture mechanics based methods**, which relate the delamination growth to the stress intensity factor (SIF) or strain energy release rate (SERR);
3. **Cohesive zone methods** (CZMs), which model the interface using cohesive elements. A damage parameter is used to progressively reduce the stiffness of the element, simulating the growth of damage;
4. **Extended finite element method** (XFEM) based models. XFEM is a technique which is used to model the propagation of various discontinuities through the use of enrichment functions. The substantial difference between this and the previous method stands in the fact that it is not necessary to predefine a crack path where delaminations will develop.

Usually, stress/strain methods are used to find a fatigue life, without giving information on the delamination growth rate. Some studies based on the use of stresses to predict the delamination growth were carried out by Ratwani and Kan [3] and Poursartip and Chinatambi [4].

Most frequently, approaches based on the fracture mechanics have been used, linking the delamination growth with the concepts of stress intensity factors and strain energy release rate.

The preference of adopting fracture mechanics for composite materials can be explained as the attempt of trying to replicate the success obtained by Paris in describing fatigue crack growth in metals [5]- [7].

CZM and XKEM are always based on fracture mechanics. Cohesive zone formulation was developed by Dugdale [8] and Barenblatt [9].

A review of the early developments of CZMs has been written by Camanho et al. [10].

In the last years, the CZM approach was widely used for delamination problems. However, the technique suffers of the lack of a direct link with the physics of the delamination process. This can be seen both in the cohesive law and in the damage parameter formulations. In fact, to correctly define the cohesive zone of all the parameters needed, only the value of G_{Ic} is determined experimentally, the others are chosen based on numerical considerations

XFEM methods [11]-[14] allow a more freedom in modelling crack growth, as they do not require to predefine the delamination path. It is also possible to include a cohesive law formulation to define the traction-separation law, modelling cohesive cracking. Even these approaches are based on fracture mechanics. However, they are computationally onerous, and their use is not always opportune.

This chapter presents the results of the modelling activities conducted with the aim of characterizing and predicting delamination growth for cross-ply laminates, using approaches based on the fracture mechanics.

5.2 Damage scenario and FE model

The damage scenario of a cross-ply laminate subjected to tension-tension fatigue loading is acknowledged in the literature. Furthermore, thanks to a recent experimental investigation, the results of which have been presented in chapter 4, the damage mechanisms sequence has been determined and documented. This can be summarized as follows: first, transverse cracks were seen to occur, growing through the thickness of the 90° plies. Then, as the cracks reached the interface, delaminations initiated from their tips, propagating at the 0/90 interface.

Consider a damaged cross-ply laminate, as schematically represented in Figure 5.1.

By assuming a pattern of equidistant transverse cracks, from the tips of which delaminations are uniformly extended through the whole width of the specimens, a unit cell of the laminate can be individuated. $2L_{del}$ represents the delamination length, while L represents the crack spacing.

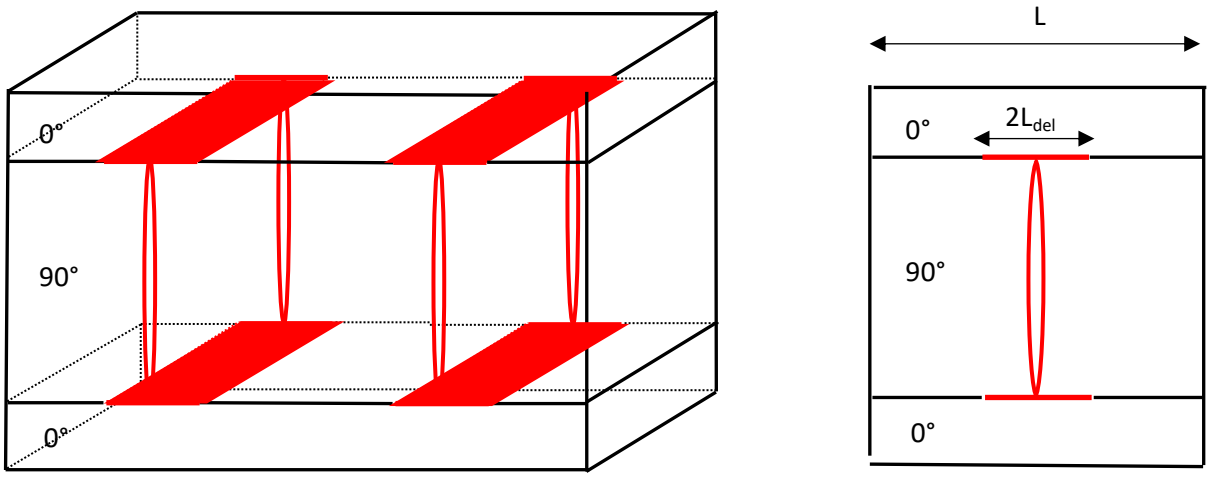

Figure 5.1. Schematization of the damaged cross-ply.

5.3 Virtual Crack Closure Technique analysis

With the aim of evaluating the Energy Release Rate (ERR) values, an extensive campaign of 2D finite element analysis was carried out, using the software Ansys ®14 package. Only a quarter of the unit cell was modelled, in virtue of to the symmetric nature of the problem, as shown in Figure 5.2. The lay-up modelled was a $[0_2/90_4]_s$ and the thickness of each ply was set equal to 0.3 mm, as

experimental measured. A uniform displacement along the x-direction was applied on the right hand-side of the laminate segment. 8 nodes isoparametric elements Plane 183 were used, with the plane strain option. The material properties used in the FE analysis are reported in Table 5.1.

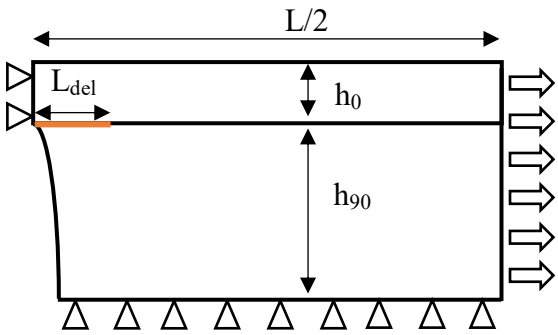

Figure 5.2. FE model

Table 5.1 Material properties used in the numerical analysis

E_1 [GPa]	48
E_2 [GPa]	14
E_3 [GPa]	14
G_{12} [GPa]	5.2
G_{13} [GPa]	5.2
G_{23} [GPa]	5
ν_{12}	0.308
ν_{23}	0.4

Mode I and Mode II ERR components, G_I and G_{II}, were calculated by means of the Virtual Crack Closure Technique. The formulations, based on the values of nodal forces and displacements in the

$$G_I = \frac{1}{2\Delta a}[Z_i(w_L - w_{L^*}) + Z_j(w_M - w_{M^*})]$$
$$G_{II} = \frac{1}{2\Delta a}[X_i(u_L - u_{L^*}) + X_j(u_M - u_{M^*})] \quad (1)$$

proximity of the crack tip, are:

The capital letters Zi, Zj, X_i and X_j indicate the nodal force components, while w_L, w_L*, w_M and w_M* indicate the nodal displacements and a indicates the dimension of the elements, as shown in Figure 5.3

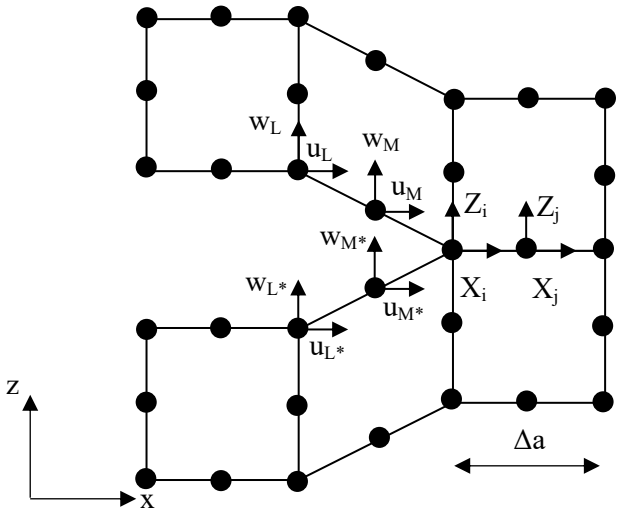

Figure 5.3. Finite element model with nodal forces and displacement for the application of VCCT.

As the stress fields assume an oscillatory behaviour, which may prevent the convergence of the single components G_I and G_{II}, a mesh-sensitivity analysis was conducted. Given the geometrical properties of the laminate and the delamination length, the element size of the mesh was varied and the correspondent ERR values were determined. The element size was chosen as the one that guarantees the right compromise between the stability of the ERR values and a reasonable number of elements in the mesh.

Figure 5.4 illustrates the variation of ERR components with the dimension of the elements. It is worth noting that, by decreasing the element dimensions, the values of the single components become unstable while the sum of these is almost constant. As a reasonable compromise, the smallest element size was chosen equal to 30 μm, in agreement with the analogous analysis conducted on the mesh sensitivity for bonded joints [27].

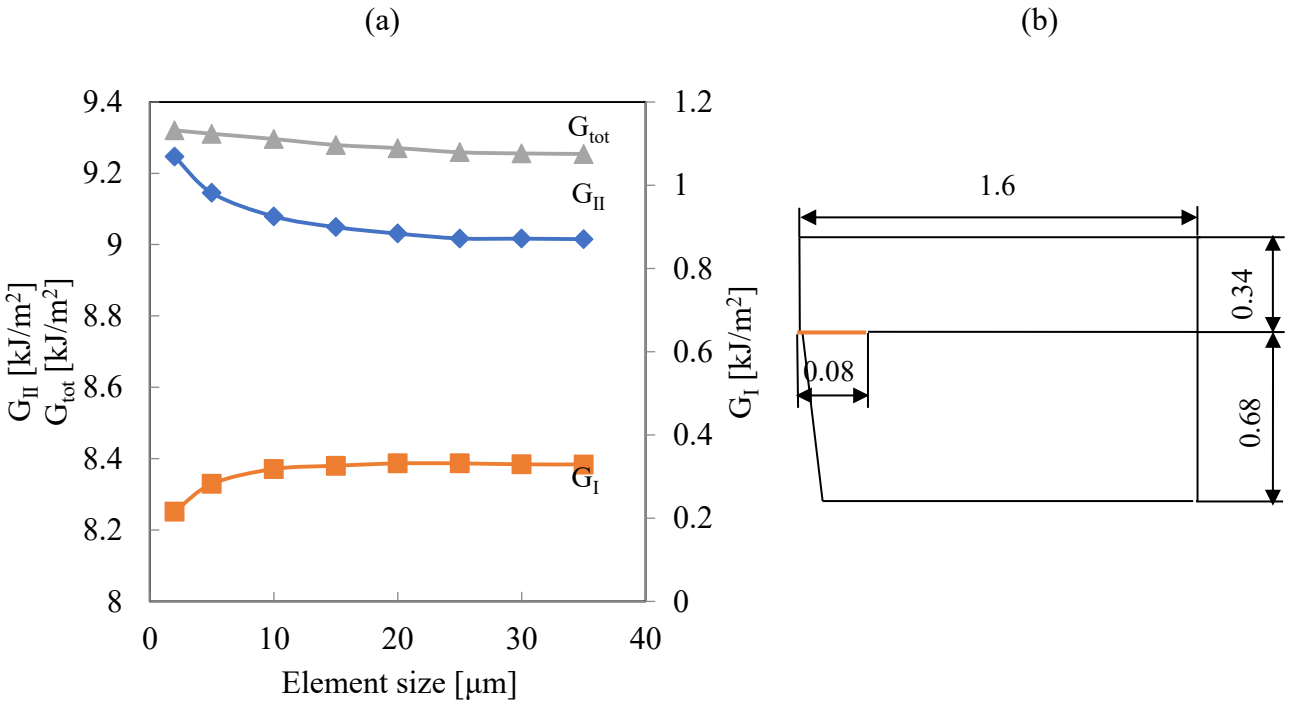

Figure 5.4 a) Strain energy release rate components G_I and G_{II} values for different element sizes (u_x=0.1mm correspondent to a global tension σ=1300 MPa) and b) geometry used for the VCCT analysis conducted to study the stability of the G_I and G_{II} values.

Once the element size of the mesh was determined, finite element analyses were performed, in order to investigate how the values of ERR components modify with respect to the variation of delamination length and crack spacing. The results are summarized in Figure 5.5. In the x axis the values of delamination length normalized to the crack spacing $2L_{del}/L$ are reported, while the y axis indicates the ERR components, normalized to the stress applied to the laminate squared (ERR/σ^2).

The curves of G_I and G_{II} are characterized by a common trend, which increases with the $2L_{del}/L$, till reaching a maximum value and then progressively decreases. This trend may be due to the fact that delaminations, formed from two neighbor cracks, grew up to a point where became sufficiently near each other to cause a stress redistribution, resulting in a decrease of ERR components.

Furthermore, as expected, an increase of the crack density results in a decrease of the ERR values. This may be consequent to the decrease of the distance between two adjacent cracks. These started to interact with each other (interactive regime), causing the decrease of the stresses between them.

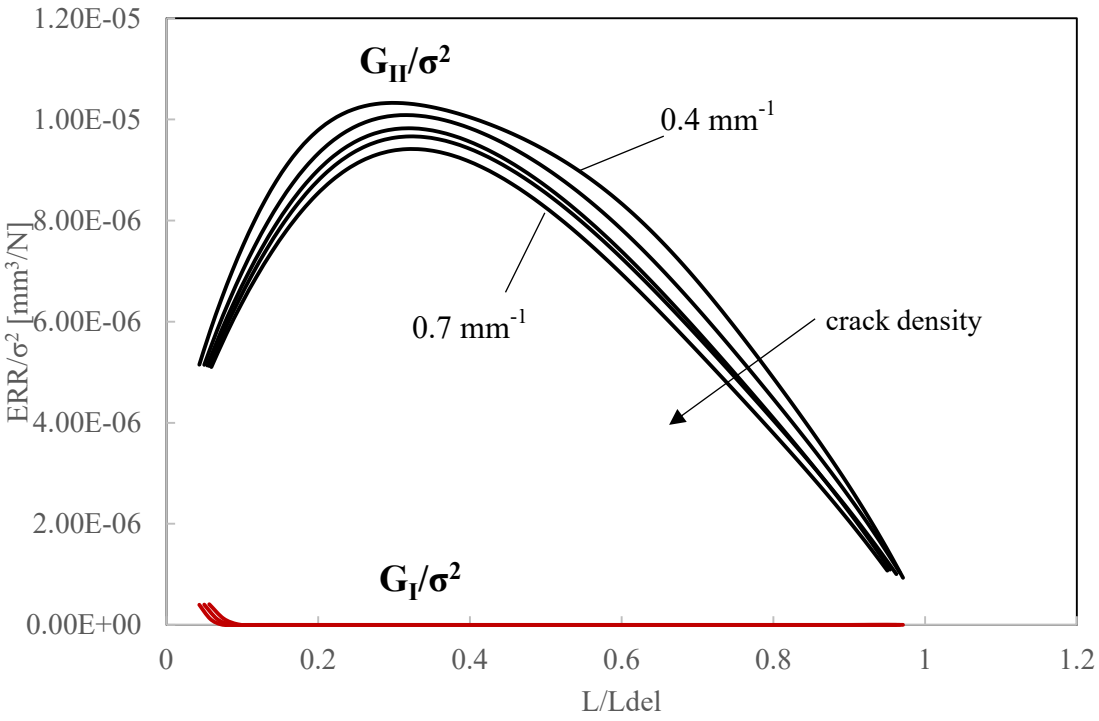

Figure 5.5. Mode I and Mode II energy release rate components G_I and G_{II} normalized to the maximum global tension applied σ^2 vs the delamination length normalized to the crack spacing. The arrows indicate the verse of increasing crack density.

As can be seen from Figure 5.5, it is reasonable to assume that the process of delaminations growth is driven by the G_{II} component, while G_I can be considered negligible. This is particularly true for $L_{del}/L>0.1$, which are the minimum delamination length values determined experimentally. As a result of this analysis, G_{II} was chosen as the most representative parameter describing delamination propagation.

5.4 Paris like curve for $[0_2/90_4]_s$ laminates

Delamination propagation was described using the well-known Paris crack growth equation, relating the delamination growth rate with the Mode II component G_{II}. This is the classic approach for the description of crack propagation, based on the fracture mechanics. The equation can be expressed in the form:

$$\frac{dL_{del}}{dN} = C G_{II}^{\ n} \tag{2}$$

For each test performed, the average delamination area was first determined by dividing the delaminated area by the number of transverse cracks, implicitly assuming that these developed the same delaminations. Then, the average delamination length L_{del} was determined dividing the delamination area by the width of the specimen.

The growth rate of half delamination length (L_{del}) was determined following the indications of ASTME 647, while the G_{II} values were obtained by finite element analyses, modelling a H-shaped delamination.

Concurrently, FE analyses of the cross-ply were carried out, modelling the real geometry of the cross-ply and varying the delamination length. Curves were fitted with Vth degree polynomials, and then used for the successive computation of the ERR components correspondent to the real conditions. By combining ERR components and the growth rate of delaminations, the Paris like curve, relating the dL_{del}/dN with the G_{II} component was obtained.

5.4.1 Results: case study of σ_{max}=140 MPa

Intermediate results obtained by applying the abovementioned operative procedure, for a test carried out with a maximum stress of 140 MPa, are reported in Figure 5.6, Figure 5.7, Figure 5.8 and Figure 5.9. In particular, Figure 5.6 shows the typical trend of growth of the equivalent delamination length during the fatigue life, which rapidly increases until reaching a plateau value.

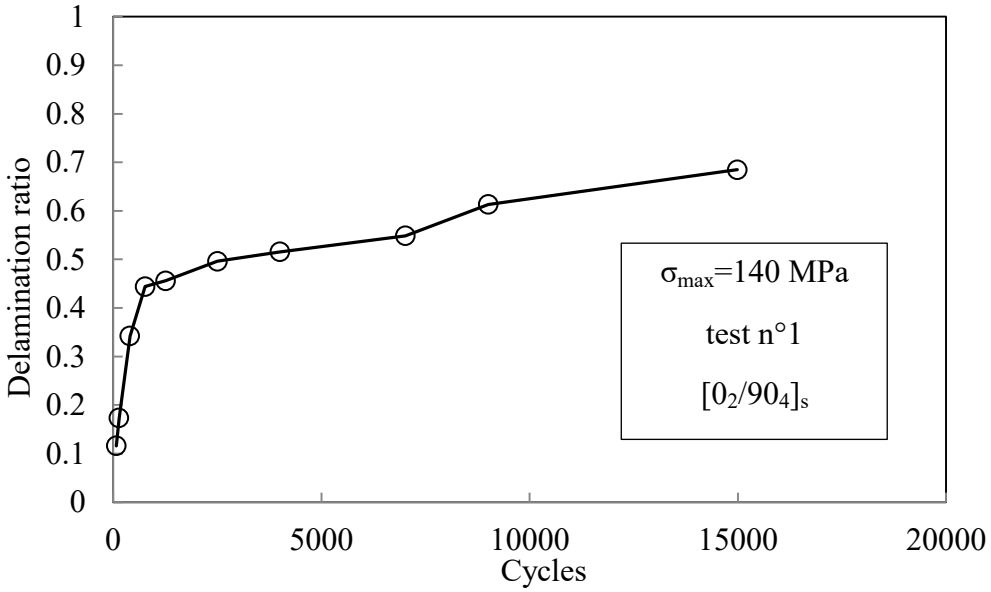

Figure 5.6. Growth of delamination length with the cycles number for a test carried out with a σ_{max}=140 MPa.

Figure 5.7 shows the G_{II} components with respect to the number of cycles, while, Figure 5.8 illustrates the delamination growth rate dL_{del}/dN with the number of cycles. It is worth noting that the trend of both curves describing G_{II} and dL_{del}/dN with the number of cycles is similar, i.e. the maximum values of delamination growth rate are found in the first part of fatigue life, when the G_{II} values are maximum, while as the G_{II} decreases, the dL_{del}/dN decreases, thus proving that the delamination growth is mostly driven by the Mode II ERR.

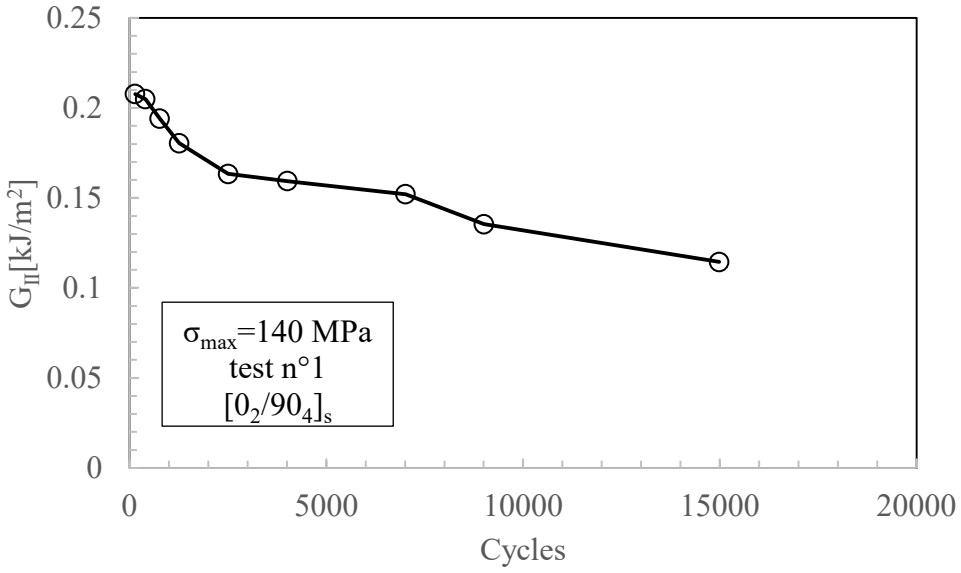

Figure 5.7. ERR components for the fatigue test carried out at a maximum stress σ_{max}=140 MPa

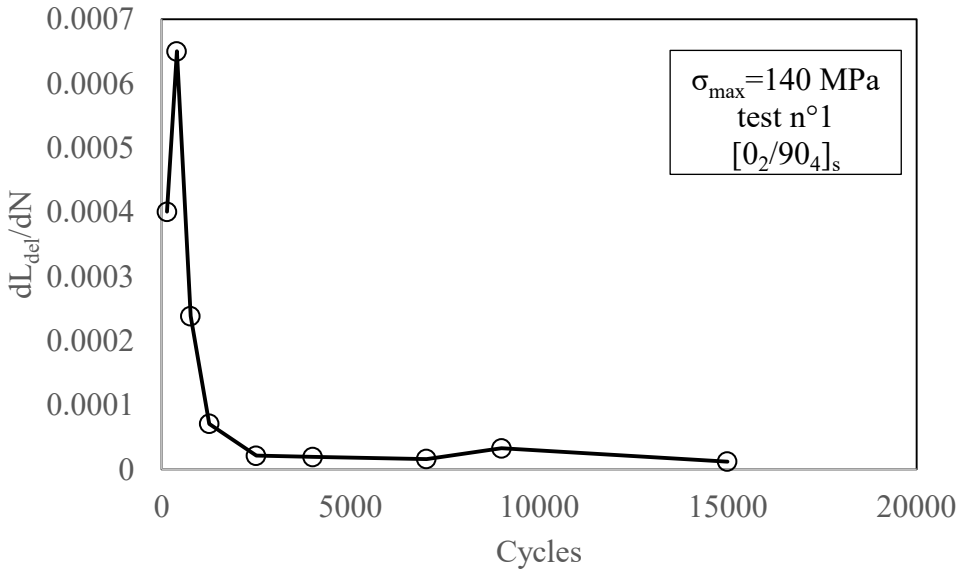

Figure 5.8. Delamination growth rate for the fatigue test carried out with a maximum stress σ_{max}=140 MPa.

Finally, delamination growth rate values were compared with the respective G_{II} values, to obtain the Paris-like curve represented in Figure 5.9.

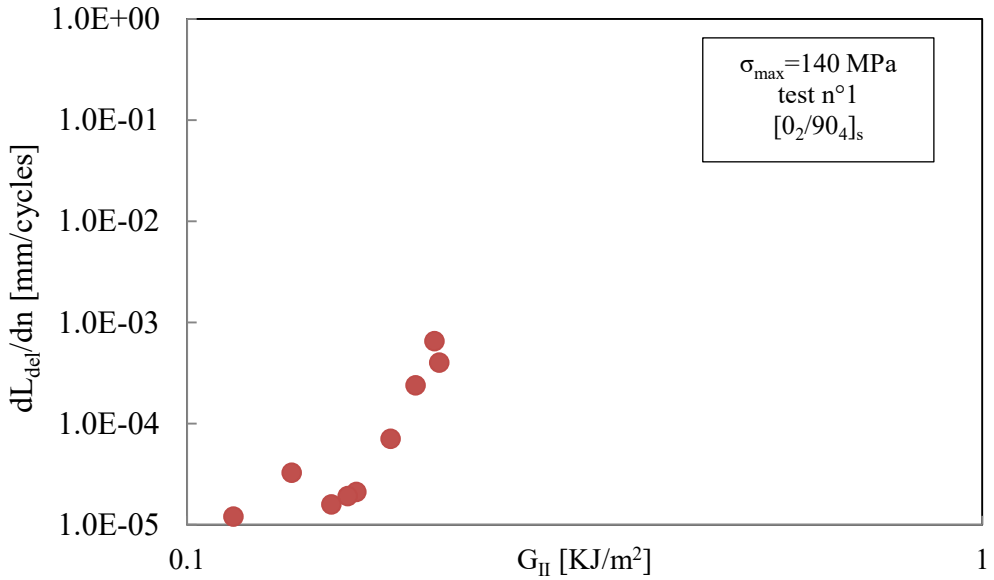

Figure 5.9. Delamination growth rate vs mode II ERR component for a fatigue test carried out with a maximum stress σ_{max}=140 MPa, represented in a double logarithm diagram.

The procedure described was repeated for each fatigue test carried out. The Paris like curve obtained considering all the experimental data is reported in Figure 5.10. Here, the 10-90% scatter band associated with the data was calculated, the coefficients of which are reported in Table 5.2.

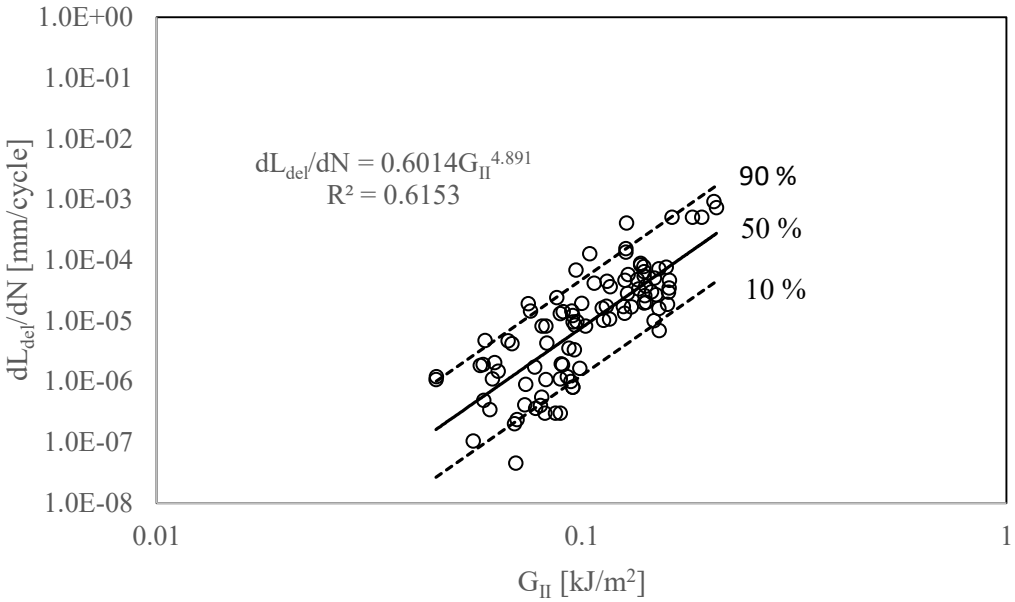

Figure 5.10. Scatter plot of G_{II} values vs. delamination growth rate.

Table 5.2 Paris curve data

	G_{II} [kJ/m^2]	
PS 50%	C=0.6014	n=4.891
PS 90%	C=3.6888	n=4.891
PS 10%	C=0.09805	n=4.891

5.5 Paris like curve for $[0/90_2]_s$

Following the procedure adopted for the $[0_2/90_4]_s$ specimens, the Paris-like curve was determined also for $[0/90_2]_s$ specimens. The curves obtained for the two lay-ups considered are shown in Figure 5.11. The data referred to $[0/90_2]_s$ specimens are reported in red color. It can be noticed that despite the dispersion of the experimental data, due prevalently to the approximations introduced by the model, all the data fall inside a single band. This suggests that the power law found for the $[0_2/90_4]_s$ laminates, can be used to describe the delamination growth for all the cross-ply laminates $[0_n/90_m]_s$, provided that the materials are the same.

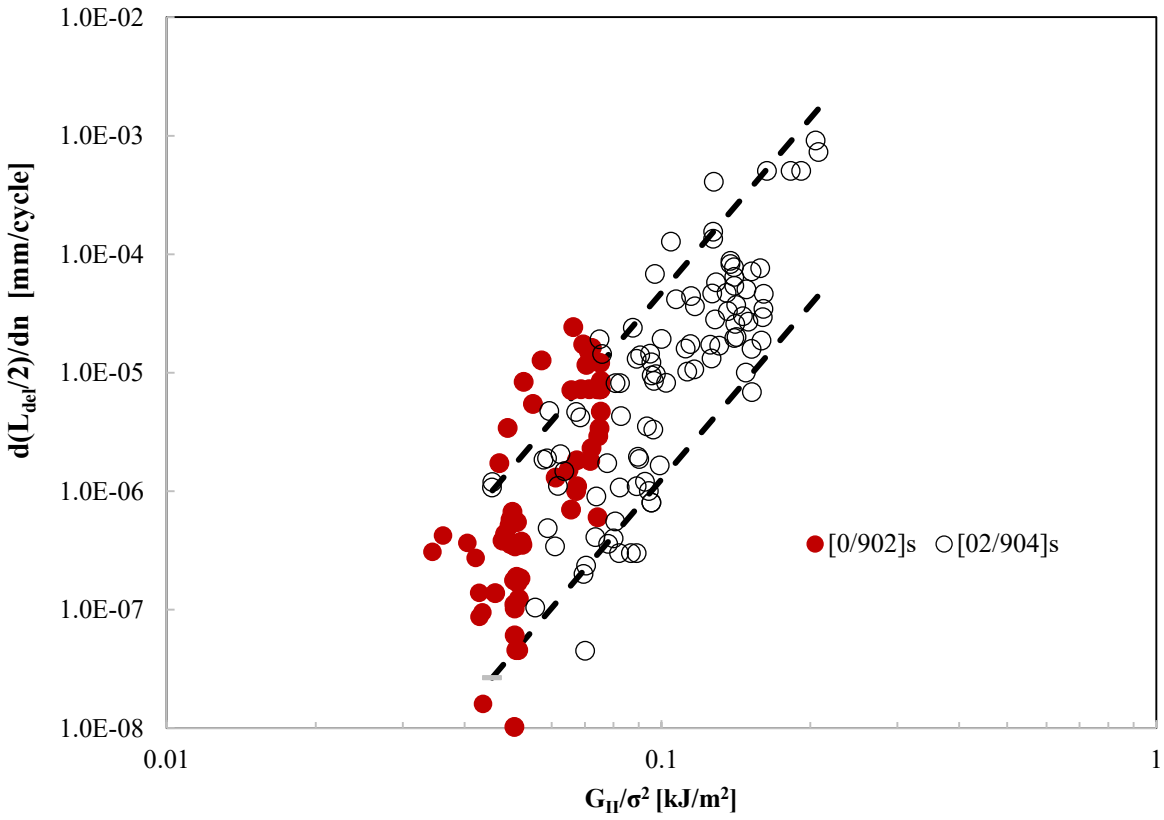

Figure 5.11. Paris-like curve of $[0/90_2]_s$ and $[0_2/90_4]_s$ specimens obtained modelling H-shaped delaminations

5.6 Life estimation

The number of cycles required to propagate a delamination up to a certain length can be evaluated by integrating the Paris-like curve:

$$\int_{N_i}^{N_f} dN = \int_{Ldeli}^{Ldelf} \frac{dL_{del}}{CG_{II}^{\ n}} \tag{2}$$

The lower limit of the integral L_{deli} was chosen as the average delamination length value determined at the beginning of the propagation phase while the N_i was the correspondent number of cycles at which L_{deli} was defined.

The curves describing the trend of the ERR component G_{II} normalized to the global applied stress G_{II}/σ^2 vs. the delamination length were fitted with Vth order polynomial curves. Since these are dependent on the crack density values, the range of crack density values determined experimentally was divided into smaller parts. For each part, the correspondent polynomial curve G_{II}/σ^2 was determined, as reported in Table 5.3.

Table 5.3 Polynomial curves fitting the G_{II}/σ^2 for the correspondent crack density range.

Crack density	G_{II}/σ^2 [kJ/m^2 MPa^2]
0<=crack density<0.16379	-5.87094E-08*L_{del}^5 + 1.84247E-07*L_{del}^4 + 3.08097E-06*L_{del}^3 - 1.96201E-05*L_{del}^2 + 3.05994E-05* L_{del} + 5.33727E-06
0.16379<=crack density<0.18103	-3.82196E-07*L_{del}^5 + 2.05964E-06*L_{del}^4 - 1.46823E-07*L_{del}^3 - 1.86508E-05*L_{del}^2 + 3.02790E-05* L_{del} + 5.27206E-06
0.18103<=crack density<0.19827	-7.31051E-07*L_{del}^5 + 3.98746E-06*L_{del}^4 - 3.34241E-06*L_{del}^3 - 1.73825E-05*L_{del}^2 + 2.92659E-05* L_{del} + 5.27745E-06
0.19827<= crack density<0.21551	-1.09963E-06*L_{del}^5 + 5.68046E-06*L_{del}^4 - 5.40216E-06*L_{del}^3 - 1.72752E-05*L_{del}^2 + 2.84192E-05* L_{del} + 5.23489E-06
0.21551<=crack density<0.232755	-1.43048E-06*L_{del}^5 + 6.86165E-06*L_{del}^4 - 6.04363E-06*L_{del}^3 - 1.82720E-05*L_{del}^2 + 2.77352E-05* L_{del} + 5.15151E-06
0.232755<=crack density<0.24205	-1.67895E-06*L_{del}^5 + 7.39208E-06*L_{del}^4 - 5.29501E-06*L_{del}^3 - 2.01440E-05*L_{del}^2 + 2.71888E-05* L_{del} +

	5.03383E-06
0.24205<=crack density <0.247625	-1.69171E-06*L_{del}^5 + 7.39384E-06*L_{del}^4 - 5.16443E-06*L_{del}^3 - 2.03327E-05*L_{del}^2 + 2.71551E-05* L_{del} + 5.02359E-06
0.247625<=crack density <0.25558	-1.77210E-06*L_{del}^5 + 7.32899E-06*L_{del}^4 - 4.09702E-06*L_{del}^3 - 2.17247E-05*L_{del}^2 + 2.68941E-05* L_{del} + 4.94613E-06
0.25558<=crack density <0.267245	-1.79772E-06*L_{del}^5 + 7.15586E-06*L_{del}^4 - 3.21348E-06*L_{del}^3 - 2.27087E-05*L_{del}^2 + 2.67609E-05* L_{del} + 4.89452E-06
0.267245<=crack density <0.28456	-1.76480E-06*L_{del}^5 + 6.17630E-06*L_{del}^4 - 5.38300E-08*L_{del}^3 - 2.57134E-05*L_{del}^2 + 2.64209E-05* L_{del} + 4.74090E-06
0.28456<=crack density <0.3103	-1.56330E-06*L_{del}^5 + 4.48458E-06*L_{del}^4 + 3.98952E-06*L_{del}^3 - 2.90048E-05*L_{del}^2 + 2.61473E-05* L_{del} + 4.57947E-06
0.3103<=crack density <0.34482	-5.52825E-07*L_{del}^5 - 1.04264E-06*L_{del}^4 + 1.43013E-05*L_{del}^3 - 3.62205E-05*L_{del}^2 + 2.59083E-05* L_{del} + 4.24425E-06
0.34482<=crack density	2.05471E-07*L_{del}^5 - 4.49789E-06*L_{del}^4 + 1.98540E-05* L_{del}^3 - 3.96712E-05*L_{del}^2 + 2.57842E-05*L_{del} + 4.09003E-06

5.7 Prediction of the Young's modulus

By using the estimated delamination length, it is possible to predict the stiffness loss that specimens undergone during the fatigue life. In the first part of the next section a predictive model will be described while, on the second part, theoretical predictions will be compared with experimental stiffness data.

5.7.1 Model

Consider a generic damaged cross-ply laminate. This can be divided into a series of delaminated and non-delaminated portions, as shown in Figure 5.12, where L_{del} represents the delamination length, h_0 the thickness of the 0° ply and h_{90} half of the thickness of the 90° ply.

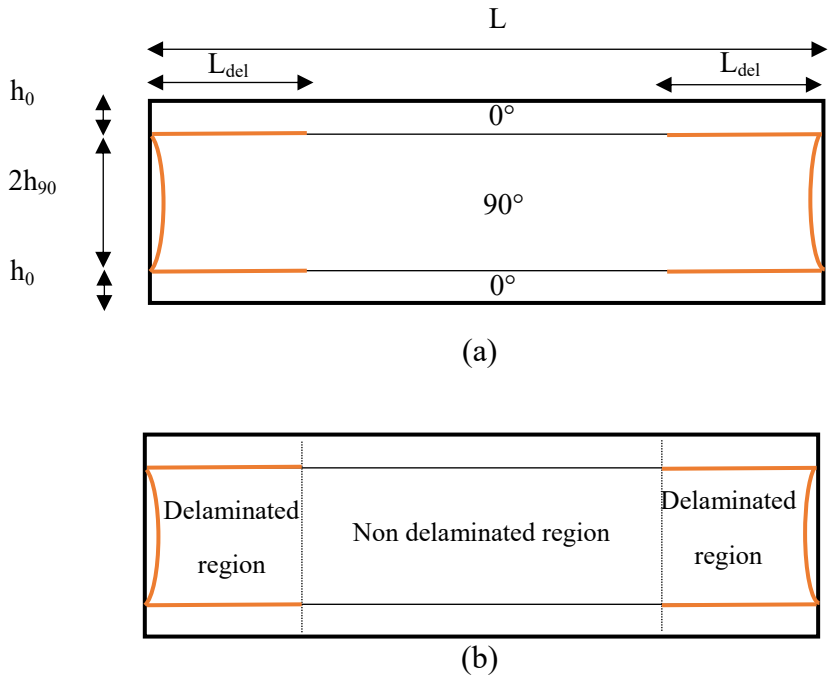

Figure 5.12. Unit cell of the damaged cross-ply interested by transverse cracks and induced delaminations(a) where different regions delaminated and non are distinguished (b).

The stiffness of the laminate can be written as the product of Young's modulus and the thickness h of the laminate divided by the crack spacing L:

$$K = \frac{E_x \ h}{L} \tag{3}$$

The two portions, delaminated and non, are characterized by different Young's modulus E_{xd} and E_{xnd}, each contributing to the global stiffness K of the laminate.

$$\frac{1}{K} = \frac{2L_{del}}{E_{xd}(h_0 + 2h_{90})} + \frac{L - 2L_{del}}{E_{xnd} h} \tag{4}$$

The Young's modulus of the laminate E_x can be therefore written as:

$$\frac{E_{x0}}{E_x} = \frac{2L_{del}}{L}\frac{E_{x0}}{E_{xd}} + \frac{L - 2L_{del}}{L}\frac{E_{x0}}{E_{xnd}} \tag{5}$$

The Young's modulus of the non-delaminated portions E_{xnd} can be determined considering only the 0° plies contributing to the global stiffness. Conversely, the modulus of the delaminated portions E_{xd} can be calculated using an approach based on the shear lag analysis, by assuming a modified crack spacing, equal to the difference between the crack spacing and the delamination length. The Young's modulus of the undamaged laminate E_{x0} was calculated by means of the CLT.

$$E_{xd} = \frac{E_1 h_0}{h_0 + h_{90}} \tag{6}$$

$$\frac{E_{x0}}{E_{xnd}} = \left[1 + Q \cdot \frac{E_2}{E_1} \cdot \frac{h_{90}}{h_0} \cdot \frac{2\rho}{\xi} \operatorname{Tanh} \frac{\xi}{2\rho}\right] \tag{7}$$

with:

$$Q = -E_1 \frac{[E_1 h_{90} + E_2 (h_0 - h\nu_{12}^2)]^2}{(E_2 h_0 + E_1 h_{90})^2 (E_2 \nu_{12}^2 - E_1)} \tag{8}$$

$$\xi^2 = H\frac{(E_2h_0 + E_1h_{90})(E_1h_0 + E_2h_{90}) - (E_2h\nu_{12})^2}{E_1E_2h_0h_{90}(E_2h_0 + E_1h_{90})} \quad (9)$$

$$H = \frac{3G_{12}G_{23}}{h_{90}G_{13} + h_0G_{23}} \quad (10)$$

In equation (7) ρ represents the modified crack density, calculated as:

$$\rho = \frac{1}{L - L_{del}}$$

5.7.2 Model validation

A comparison between the stiffness predictions obtained using the 10%-50%-90% probability survival curves and the experimental data of stiffness loss recorded during the tests is reported on Figure 5.13, Figure 5.14, Figure 5.15, Figure 5.16 and Figure 5.17. It is evident that the model predicts with a certain degree of accuracy the stiffness loss. The scatter existing between the 10 and 90% curves is a consequence of the dispersion of the experimental data, related by a Paris like curve in terms of G_{II}. In the following section, a different power law relating the delamination growth rate with the average principal stress, calculated in a process zone near the delamination tip, will be proposed.

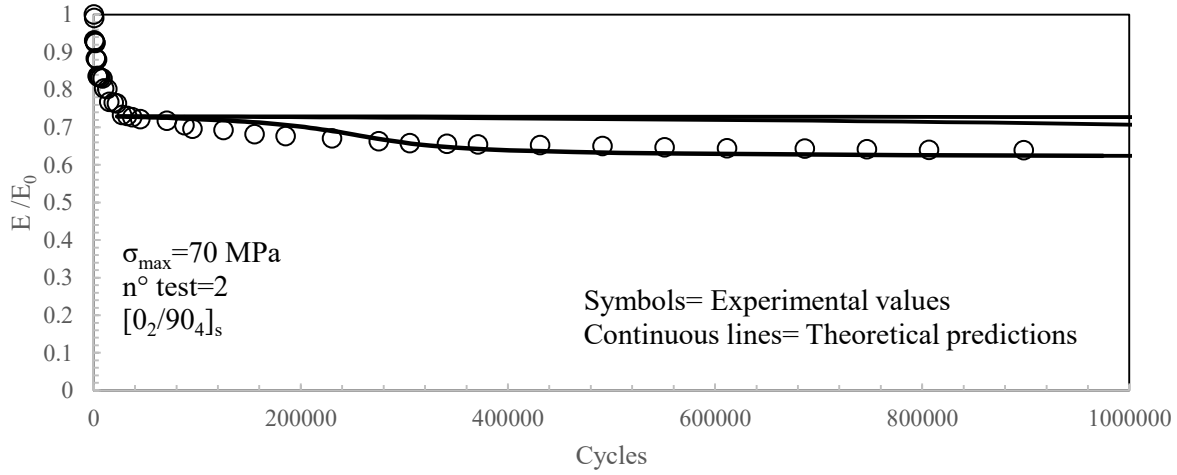

Figure 5.13. Comparison between the data of stiffness experimentally determined and theoretical predictions for the test performed with σ_{max}=70 MPa

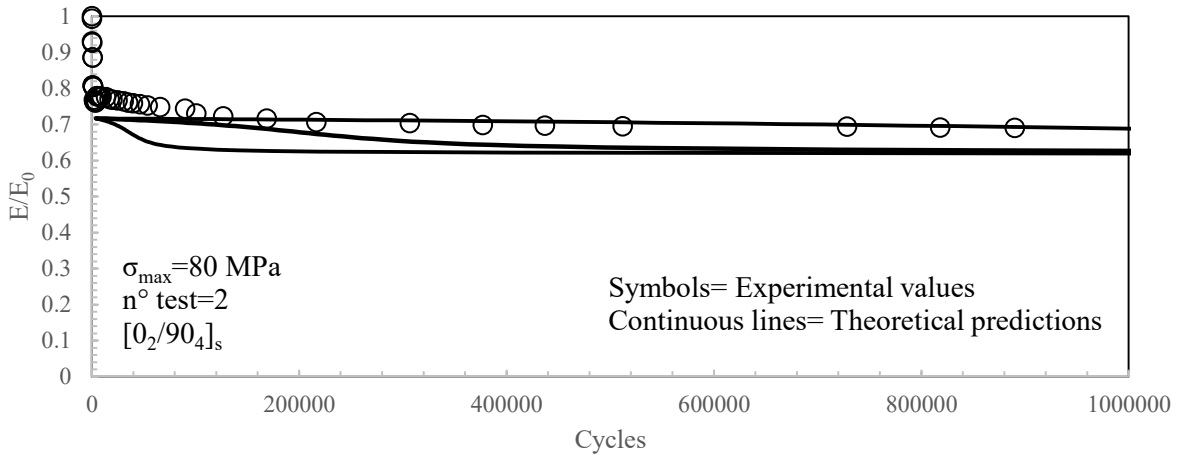

Figure 5.14. Comparison between the data of stiffness experimentally determined and theoretical predictions for the test performed with σ_{max}=80 MPa

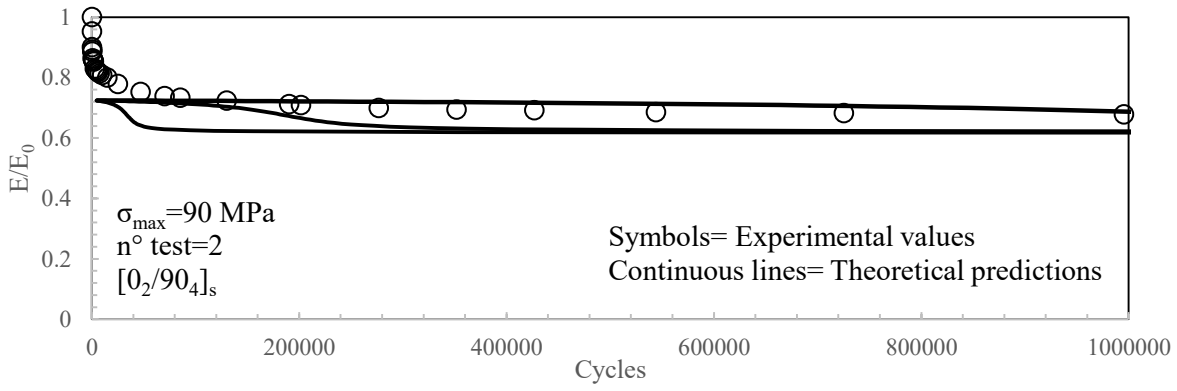

Figure 5.15. Comparison between the data of stiffness experimentally determined and theoretical predictions for the test performed with σ_{max}=90 MPa

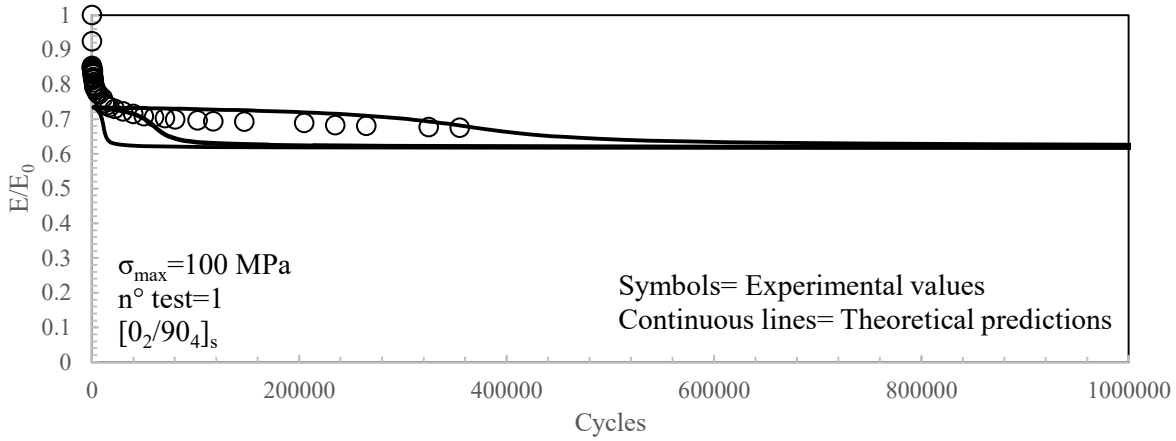

Figure 5.16. Comparison between the data of stiffness experimentally determined and theoretical predictions for the test performed with σ_{max}=100 MPa

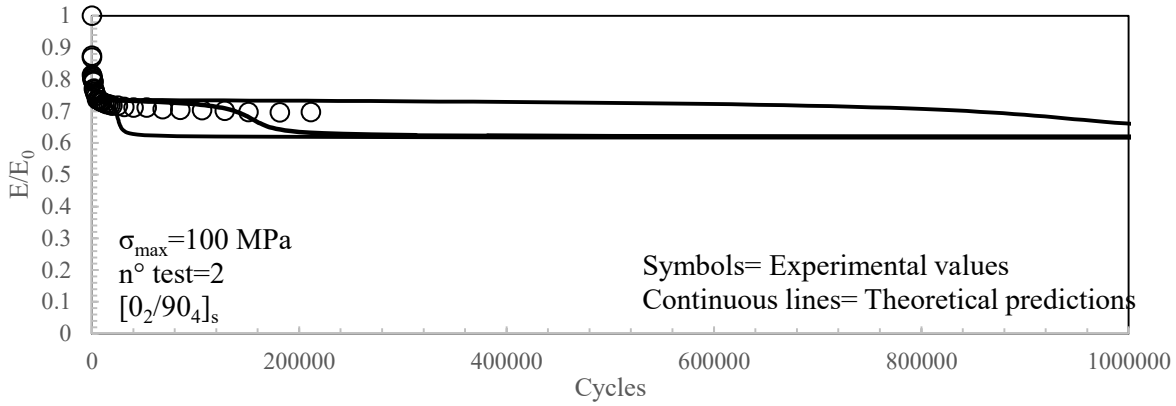

Figure 5.17. Comparison between the data of stiffness experimentally determined and theoretical predictions for the test performed with σ_{max}=100 MPa

5.8 Prediction of the Poisson's ratio

The Poisson's ratio has been observed to decrease during the fatigue tests with a trend similar to the Young's modulus, due to the combined effect of formation of new matrix cracks and growth of delaminations.

The changes of Poisson's ratio can be modelled following the formulation given first by Varna and Berglund [16] and furtherly developed by Akshantala and Talreja [17]. In the following section, the formulation adopted in this context to model the Poisson's ratio will be explained. This slightly differs from the ones above mentioned, since the stresses will be calculated by means of the shear-lag analysis.

5.8.1 Model

The Poisson's ratio is defined as:

$$\upsilon_{xy} = -\frac{\varepsilon_y}{\varepsilon_x} \tag{11}$$

The convention adopted for the axis is shown in Figure 5.18, where the schematic of the unit cell of the damaged laminate is represented.

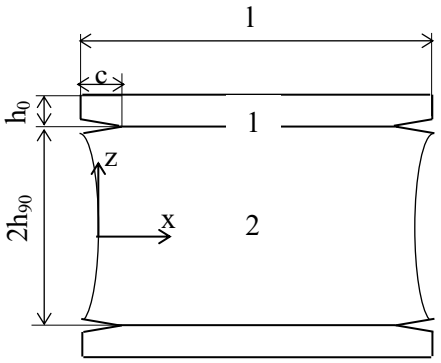

Figure 5.18 Schematic of the unit cell of the damaged cross-ply laminate

In the following formulation, the superscript 1 refers to the 0° lamina, while the superscript 2 refers to the 90° lamina.

The strains in the 0° and 90° plies can be calculated as:

$$\varepsilon_y^{(2)} = \frac{\sigma_{yy}^{(2)}}{E_y} - \frac{\upsilon_{12}\sigma_{zz}^{(2)}}{E_z} - \frac{\upsilon_{12}\sigma_{xx}^{(2)}}{E_x} \qquad \varepsilon_y^{(1)} = \frac{\sigma_{yy}^{(1)}}{E_y} - \frac{\upsilon_{12}\sigma_{zz}^{(1)}}{E_z} - \frac{\upsilon_{12}\sigma_{xx}^{(1)}}{E_x} \tag{12}$$

The absence of forces applied in the y direction implicates that the resultant in that direction must be null:

$$2\int_0^d \left[\int_0^{h_{90}} \sigma_{yy}^{(2)} dz + \int_{h_{90}}^{h_{90}+h_0} \sigma_{yy}^{(1)} dz\right] dx + \int_d^{\frac{l}{2}-d} \left[\int_0^{h_{90}} \sigma_{yy}^{(2)} dz + \int_{h_{90}}^{h_{90}+h_0} \sigma_{yy}^{(2)} dz\right] dx = 0 \tag{13}$$

Substituting Eqs. (11) and (12) into (13), ε_y can be written as follows:

$$\varepsilon_y = 2\int_0^d [\int_0^{h_{90}} E_A(\sigma_{zz}{}^{(2)} + \sigma_{xx}{}^{(2)})dz + \int_{h_{90}}^{h_{90}+h_0} (\frac{\upsilon_T E_A}{\upsilon_A}\sigma_{zz}{}^{(1)} + E_T\sigma_{xx}{}^{(1)})dz]\, dx + \int_d^{\frac{l}{2}-d} [\int_0^{h_{90}} E_A\sigma_{xx}{}^{(2)}dz + \int_{h_{90}}^{h_{90}+h_0} E_T\sigma_{xx}{}^{(1)}dz]\, dx \tag{14}$$

The laminate interested by the transverse cracks and delaminations can be considered equivalent to a laminate interested only by transverse cracks, evenly spaced by a distance equal to the spacing between the delamination tips in the original laminate.

The shear lag analysis allows to describe the stresses as function of the x coordinate:

$$\sigma_x{}^{(2)} = \frac{E_2}{E_0}\sigma_a\left(1 - \frac{\cosh(\frac{\alpha(l-2d)}{2} - \alpha(x-d))}{\cosh(\frac{\alpha(l-2d)}{2})}\right) \tag{15}$$

$$\sigma_x{}^{(1)} = \frac{E_1}{E_0}\left\{1 + \frac{E_2}{E_1}\frac{h_2}{h_1}\frac{\cosh(\frac{\alpha(l-2d)}{2} - \alpha(x-d))}{\cosh(\frac{\alpha(l-2d)}{2})}\right\}\sigma_a \tag{16}$$

$$\sigma_z{}^{(2)} = \alpha^2\frac{E_2h_2}{E_1h_1}\left(\frac{h_1}{2} + \frac{h_2{}^2 - z^2}{2h_2}\right)\frac{\cosh(\frac{\alpha(l-2d)}{2} - \alpha(x-d))}{\cosh(\frac{\alpha(l-2d)}{2})}\sigma_a \tag{17}$$

$$\sigma_z{}^{(1)} = \alpha^2\frac{E_2h_2}{E_1h_1}\frac{(h_1+h_2-z)^2}{2h_1}\frac{\cosh(\frac{\alpha(l-2d)}{2} - \alpha(x-d))}{\cosh(\frac{\alpha(l-2d)}{2})} \tag{18}$$

with:

$$\alpha^2 = \frac{(h_1 + h_2)E_0}{h_1 h_2 E_1 E_2} H \tag{19}$$

=

$$H = \frac{3G_{12}G_{23}}{h_1 G_{23} + h_2 G_{12}} \tag{20}$$

The average stresses in the delaminated portion of 0° plies are assumed equal to the stresses calculated with Eqs. (16) and (18) for x=d:

$$\sigma_x^{(1)} = \frac{E_1}{E_0}\left\{1 + \frac{E_2}{E_1}\frac{h_2}{h_1}\frac{\cosh(\frac{\alpha(1-2d)}{2})}{\cosh(\frac{\alpha(1-2d)}{2})}\right\}\sigma_a \tag{21}$$

$$\sigma_z^{(1)} = \alpha^2 \frac{E_2 h_2}{E_1 h_1}\frac{(h_1 + h_2 - z)^2}{2h_1} \tag{22}$$

5.8.2 Validation

In order to evaluate the accuracy of the simplified model above described, the Poisson's ratio obtained through the experimental tests has been compared with the theoretical predictions. The results are shown in Figure 5.19, Figure 5.20 and Figure 5.21. It is evident that the evolution of Poisson's ratio predicted is in a satisfactory agreement with experimental results.

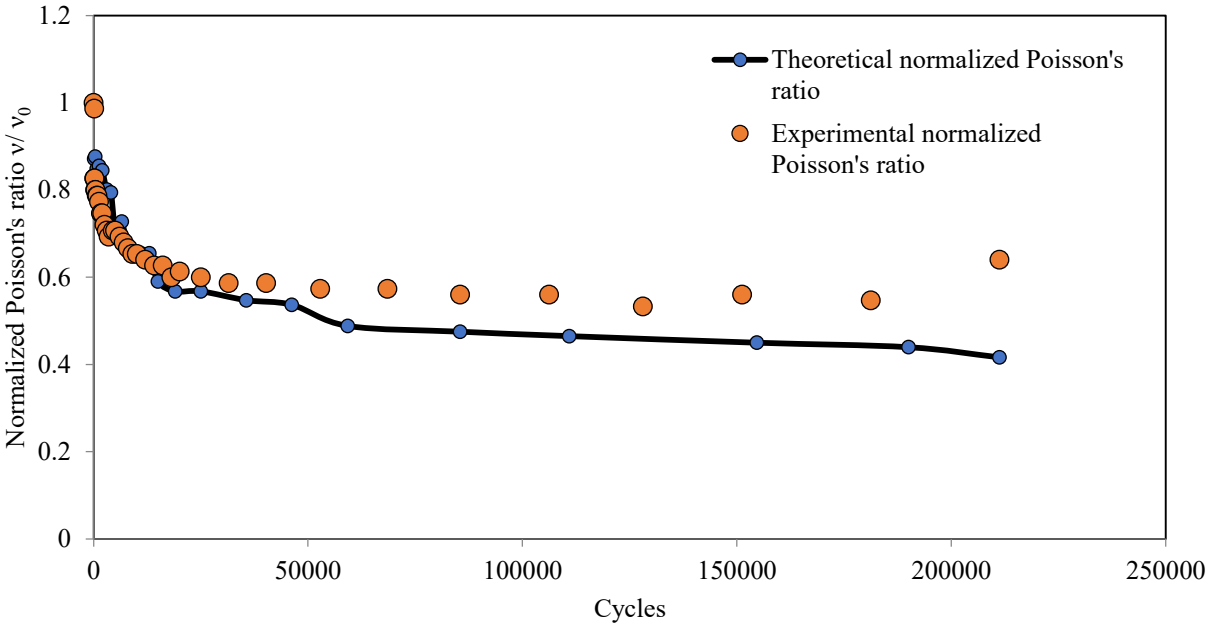

Figure 5.19 Comparison between normalized Poisson's ratio both predicted and experimentally obtained for a test carried out at a maximum stress of 100 MPa

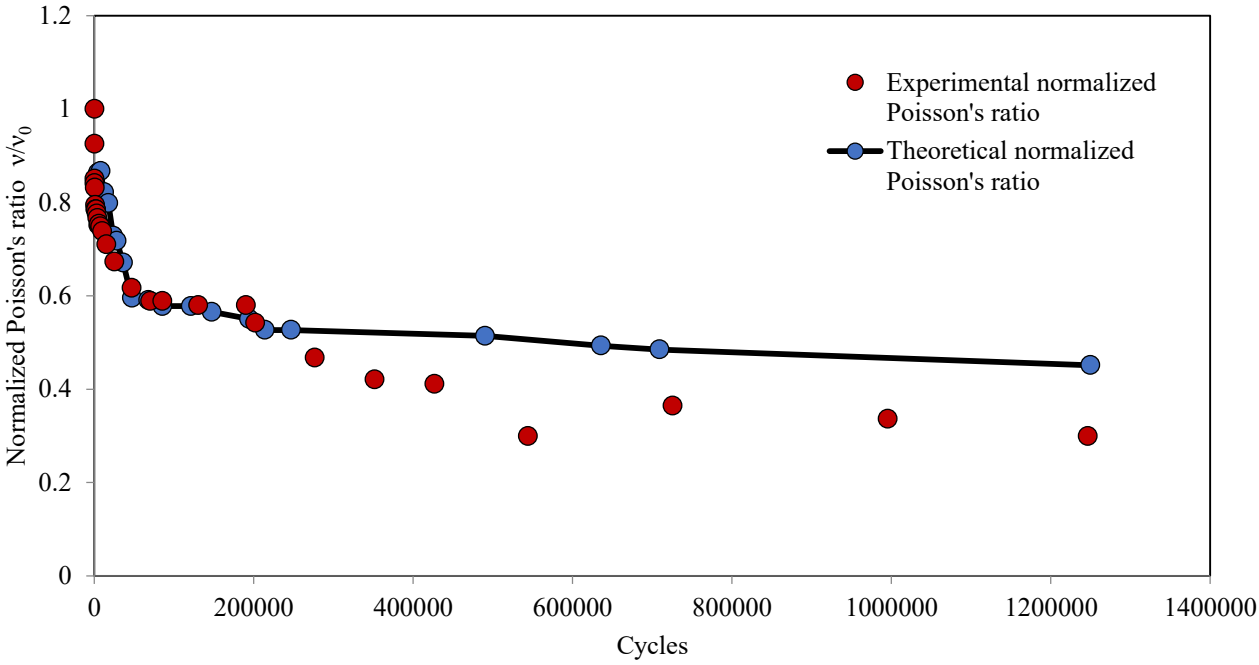

Figure 5.20 Comparison between normalized Poisson's ratio both predicted and experimentally obtained for a test carried out at a maximum stress of 90 MPa

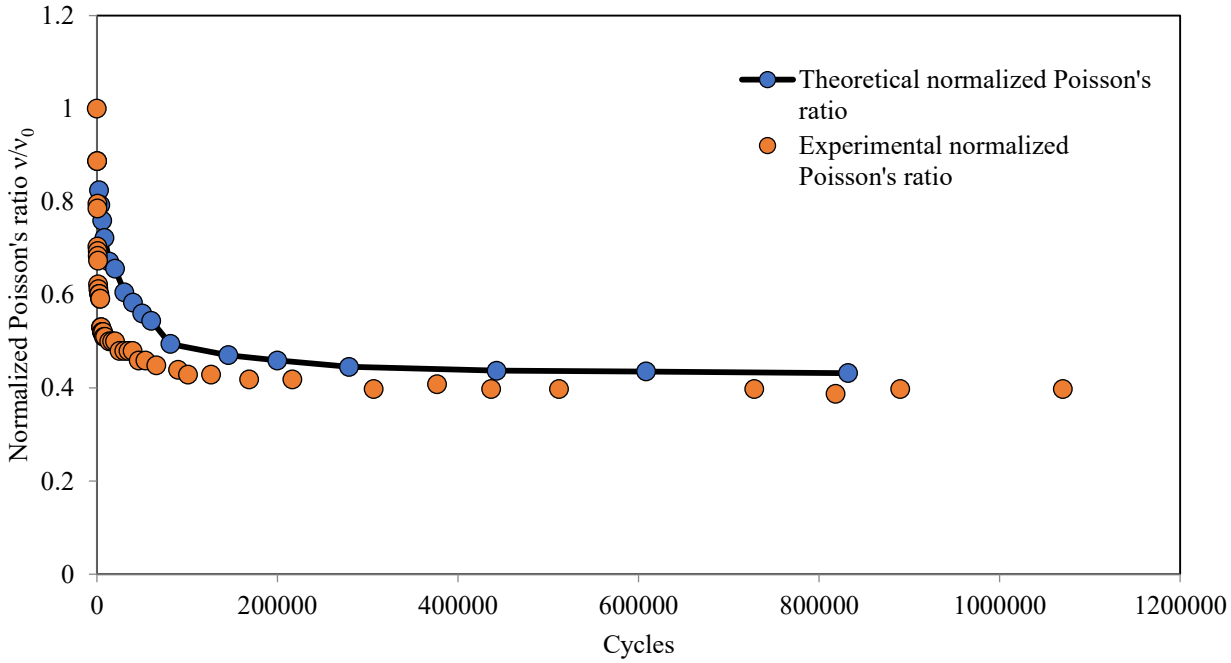

Figure 5.21 Comparison between normalized Poisson's ratio both predicted and experimentally obtained for a test carried out at a maximum stress of 90 MPa

5.9 Effect of stress-free edge on delaminations

Delaminations were seen to initiate and grow both at the edges, as well as in the central part of the specimens. Free-edge effect may influence the growth of delaminations, as already investigated in the past by Salpekar and O'Brien [3]. The authors carried out 3D finite element analyses, modelling two lay ups $[0_2/90_4]_s$ and $[\pm 45/90_4]_s$. Delaminations were assumed having three different configurations, one uniform along the width of the specimen, growing perpendicular to the matrix cracks, while the other two were triangular-shaped. The magnitude of the total strain energy release rate, calculated by using the virtual crack closure technique, was shown to increase near the free edges. The authors suggested that, since the delamination pattern is not known a priori, the maximum ERR value has to be considered for predicting the initiation and growth of delaminations.

In order to quantify the approximation introduced in the calculation of ERR performing 2D finite element analyses, 3D finite element analyses were performed, using 20 nodes elements. Only a portion of the laminate was modelled in virtue of the symmetry of the problem, as shown in Figure 5.22, applying a uniform displacement at the nodes located at x=L along the x direction and

symmetry conditions were applied to the nodes located on the planes y=0 and x=0 (with $y>h_{90}$). The width of the laminate was equal to 20 mm.

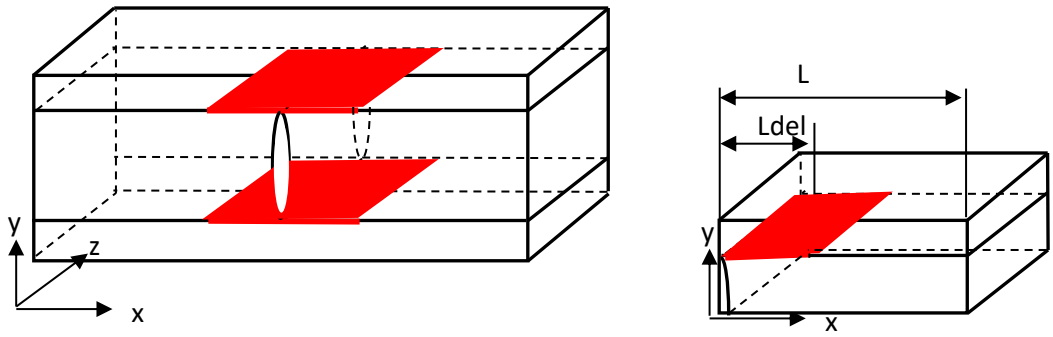

Figure 5.22. Schematic of the damaged laminate

While keeping unvaried the geometry of the laminate, the length of the delamination L_{del} was varied such as the ratio between the delamination length and the half crack spacing a/L was equal to 1/4, 1/2 and 3/4. The energy release rate components were calculated using the formulation of Virtual Crack Closure Technique for 20 nodes elements:

$$G_I = -\frac{1}{2\Delta A_L}\left[\frac{1}{2}Z_{Ki}(w_{Kl} - w_{Kl^*}) + Z_{Li}(w_{Ll} - w_{Ll^*}) + Z_{Lj}(w_{Lm} - w_{Lm^*}) + \frac{1}{2}Z_{mi}(w_{Ml} - w_{Ml^*})\right] \quad (23)$$

$$G_{II} = -\frac{1}{2\Delta A_L}\left[\frac{1}{2}X_{Ki}(u_{Kl} - u_{Kl^*}) + X_{Li}(u_{Ll} - u_{Ll^*}) + X_{Lj}(u_{Lm} - u_{Lm^*}) + \frac{1}{2}X_{mi}(u_{Ml} - u_{Ml^*})\right]$$

$$G_{III} = -\frac{1}{2\Delta A_L}\left[\frac{1}{2}Y_{Ki}(v_{Kl} - v_{Kl^*}) + Y_{Li}(v_{Ll} - v_{Ll^*}) + Y_{Lj}(v_{Lm} - v_{Lm^*}) + \frac{1}{2}Y_{mi}(v_{Ml} - v_{Ml^*})\right]$$

Where X, Y, Z are the nodal forces at the delamination front, while u, v and w are the displacements of the nodes behind the delamination front (see Figure 5.23).

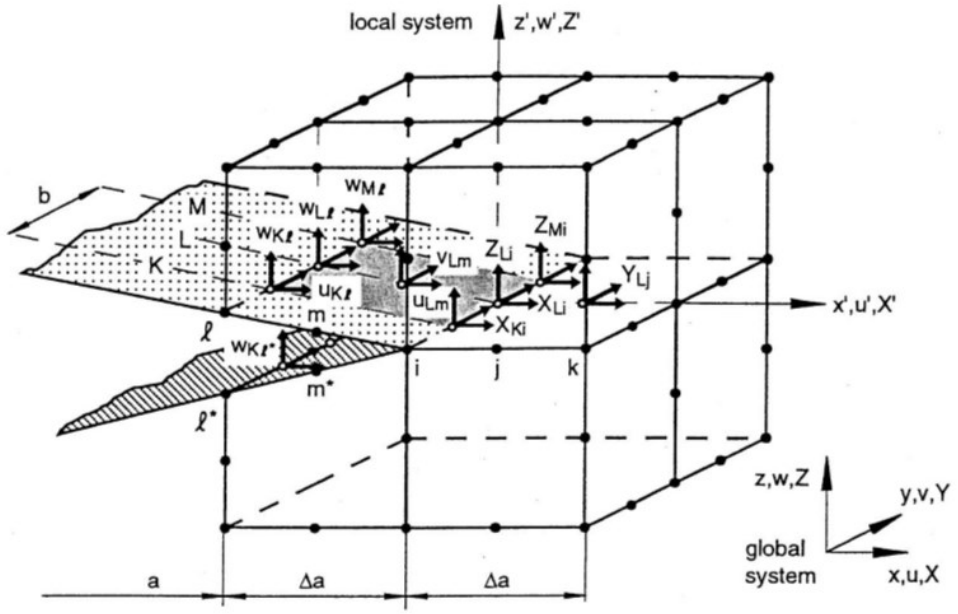

Figure 5.23 VCCT for corner nodes in 20-node solid elements [18]

The results are summarized in Figure 5.24. The outcomes that can be drawn are:

1. Values of components G_I, G_{II} and G_{III} change along the width, moving away from the free edge. However, this variation is not sufficient to justify the creation of 3D finite element analyses, more computationally onerous than simple 2D analyses;
2. Values of G_I can be assumed negligible compared to the G_{II} component for the three modelled configurations.

a) $\frac{L_{del}}{L} = \frac{1}{4}$ $[0_2/90_4]_s$

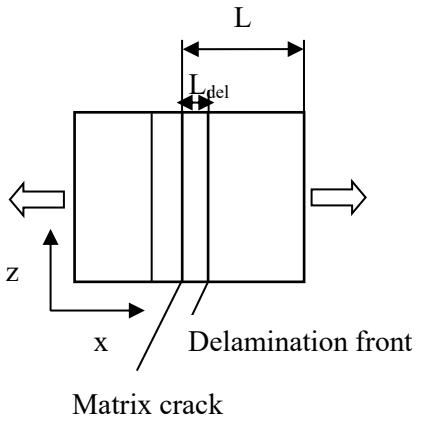

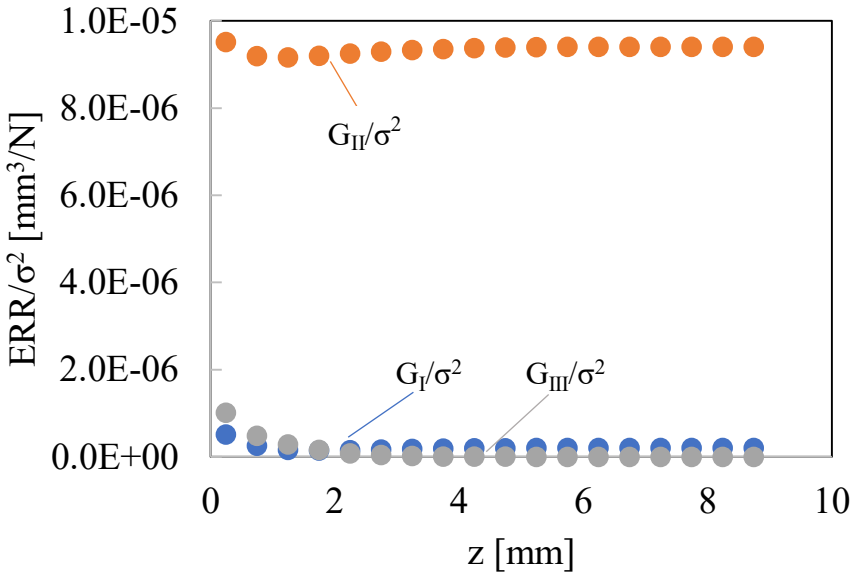

b) $\frac{L_{del}}{L} = \frac{1}{2}$ $[0_2/90_4]_s$

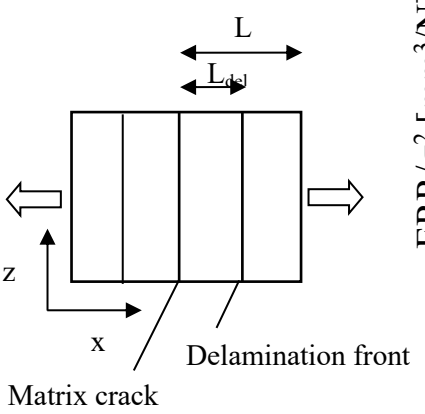

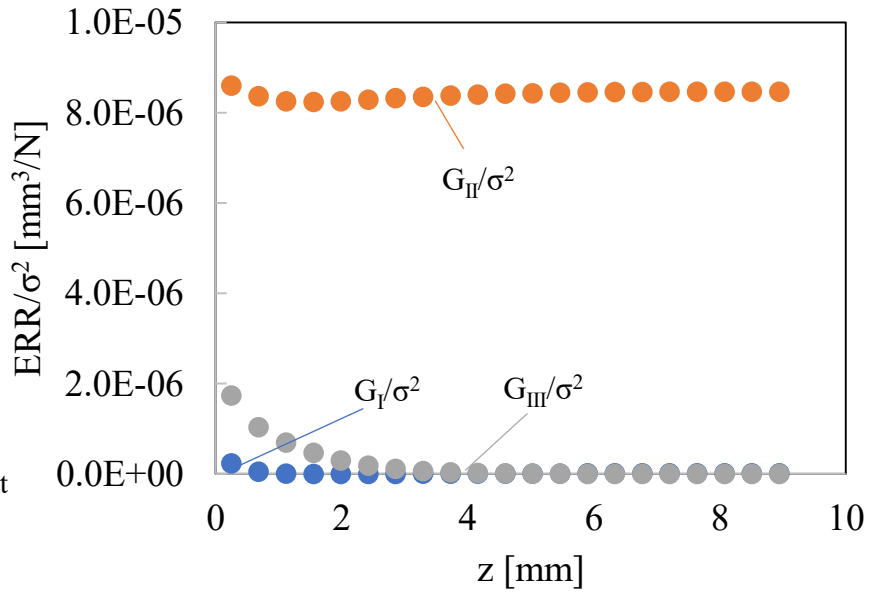

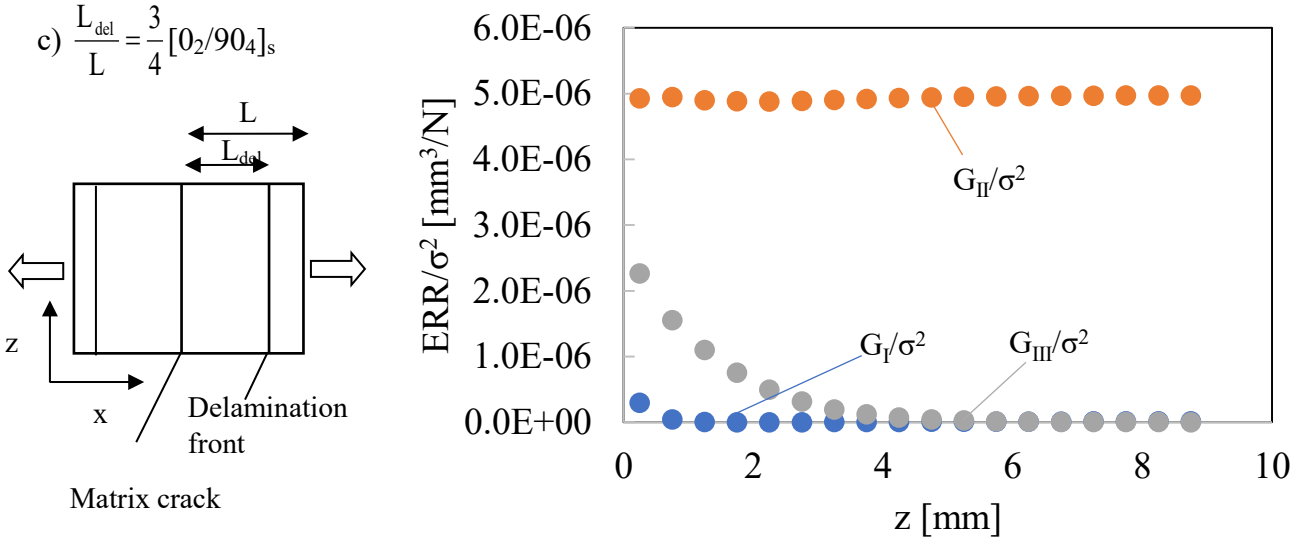

Figure 5.24 ERR components for a) Ldel/L=1/4 b) Ldel/L=1/2 and Ldel/L=3/4.

5.10 Reanalysis of the Paris like curve

As above mentioned, the experimental data, fitted with a Paris like curve relating delamination growth rate with Mode II ERR component, presented a considerable scatter, which affected the successive analyses. In order to decrease this scatter, an alternative fitting power law will be proposed in the following section, relating the dL_{del}/dN with the average principal stress calculated in a process zone.

5.10.1 FE Model

FE analyses were performed modelling a unit cell of a damaged cross-ply laminate, as represented inFigure 5.25. In particular, a $[0_2/90_4]_s$ laminate was modelled.

Differently from the analyses already carried out, a resin rich region was modelled in correspondence of the interface 0°/90°.

The properties used for this particular region were the ones typical of epoxy matrix, i.e. E =3500 MPa and ν=0.3, while the choice of its thickness will be discussed in the following.

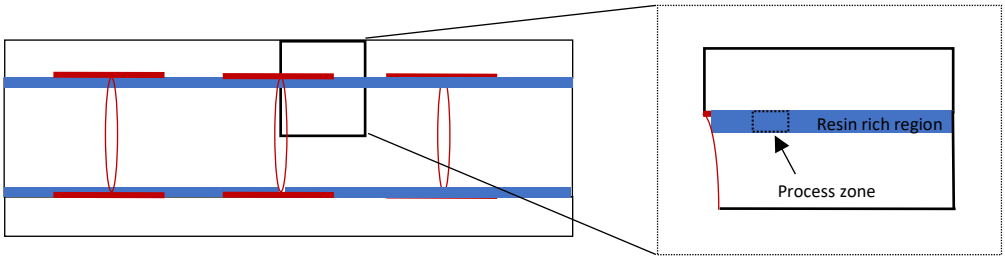

Figure 5.25 Schematic of the damaged cross-ply and individuation of a unit cell. Here, the resin rich region and the process zone used in the following analyses are indicated.

As illustrated in Figure 5.25, only a quarter of the damaged laminate was modelled. A uniform displacement was applied to the right hand-side, while symmetric boundary conditions were applied to the bottom and left hand-side of the model.

Important aspects, that will be clarified in the following sections, are the choice of the process zone dimensions and the impact of these on the average stress values.

5.10.2 Mesh sensitivity

A preliminary aspect investigated regards the sensitivity of the average of the stress to the element size used for the mesh of the process zone. A detail of the mesh used in the proximity of the interface is shown in Figure 5.26

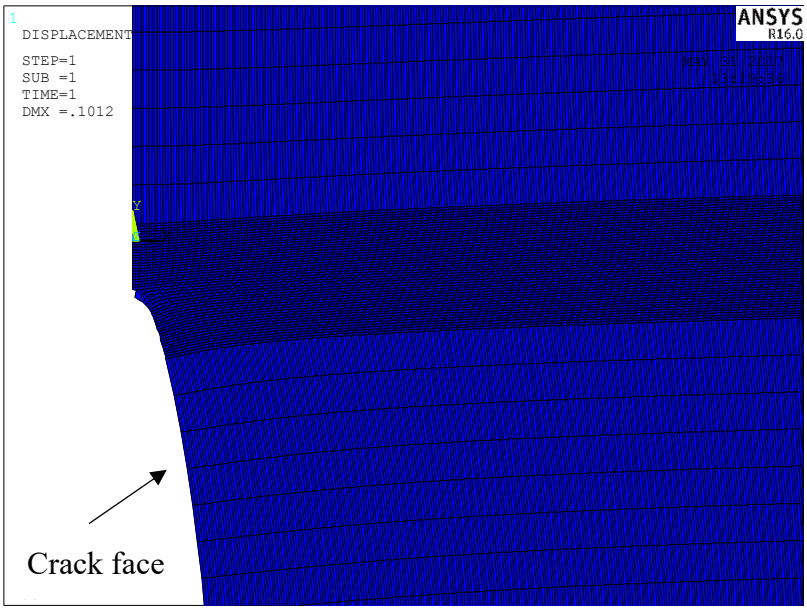

Figure 5.26 Detail of the mesh used for the process zone and the adjacent areas.

The results obtained from the convergence analysis are reported in Figure 5.27, which shows the principal stress values obtained for different element size of the mesh. It is evident that the average values of the three principal components of stress are not strongly influenced by the element size of the mesh used. For the successive analyses, it was decided to use an element size equal to 0.002 mm.

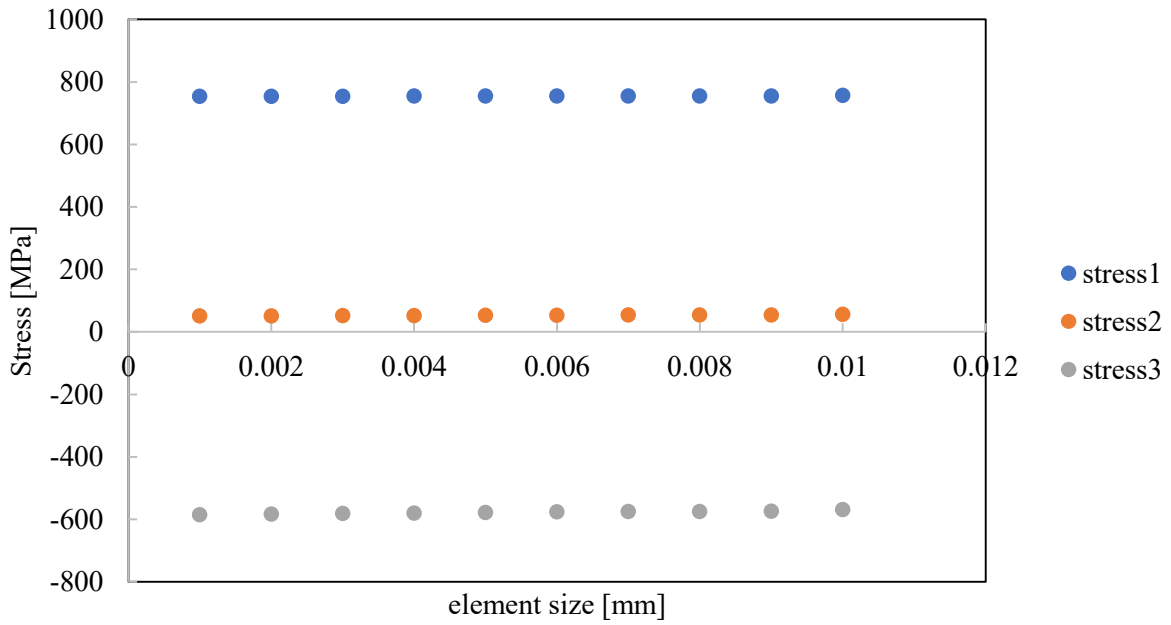

Figure 5.27 Principal stress values vs mesh element size for the convergence analysis of the mesh.

The principal dimensions used for the model were crackspacing=2.52 mm, Ldel=crackspacing/4, width of the process zone =0.054 mm, thickness of the process zone=0.010 mm

5.10.3 Dimensions of the process zone

Another investigated aspect consisted in the influence of the thickness values of the process zone, on the average value of the 1st principal stress (S), calculated within the process zone. To this aim, a series of parametric analyses was performed, varying the thickness of the process zone while keeping constant the other parameters (crack spacing= 2.071 mm, width of the process zone=0.054 mm). Moreover, different delamination length values were used to analyze the variation of the principal stress average value during the delamination growth process.

The results are illustrated in Figure 5.28. Here, the average values of 1st principal stress were normalized to the global stress applied to the model.

Information that can be gathered from the figure, can be summarized as follows:

1. the average values of the 1st principal stress decreases with the increase of the thickness of the process zone;
2. the curves of normalized 1st principal stress vs the increase of delamination length obtained for each thickness value keep the same trend.

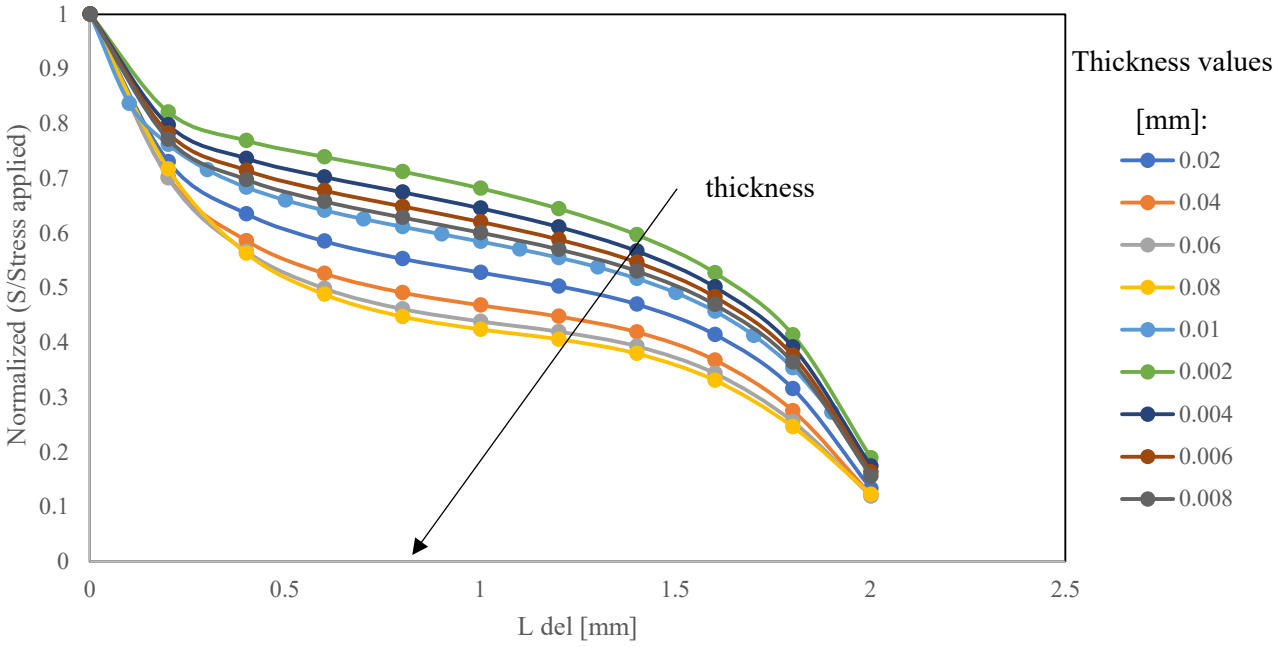

Figure 5.28 1st principal stress normalized to the global stress applied to the laminate for different thickness values of the process zone.

Furthermore, the influence of the width values of the process zone on the average value of 1st principal stress was analyzed, following an approach similar to the one above described.

A series of parametric analyses was performed varying the width of the process zone and delamination length values while keeping the crack spacing and thickness of the process zone unaltered (equal respectively to 2.071 mm and 0.010 mm). The results are shown in Figure 5.29.

The following main conclusions can be drawn:

1. the average values of the 1st principal stress decrease with the increase of the width of the process zone;
2. the curves of normalized 1st principal stress vs the increase of delamination length obtained for each width value keep the same trend.

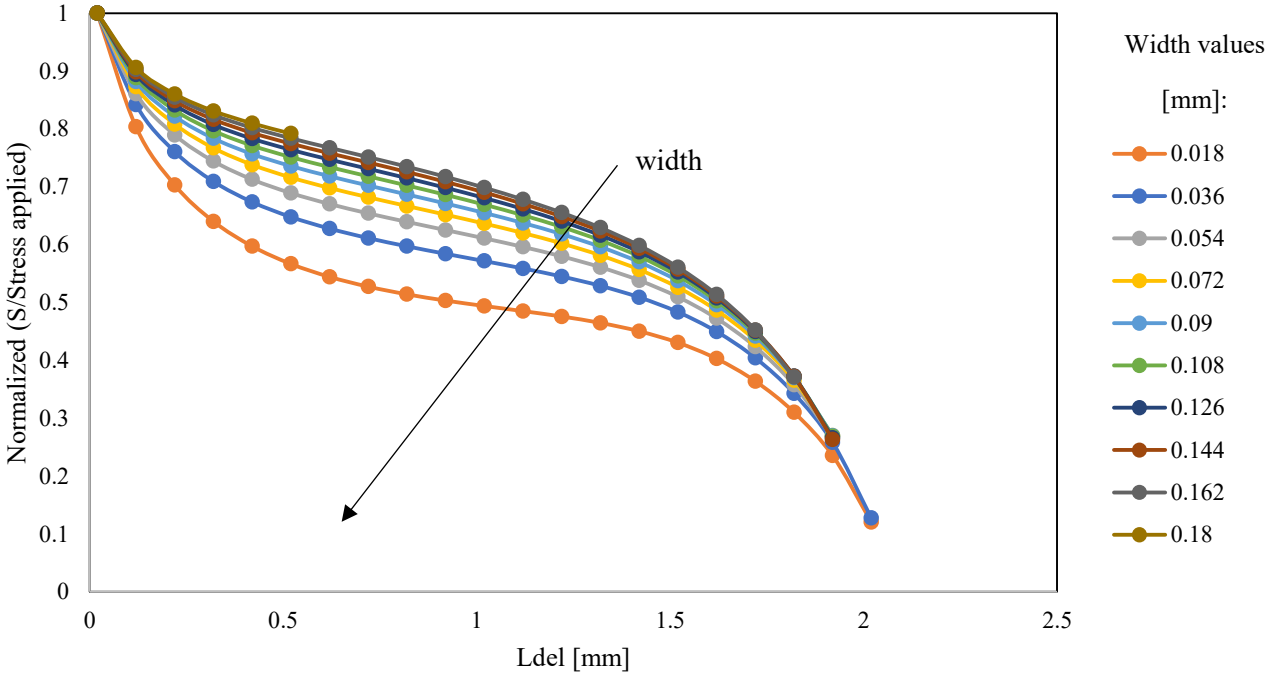

Figure 5.29 1st principal stress normalized to the global stress applied to the laminate for different width values of the process zone.

In the analysis that will be described in the following section, the dimensions used for the process zone were respectively 0.01 mm for the thickness 0.054mm for the width (~3 diameter of a fibre).

5.10.4 Paris like curve for equivalent average delaminations

The data elaborated by considering the Mode II component of ERR vs the delamination growth rate to obtain a Paris-like curve, were widely scattered, possibly due to the modelling assumptions. The resultant curve is shown in Figure 5.30. Here, the delamination length considered is the average

delamination formed at the tip of each transverse crack, obtained dividing the delamination ratio ($A_{del}/A_{interface}$) by the transverse crack density.

The data relative to the delamination length growth were re-analyzed and related to the average values of 1st principal stress. The resultant Paris-like curve is shown in Figure 5.31. By comparing the two figures, it is evident that the scatter that characterizes experimental data is reduced, suggesting that the approach based on the average 1st principal stress better describes the delamination growth.

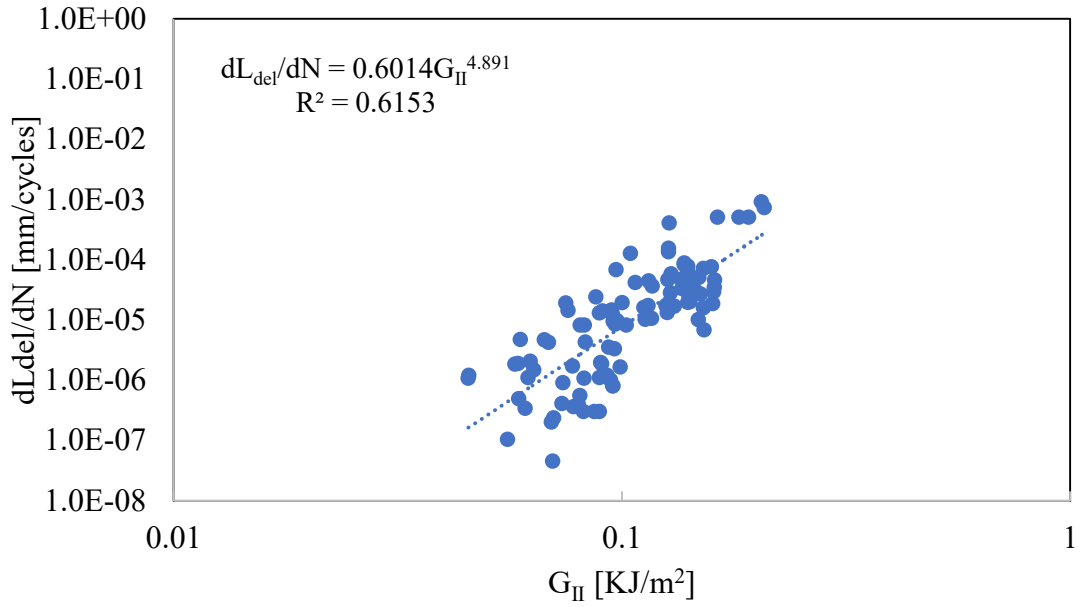

Figure 5.30 Paris like curve obtained considering the average 1st principal stress vs Mode II ERR G_{II}

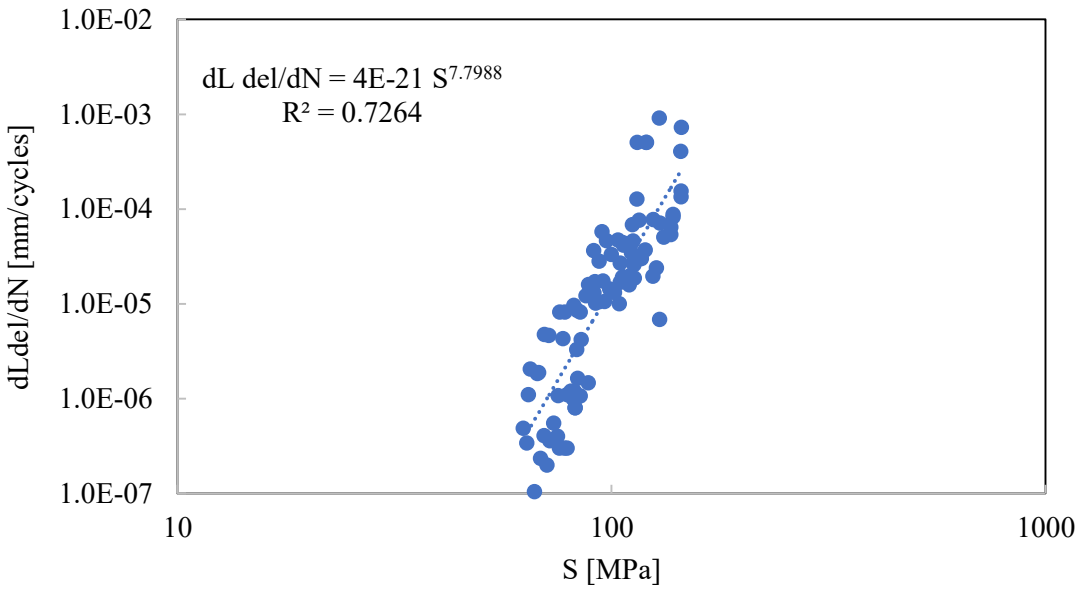

Figure 5.31 Paris like curve obtained considering the average 1st principal stress vs the delamination growth rate

5.10.5 Paris like curves for real delaminations, singularly considered

Some of the Paris like curves obtained considering the evolution of delaminations individually considered, were re-analyzed in terms of the average values of 1st principal stress within the process zone. Figure 5.32 illustrates the delamination growth data represented versus both the Mode II ERR component G_{II} and the 1st principal Stress. By comparing the two figures, it can be noticed that the reanalysis in terms of average stress improves the interpretation of the experimental delamination growth data, since the curves assume a positive slope.

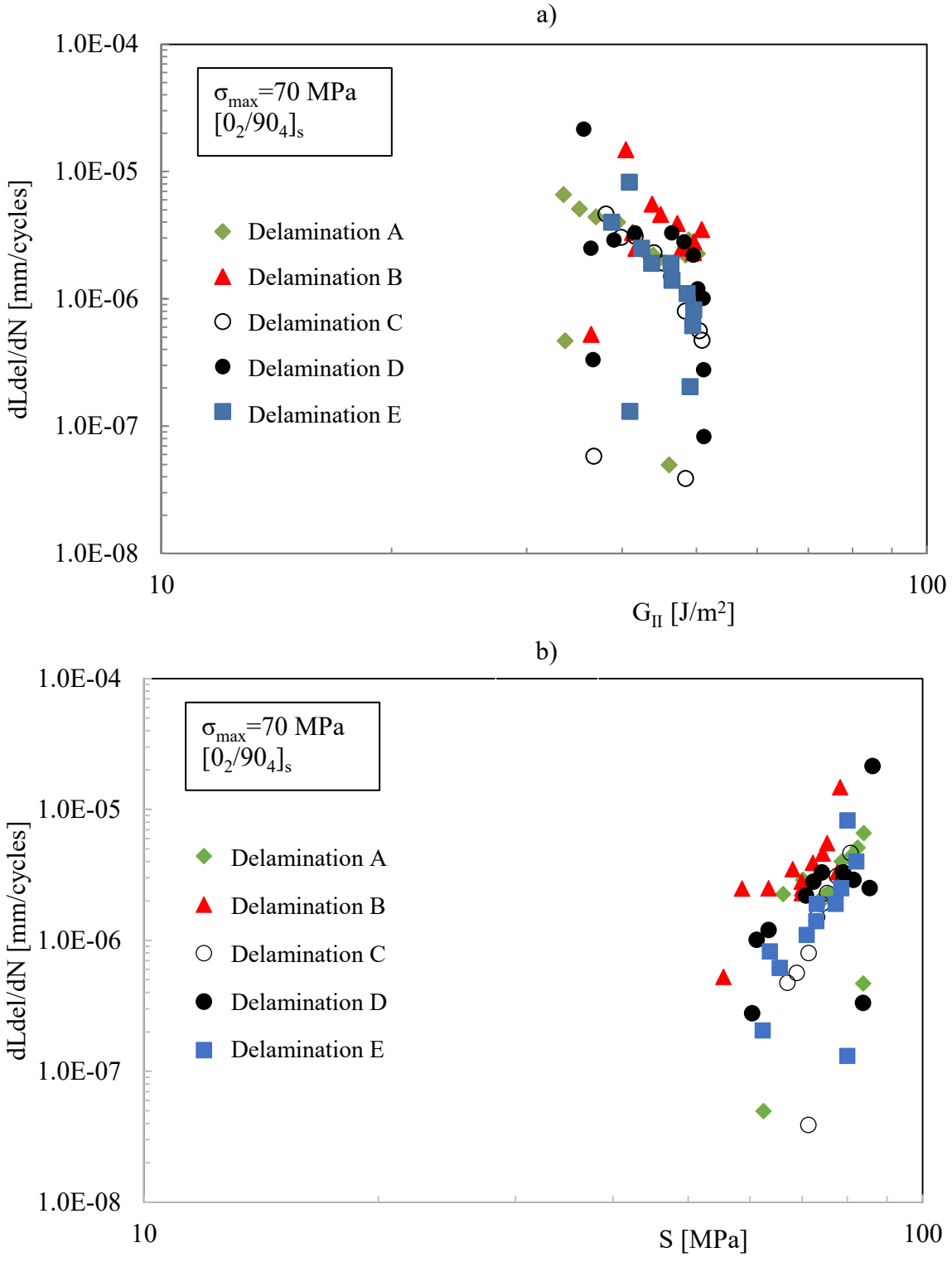

Figure 5.32 Paris like curves obtained by correlating the delamination growth rate with a) G_{II} or b) S1. In this case, the propagation of single delaminations was considered. Different delaminations have been indicated with different symbols.

5.11 Conclusions

In this work, the delamination growth occurring from the matrix cracks in cross-ply laminates subjected to tensile-tensile fatigue loading has been investigated. Delamination propagation was verified to be a phenomenon driven by the mode II of ERR. In particular, experimental data of delamination propagation for $[0_2/90_4]_s$ laminates, presented in the first part of the chapter, were related with the correspondent G_{II} values, calculated by means of the virtual crack closure technique. This allowed the definition of a Paris like curve. The same power law was verified to describe appropriately the propagation of delaminations in $[0/90_2]_s$ laminates. Since the experimental data of delamination growth rate related to the G_{II} values presented a wide scatter, an alternative approach based on the principal stress S was presented. The data were related to the average of the principal stress values calculated on a process zone in front of the delamination tip and a different power law relating the delamination growth rate with the S values was determined. The experimental data fitted with the new Paris law presented a minor scatter, suggesting that the use of a power law in terms of the principal stress to describe the delamination growth is preferable. Finally, a model to describe the Young's modulus and Poisson's ratio loss was proposed and validated.

References of chapter 5

[1] Degrieck, Joris, and Wim Van Paepegem. "Fatigue damage modeling of fibre-reinforced composite materials." *Applied mechanics reviews* 54.4 (2001): 279-300

[2] Pascoe, J. A., R. C. Alderliesten, and R. Benedictus. "Methods for the prediction of fatigue delamination growth in composites and adhesive bonds–a critical review." *Engineering Fracture Mechanics* 112 (2013): 72-96.

[3] Ratwani M, Kan HP. Compression fatigue analysis of fiber composites. J Aircraft 1981;18(6):458–62.

[4] Poursartip A, Chinatambi N. Fatigue damage development in notched $(0_2/\pm45)$s laminates. In: Lagace PA, editor. Composite materials: fatigue and fracture. ASTM STP 1012, vol. 2. Philadelphia: American Society for Testing and Materials; 1989. p. 45–65

[5] Paris P, Gomez M, Anderson W. A rational analytic theory of fatigue. Trend Engng 1961;13:9–14.

[6] Paris P. The fracture mechanics approach to fatigue. In: 10th Sagamore army materials research conference. Syracuse University Press; 1964. p.107–32.

[7] Paris P, Erdogan F. A critical analysis of crack propagation laws. J Basic Engng 1963;85(4):528–33.

[8] Dugdale DS. Yielding of steel sheets containing slits. J Mech Phys Solids 1960;8(2):100–4.

[9] Barenblatt GI. The mathematical theory of equilibrium cracks in brittle fracture. In: Dryden H, Kármán Tv, Kuerti G, Dungen FHvd, Howarth L, editors.

[10] Camanho P, Dávila C, Ambur D. Numerical simulation of delamination growth in composite materials. Tech Rep NASA/TP-2001-211041, NASA; 2001 Advances in applied mechanics. vol. 7. Elsevier; 1962. p. 55–129

[11] Moës N, Belytschko T. Extended finite element method for cohesive crack growth. Engng Fract Mech 2002;69(7):813–33.

[12] Huynh DBP, Belytschko T. The extended finite element method for fracture in composite materials. Int J Numer Methods Eng 2009;77(2):214–39.

[13] Iarve E, Gurvich M, Mollenhauer D. Discrete modeling of arbitrary matrix cracking and delaminations in laminated composites. In: International conference on composite materials: ICCM-17.

[14] Campilho RDSG, Banea MD, Chaves FJP, Silva LFM d. eXtended finite element method for fracture characterization of adhesive joints in pure mode I.Comput Mater Sci 2011;50(4):1543–9.

[15] Salpekar, Satish Annaji, and T. Kevin O'Brien. "Combined effect of matrix cracking and free edge on delamination." *Composite Materials: Fatigue and Fracture (Third Volume)*. ASTM International, 1991.

[16] Varna, Janis, and Lars Berglund. "Multiple transverse cracking and stiffness reduction in cross-ply laminates." *Journal of Composites, Technology and Research* 13.2 (1991): 97-106.

[17] Akshantala, Nagendra V., and Ramesh Talreja. "A micromechanics based model for predicting fatigue life of composite laminates." *Materials Science and Engineering: A* 285.1 (2000): 303-313.

[18] Krueger, Ronald. "Virtual crack closure technique: history, approach, and applications." *Applied Mechanics Reviews* 57.2 (2004): 109-143.

A.1 Influence of the delamination shape on the Paris curve.

Experimental investigations highlighted the existence of different preferential patterns for the delamination growth. Delaminations started from the tip of the transverse crack and developed either in both direction symmetrically to the transverse crack plane or asymmetrically, growing preferentially only in a direction, as illustrated in Figure A. 1.

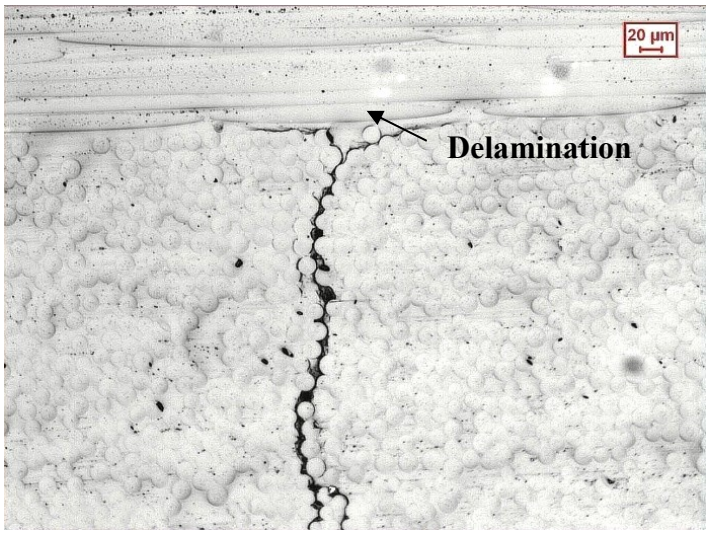

(a)

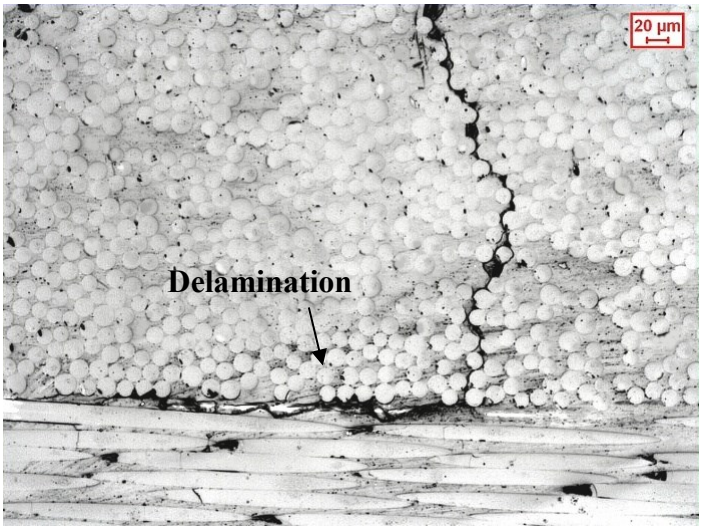

(b)

Figure A. 1 Different patterns of delamination growth, respectively a) symmetric and b) asymmetric respect to the transverse matrix crack plane

A similar damage development was already reported by Gamstedt and Sjogren [1].

The authors observed that the majority of the delaminations grew symmetrically in both directions from the tips of the transverse cracks. However, some delaminations grew asymmetrically. They assumed that this dual behaviour might be due to either local variations in microstructure along the interface or to the relaxing effect of adjacent cracks, but not investigated the aspect in depth. Since the experimental results obtained in the present work have revealed that the majority of delaminations grew prevalently in a single direction, it was considered appropriate to deepen the investigation.

A.1.1 Statement of the problem

Consider a representative section of a cross-ply laminate, with a transverse crack extended along the whole thickness of the 90° plies. Assuming that a single micro-delamination has originated from the tip of the crack, the successive potential locations where delamination initiate need to be determined. To this end, a campaign of finite element analyses has been performed, modelling a unit cell of the laminate (see the schematic in Figure A. 2), using 8 nodes isoparametric elements (PLANE 183), with the plane strain option.

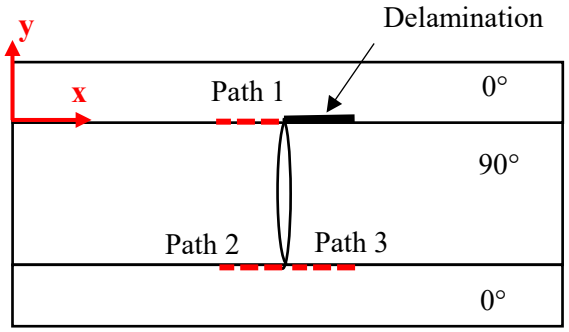

Figure A. 2 Schematic of the laminate interested by a single delamination originated from the tip of a transverse crack.

Stress components σ_y and σ_{xy} were evaluated along the paths represented in Figure A. 2. The results are shown in Figure A. 4 and Figure A. 5. Moreover, the effects of the presence of the friction were

examined, performing FE contact analyses in which both the absence and the presence of a friction coefficient between the two opposite faces of the delaminated plies was simulated. The friction coefficient was chosen equal to 0.36, accordingly to the study of Schön [2].

In this work, the author studied the changes of the friction coefficient during the fatigue life for adjacent plies with different fibre orientation, as illustrated in Figure A. 3, taken from his work.

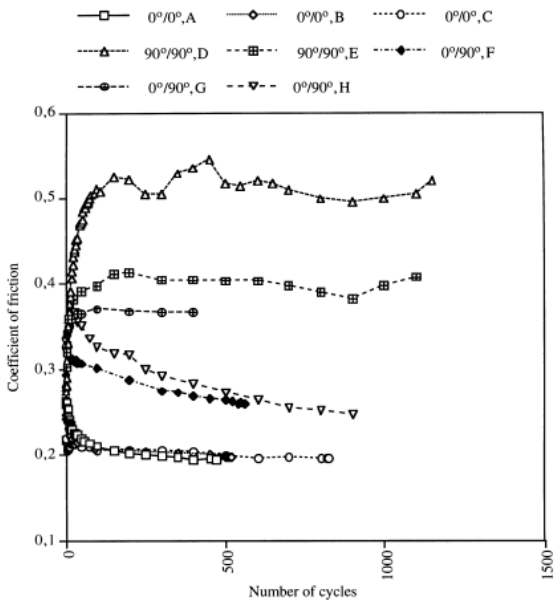

Figure A. 3 Coefficient of frictions with number of cycles [2].

By means of the virtual crack closure technique, the generalized strain energy release rate was valued at three different locations, represented in Figure A. 2. This allows to individuate where the delamination is more likely to develop. Table A. 1 reports the values of the strain energy release rate for two different conditions modelled, simulating the presence or less of a friction coefficient. Based on the results obtained, the conclusion that can be drawn is that delaminations are more likely to develop following a preferential direction, asymmetrically respect to the transverse crack plane (i.e. along path 2).

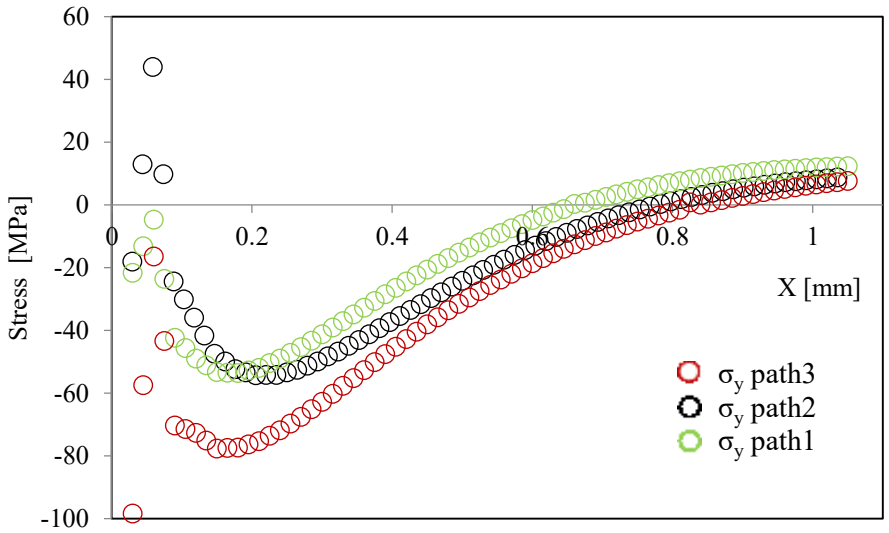

Figure A. 4 Stress components σ_y valued along three different paths

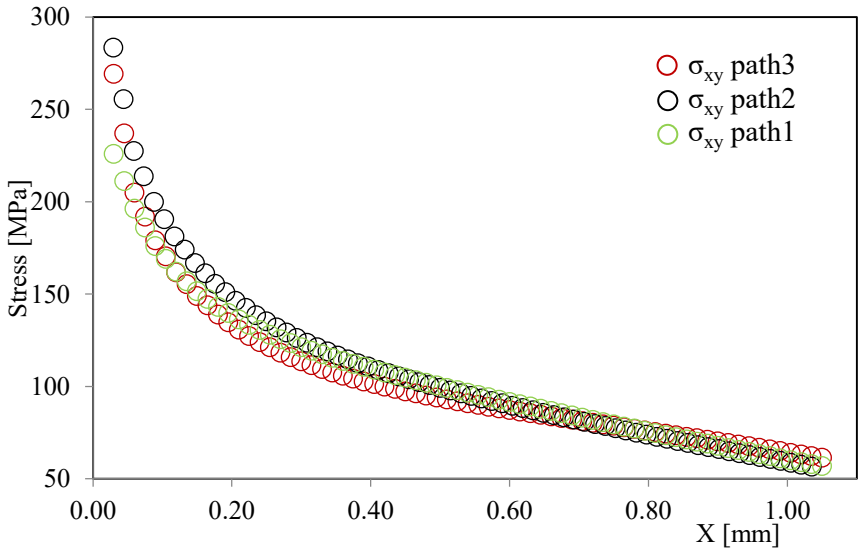

Figure A. 5 Stress components σ_{xy} valued along three different paths

Table A. 1 Strain energy release rate G_I and G_{II} values for the different paths, calculated both in presence and absence of friction.

Coefficient of friction μ=0.36

	G_I [kJ/m^2]	G_{II} [kJ/m^2]
path1	0.00000719	0.37247
path2	0	0.7644
path3	0	0.714

Coefficient of friction μ=0

	G_I [kJ/m^2]	G_{II} [kJ/m^2]
path1	0.00049	0.6054
path2	0	1.15955
path3	0	1.097

A.1.2 Comparison between Paris like curves of symmetric and asymmetric delaminations.

The analysis of the fatigue data has been repeated simulating three different configurations for the evolution of delaminations, shown in Figure A. 6:

a. Asymmetric to the transverse crack plane, with applied periodic boundary conditions (Z-shaped);

b. Asymmetric to the transverse crack plane, with applied symmetric boundary conditions (Z-shaped);

c. Symmetric to the transverse crack plane (H-shaped).

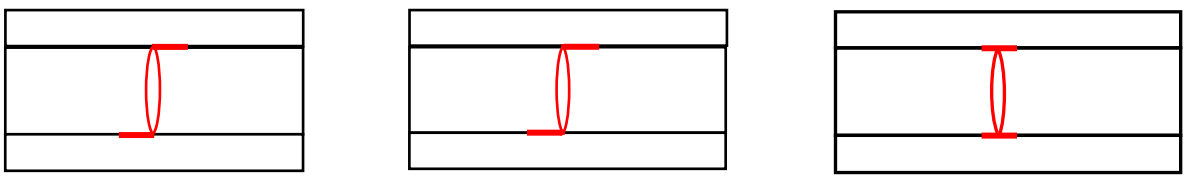

(a) (b) (c)

Figure A. 6 Schematic of the different configurations of the damaged laminate

The procedure above explained for obtaining the Paris like curve was repeated for the three different configurations.

The curves obtained are illustrated in Figure A. 7. In the figures, the scatter bands referred to ±2 std dev are represented. It can be seen that the configuration chosen to model the delaminations does not influence in a significative way the equations of the curves, particularly if the scatter of the data is considered.

a)

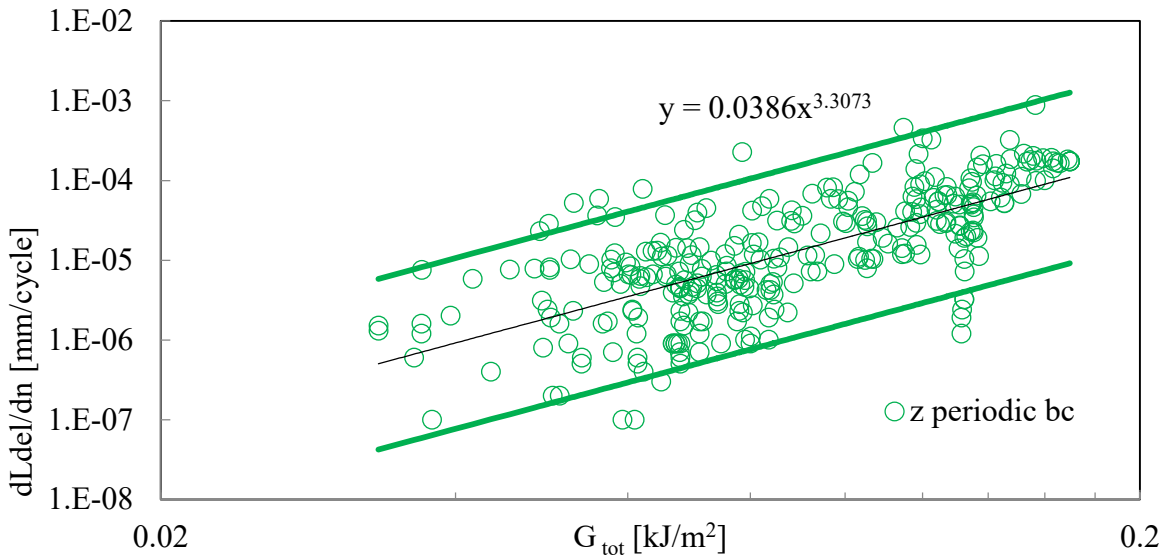

b)

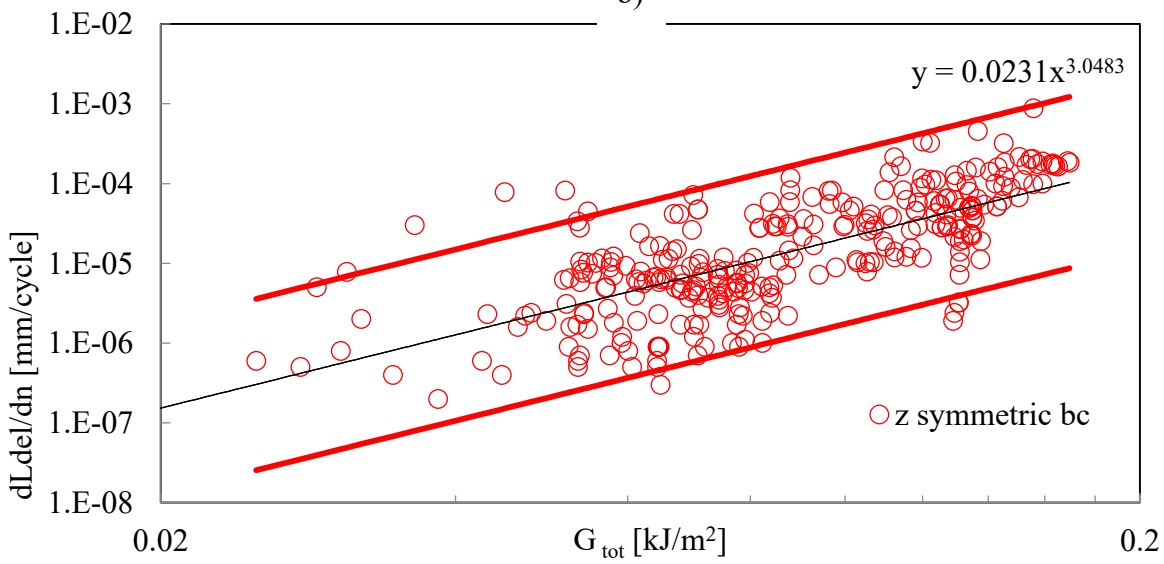

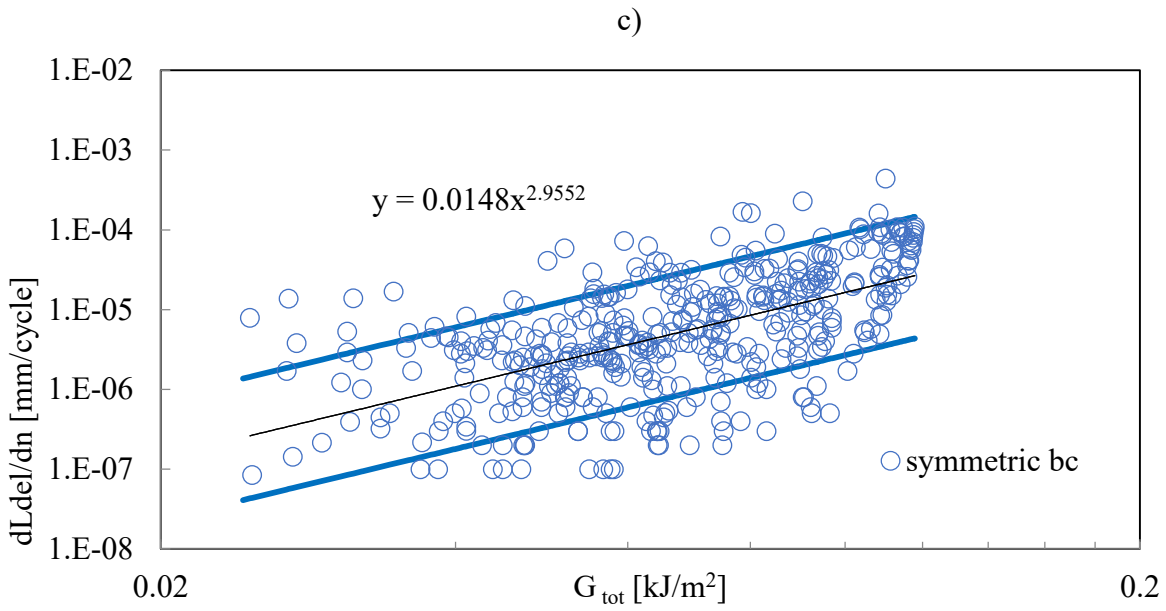

Figure A. 7 Paris like curves for delaminations: a) asymmetric to the transverse crack plane, with applied periodic boundary conditions (green symbols), b) asymmetric to the transverse crack plane, with applied symmetric boundary conditions (red symbols) and c) symmetric to the transverse crack plane (blue symbols).

A.1.3. Effect of friction on delamination growth

As observed from Talreja and coauthors [3], [4] it is reasonable to assume the presence of a frictional sliding at the interface of 0° and 90° delaminated faces, responsible of changes in the stress state within the laminate under fatigue loading.

In order to study the possibility that the presence of the friction may affect the ERR values, 2D FE contact analyses were performed, simulating the growth of a delamination for a $[0_2/90_4]_s$ laminate. 2D 8-node elements (Plane 183) were used, with the plane strain option.

Each ply was modelled with a thickness of 0.3 mm and the crack spacing was kept unaltered (L=1.3mm), while the delamination length was progressively increased. For each delamination length value, the mode II component of ERR was calculated, by using the VCCT. G_I was found negligible, such as its value won't be represented in the following figures.

Two different models of the damaged laminate were developed, assuming that the delaminations grew symmetrically with respect to the transverse crack plane (H shaped) or asymmetrically (Z shaped). The schematic is represented in Figure A. 8.

Three values of coefficients of friction were used, $\mu=0$ (complete absence of friction), $\mu=0.3$ and $\mu=0.5$.

The coefficient defining the amount of allowable penetration between the delaminated surfaces was set equal to 0.1, modifying the default value of Ansys of 1, in order to obtain more accurate solutions. A value lower than 0.1 could have produced even more accurate results; nonetheless preliminary analyses performed showed that the solutions of the FEA did not converge.

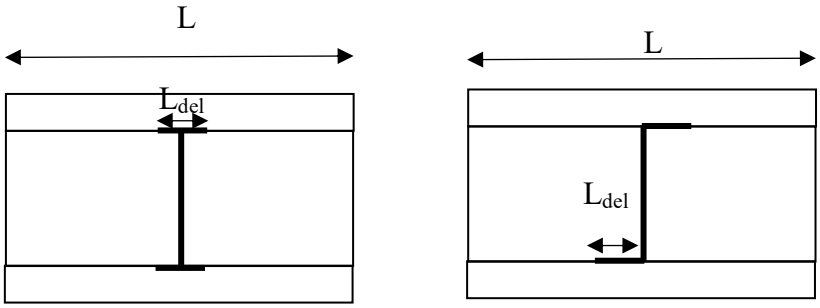

Figure A. 8 Schematic of the FE models

The resultant curves of G_{II}, relative to the H-shaped and Z-shaped configurations are reported respectively in Figure A. 9 and Figure A. 10. The ERR values were normalized to the square of the stress remotely applied to the laminate, and are represented in the slide vs the normalized delamination length. By comparing the curves obtained with different friction coefficients, it is evident that there is not a significative difference between the ERR values obtained varying the μ value or simulating a frictionless contact.

The results of this analysis justify the choice of ignoring the effects of the friction between the delaminated layers, which would complicate the problem without improving the soundness of the results.

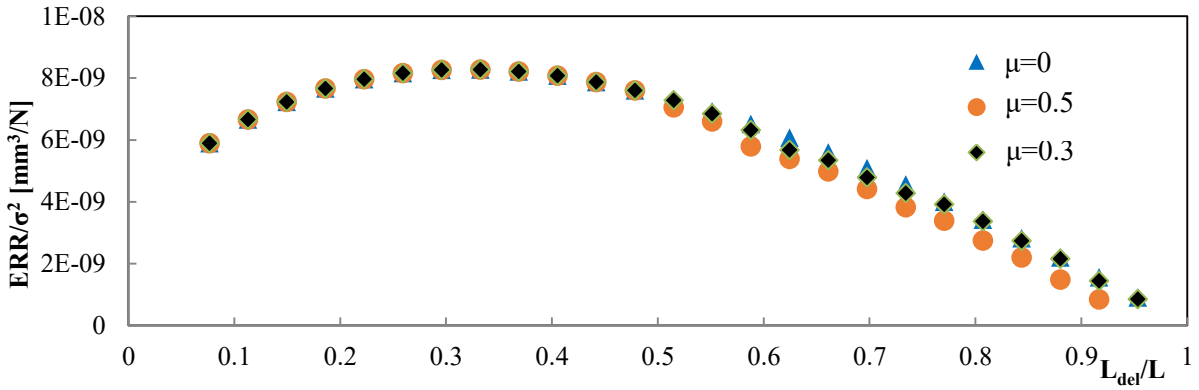

Figure A. 9 Curves of ERR obtained with three different coefficients of friction for a delamination with a configuration of H.

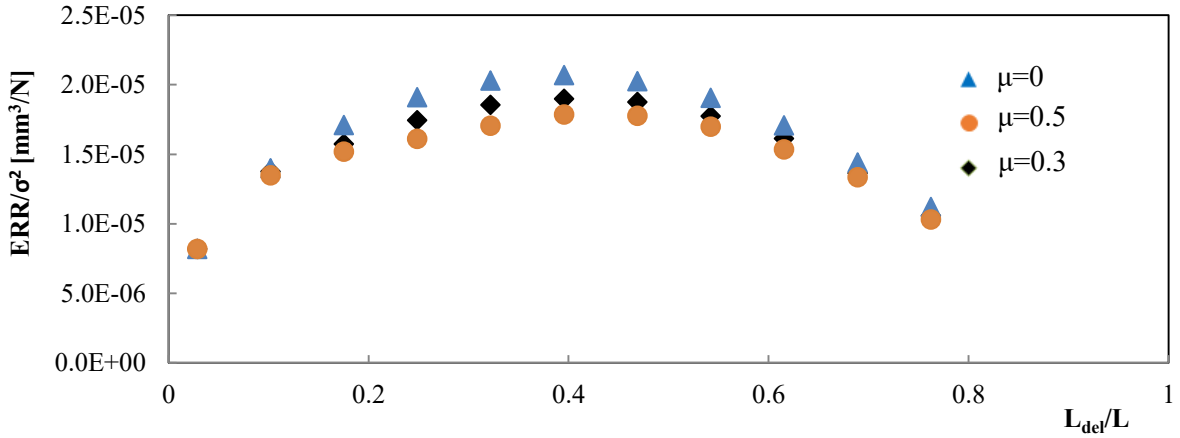

Figure A. 10 Curves of ERR obtained with three different coefficients of friction for a delamination with a configuration of Z.

References of Appendix

[1] Gamstedt, E. Kristofer, and B. A. Sjögren. "An experimental investigation of the sequence effect in block amplitude loading of cross-ply composite laminates." *International Journal of Fatigue* 24.2 (2002): 437-446.

[2] Schön, Joakim. "Coefficient of friction of composite delamination surfaces." Wear 237.1 (2000): 77-89.

[3] Akshantala, Nagendra V., and Ramesh Talreja. "A mechanistic model for fatigue damage evolution in composite laminates." *Mechanics of Materials* 29.2 (1998): 123-140.

[4] Akshantala, Nagendra V., and Ramesh Talreja. "A micromechanics based model for predicting fatigue life of composite laminates." *Materials Science and Engineering: A* 285.1 (2000): 303-313.

6 *Delamination evolution of generic laminates subjected to fatigue loading*

6.1 Introduction

The threat of delaminations, arising from in-service loading, is one of the factors that limited the extended use of laminated composite materials for main structure. Delaminations are primarily caused by the interlaminar tension and shear stresses that develop due to different factors. These include geometric or materials discontinuities (e.g. edges, holes, dropped ply). However, they may also occur from internal mechanism failure, such as matrix cracks. Matrix cracks acts as initiator of delaminations, thus spreading at different locations of the laminate.

Many studies have been focused on delaminations, mostly on damage evolution in cross-ply laminates (for a review the reader can refer to [1] and references cited therein or [2]). On the contrary, few have deepened the mutual influence that matrix cracks have on delamination formation and growth.

Early studies [3], [4], [5] documented the occurrence of local delaminations induced by the presence of matrix cracks in off-axis plies, extensively developed in correspondence of the free-edges, for unnotched, notched and tapered laminates.

One of the first studies dedicated to the investigation of damage evolution, subjected to quasi-static tests, was performed by Crossman and Wang [6]. The authors found out that for laminates characterized by the stacking sequence $[25/-25/90_n]_s$, the damage formation was dependent on the thickness of the 90° plies; for $n \leq 3$ delaminations initiated at the edges, while for higher values delaminations were seen to form uniformly across the width of the specimens.

O'Brien and Hooper [7] conducted quasi-static tests on $[0_2/\theta_2/-\theta_2]_s$ graphite epoxy laminates, for different laminate configurations (θ=15°, 20°, 25°, 30°). The initiation of delamination was

documented by using the x-radiography. By means of 3D finite element analysis, the stresses in the off-axis plies, responsible for the matrix cracking formation, were determined.

In a successive study, O'Brien [8] performed tension-tension fatigue tests, analyzing the same configurations of laminates $[0_2/\theta_2/-\theta_2]_s$. The onset of matrix cracking and the successive formation of delaminations, developed at the intersection of the matrix cracks with the free edge, was documented.

Results collected from quasi-static and fatigue tests showed that the damage type was the same: the local delaminations were present as triangular shaped shaded areas, bounded by matrix cracks and free edges. Then, different SERR expressions were determined, dependently on the configuration of delamination assumed, and the values were used to correlate the onset of delamination with different lay ups. SERR values were independent on the delamination area and matrix crack density.

Salpekar and O'Brien [9] published the results of a series of 3D finite element analyses, aimed at characterizing the SERR driving the delamination propagation for $[0_2/90_4]_s$ and $[\pm45/90_4]_s$ laminates. Further 3D finite element analyses were performed by Salpekar and other [10], which compared the SERR of delaminations for different stacking sequences of laminates ($[0/\theta/-\theta]_s$ and $[-\theta/\theta/0]_s$) using different techniques, i.e. the virtual crack closure technique (VCCT), the equivalent domain integral (EDI) and a global energy balance technique.

Recently, Johnson and Chang [11], [12] published the results of an experimental campaign aimed at characterizing the matrix crack induced damage progression, by developing analytical models. Delamination initiation was predicted using an energy based approach.

Further experimental studies, which highlighted the importance of delamination induced by matrix cracks on the failure process, were conducted more recently by Hallet et al. [13], Guillamet et al. [14] and Zubillaga et. al. [15].

In this chapter, the results of tensile-tensile fatigue tests performed on both balanced and unbalanced laminates are presented. The experimental campaign is aimed at better understanding the damage evolution, with particular attention to the formation of delaminations induced by matrix cracks.

6.2 Choice of stacking sequence: preliminary tests on $[0/45/-45]_s$ and $[0/45]_s$

As a first attempt of studying the evolution of delaminations induced by off axis cracks, preliminary fatigue tests were performed on $[0/45_2/-45_2]_s$ laminates.

Specimens were produced by using the liquid resin infusion technique, combining dry unidirectional glass fibres UT-E250 (250 g/m^2, Gurit) with the epoxy system EC157-W152LR (Elantas). The laminates were cured for three days at room temperature and then post-cured in an oven at 60°C for 12 hours. From these, specimens of 25 mm x 250mm were cut and polished at the edges, in order to ease microscopic observations of the interfaces where delamination might grow. Finally, tabs were applied at the ends of the specimens, thus the gage length was reduced to 140 mm.

During the fatigue tests, photographs were taken periodically by using a linear camera and images collected allowed to reconstruct the damage process.

However, with this layup, it was difficult to observe the evolution of delaminations occurring at the 0/45 interface, since it was hard to separate these from delaminations at the 45/-45 interface.

Therefore, specimens characterized by a different stacking sequence $[0/45_2]_s$ were produced, using the same materials and manufacturing technique.

This lay-up was considered more suitable to investigate delamination evolution, for two main reasons. First, a minor number of interfaces eases the location of the right interface where delaminations occur. Then, delaminations are seen to propagate more extensively at the interface 0/45 for the case of unbalanced laminates $[0/45_2]_s$ with respect to balanced laminates $[0/45_{2/}-45_2]_s$.

6.3 Fatigue tests

Tensile-tensile fatigue tests were conducted at room temperature with a sine waveform under load control conditions using a servo-hydraulic testing machine MTS 858, equipped with a 100 kN load cell.

All tests were carried out with a stress ratio of R=0.05 and a frequency of 4 Hz, sufficiently low to avoid an excessive increase of the temperature of specimens during the tests.

Different maximum values of stress were applied, as reported in Table 5.1. Stress levels were chosen to ease the observation of the onset and development of delaminations induced by transverse cracks.

Table 6.1 Stress levels and stacking sequence of performed fatigue tests

Stacking sequence	Maximum stress [MPa]
$[0/45_2/-45_2]s$	σ_{max}=130,120 MPa
$[0/45_2]s$	σ_{max}=130, 120, 110 MPa

The evolution of both axial and transverse strain during the fatigue life was monitored using a biaxial extensometer. During the tests, damage development was monitored and documented by taking pictures at the backlit specimens. The camera used was a digital reflex Canon EOS 700D with a 60mm macro lens. Young's modulus and Poisson's ratio evolution were monitored by applying a biaxial extensometer to the specimens.

Furthermore, specimens were frontally illuminated with a LED light, allowing the detection of delaminated areas. The observation area of the specimens was restricted to a length of about 60 mm in the central region, to avoid the influence of the end tabs on the damage process formation and growth.

Tests were interrupted when new damage mechanisms were seen to occur and specimen edges were analyzed using an optical microscope to collect a series of images detailing the accumulation of damage of the observed failure modes.

In order to quantify the delamination propagation, the delamination ratio parameter was introduced, defined as the ratio between the delaminated and the interface areas. To this aim, an image analysis tool was developed in Matlab aimed at processing photos and calculating the delamination ratio. First, images were trimmed for selecting the central part of the specimen, unaffected from the free-edge effect. Then, by binarizing and filtering the images, the delaminated areas were highlighted and measured. An example of the intermediate images obtained during the procedure is represented in Figure 6.1.

Since not all the cracks were extended through the whole width of specimens, the crack density was calculated taking into account and weighting each crack for its length and then dividing the sum by the length of the observation zone, measured perpendicularly to the propagation direction.

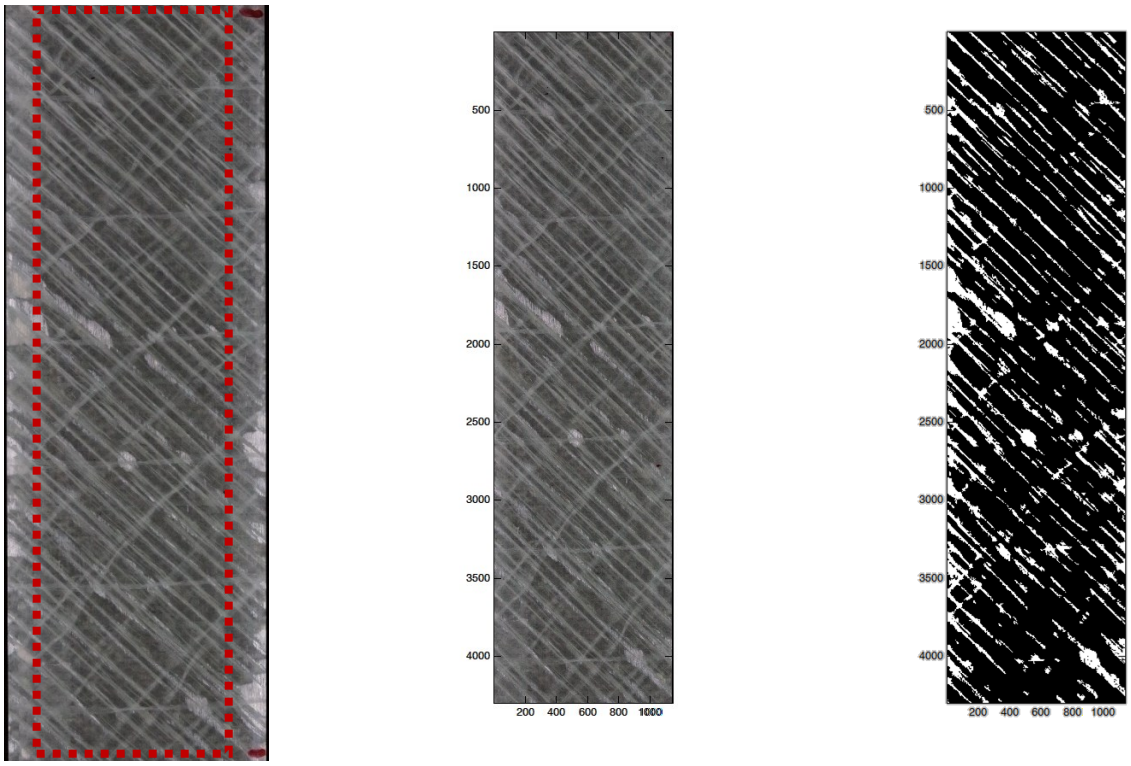

Figure 6.1 Operative procedure for calculating the delamination ratio

6.4 Damage analysis

The evolution of off axis cracks and delaminations observed for the test carried out with a σ_{max}=120 MPa on a $[0/45_2/-45_2]_s$ laminate are represented respectively in Figure 6.2 and Figure 6.3.

As regards cracks, these were seen forming both from the edges as well as within the central part of the specimens in the off-axis plies. Then these progressively grow and multiply in number. Cracks start interacting as the crack spacing decreases, providing a shielding effect that reduces the stresses between adjacent cracks and leads to the reaching of a saturation condition.

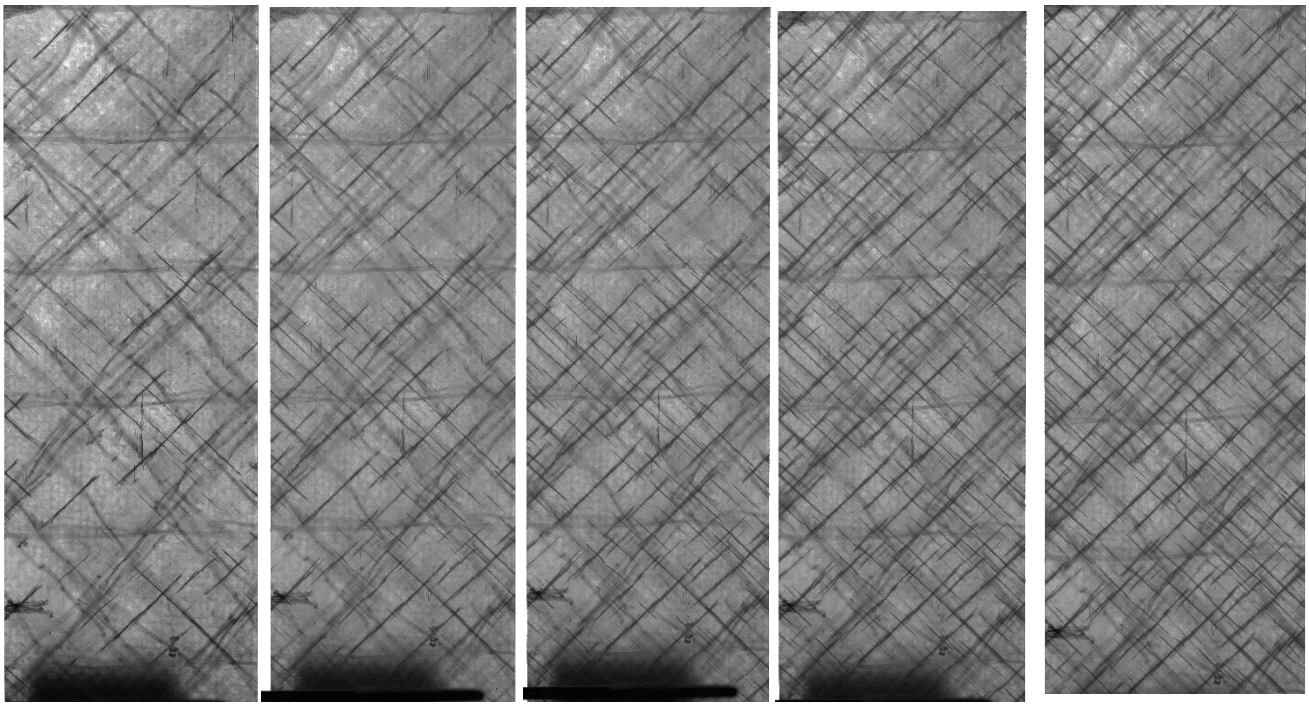

(a) (b) (c) (d) (e)

Figure 6.2 Off axis crack evolution for a $[0/45_2/-45_2]s$ laminate fatigue stresses with a σ_{max}=120 MPa Photographs were taken after a) 200, b) 600, c) 1000 d) 1400 cycles and e) 1800 cycles.

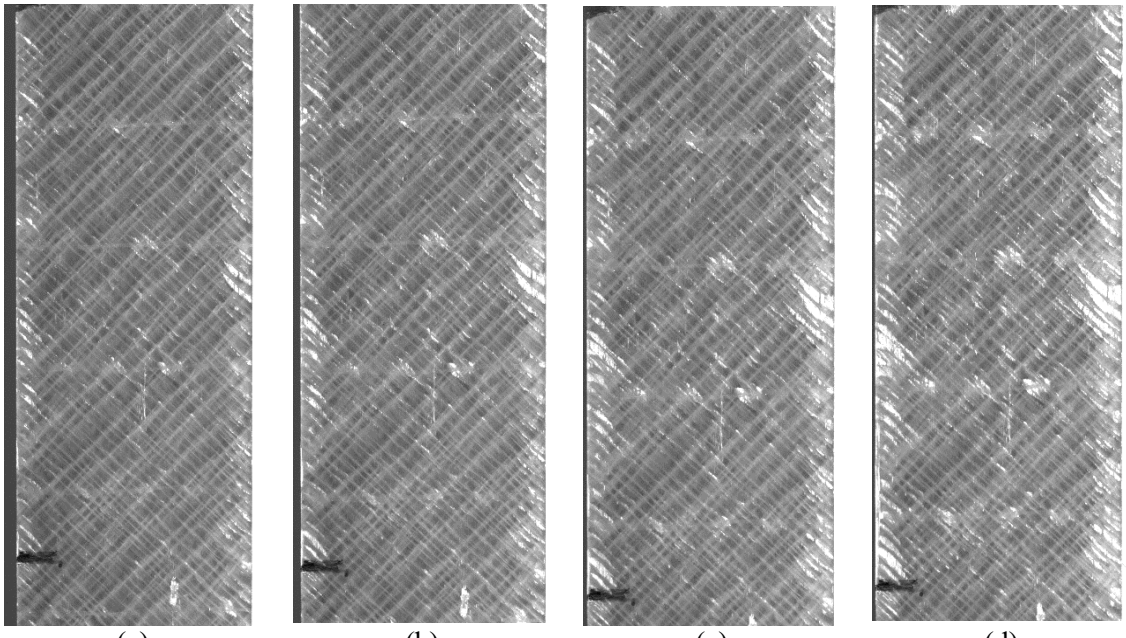

(a) (b) (c) (d)

Figure 6.3 Delamination evolution for a $[0/45_2/-45_2]_s$ laminate fatigue stresses with a σ_{max}=120 MPa. Photographs were taken after a) 82000, b)162000, c) 262000 and d) 362000 cycles

Conversely, as can be seen in Figure 6.3, delaminations generally forms on the edges, and then progressively propagate within the central part. However, this growth is limited, particularly if free

edges are excluded from the analysis, and this makes the investigation of the delamination evolution difficult.

As explained above, tests were periodically interrupted and micrographs of the specimen edges were collected after each interruption, to monitor the evolution of delaminations. Some progressive images are shown in Figure 6.4, which illustrates the stages of the damage development observed for a $[0/45_2/-45_2]s$ laminate. Matrix cracks were seen to develop through the thickness of both 45° and -45° plies. Then, delaminations formed both in correspondence of the interface 45°/-45°, growing until connecting the two transverse crack tips, and of the interface 0°/45° plies. As delaminations developed, fibre breaks were seen to form in the 0° ply, in the proximity of the delamination tips.

However, delaminations grew prevalently at the interface shared between the 45°/-45° while the growth at the interface 0/45 was limited.

(a)

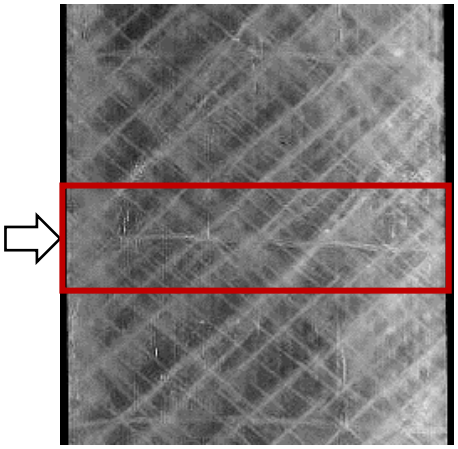

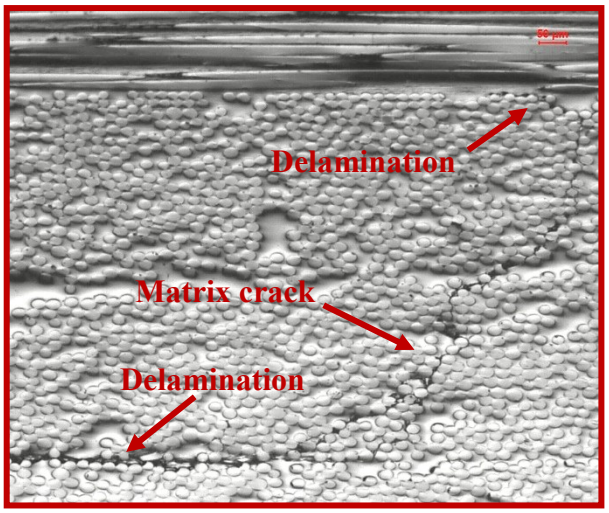

(b)

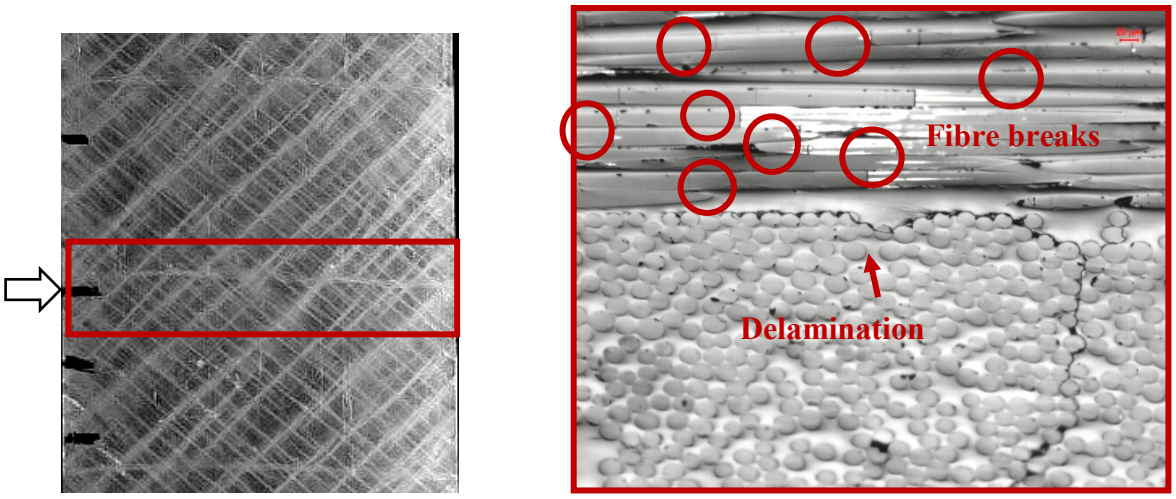

Figure 6.4: Damage development observed in $[0/45_2/-45_2]_s$ specimen fatigue tested with a σ_{max}=130 MPa. Images were taken respectively after a) 2818 cycles, b) 10322 cycles. The specimen failed after 25116 cycles.

6.5 FE analyses

Preliminary FE analyses were carried out in order to study the stress distribution of a $[0/45_2]_s$ laminate subjected to tensile loading. In particular, the purpose was to verify if there was a wide zone in the central part of the specimens, where stresses could be considered uniform. FE analyses were carried out using the software Ansys package. The elements used were 8-Node Structural Shell (Shell281), and the model implemented is schematized in Figure 6.5, where dimensions are reported in mm. Specimens were modelled complete of the tabs (25mm long) and the loading conditions applied during the tests were simulated by restraining all the displacements of the nodes of the tabs on the left-hand side and applying a displacement of 0.1 mm along the x direction to the nodes of the tabs on the right hand side.

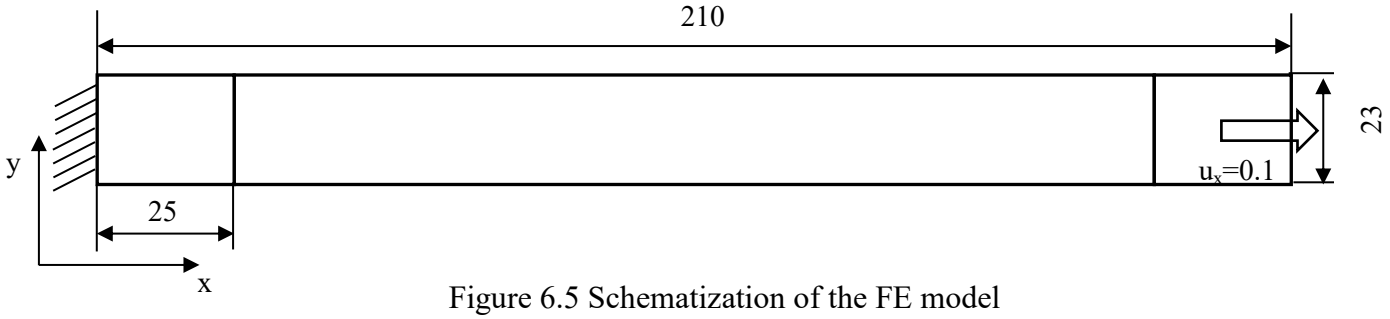

Figure 6.5 Schematization of the FE model

The principal stresses σ_1, σ_2 and σ_3 were evaluated along multiple paths, differently affected by the vicinity of the tabs, all within the 45° layers. The results are shown in Figure 6.6, where the FE results are compared with the theoretical stress values predicted by the classical lamination theory. Below each graph representing the stress values, the schematization of the specimen is drawn, to indicate the path along which the stresses are evaluated.

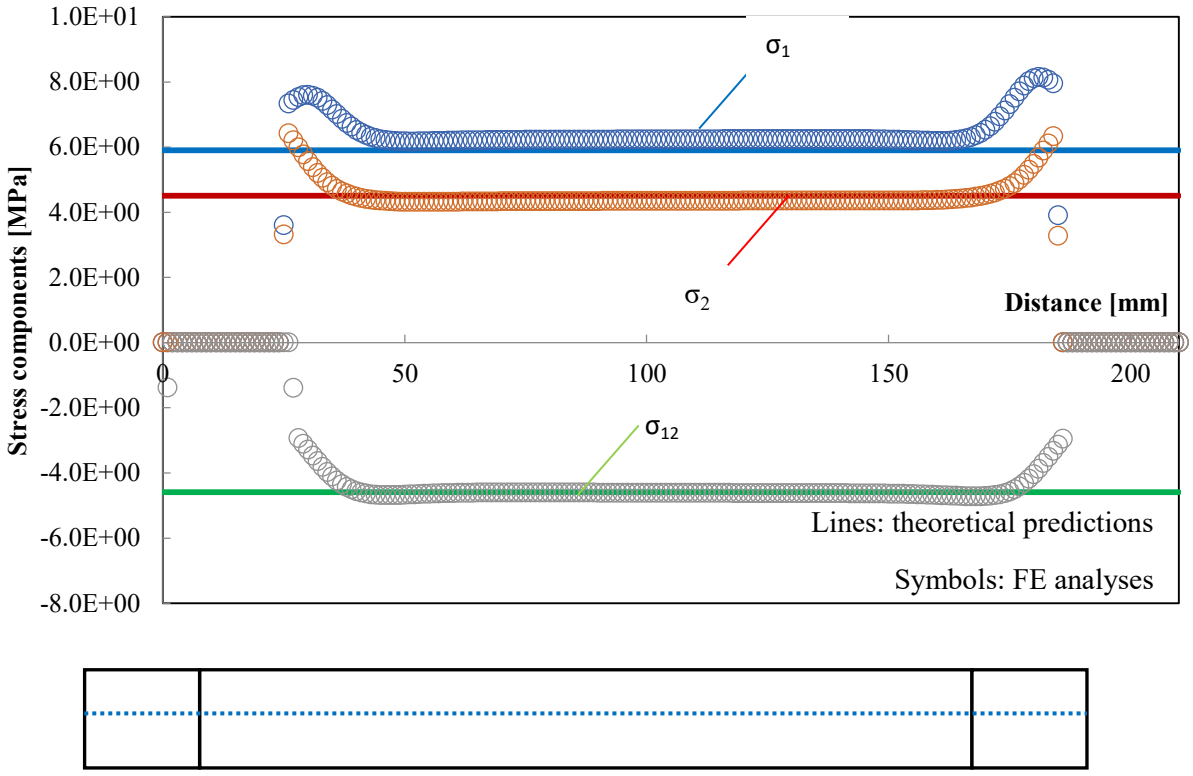

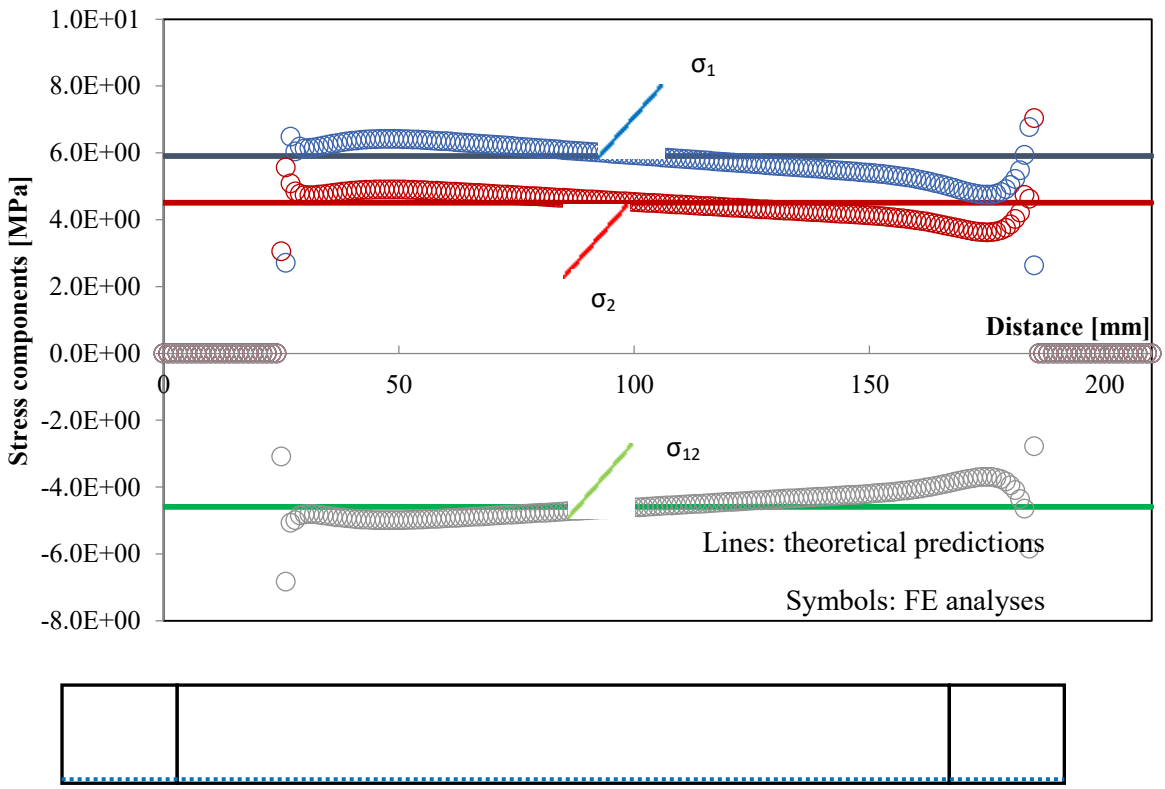
1.0E+01
8.0E+00
6.0E+00
4.0E+00
2.0E+00
0.0E+00
-2.0E+00
-4.0E+00
-6.0E+00
-8.0E+00
Stress components [MPa]
σ1
σ2
σ12
Distance [mm]
0
50
100
150
200
Lines: theoretical predictions
Symbols: FE analyses

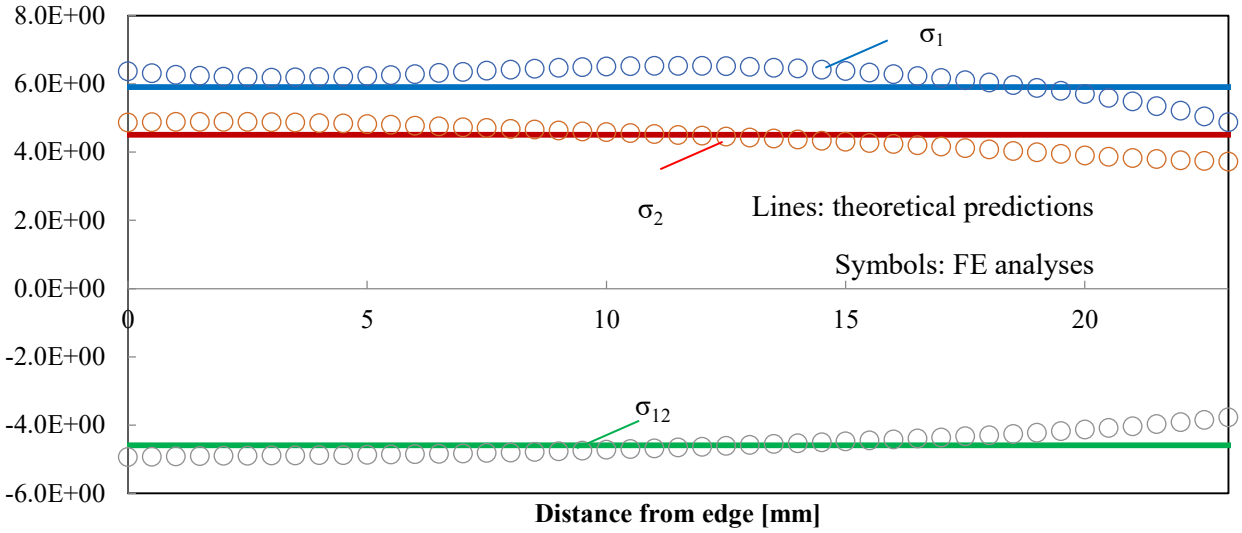
8.0E+00
6.0E+00
4.0E+00
2.0E+00
0.0E+00
-2.0E+00
-4.0E+00
-6.0E+00
σ1
σ2
σ12
Lines: theoretical predictions
Symbols: FE analyses
0
5
10
15
20
Distance from edge [mm]


25

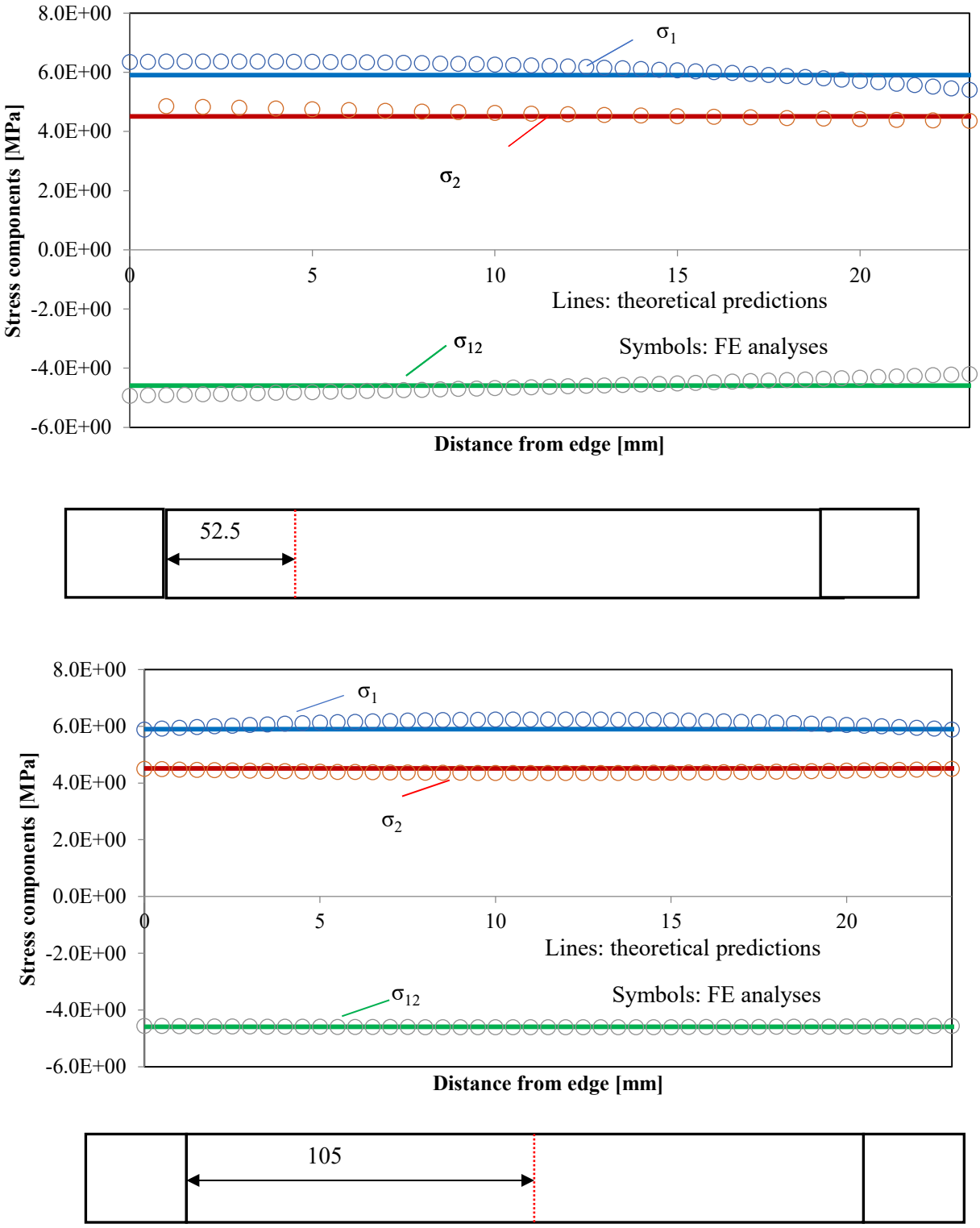

Figure 6.6 Comparison between FE results and theoretical predictions for stresses evaluated along different paths.

As illustrated in Figure 6.6, the values of the stresses do not differ much from the theoretical predictions, particularly in the central part of the specimen far from the tabs, and appear uniform on a wide zone.

The small deviation between the FE results and the values predicted by the classical lamination theory is evident in Figure 6.7, where only the principal stress values obtained by FE analyses included between the theoretical value σ_{th} ±5% ±7% and ±10% are represented. These results confirm that there is a wide central part of the specimens where stresses are uniform and the values of which can be easily predicted by means of the CLT:

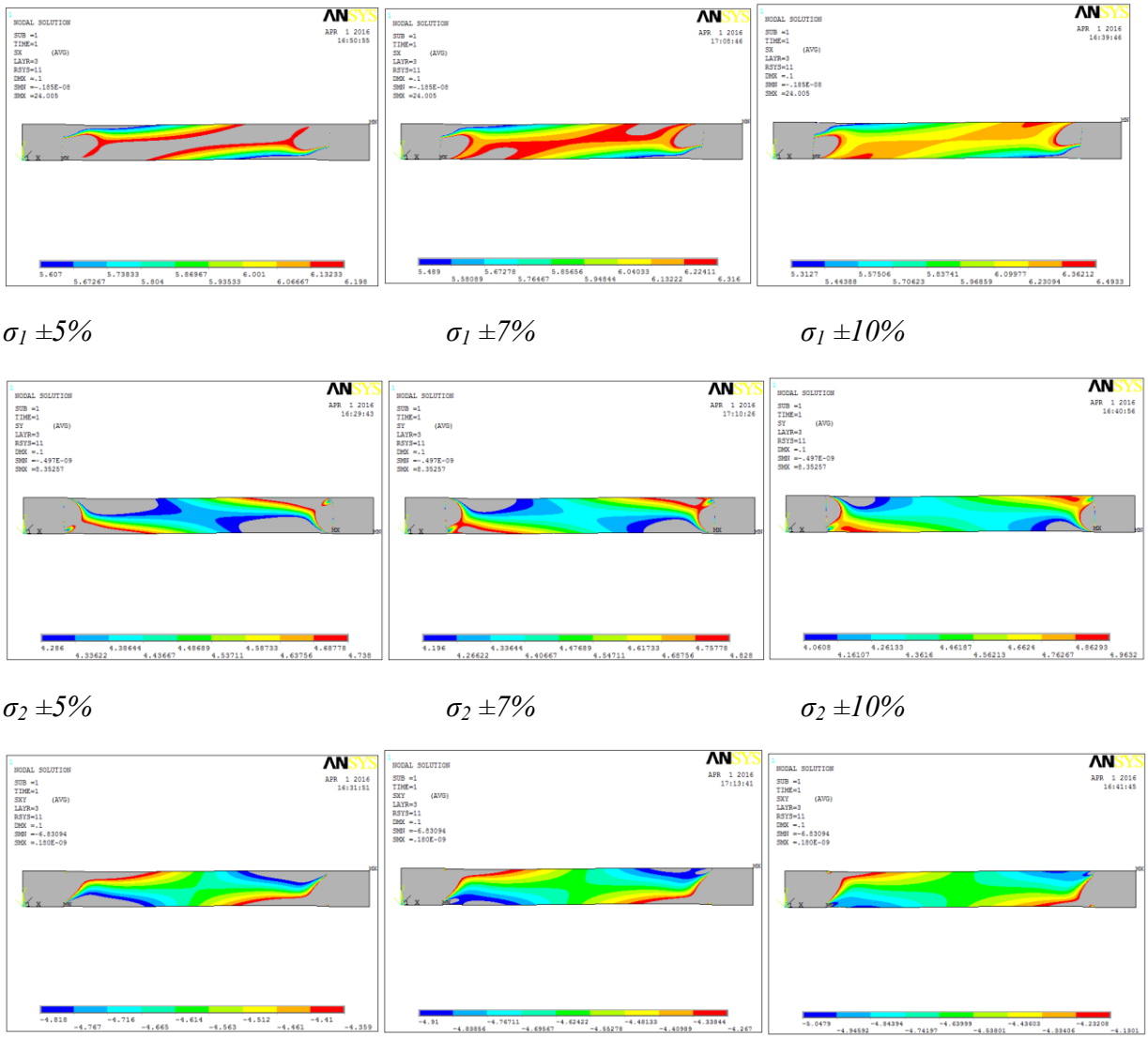

σ_1 ±5% *σ_1 ±7%* *σ_1 ±10%*

σ_2 ±5% *σ_2 ±7%* *σ_2 ±10%*

σ_{12} ±5% *σ_{12} ±7%* *σ_{12} ±10%*

Figure 6.7 Principal stresses determined by a FE analysis, included between the ±5%, ±7% and ±10% of the values theoretically predicted.

6.6 Young's modulus and Poisson's ratio evolution

During the tests conducted on $[0/45_2]_s$ laminates, the variation of the Young's modulus, the Poisson's ratio, the weighted crack density and the delamination ratio were documented. In this section, the curves obtained are presented.

Figure 6.8-Figure 6.13 show the results obtained for the tests performed respectively with a maximum stress of 110 MPa, 120 MPa and 130 MPa. Two tests were conducted for each stress level.

In the figures, the Young's modulus and Poisson's ratio values have been normalized to their initial values.

It is worth to notice that in the Figure 6.10 and Figure 6.13 the crack density was calculated until the condition of saturation was reached; this means that from the interruption of the curve to the final failure of the specimen, where no further points are reported, the crack density values kept unaltered.

By comparing the normalized stiffness with the crack density values, it can be seen that two phases characterize both the curves. In the first, the crack density rapidly increases until reaching a saturation condition. This rapid increase was recorded concurrently with the initial severe drop of the Young's modulus, which, in correspondence of the crack density saturation condition, reached a value that remained almost unaltered until the final failure of the specimen.

In fact, after the crack density saturation, the other damage mechanism predominant consists of the formation of delaminations. However, this phenomenon had a small influence on the stiffness drop. A similar trend for the Young's modulus was already observed also for cross-ply laminates, subjected to tensile-tensile loading.

The Poisson's ratio shows a peculiar trend, increasing in the very first cycles of fatigue life, and then decreasing until leveling off. The trend of the curve is still object of study, since there are

discrepancies with results of FE analyses, which predict an increase of the Poisson's ratio with the increase of crack density and formation of delamination.

Table 6.2 lists all data relative to the number of cycles at which delaminations were seen to occur, the crack density saturation, number of cycles at which specimens failed. Furthermore, it reports also the amount of stiffness drop registered until the crack density saturation and the stiffness drop due to delamination propagation. By comparing the two data for each test, it is evident that stiffness loss is due prevalently to the matrix cracking.

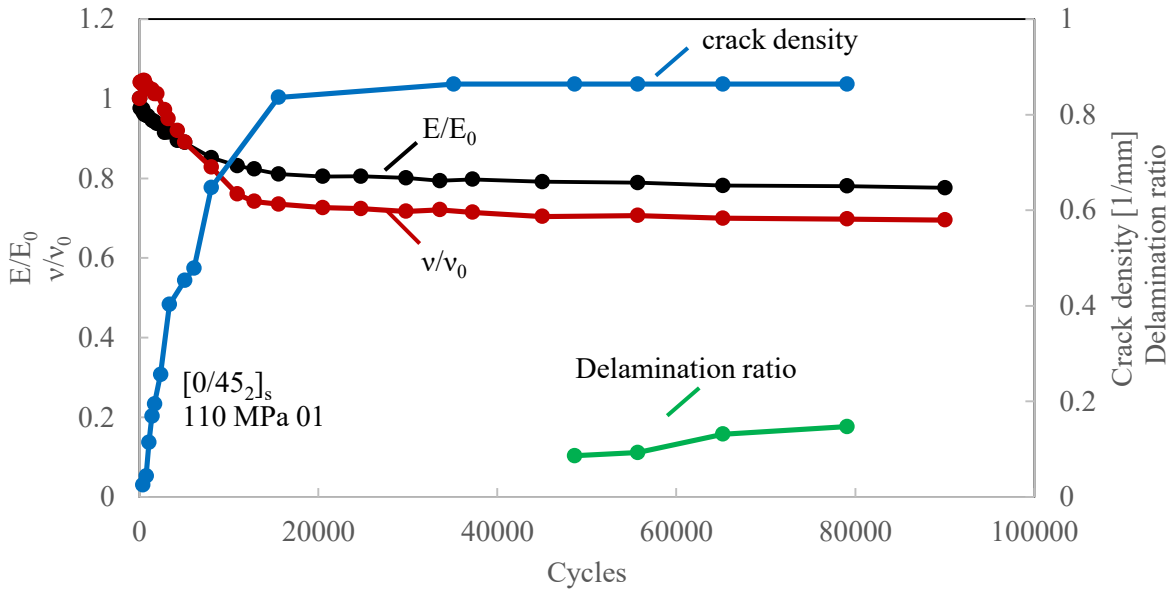

Figure 6.8 Young's modulus, Poisson's ratio, crack density and delamination ratio for [0/45]s laminate subjected to a σ_{max}=110 MPa, test 01

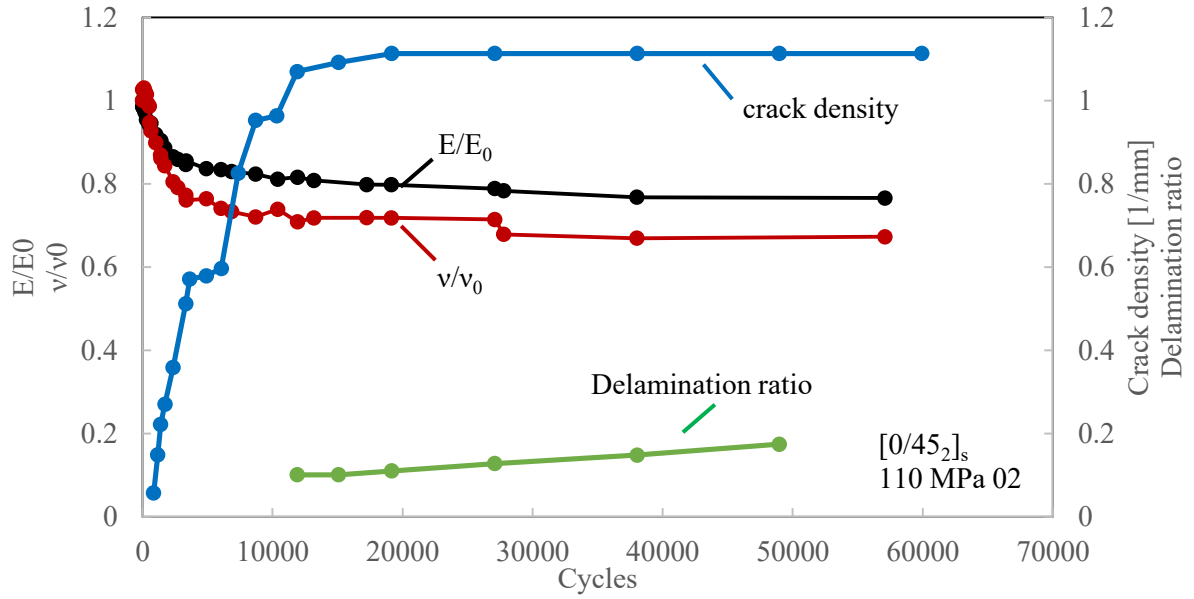

Figure 6.9 Young's modulus, Poisson's ratio, crack density and delamination ratio for [0/45]s laminate subjected to a σ_{max}=110 MPa, test 02

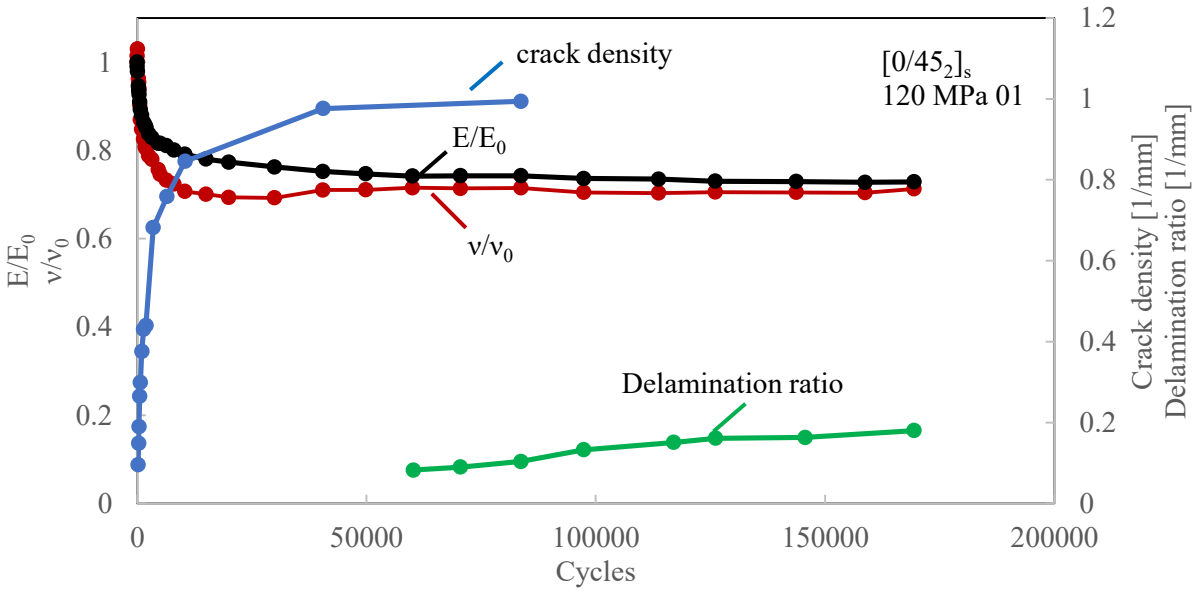

Figure 6.10 Young's modulus, Poisson's ratio, crack density and delamination ratio for [0/45]s laminate subjected to a σ_{max}=120 MPa, test 01

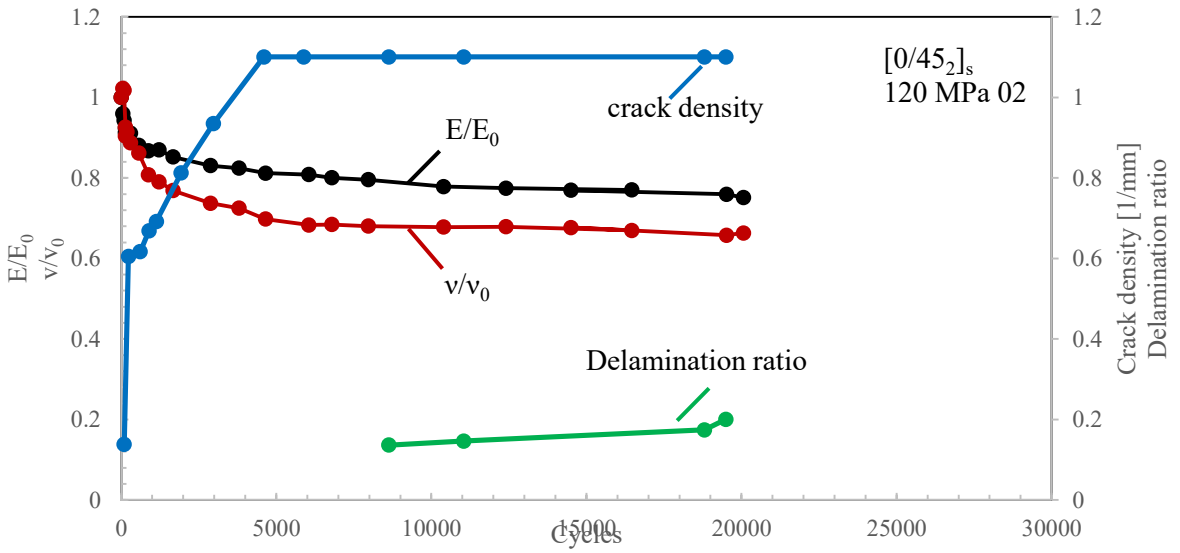

Figure 6.11 Young's modulus, Poisson's ratio, crack density and delamination ratio for [0/45]s laminate subjected to a σ_{max}=120 MPa, test 02

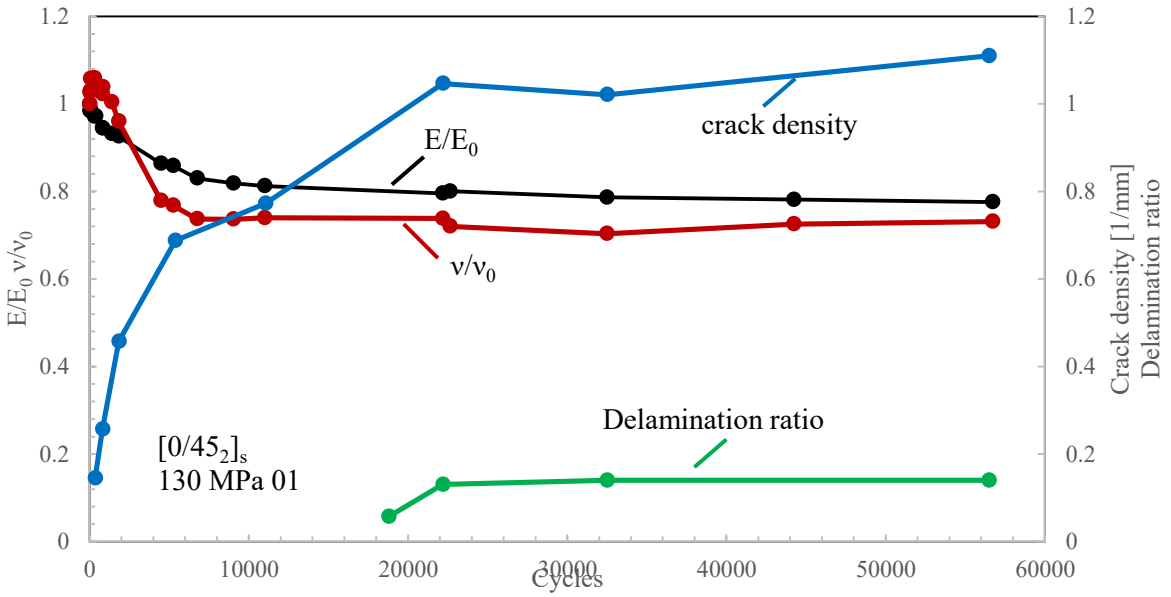

Figure 6.12 Young's modulus, Poisson's ratio, crack density and delamination ratio for [0/45]s laminate subjected to a σ_{max}=130 MPa, test 01

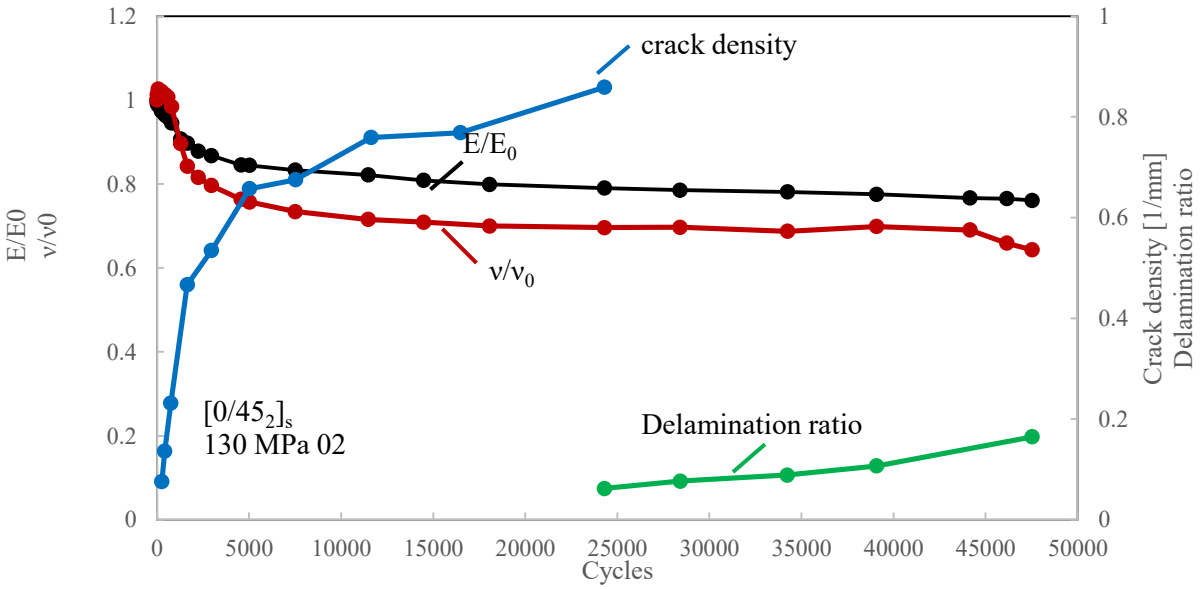

Figure 6.13 Young's modulus, Poisson's ratio, crack density and delamination ratio for [0/45]s laminate subjected to a σ_{max}=130 MPa, test 02

Table 6.2 Experimental data

Maximum stress σmax [MPa]	Number of cycles for delamination onset	Number of cycles for crack density saturation	Number of cycles for final failure	Stiffness drop due to transverse cracks [%]	Stiffness drop due to delaminations [%]
110 MPa 01	8035	35109.5	94821	0.20626	0.017426
110 MPa 02	3333	19159	59913	0.202568	0.031654
120 MPa 01	6509	83709	171406	0.285014	0.011038
120 MPa 02	1131	4598	26694	0.187932	0.060909
130 MPa 01	1837	22185	59660	0.204429	0.019684
130 MPa 02	5022	24295	47812	0.178395	0.060733

6.7 Damage evolution for $[0/45_2]_s$ laminates

By collecting and comparing micrographs taken at different moments during fatigue life, the progressive damage development has been monitored and documented, as already been mentioned. In this section, the results obtained from the image analysis are shown.

The $[0/45_2]_s$ lay-up was selected because of the presence of a reduced number of interfaces (just two between the 0° and 45° layers). This simplifies the visual identification of the formation of damage mechanisms and avoids misunderstandings of which interface is delaminating.

Damage development is illustrated in Figure 6.14. In the left-hand side of the figure, the photograph of the frontal side of the specimen is reported together with an arrow. This indicates the point on the edge where the micrograph has been taken, reported on the right-hand side of the figure.

Damage evolution can be summarized as follows: first transverse cracks form and develop through the thickness of the 45° ply, reaching the interface shared with the 0° ply. As soon as transverse cracks approach to the interface, these deviate, originating the initial delaminations. By increasing the number of cycles, delaminations grow along the interface, while the first fibre breaks are seen to form in the 0° ply, in the proximity of the delamination tips.

Matrix crack induced delaminations can be grouped into two categories: interior delaminations and edge delaminations. Generally, it was seen that delaminations initiate at the edges, heavily influenced by the stresses arisen at the laminate free edge, while in the late fatigue life uniformly grow across the width of the specimens. The distinction in separate categories is important and must be considered to fully understand the next sections of the work. In fact, the two types of delaminations have been analyzed adopting different approaches.

(a)

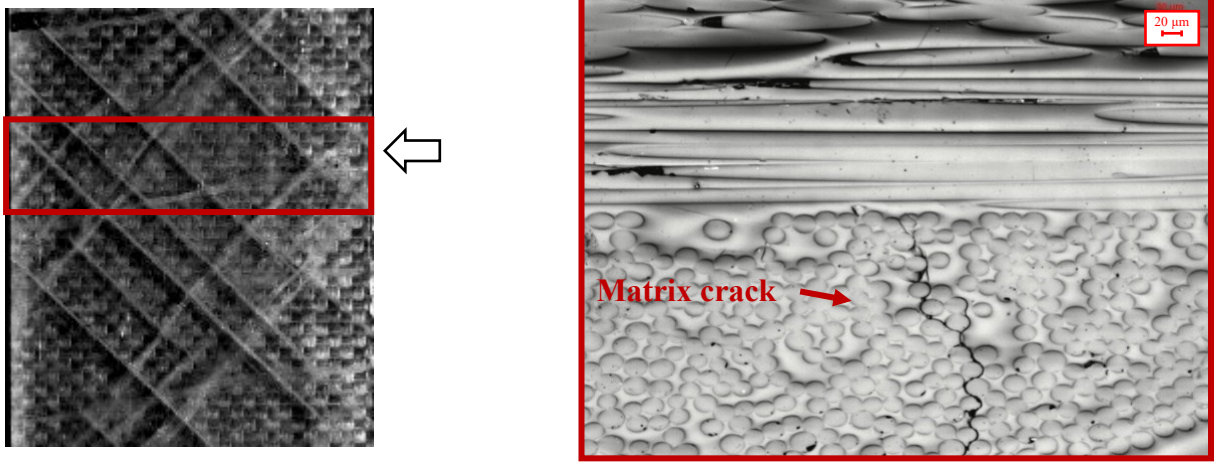

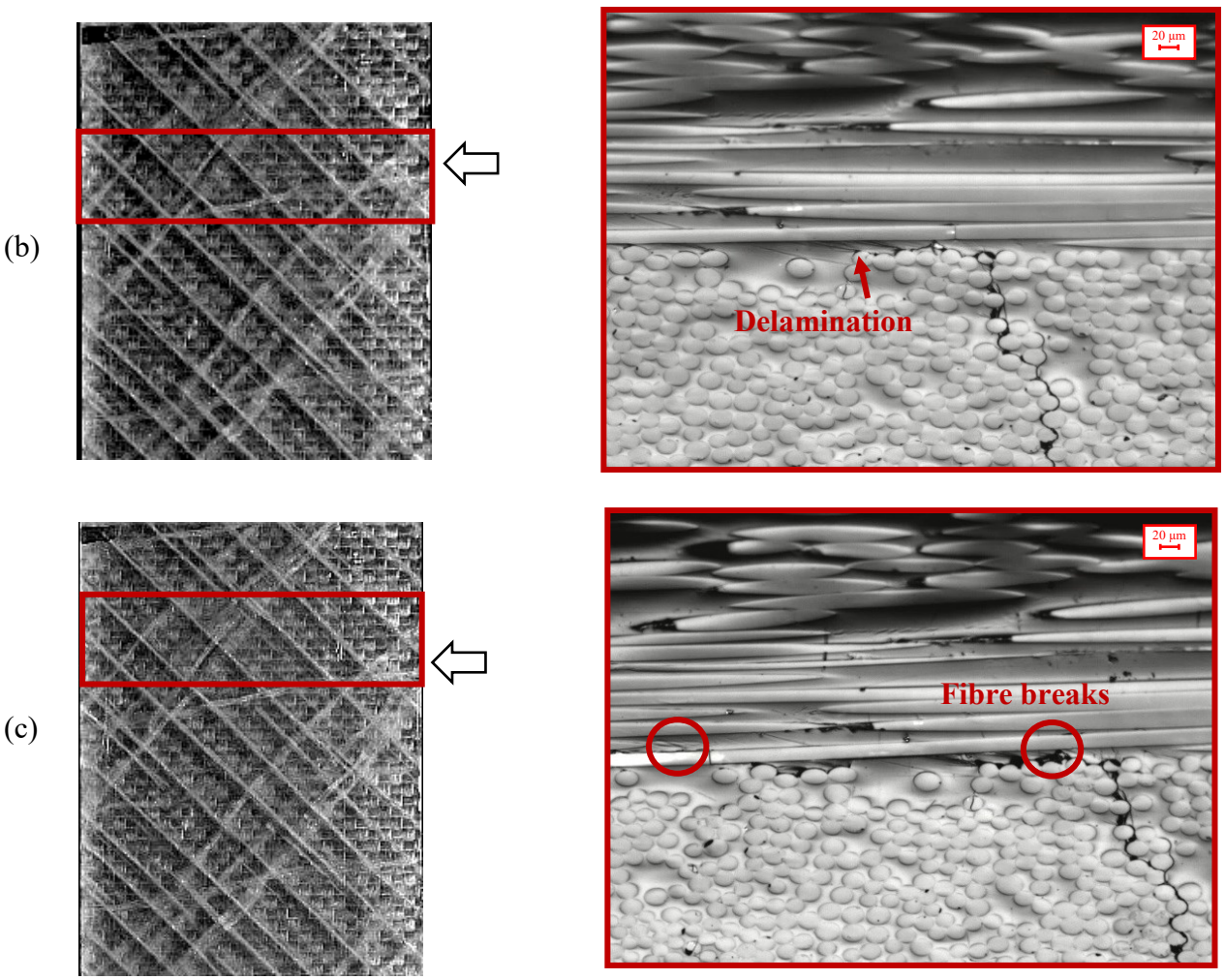

Figure 6.14 Damage development observed in $[0/45]_s$ specimen fatigue tested with a σ_{max}=130 MPa. Images were taken respectively after a) 353 cycles, b) 817 cycles and c)1817 cycles.

Summarizing, the microscopic observations realized suggest that the phases that characterize the damage evolution for the four laminates are three: the formation of transverse cracks, the onset and propagation of delaminations, followed by the breakage of the fibres of 0° layers. The same phases were observed to occur for the damage development of cross-ply laminates, as described in the previous chapters.

6.8 Paris like curve

In analogy with the procedure adopted for cross-ply laminates, a Paris like curve relating the growth rate of delaminations for $[0/45_2]_s$ with the ERR was determined. In this section first the FE model used and results obtained are described.

6.8.1 FE model

In order to evaluate ERR associated with the delamination growth, 3D finite element models were developed using the Ansys code. A unit cell of the laminate was individuated, and modelled using 20 node solid elements (SOLID 186). The size of the element used was of 30μm. This dimension was chosen as the compromise between a mesh resulting not too raw and a size that allows the convergence of the ERR components. In fact, when dealing with bi-material interface problems, the stress fields near the crack tip have oscillatory nature and this may prevent the converge of ERR components.

However, Sun and Jih [16] reported that the region interested by the oscillatory perturbation of the stress field is very small and therefore if the element size at the crack tip is larger than this region, the G_I and G_{II} components are almost constant and may be used for practical purposes.

The size was chosen after performing a preliminary investigation of mesh sensitivity for the geometry and materials under analysis.

To simplify the modelling procedure and reduce the calculation time, it was decided to take into account only the growth of delaminations developed in the central area of the specimens, far from the free edges. Boundary conditions were applied as follows: symmetry conditions were applied on the plane z=0, periodic boundary conditions were applied on the opposite uncracked faces while cracked faces were left free of constraints.

The elastic properties of the material used are reported in

Table 6.3.

Table 6.3 Elastic properties

E_1=48000 MPa
E_2=E_3=14000 MPa
G_{12}=G_{13}=5200 MPa
ν_{12}=0.308
ν_{23}=0.4

The mode I, mode II and mode III components of the ERR associated with the propagation of the delamination, (G_I, G_{II} and G_{III}), were calculated by using the VCCT. The approach calculates the ERR components starting from the nodal displacements and forces in the proximity of the crack tip as shown in Figure 6.15. The equations are reported as following:

$$G_I = -\frac{1}{2\Delta A}\left[\frac{1}{2}Z_{Ki}\left(w_{Kl}-w_{Kl^*}\right)+Z_{Li}\left(w_{Ll}-w_{Ll^*}\right)+Z_{Lj}\left(w_{Lm}-w_{Lm^*}\right)+\frac{1}{2}Z_{Mi}\left(w_{Ml}-w_{Ml^*}\right)\right] \quad (2)$$

$$G_{II} = -\frac{1}{2\Delta A}\left[\frac{1}{2}X_{Ki}\left(u_{Kl}-u_{Kl^*}\right)+X_{Li}\left(u_{Ll}-u_{Ll^*}\right)+X_{Lj}\left(u_{Lm}-u_{Lm^*}\right)+\frac{1}{2}X_{Mi}\left(u_{Ml}-u_{Ml^*}\right)\right]$$

$$G_{III} = -\frac{1}{2\Delta A}\left[\frac{1}{2}Y_{Ki}\left(v_{Kl}-v_{Kl^*}\right)+Y_{Li}\left(v_{Ll}-v_{Ll^*}\right)+Y_{Lj}\left(v_{Lm}-v_{Lm^*}\right)+\frac{1}{2}Y_{Mi}\left(v_{Ml}-v_{Ml^*}\right)\right]$$

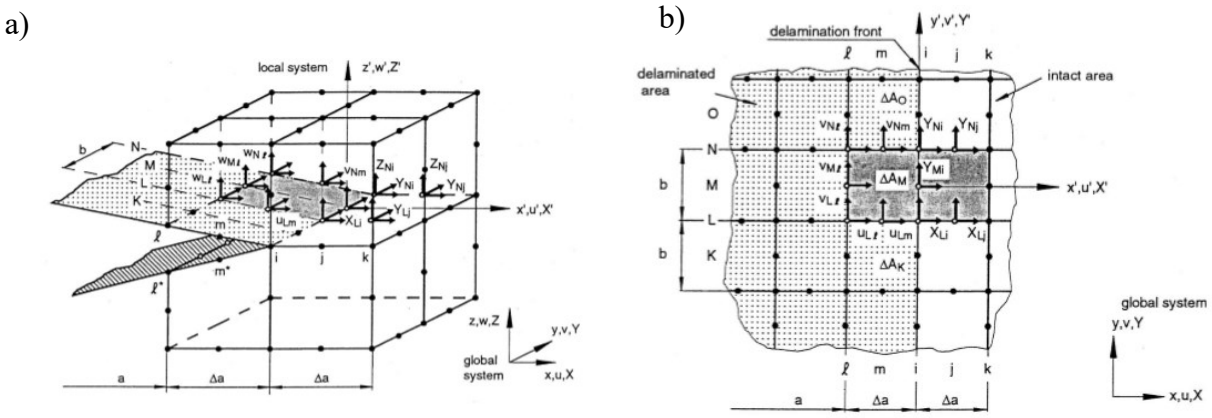

Figure 6.15 Virtual crack closure technique for 20 node elements a) 3D view and b) top view (from [17])

The data relative to the propagation phase of delaminations were described by means of a power law correlating the crack growth rate data with the total ERR.

$$\frac{dL_{del}}{dN} = C G_{tot}^{n} \qquad (3)$$

It is worth mentioning that the values of the Mode I component of ERR were negligible or null for the length of the analyzed delaminations. Therefore, the sum of the components G_{tot} is totally composed by the Mode II and Mode III components such as it can be asserted that the delamination propagation is mostly driven by the shear components of ERR.

An analysis of the variation of the ERR value dependent on the crack density and delamination length will be reported in Chapter 7.

6.8.2 Results

The equivalent delamination area was calculated by dividing the delamination ratio by the crack density values. Then, the delamination growth rate values were assessed by the incremental

polynomial method, indicated in the normative ASTM E-647-00. By combining the growth rate data with the ERR values, the Paris like curve was obtained.

Data collected from all experiments carried out on $[0/45_2]_s$ glass epoxy laminates are reported in Figure 6.16.

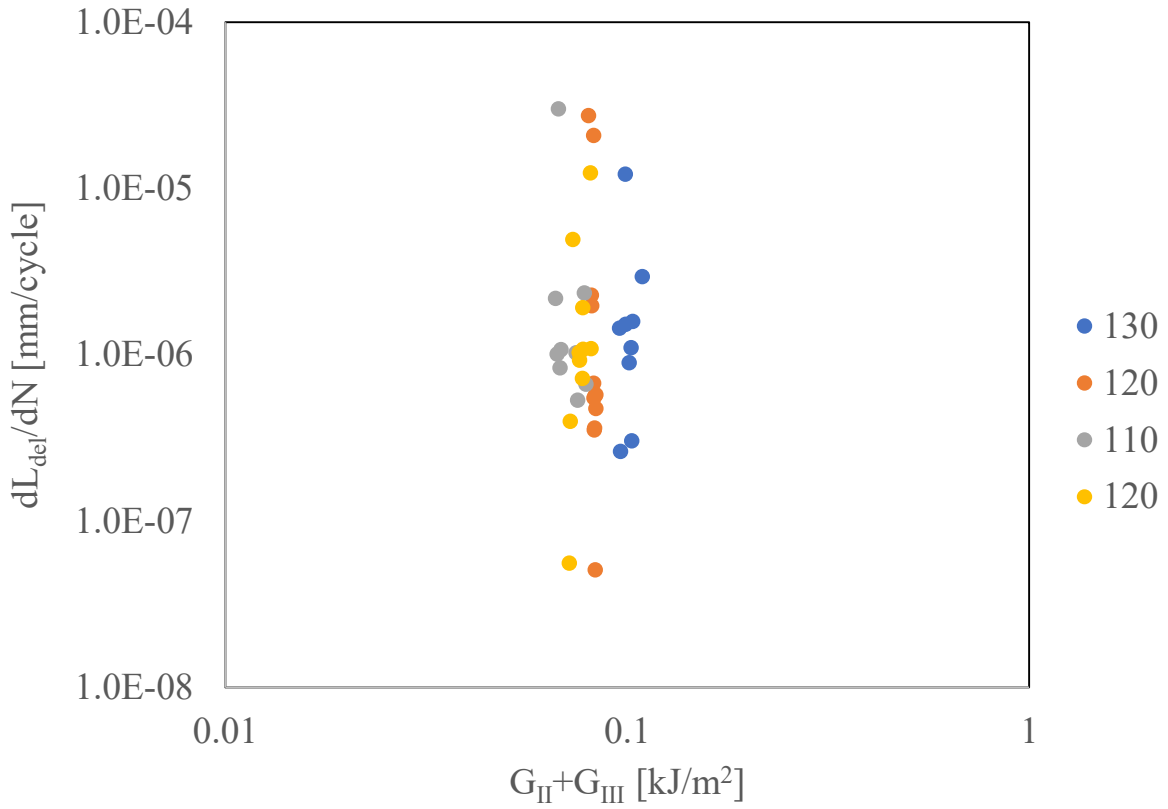

Figure 6.16 Paris like curve for $[0/45_2]_s$ laminates relating the delamination growth rate with the sum of G_{II} and G_{III}

It is evident that the use of a Paris like curve does not describe in a proper way the propagation of delaminations for these laminates. This apparent lack of correlation can be attributed to two factors: the limited growth of delaminations observed and to the procedure of considering an average delamination area starting from each transverse crack, used then for calculating an equivalent delamination length.

In fact, differently from the case of cross-plies, for which the use of a Paris like curve was found to be effective for describing the delamination propagation, delamination areas determined for $[0/45_2]_s$

laminates were limited, reaching maximum values of delamination ratio around 0.3, and the propagation occurred very slowly, almost imperceptible.

Furthermore, since the procedure takes into account the propagation of an average equivalent delamination, even if experimentally it was observed that some transverse cracks induced the growth of relevant delaminations at the interface, the determination of the average delamination distributed the increment of the delamination area between all the cracks, resulting in a small average growth.

6.8.3 Alternative approach based on the S_1

In accordance with the procedure adopted for cross-plies, the propagation of delaminations was modelled following a different approach, based on the determination of the average first principal stress S, calculated in the proximity of the delamination tip. A schematic of the model used is represented in Figure 6.17. A resin rich region was modelled at the interface shared between the 0° and 45° plies. The properties used are the one typical of epoxy matrix E=3500 MPa and ν=0.3.

A unit cell was modelled, imposing periodic boundary conditions on the opposite sides not interested by cracks and leaving the crack faces free of constraints. Symmetry conditions were applied on the z=0 plane. A process zone was defined in the vicinity of the delamination tip, with a thickness of 0.01 mm and a width of 0.054mm (~3 diameter of a fibre), always in accordance with the analysis performed for cross-ply laminates. This region was defined for then calculating the average 1st principal stress correspondent to a certain damage scenario, i.e. crack spacing and delamination length.

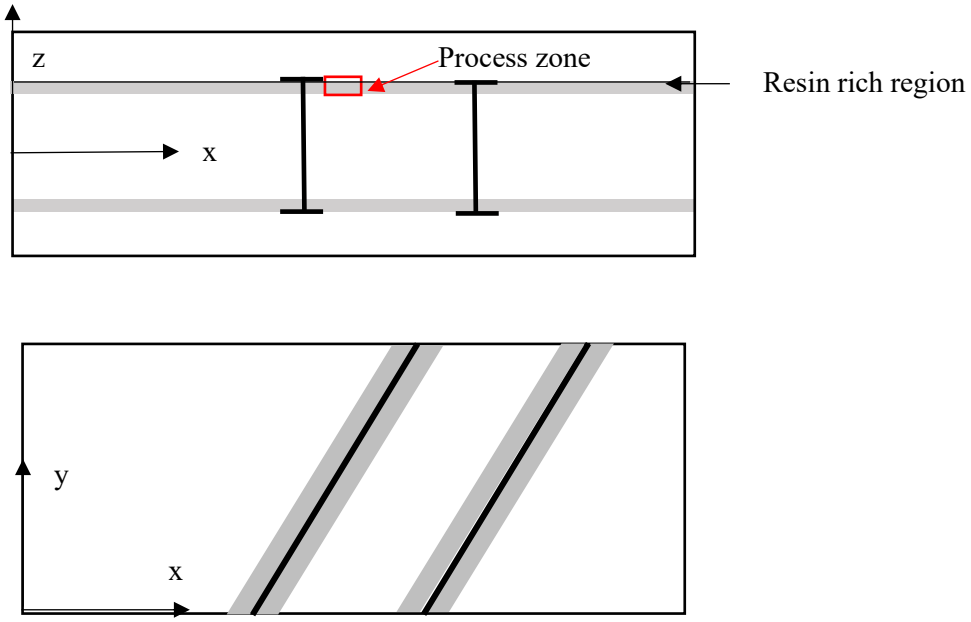

Figure 6.17 Schematic of the damaged laminate

Thus, the data relative to the delamination length growth were re-analyzed and related to the average values of 1st principal stress. The resultant Paris-like curve is shown in Figure 6.18. By observing the figure, it is evident that the scatter is so large that that this approach does not allow to describe effectively the delamination propagation for these laminates. The main reason, as already explained in the case of Paris like curves relating the delamination growth rate with the ERR, is the scarce propagation of delamination for the lay-up tested ($[0/45_2]_s$), which makes difficult to make reliable measurements of delamination areas and determine a growth of these.

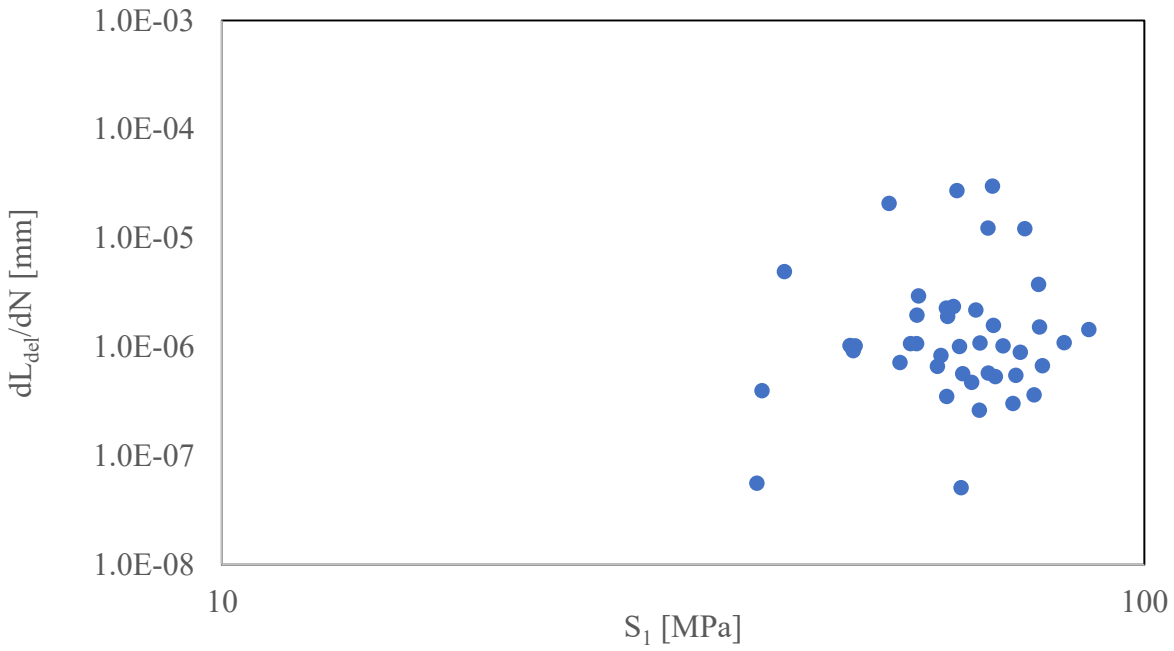

Figure 6.18 Paris like curve for $[0/45_2]_s$ laminates relating the delamination growth rate with the sum of S_1

6.9 Conclusions

In this chapter, the results of an experimental campaign conducted both on balanced and unbalanced laminates are presented. Tensile-tensile fatigue tests were performed with the aim of investigating damage evolution, dedicating particular attention to the delamination formation induced by the presence of matrix cracks. Damage evolution was monitored during the entire fatigue life of specimens and the fracture events sequence was determined by comparing the photographs, taken from the frontal side of the damaged coupons, with the optical micrographs of the edges.

Finally, the experimental data of the delamination growth, collected from the tests performed on $[0/45_2]$ glass epoxy laminates, were analyzed. In agreement with the activity conducted on cross-ply laminates, the process of growth was described by means of a Paris-like curve, relating the growth rate both with ERR and with the average value of principal stress, calculated within a process zone in the closeness of the delamination tip.

Unlike the research carried out in cross ply laminates, the Paris like curve failed to predict in a satisfactory way the delamination growth, due possibly to the limited growth of delaminations. New configurations of test should be designed to promote the delamination growth. These topics are deferred to future works.

References of chapter 6

[1] Berthelot, Jean-Marie. "Transverse cracking and delamination in cross-ply glass-fiber and carbon-fiber reinforced plastic laminates: static and fatigue loading." Applied Mechanics Reviews 56.1 (2003): 111-147.

[2] Pagano, N. J., and G. A. Schoeppner. "Delamination of polymer matrix composites: problems and assessment." Comprehensive composite materials 2 (2000): 433-528.

[3] Reifsnider, K. L., and A. Talug. "Analysis of fatigue damage in composite laminates." International Journal of Fatigue 2.1 (1980): 3-11.

[4] Kress, Gerald R., and W. W. Stinchcomb. "Fatigue response of notched graphite/epoxy laminates." Recent Advances in Composites in the United States and Japan. ASTM International, 1985

[5] Murri, Gretchen B., Satish A. Salpekar, and T. Kevin O'Brien. "Fatigue delamination onset prediction in unidirectional tapered laminates." Composite Materials: Fatigue and Fracture (Third Volume). ASTM International, 1991.

[6] Crossman, F. W. and Wang, A. S. D,, "The Dependence of Transverse Cracking and Delamination on Ply Thickness in Graphite/Epoxy Laminates," Damage in Composite Materials, ASTMSTP 775, K. L. Reifsnider, Ed., American Society for Testing and Materials, 1982, pp. 118-139.

[7] O'Brien, T.K. and Hooper, S.J. "Local delamination in laminates with angle ply matrix cracks, part I: tension tests and stress analysis", Composite Materials: fatigue and fracture, Fourth Volume, ASTM STP 1156, W.W. Stinchcomb and N.E. Ashbaugh, Eds., American Society for Testing and materials, Philadelphia, 1993, pp.491-506.

[8] O'Brien, T.K., "Local delamination in laminates with angle ply matrix cracks, part II: Delamination Fracture analysis and fatigue characterization.", Composite Materials: fatigue and fracture, Fourth Volume, ASTM STP 1156, W.W. Stinchcomb and N.E. Ashbaugh, Eds., American Society for Testing and materials, Philadelphia, 1993, pp.507-538.

[9] Salpekar, Satish Annaji, and T. Kevin O'Brien. "Combined effect of matrix cracking and free edge on delamination." *Composite Materials: Fatigue and Fracture (Third Volume)*. ASTM International, 1991.

[10] Salpekar, Satish A., T. Kevin O'Brien, and K. N. Shivakumar. "Analysis of local delaminations caused by angle ply matrix cracks." *Journal of Composite Materials* 30.4 (1996): 418-440.

[11] Johnson, Patrick, and Fu-Kuo Chang. "Characterization of matrix crack-induced laminate failure—Part I: Experiments." *Journal of composite materials* 35.22 (2001): 2009-2035.

[12] Johnson, Patrick, and Fu-Kuo Chang. "Characterization of Matrix Crack-Induced Laminate Failure—Part II: Analysis and Verifications." *Journal of composite materials* 35.22 (2001): 2037-2074.

[13] Hallett, Stephen R., et al. "Modelling the interaction between matrix cracks and delamination damage in scaled quasi-isotropic specimens." *Composites Science and Technology* 68.1 (2008): 80-89.

[14] Guillamet, G., et al. "Damage occurrence at edges of non-crimp-fabric thin-ply laminates under off-axis uniaxial loading." *Composites Science and Technology* 98 (2014): 44-50.

[15] Zubillaga, L., et al. "An experimental study on matrix crack induced delamination in composite laminates." *Composite Structures* 127 (2015): 10-17.

[16] Sun, Ch T., and C. J. Jih. "On strain energy release rates for interfacial cracks in bi-material media." Engineering Fracture Mechanics 28.1 (1987): 13-20.

[17] Krueger, Ronald. "Virtual crack closure technique: history, approach, and applications." *Applied Mechanics Reviews* 57.2 (2004): 109-143.

Appendix: Free edge effect on delamination initiation

In this appendix, the issue of the initiation of delaminations starting from the free edges is discussed. In particular, the results of a FE analysis, carried out to detect if delaminations initiated in predefined locations, are presented.

As above described, it is acknowledged that the first damage mechanism for $[0/45_2]_s$ laminates subjected to tensile-tensile fatigue loading consists of the matrix cracking of the 45° plies. Then, delaminations occur starting from the tips of transverse cracks and progressively grow at the interface. Consider a damaged laminate, as schematically represented in Figure A.1. It is possible to define a unit cell, by isolating the volume portion included between two adjacent cracks. 3D finite element analyses were performed modelling the unit cell and using 20-nodes elements (Solid 186).

Symmetric boundary conditions were imposed in correspondence of the z=0 plane and the following periodic boundary conditions at the correspondent nodes of the faces II and III were assigned:

$$\begin{aligned} u_z^{III} - u_z^{II} &= 0 \\ u_x^{III} - u_x^{II} &= \varepsilon_x L \\ u_y^{III} - u_y^{II} &= u_y^{N_{II}} \end{aligned} \qquad \text{(A1)}$$

Node II is free to every constraint, while the displacements of Node I are restrained along the x and z directions ($u_x^{N_I} = u_z^{N_I} = 0$).

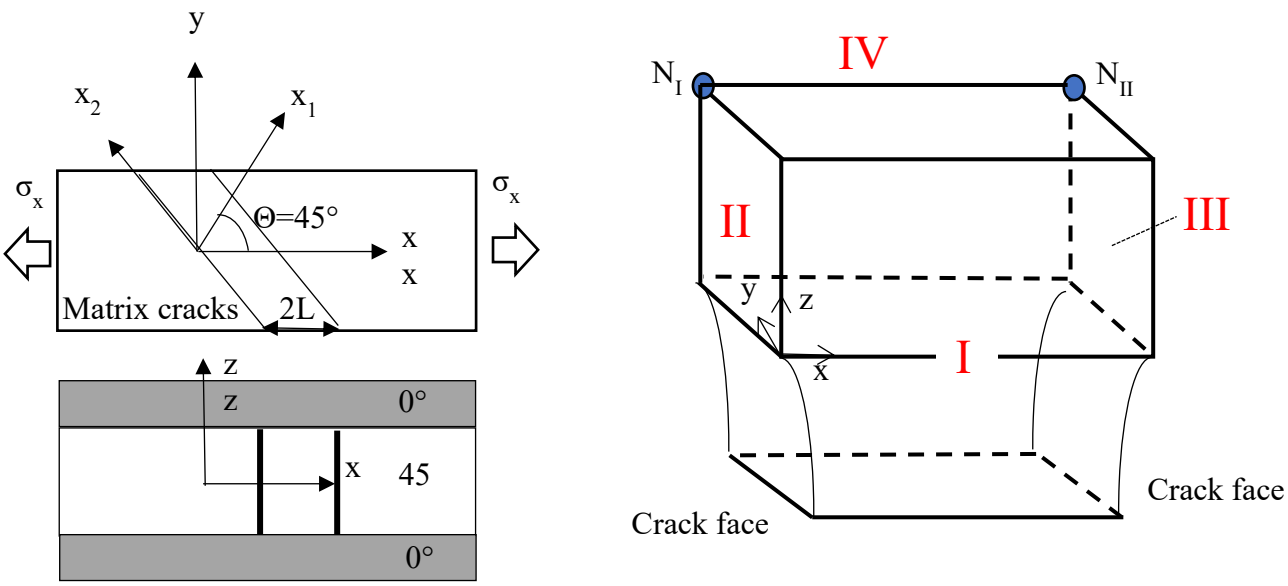

Figure A.1 Schematic of the damaged laminate $[0/45_2]_s$

Stresses were evaluated at the interface 0/45 in the proximity of both crack tips, following two different paths, as shown in Figure A.2. The stresses evaluated along the path traced on the right-hand side of the unit cell are illustrated with empty symbols, while the ones evaluated starting from the left-hand side are represented with filled symbols.

By observing the figure, it is evident that the stresses values are different along the paths and, in particular, given a distance from the matrix cracks, the stress values along the right path are higher than the correspondent values along the left path.

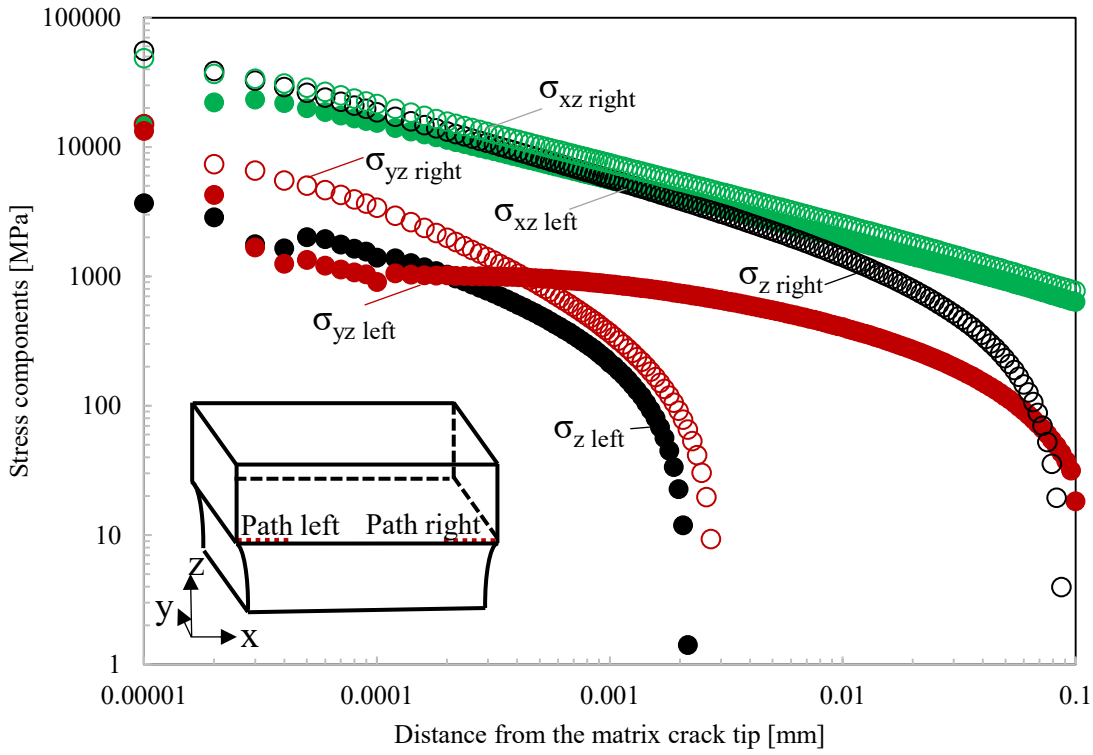

Figure A.2 Stress fields at the interface of [0/45]s

Then, stresses were evaluated along two other paths, this time traced in the central part of the unit cell, far from the free-edges, as shown in A.3. Differently from the former case, given a distance from the matrix cracks, stress values were found equal, regardless the considered path.

The findings of this analysis support the idea that the inequality between the stresses evaluated along the paths on the edges was caused by the presence of edges. This implies that a different behavior of delamination initiation from the edges should be expected, i.e. that in a unit cell delaminations will be more likely to occur in one of the two opposite edges. This statement was found to be consistent with the experimental observation, as documented in Figure A.4. The figure reports the image taken from the frontal side of a $[0/45_2]_s$ specimen. It is evident that delaminations formed preferentially following the so-called path right in correspondence of the free-edges.

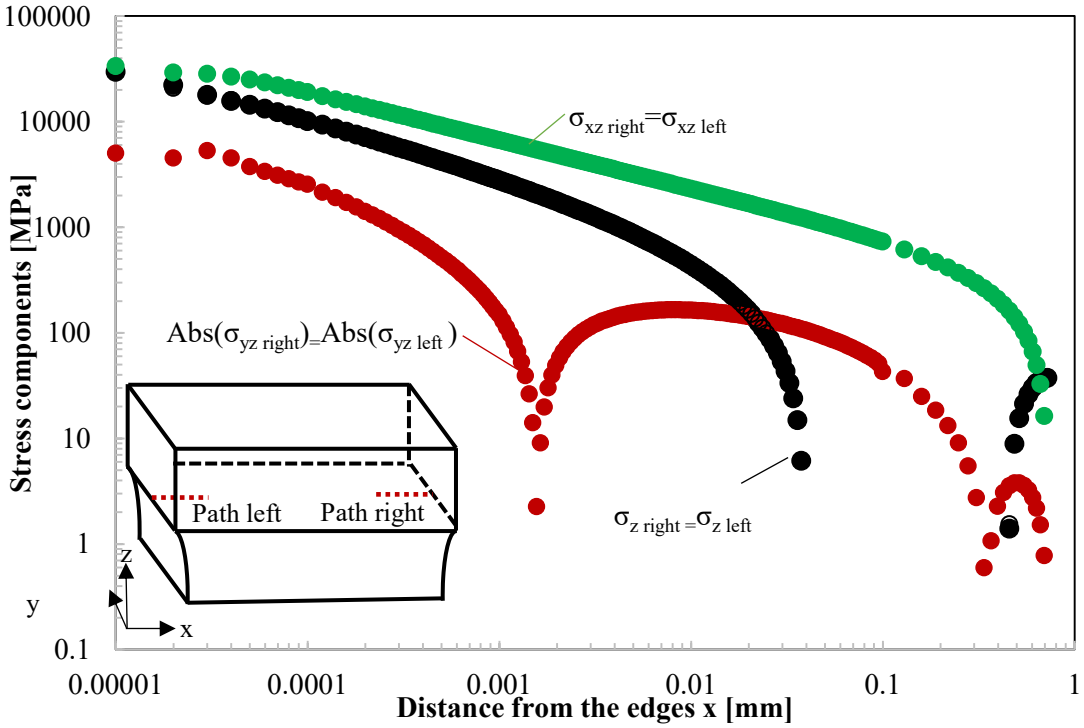

Figure A.3 Stress fields at the interface of [0/45]s

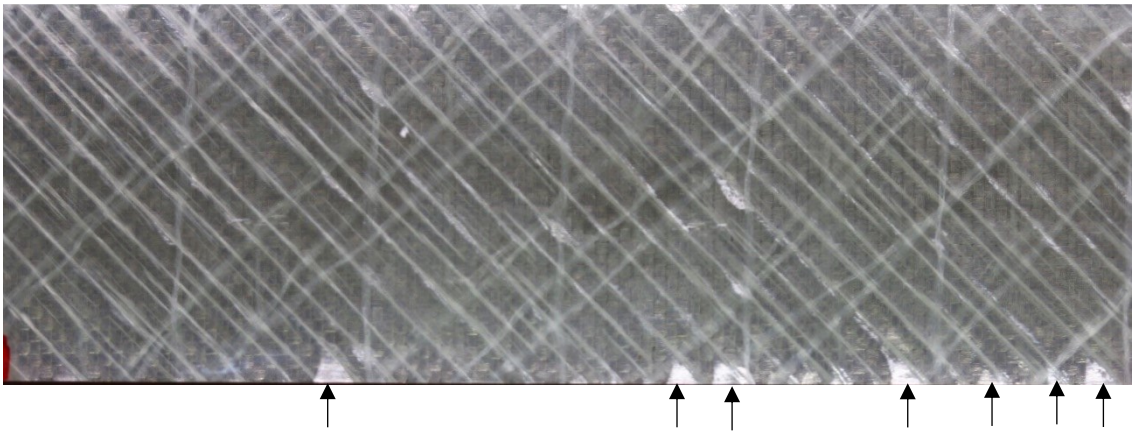

Figure A.4 Image of a damaged $[0/45_2]_s$ laminates. Delaminations started from the edges are indicated with arrows.

7. Angle-ply edge delaminations

7.1 Introduction

As already mentioned in the previous chapters, damage mechanisms of composite laminates can be summarized according to the following points, based on the observations collected from experimental tests:

- **Matrix cracking**: Matrix cracks start forming and progressively accumulate by growing both in length and in number.
- **Matrix crack-induced delaminations**: Delaminations form after matrix cracks approach the interface shared between two adjacent plies.
- **Angle-ply edge delaminations**: Delaminations occur at the free edge of the laminate, particularly in the case of off-axis plies. Usually their extent is limited to the area included between a matrix crack and the laminate free edge.

In the following section, the principal works addressing the problem of angle ply edge delaminations, are presented.

In the literature, both experimental and numerical approaches have been presented.

Bjeletich, Crossman and Warren [3] tested laminates with 0°, 45° and 90° plies, using six different stacking sequences. The authors observed that the tendency to delaminate was dependent on the stacking sequence and that a major propagation of free edge delamination was the cause of a lowered tensile strength.

Similar quasi-static tests were performed by Rodini and Eisenmnann [2] , who observed that additional parameters influencing the formation of edge delamination were the laminate thickness and test temperature. Quasi-static tests were performed on $[\pm 45_n/0_n/90_n]_s$ graphite epoxy laminates, with n=1, 2, 3 and it was observed that the stress at which delaminations initiated, decreased with the increase of n.

Thickness effect on the formation of edge delaminations was also studied by Wang and Crossman [3] . The authors carried out quasi-static tests on $[25/-25/90_n]_s$ laminates and found out that for $n < 3$, delaminations occurred at the edge of the coupon while, for $n > 4$, these formed across the entire width of the coupon, as a consequence of the formation of transverse cracks in the 90° ply.

Moreover, several studies were dedicated to the development of analytical model for the computation of interlaminar stresses. Hayashi [4] proposed a model for angle ply laminates subjected to axial tension. Puppo and Evensen [5] modelled the laminate as a series of anisotropic layers separated by isotropic adhesive layers. By writing four equilibrium differential equations in terms of the displacements and imposing the respect of boundary conditions at the free edges, they determined the expressions of the stresses in terms of hyperbolic functions. This formulation is not exact, but represents a useful approximate theory.

Pipes and Pagano [6] derived the reduced form of the elasticity field equations, for a symmetric laminate under uniform axial strain, and adopted the finite difference method to determine the solutions. In this way, the authors defined the free-edge stress field, concluding that the presence of both interlaminar shear and normal stress was important in causing delamination.

Further studies, aimed at calculating the three-dimensional stresses, were conducted by Tang and Levy [7], and Wang and Crossman [8]. The former authors analytically determined all interlaminar stresses in the proximity of free edges of composite laminates, while the latter were the first to study the free edge problem using quasi three-dimensional finite element method. The stress fields near the edge were obtained for five types of laminates, loaded under uniaxial tension.

In the last years, FE analyses become the favorite method for evaluating intelaminar stresses, thanks to the increase in computational power, see for example [9]-[13].

Salpekar and O'Brien [14] conducted FE analyses to calculate strain energy release rates associated with delaminations formed at the intersection of the matrix crack with the free edge. The authors

studied the stress field and individuated a sharp increase of interlaminar normal stress in the vicinity of the intersection of the matrix crack with the free edge, indicating a potential site for the delamination onset. Fish and O'Brien [15] examined the $[15/90_n/-15]_s$ laminates and similarly concluded that interlaminar tensile stresses, due to the cracking in the 15° layer, played an important role in the process of delamination formation. O'Brien [16] also determined a SERR for edge delamination, including the effect of matrix cracking.

Kashtalyan and Soutis [17] developed a theoretical model to describe the SERR associated with local delaminations, growing from the tips of pre-existing matrix cracks in the mid-layer of a general symmetric laminate loaded in tension.

In this chapter, the numerical modelling activity conducted on generic laminates is presented, particularly aimed at clarifying the role of edges on the delamination formation.

First, a unit cell of a [0/45]s laminate with angle ply edge delaminations was modelled and ERR values were calculated along the delamination front.

Then, a procedure for determining the growth of generic delaminations, where the term generic indicates a growth process where delaminations can develop without being self-similar, was ideated and implemented. The procedure proposed can be used to describe the delamination growth for laminates subjected to quasi-static loading.

Finally, the results of a comparison between the ERR associated with the delamination growth for the unbalanced and balanced laminates are presented.

7.2 Angle-ply edge delamination: FE model

In order to determine ERR values linked with the growth of angle-ply edge delaminations, a FE model ad hoc was developed.

Angle-ply edge delaminations were modelled as triangular shaped, according to experimental observations. The angle formed between the matrix crack plane and the delamination front was set equal to 90°, as shown in Figure 7.1.

FE analyses were carried out with Ansys software package, using 3D 20 node solid elements. The stacking sequence modelled was $[0/45_2]_s$, each ply having a thickness of 0.3 mm.

By using the virtual crack closure technique, the three ERR components were calculated along the delamination front.

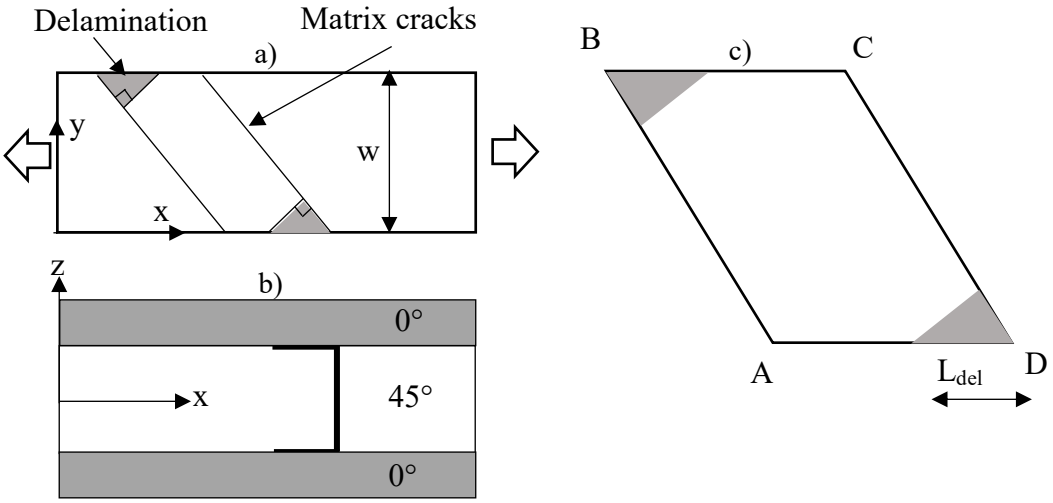

Figure 7.1 Schematic of the FE model: a) top view, b) lateral view and c) unit cell o

Attention was devoted to the mesh construction in the vicinity of the delamination front. The elements dislocated in the immediate proximity of the delamination front were set orthogonal to this, thus satisfying the requirement of orthogonality of the VCCT, and their size was equal to 30 μm.

A unit cell was individuated within the laminate, isolating the portion of the laminate included between two adjacent cracks, as illustrated in Figure 7.1.

Nodes of the AB segment were constrained with the correspondent node of the segment CD through periodic boundary conditions, while the segments AD and BC, correspondent to the free edges, were left free from constraints. The unit cell was subjected to a uniform strain equal to 0.1 along the x direction. In the figure, w indicates the width of the specimen, equal to 23 mm. Only the superior half of the laminate was modelled, by virtue of the symmetric nature of the problem, and symmetry boundary conditions were applied on the z=0 plane.

ERR values were calculated along the front of the delamination terminating at the free edge AD. In order to analyze how ERR values vary with the extent of the delaminations, different analyses were performed. The delamination area was assumed to propagate similarly to itself, i.e. maintaining unaltered the angles formed between the delamination front and, respectively, the matrix crack plane and the free edge. Results are reported in Figure 7.2 and Figure 7.3. In order to compare different delamination areas, the x-axis indicates the distance from the free edge of the node, for which ERR has been calculated, normalized to the length of the entire front. Different curves refer to different ratios of delamination front length to crack spacing.

The Mode I component of ERR is not reported in the graphs, since its value was found equal to zero or negligible compared to the other components for the values of delamination areas analyzed.

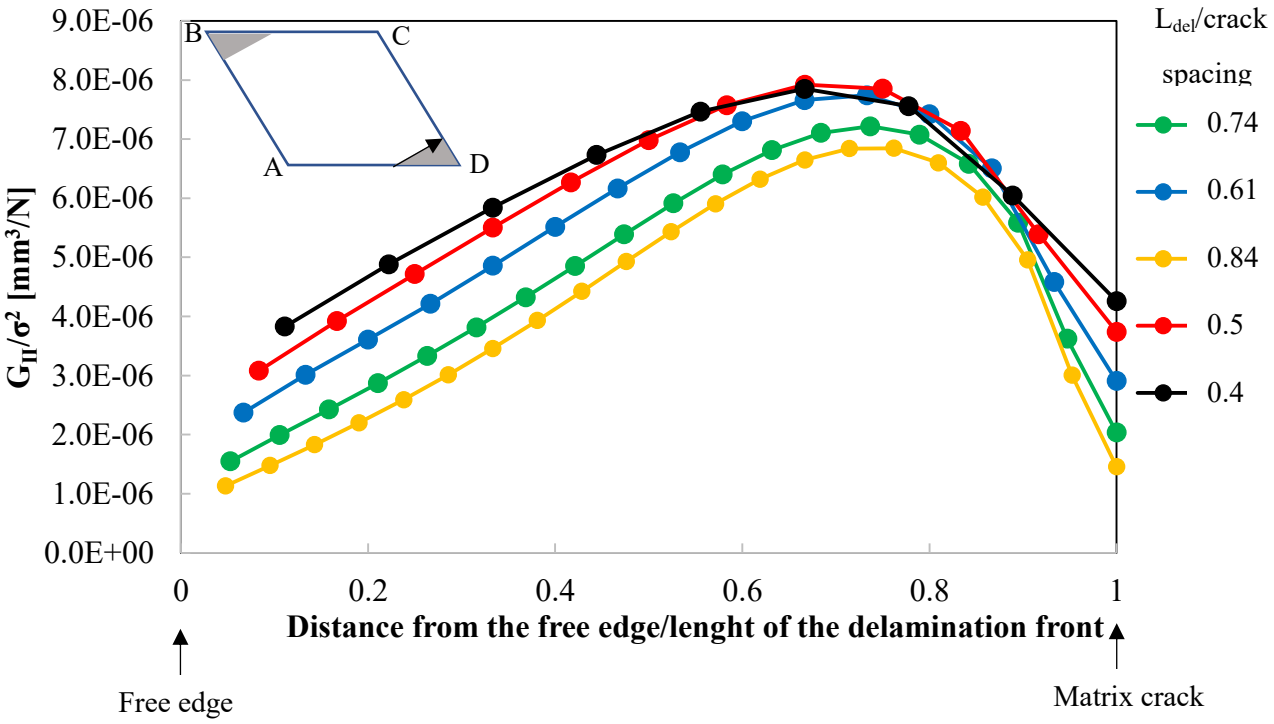

Figure 7.2 Distribution of mode II component of ERR along the delamination front

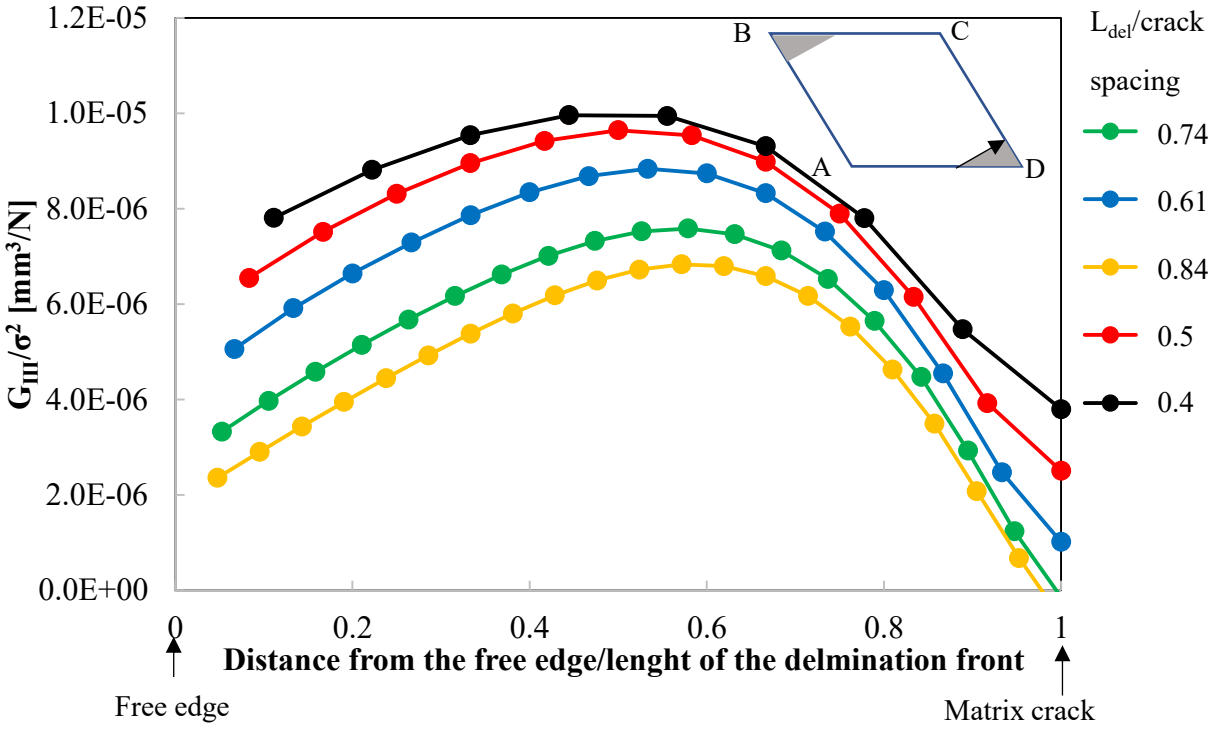

Figure 7.3 Distribution of mode III component of ERR along the delamination front

The ERR distribution along the delamination profile is non-uniform. This result seems to indicate that the original delamination shape may change during fatigue life. With the aim of better understanding the initial phases of evolution of delaminations, further analyses were conducted, modelling small delamination areas (L_{del}/crack spacing=0.2 and 0.3). The resultant ERR components are represented in Figure 7.4. Differently from the cases analyzed before, the Mode I component G_I was found to have an important role in the propagation of small delamination: near the matrix crack apex it reaches the peak value and then gradually lowers moving towards the free edge. However, moving away from the matrix crack, G_{II} and G_{III} become prevalent. This suggests that the growth of edge delaminations is mostly driven by the shear components, but in the proximity of a matrix crack the damage scenario changes and the propagation is driven in a mixed mode configuration where the mode I component plays a significant role.

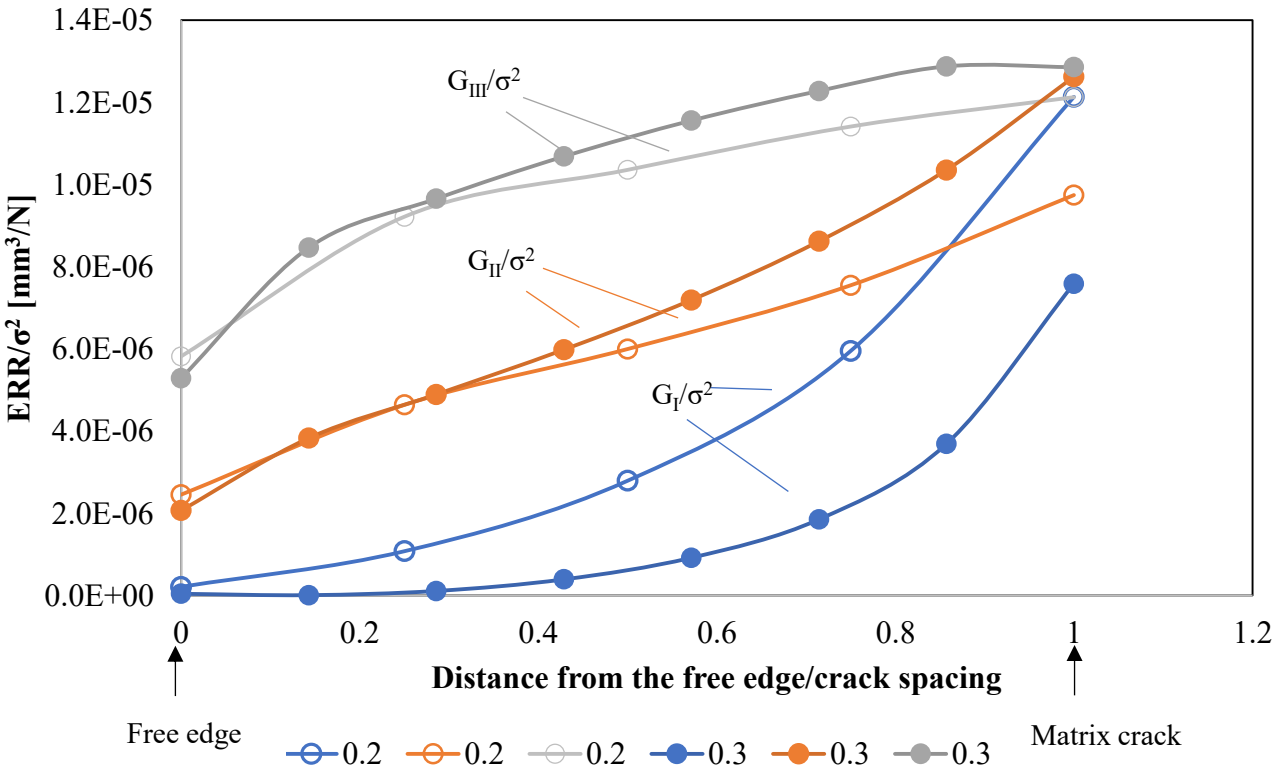

Figure 7.4 ERR distribution along the delamination front

7.3 Simulation of delamination growth

Based on the experimental observations, it was assumed that angle-ply edge delaminations developed respecting the conditions of similarity, i.e. keeping unaltered their form. However, as shown in the previous section, ERR values were found to be nonconstant along the delamination front, suggesting that the initial shape may change.

In this paragraph, a procedure for simulating the progressive propagation of delamination induced by matrix cracks is presented. This approach is valid for describing the delamination growth only under quasi-static loading.

Initially, a laminate interested by a single crack in the off-axis ply was modelled. FEA was performed, simulating the presence of an early delamination (one element long), at the tip of the crack. This was necessary to evaluate the ERR components, since the application of the VCCT requires an initial delamination.

G_I, G_{II} and G_{III} were evaluated for each element along the delamination front, by using the VCCT.

A fracture criterion was then defined to determine the growth of the delamination front. It was assumed that failure occurred when the following linear correlation between all the components of ERR was equal or higher than 1:

$$\frac{G_I}{G_{Ic}} + \frac{G_{II}}{G_{IIc}} + \frac{G_{III}}{G_{IIIc}} > 1 \qquad (1)$$

The stress level was increased until the fracture criterion was satisfied for one element at least. Then for those elements, delaminations were extended, and a new FE analysis, with the updated delamination area, was run. The whole procedure is schematized in Figure 7.5.

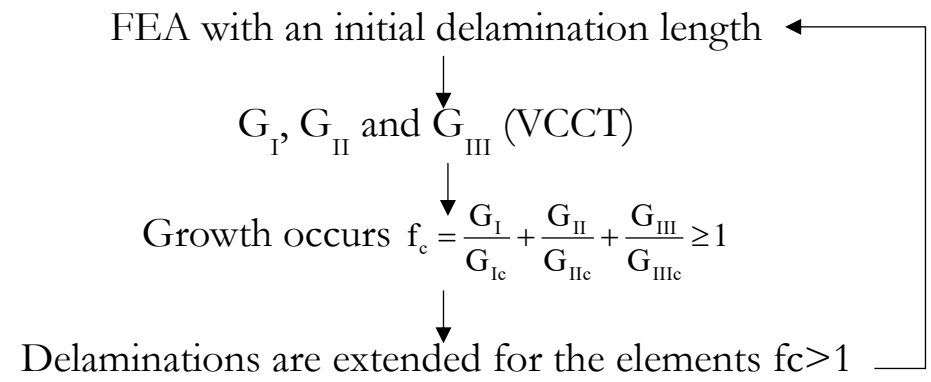

Figure 7.5 Algorithm for the assessment of delamination evolution

7.3.1 Algorithm for the assessment of delamination evolution

The procedure was implemented, modelling a laminate $[0/45_2]_s$ 23 mm wide, in presence of a single matrix crack in the 45° plies. The laminate was subjected to a uniform axial displacement along the x direction, applied on the right-hand side of the laminate, while the displacements along the x and y directions were constrained for the nodes on the left-hand side of the model. Thanks to the symmetric nature of the geometry, only the superior part of the laminate was modelled and symmetry boundary conditions were applied on the z=0 plane. The schematic of the FE model used is reported in Figure 7.6. In order to account for the free edge effects, the entire width of the laminate was modelled.

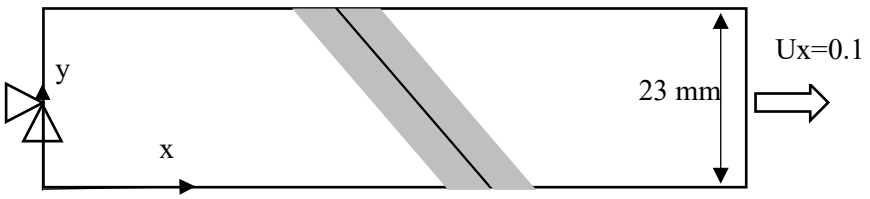

Figure 7.6 Schematic of the FE model

As above mentioned, a uniform delamination, the length of which was equal to the size of one element, was modelled at both sides of the crack. The ERR components were evaluated along the front of the delamination situated at the right-hand side of the crack. It was verified that the

delamination front, situated on the left-hand side respect to the crack, exhibited the same values of ERR calculated for the front situated on the right-hand side, but covering the delamination fronts in opposite directions. The results obtained for one front therefore could be easily extended to the opposite delamination front.

The profile of the three components G_I G_{II} and G_{III} obtained for the initial delamination are shown in Figure 7.7 a). Each point of the graph corresponds to a node of the delamination front where the value of ERR was evaluated. Furthermore, it was verified that G_I components were calculated only when there was no interpenetration of the two faces of the delaminations, avoiding meaningless results deriving from numerical miscalculations. Figure 7.7 b) reports the values of the failure function, assessed along the delamination front. The x-axis reports the coordinates of the node for which the failure function was major than 1. Delamination was then extended for that node and the updated profile of the delamination is reported in Figure 7.7 c).

a)

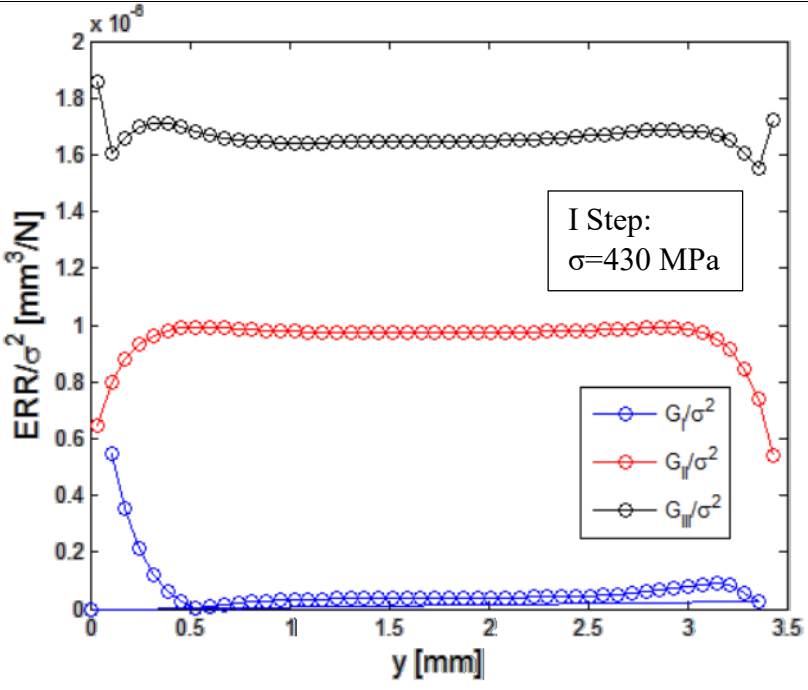

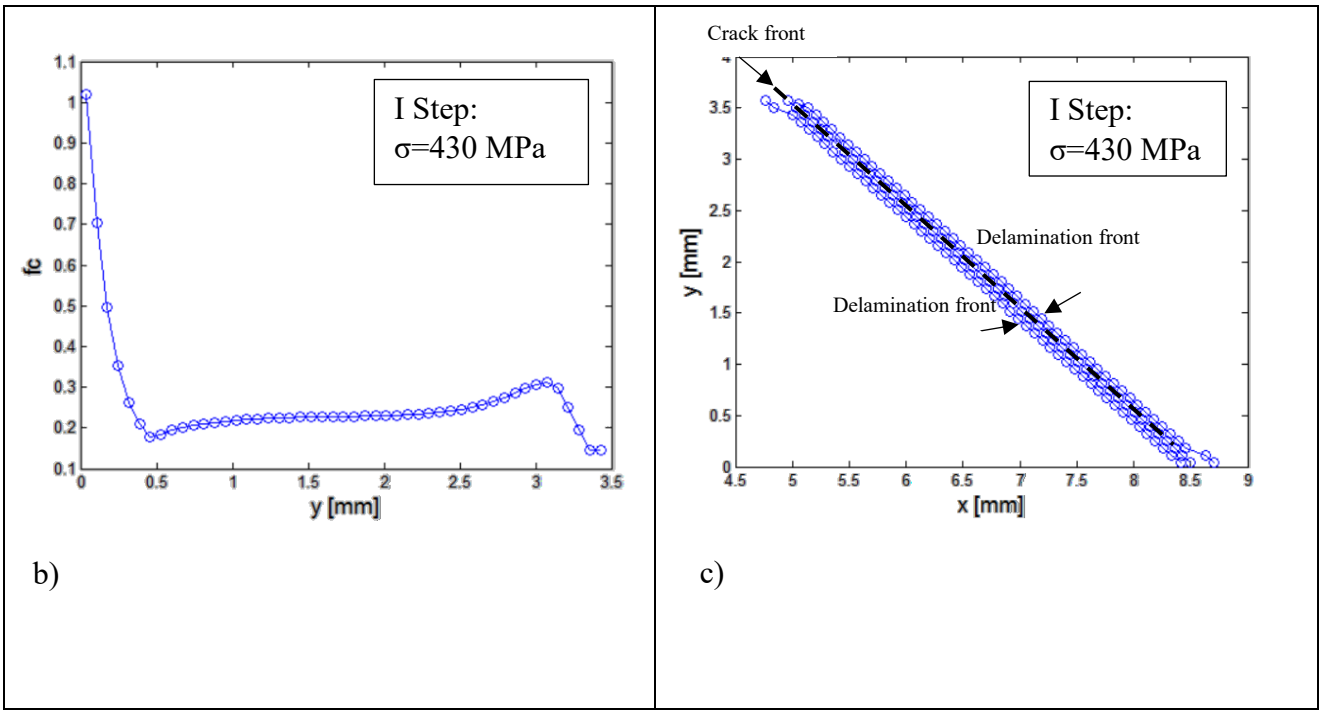

Figure 7.7 a) Components of ERR evaluated along the delamination front situated on the right hand-side of the crack, b) failure function along the delamination, c) evolution of the delamination profile

Then, a new FE analysis was carried out, updating the delamination front, and the components of ERR were evaluated along the new profile, as shown in Figure 7.8 a). In a similar way, the failure function was estimated and the stress applied was increased until was found that the fc≥1 at least for a node (Figure 7.8 b). The delamination profile was then updated (Figure 7.8 c). The procedure was iterated for obtaining the progressive growth of delamination, as illustrated in Figure 7.9.

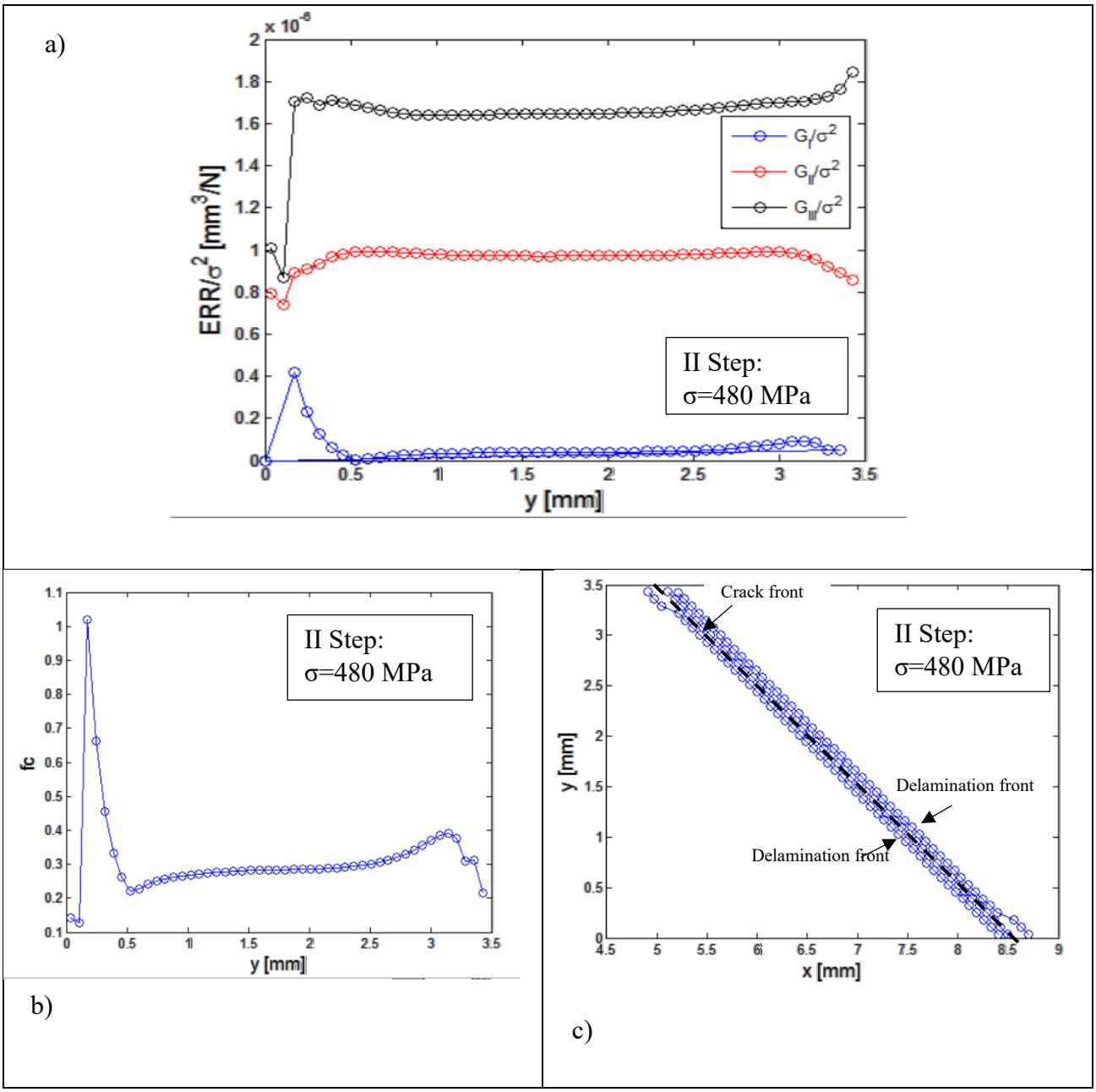

Figure 7.8 a) Components of ERR evaluated along the delamination front situated on the right hand-side of the crack, b) failure function along the delamination, c) evolution of the delamination profile

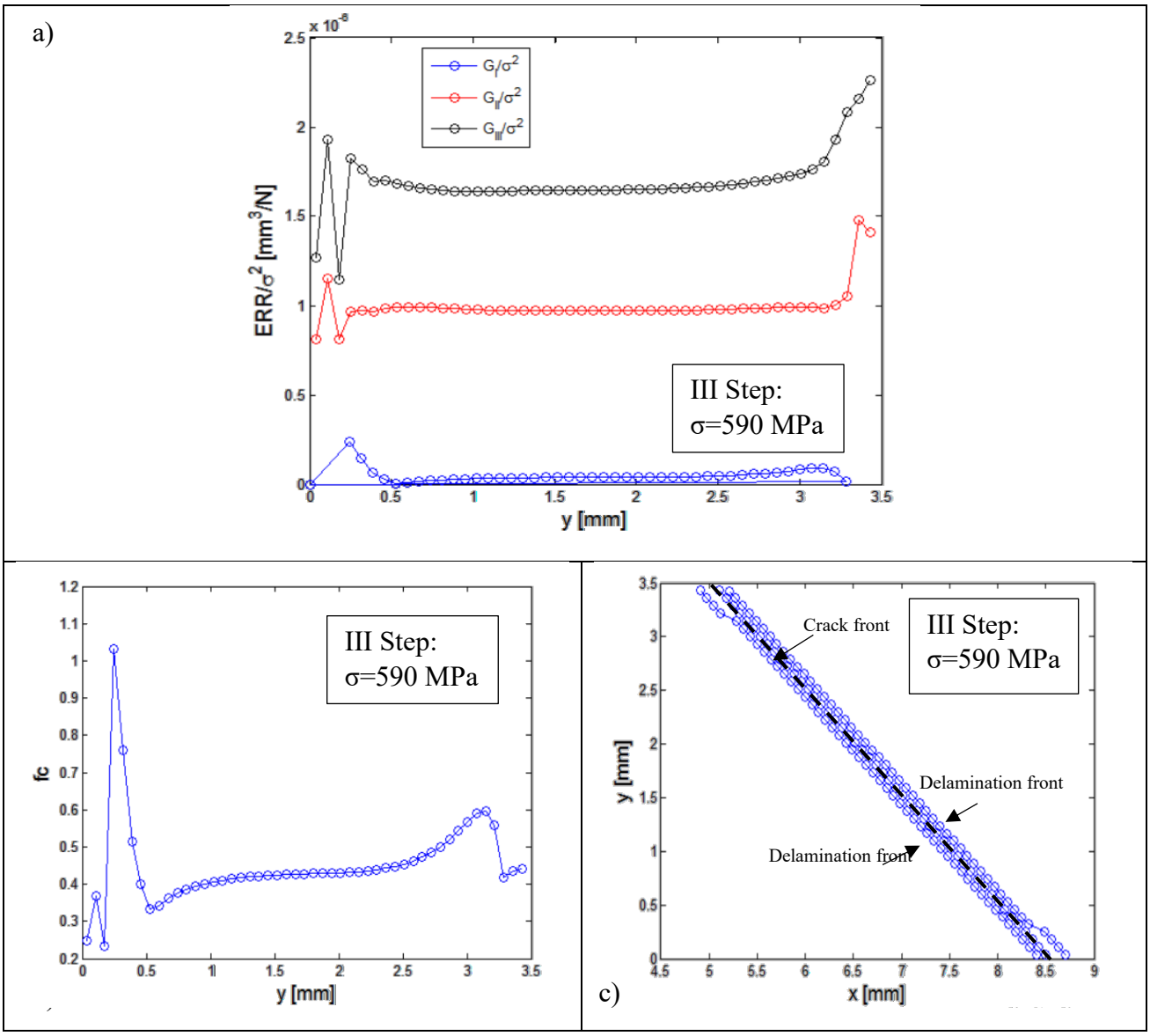

Figure 7.9 a) Components of ERR evaluated along the delamination front situated on the right hand-side of the crack, b) failure function along the delamination, c) evolution of the delamination profile

7.4 Effects of the orientation on ERR values

So far, the investigations conducted were focused on the analysis of the behavior of damaged [0/45]s or $[0/45/-45]_s$ laminates. However, the orientation of the θ ply, for those laminates having a stacking sequence including 0/θ layers, may affect the delamination development.

To provide a way of characterizing the influence of the angle of the off-axis plies on the values of G_I G_{II} and G_{III}, which are thought to be the driving forces of the delamination propagation, a series

of parametric finite element analyses was performed. The model of the damaged laminate used is shown in Figure 7.10.

A unit cell of the damaged laminate was considered and modelled. Periodic boundary conditions were applied to all the opposite sides, while leaving the crack faces free of constraints.

In this case, the θ angle of the unbalanced stacking sequence $[0/\theta_2]_s$ laminate was varied, starting from an initial value of 20° until 80° with increments of 5°. The crack density and delamination length were kept constant for all the cases analyzed (crack density=0.65 mm^{-1} and delamination length of 0.5 mm), to ease the comparison between the different configurations of laminates.

The results obtained are illustrated in Figure 7.11. By observing this, it is possible to draw the following conclusions:

- For θ<40° the delamination propagation occurs mainly following the Mode III of deformation, (out of plane shear), since the G_{III} component is higher than the G_{II};
- For 40°<θ<60° the delamination propagation occurs under the combined effect of shear deformations, since both components of ERR associated with Modes II and III are relevant;
- For θ>60° the contribution of the Mode II overcomes the one of Mode III, G_{II}> G_{III}, until G_{III} is null for the case of θ=90°.

Results support the idea that for the case of $[0/45_2]_s$ laminate, for which experimental tests were carried out and object of most of the FE analyses performed, both G_{II} and G_{III} need to be considered for effectively describing the delamination propagation.

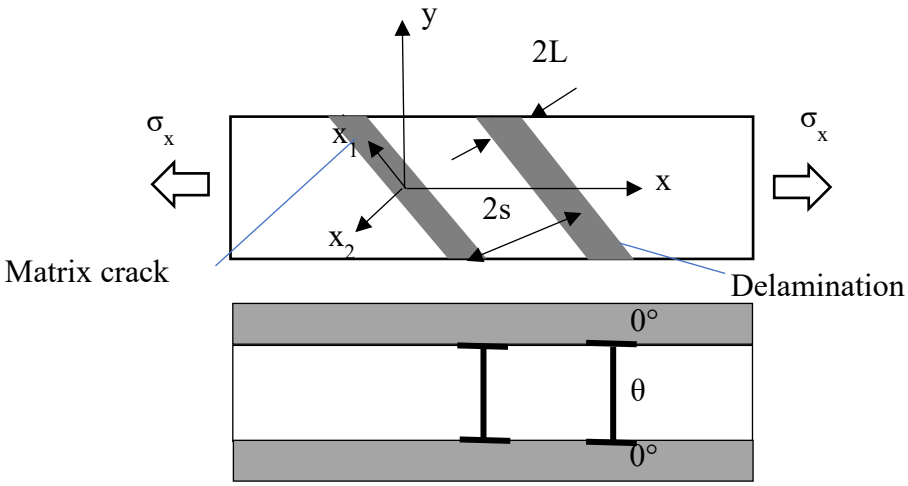

Figure 7.10 Schematic of the FE model

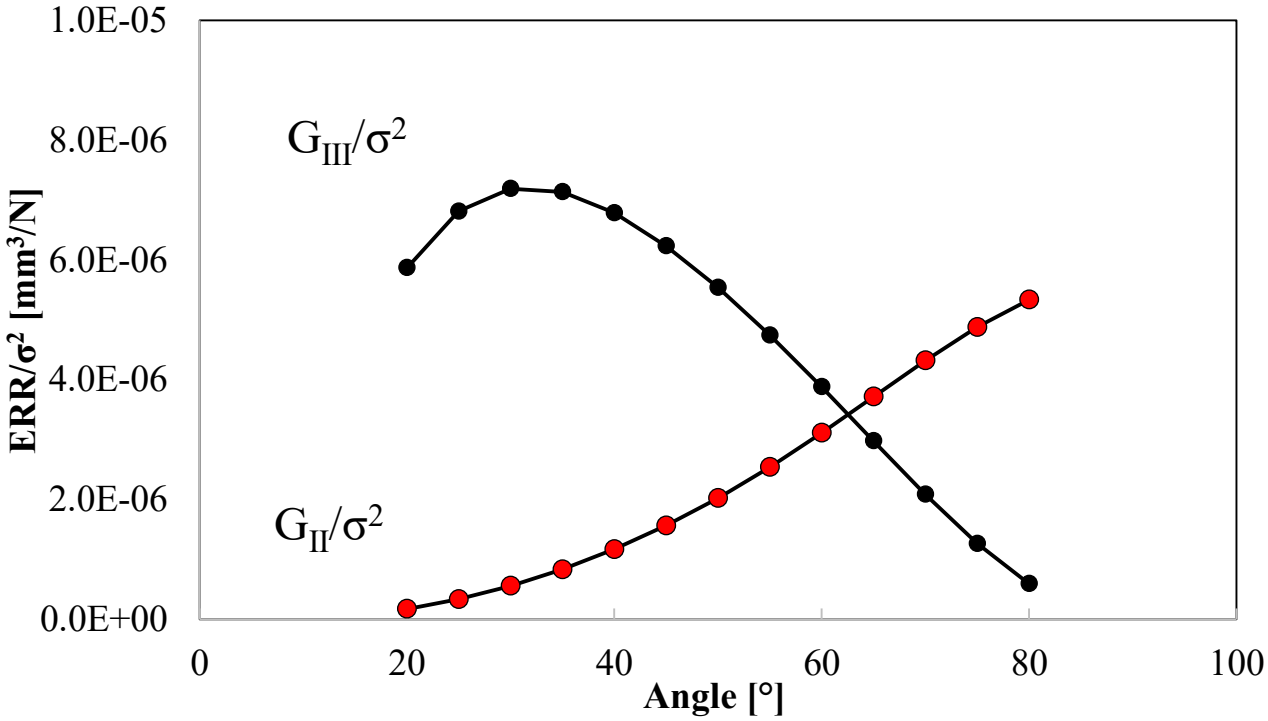

Figure 7.11 Variation of the ERR components with the θ angle value

7.5 Effects of the delamination length and crack density on ERR values

The purpose of the previous section was to describe the variation of ERR with the orientation of the plies. However, once fixed the stacking sequence, ERR values vary with the evolution of damage, i.e. with the variation of crack density and delamination length. This section is aimed at quantifying this variation, taking into exam the case of the $[0/45_2]_s$ stacking sequence. In this case, free edge

effects were not considered, and delaminations were assumed to develop keeping unaltered its shape (under similarity conditions).

FE analyses were carried out using the Ansys software and ERR values were calculated by means of the VCCT. A unit cell for both laminates was isolated from the damaged laminate, as represented in Figure 7.12. 3D structural elements with 20 nodes were used. Only the superior half of the entire thickness of the laminate was modelled, imposing symmetry conditions on the plane of the symmetry, while periodic boundary conditions were applied to the $[0/45_2]_s$ unit cell as follows, where γ is the shear strain:

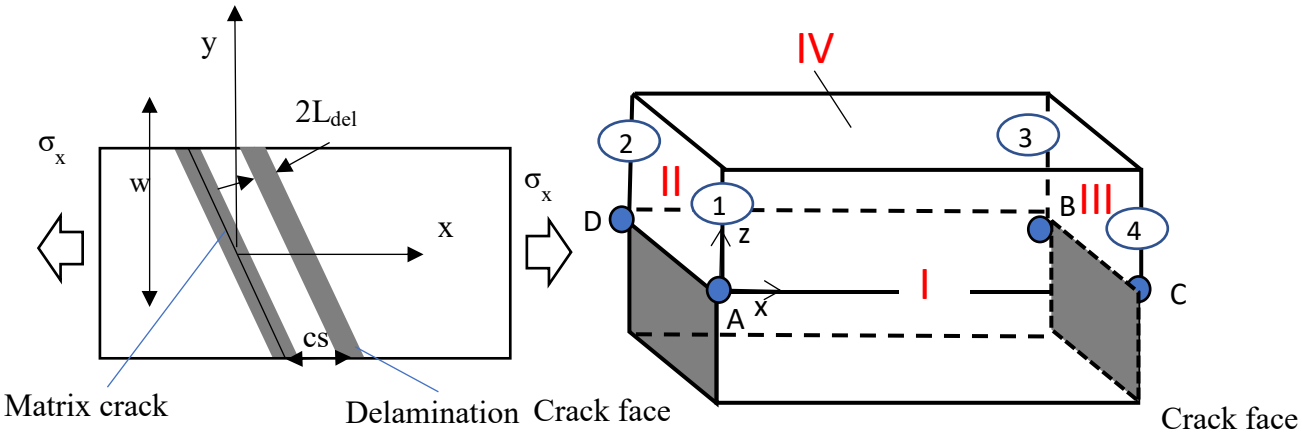

Figure 7.12 Unit cell for the $[0/45_2]_s$ laminate

Edges 4-2 [1]

$u_x^4-u_x^2=\varepsilon_x*(w*\tan(45°)+cs)+\gamma w$

$u_y^4-u_y^2=u_y^C$

$u_z^4-u_z^2=0$

Edges 2-1

$u_{x_1}^1-u_{x_2}^2=\varepsilon_x^A*w*\tan(45°)+\gamma w$

$u_{y_1}-u_{y_2}=u_y$

$u_z-u_z=0$

Edges 2-3

$u_x^3 - u_x^2 = \varepsilon_x * cs + \gamma w$

$u_y^3 - u_y^2 = u_y^B$

$u_z^3 - u_z^2 = 0$

Faces IV-III

$u_{x_{IV}}^{IV} - u_{x_{III}}^{III} = \varepsilon_{x_A}^{x} * w * \tan(45°) + \gamma w$

$u_{y_{IV}} - u_{y_{III}} = u_y$

$u_z - u_z = 0$

Faces II-I

$u_x^{II} - u_x^{I} = \varepsilon_x * cs$

$u_y^{II} - u_y^{I} = u_y^B$

$u_z^{II} - u_z^{I} = 0$

Node D

$u_x^D = u_y^D = u_z^D = 0$

The material properties used are summarized in Table 7.1.

Table 7.1 Properties used for FE analyses

E_1	48000 MPa
$E_2=E_3$	14000 MPa
$G_{12}=G_{13}$	5200 MPa
$\nu_{12}= \nu_{12}$	0.308
ν_{23}	0.4

The results obtained are reported in Figure 7.13, which reports the Mode II and Mode III components of ERR represented with respect to the delamination length divided by the crack spacing. Here, ERR values are normalized to the global tension applied to the laminate squared. Mode I components are not represented since their value was null or negligible.

By observing the figure, the following conclusions can be drawn:

1. With the increase of the crack density, the curves of both G_{II} and G_{III} decrease
2. The values of G_{II} are lower than the respective values of G_{III}, considering the same L_{del} and crack density.
3. As the crack density values decrease, the curves of both component flatten out.

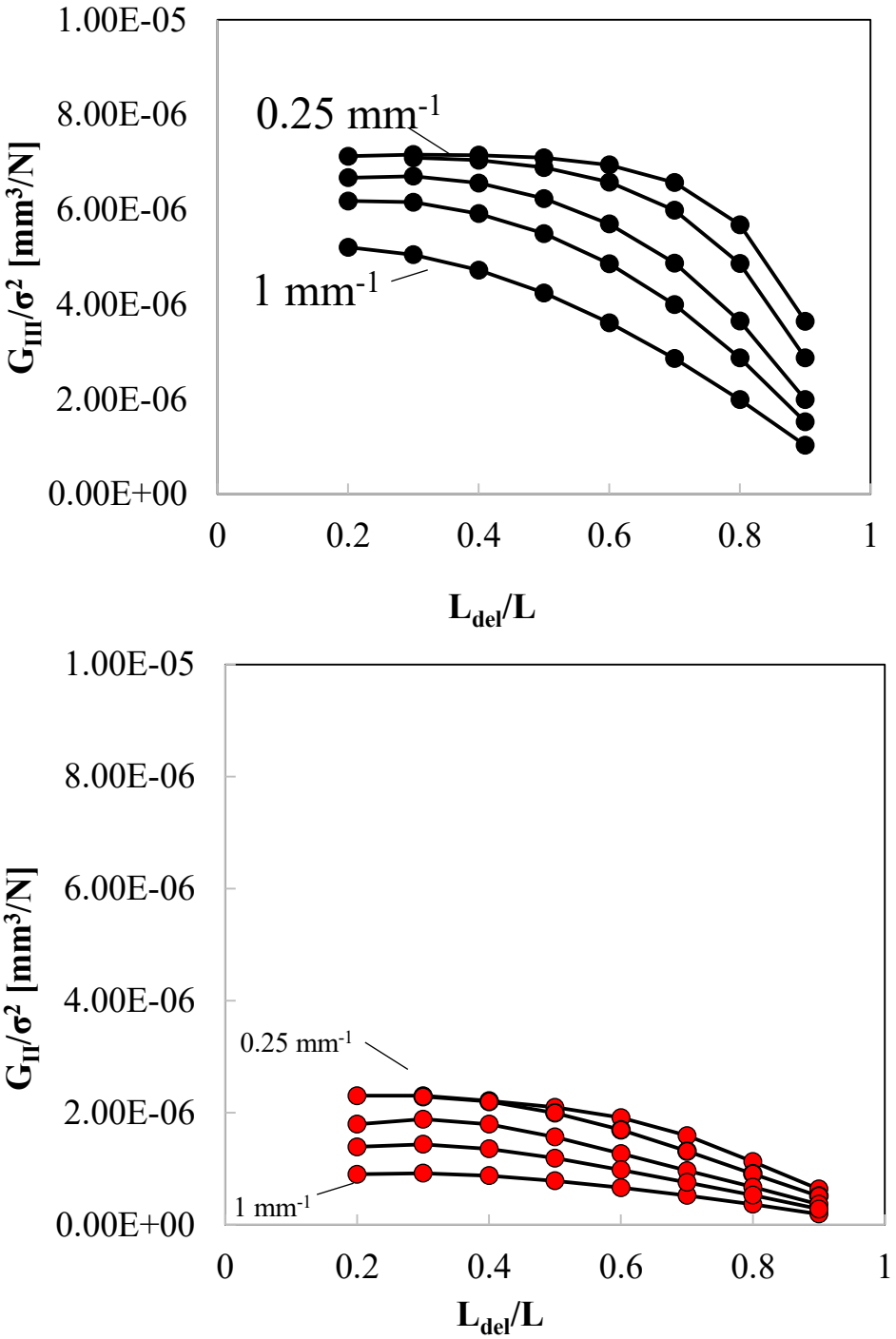

Figure 7.13 ERR curved obtained varying the crack density values and delamination length.

7.6 Comparison between balanced and unbalanced laminates

In the next paragraphs further numerical analyses will be conducted to compare the balanced with unbalanced laminates, taking as referee the stacking sequences of $[0/45_2]_s$ and $[0/45_2/-45_2]_s$.

7.6.1 Preliminary FE analysis

A preliminary analysis was conducted in order to verify if the fronts of delamination, developed at both sides of the matrix crack, were expected to propagate similarly.

In this case, a single crack was modelled and delaminations were assumed to develop at the interface 0°/45° symmetrically respect to the plane of the transverse crack. A uniaxial displacement of 0.1 mm along the x-direction was applied and delamination 0.2 mm long was modelled. ERR components were calculated by using the VCCT, along both delamination fronts. Outcomes obtained are represented in Figure 7.14.

It can be seen that the delamination fronts present ERR values equal one each other, following the delamination fronts in opposite ways. This means that ERR can be evaluated along a single front and results can be extended to the opposite one.

The specimen width was modelled of only 3.5 mm, in order to cut computational times, however the reduced size does not influence the considerations that will be reported, since these remain valid for cases of higher width.

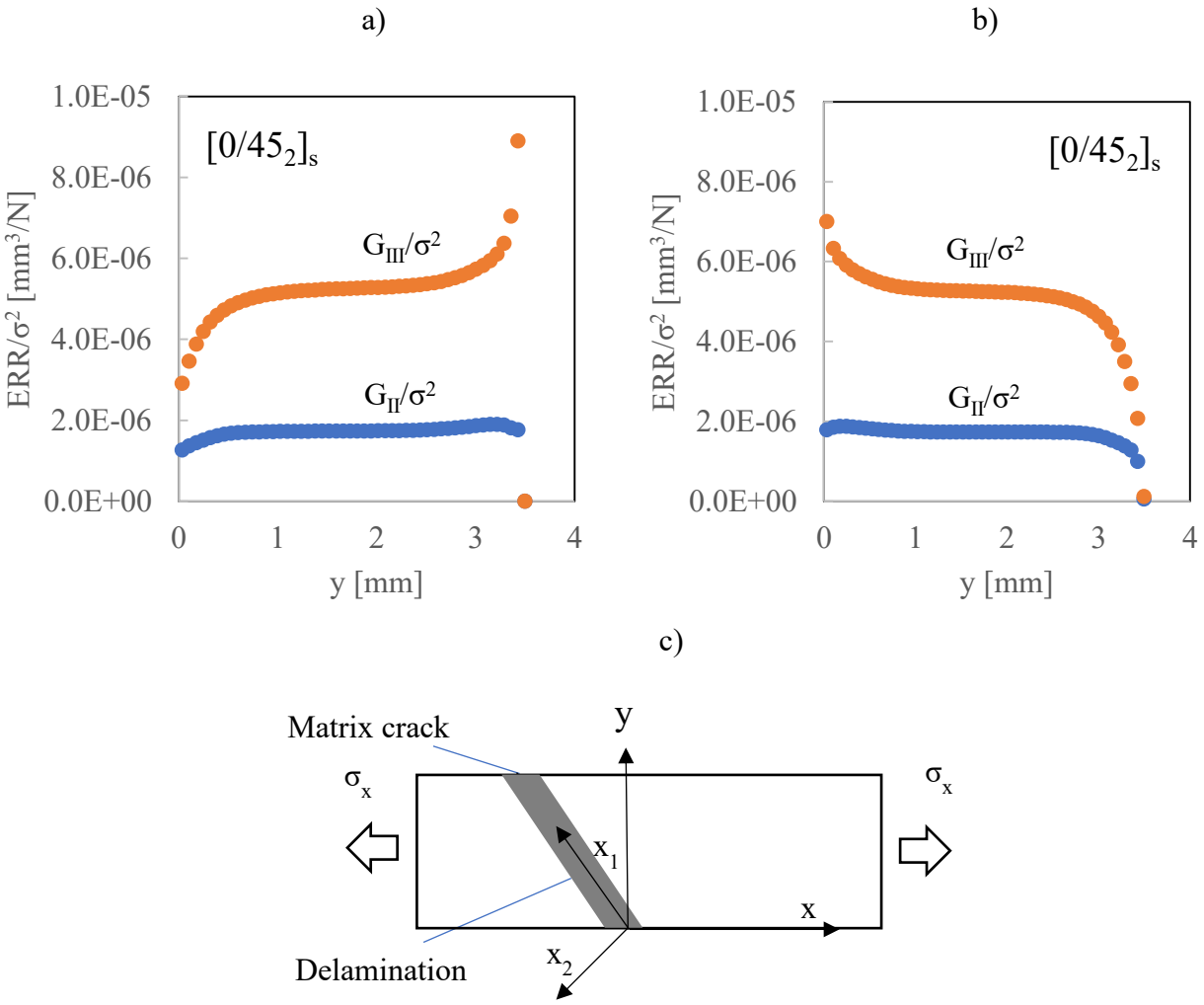

Figure 7.14 ERR components evaluated along both delamination fronts: a) right front (x_2=L_{del}) and b) left front (x_2=-L_{del}) for the FE model schematized in c).

7.6.2 Balanced vs unbalanced damaged laminates

After this preliminary study, further FE analyses were carried out to determine ERR values for both damaged unbalanced $[0/45_2]_s$ and balanced $[0/45_2/-45_2]_s$ laminates, with the aim of comparing the delamination propagation for both configurations.

Laminates were assumed to present a single crack in the 45° plies, developed through the entire width and subjected to uniaxial tensile loading. Two delamination lengths were modelled with a length of 0.7 mm and 1.4 mm, in correspondence of the interface 45°/0°. The thickness of each layer was set equal to 0.3 mm. A schematic of the models used is reported in Figure 7.15.

Three-dimensional finite element analyses were performed with the software Ansys, using 20 node elements. The properties used are the typical ones of glass epoxy laminates, indicated in Table 7.1.

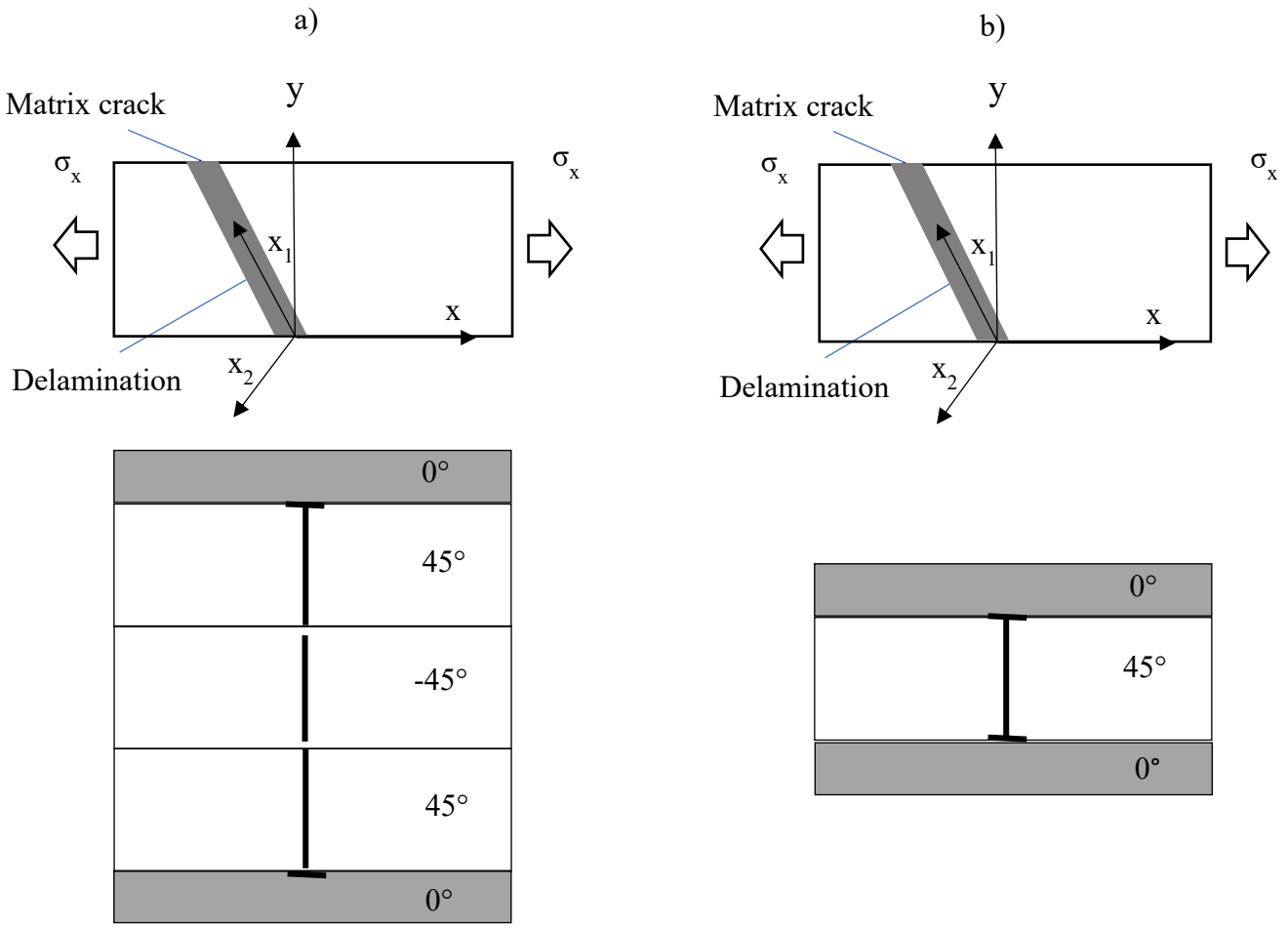

Figure 7.15 Schematic of the a) balanced $[0/45_2/-45_2]_s$ and b) unbalanced $[0/45_2]_s$ laminates

Results obtained are shown in Figure 7.16 and Figure 7.17. G_{II} and G_{III} are divided by the tension remotely applied σ_x squared. The conclusions that can be drawn are summarized as follows:

- The edge effects influence the ERR values near the free edges of the laminates and the curves assume irregular trends. However, by ignoring the free edges and focusing on the central part of the laminate, the ERR values can be assumed constant;

- Comparing the curves of $[0/45_2]_s$ and $[0/45_2/-45_2]_s$ laminates, it is evident that the balanced laminates exhibit lower values of both G_{II} and G_{III} than the correspondent unbalanced configuration.

The evidence from this analysis implies that the balanced configuration $[0/\theta/-\theta]_s$ is less affected by delamination growth when compared to the correspondent unbalanced stacking sequence $[0/\theta]_s$. This is a remarkable result, as the use of balanced configurations, so far adopted to avoid the extension-shearing coupling, also presents the advantage of a reduced growth of delaminations at the interface $0/\theta$.

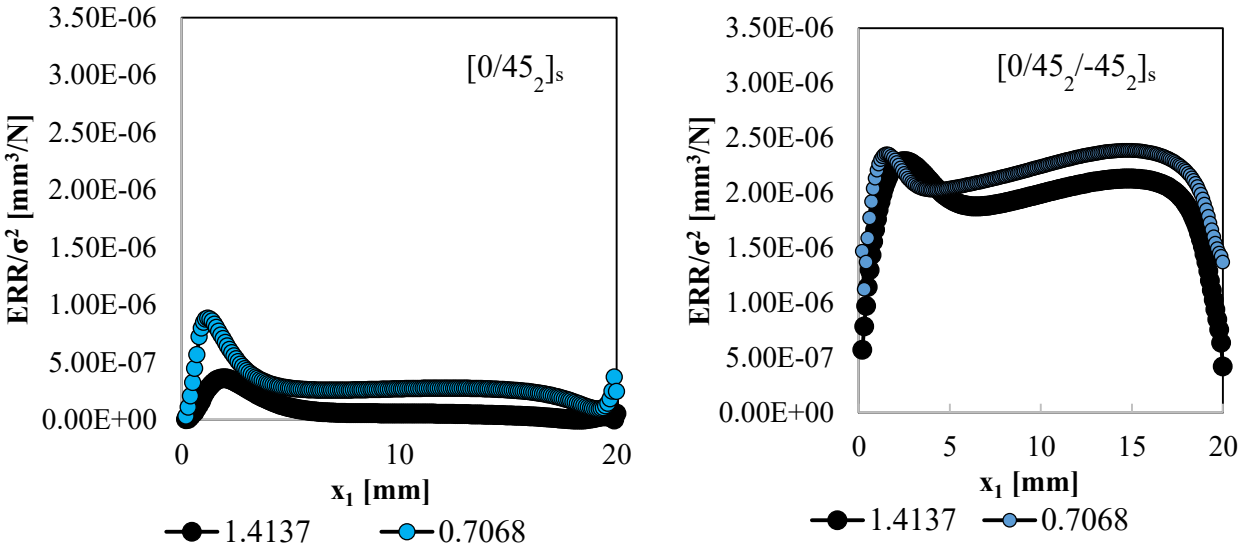

Figure 7.16 G_{II} values for $[0/45_2]_s$ and $[0/45_2/-45_2]_s$ laminates determined along the delamination front, with L_{del}=0.7068 and 1.4137 mm.

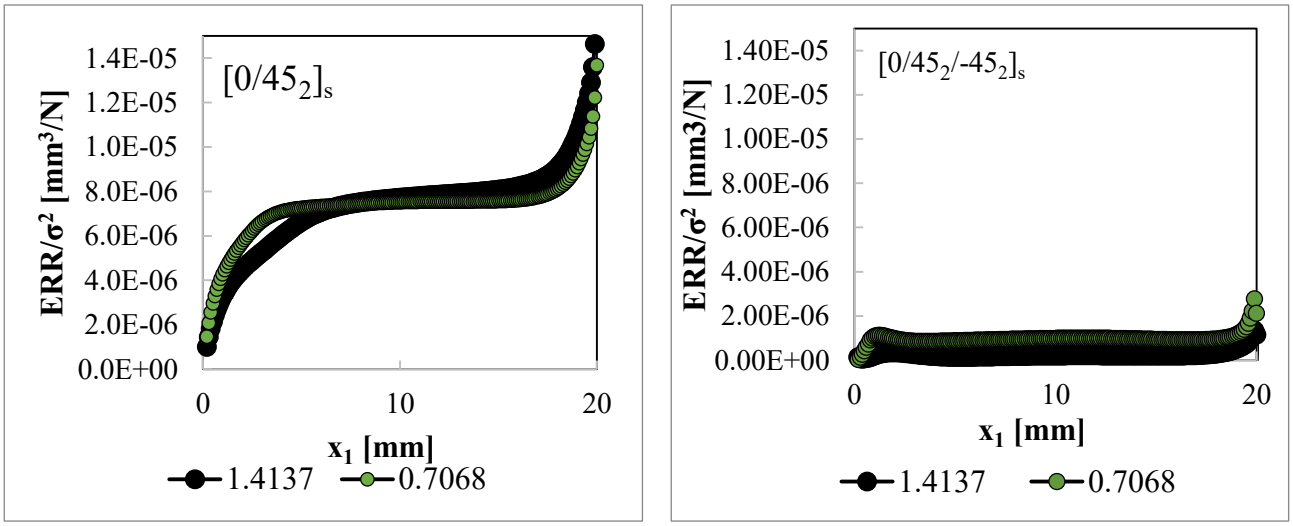

Figure 7.17 G_{III} values for $[0/45_2]_s$ and $[0/45_2/-45_2]_s$ laminates determined along the delamination front

7.6.3 Balanced vs unbalanced undamaged laminates

Free-edge influence on the stress field of undamaged laminates was investigated, in order to verify if there were any differences between the unbalanced and balanced laminate before any cracks and delaminations were formed. To this aim, 3D finite element analyses were performed and the entity of the edge effects on the stress fields, possibly affecting the initiation of delaminations, was examined.

For the model, the material properties typical of glass/epoxy laminates were used (see Table 7.1). Both stacking sequences $[0/45_2]$s and $[0/45_2/-45_2]$s were modelled, using the 20-nodes structural element (Solid 186). The schematic of the undamaged laminates is represented in Figure 7.18. A unitary displacement was applied along the x -axis.

Stresses were evaluated at the interface along a path, drawn starting from the free edge and going towards the central part of the specimen, as represented in the figure.

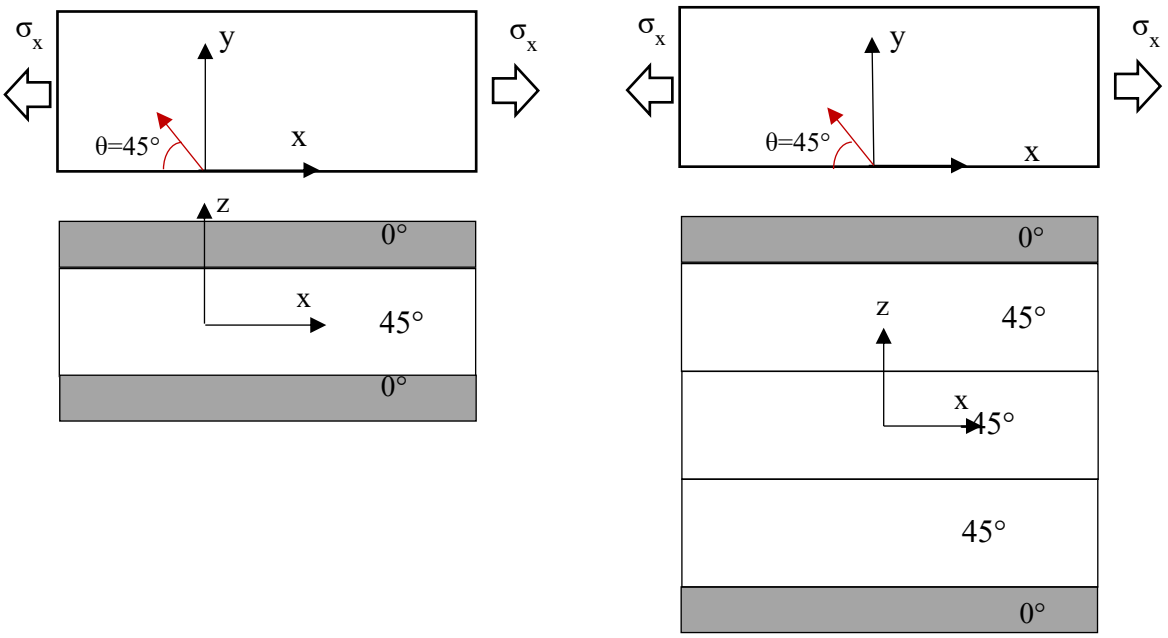

Figure 7.18 Schematic of the unbalanced and balanced lay-ups.

The results obtained are reported in Figure 7.19, Figure 7.20, which are respectively referred to the cases of unbalanced and balanced configurations. The stress values were normalized to the global stress applied to the laminate, σ_x, and were represented in function of the y coordinate, divided by the thickness of the laminate.

The two figures show that the influence of free edges exhaustes within a distance of about 3 times the thickness of the laminate, without any significant difference between the two configurations. The result supports the idea that the difference between the two configurations arises only when some damage (matrix cracks or delamination) is present in the laminate.

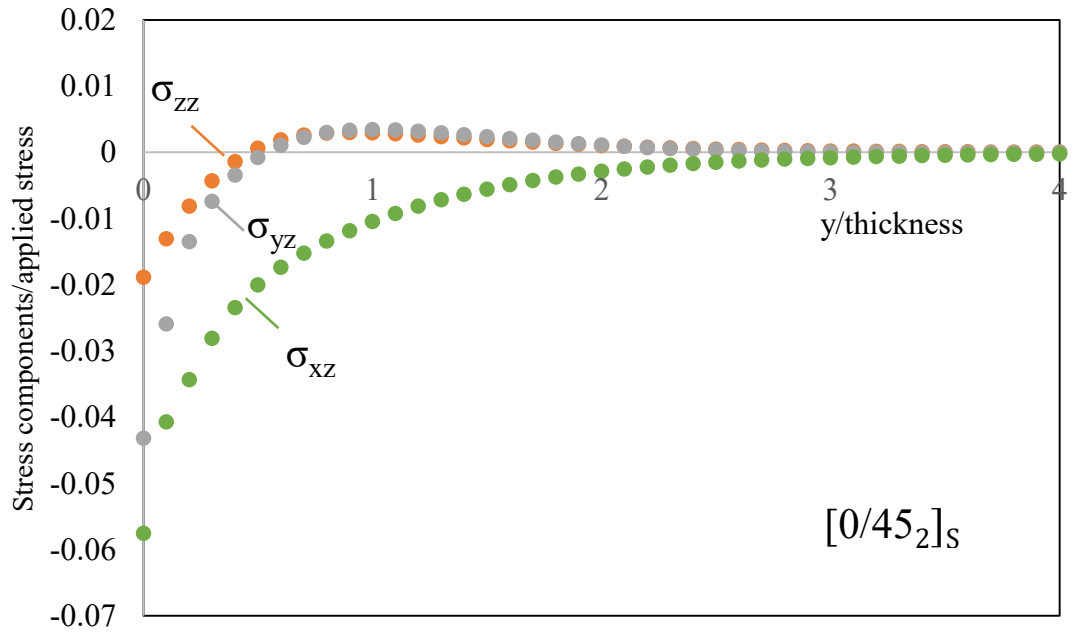

Figure 7.19 Stress fields evaluated for a $[0/45_2]$s laminate at the interface 0/45.

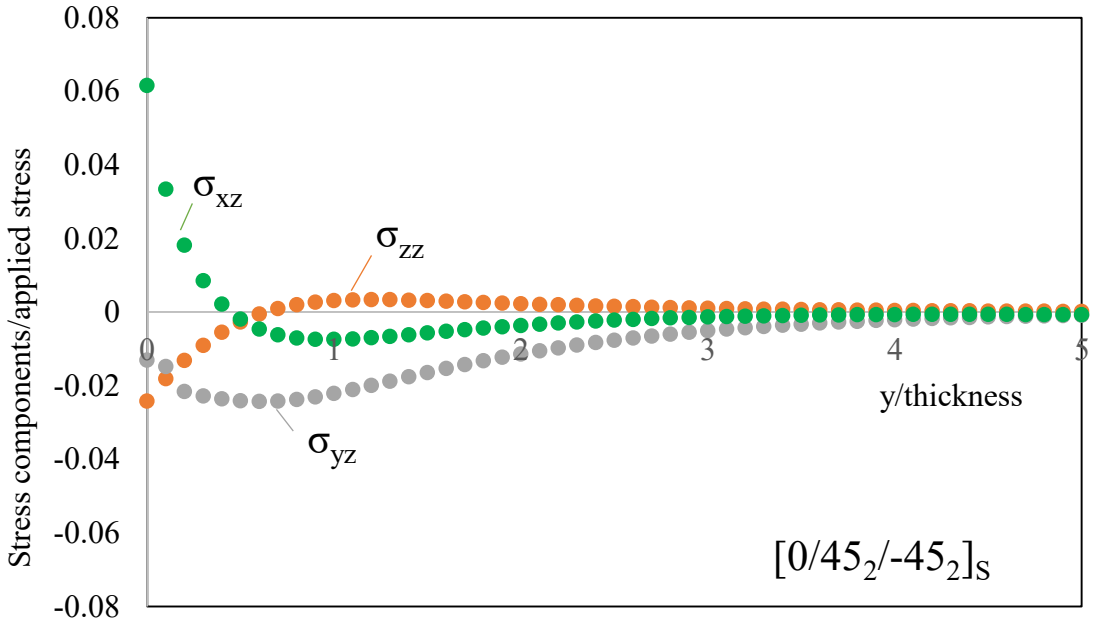

Figure 7.20 Stress fields evaluated for a $[0/45_2/-45_2]$s laminate at the interface 0/45.

7.7 Conclusions

In this chapter, the results of different numerical modelling activities, performed on both balanced and unbalanced laminates, have been presented.

First, a FE model of a $[0/45_2]_s$ damaged laminate, in presence of edge delaminations, was developed and ERR values were determined along the delamination front. As it was found that the values varied along the delamination profile, a procedure for describing the delamination evolution was defined, which allowed the presence of free edges to be considered.

Then, the effects of the orientation of the plies on the ERR values were discussed, together with the influence of the damage extent. To this aim, laminates having different crack density values and delamination lengths were modelled and ERR were determined by using the VCCT.

Finally, the chapter presents a comparison between ERR values associated with the delamination growth for unbalanced and balanced laminates. The results obtained seem to indicate that unbalanced laminates are more prone to this type of damage, as manifest higher values of ERR.

References of chapter 7

[1] Bjeletich, J. G., F. W. Crossman, and W. J. Warren. "The influence of stacking sequence on failure modes in quasi-isotropic graphite-epoxy laminates." Failure Modes in Composites–IV (1979).

[2] Rodini Jr, B. T., and J. R. Eisenmann. "An analytical and experimental investigation of edge delamination in composite laminates." Fibrous Composites in Structural Design. Springer US, 1980. 441-457.

[3] Crossman, F. W., and ASDd Wang. "The dependence of transverse cracking and delamination on ply thickness in graphite/epoxy laminates." *Damage in Composite Materials: Basic Mechanisms, Accumulation, Tolerance, and Characterization*. ASTM International, 1982.

[4] Hayashi, Tsuyoshi. "Analytical study of interlaminar shear stresses in laminated composite plate." *Space Technology and Science*. 1968.

[5] Puppo, A. H., and H. A. Evensen. "Interlaminar shear in laminated composites under generalized plane stress." *Journal of composite materials* 4.2 (1970): 204-220.

[6] Pipes, R. Byron, and N. J. Pagano. "Interlaminar stresses in composite laminates under uniform axial extension." *Journal of Composite Materials* 4.4 (1970): 538-548.

[7] Tang, S., and A. Levy. "A boundary layer theory-part II: extension of laminated finite strip." *Journal of Composite Materials* 9.1 (1975): 42-52.

[8] Wang, A.S.D and Crossman, F.W., “Some New Results on Edge Effects in Symmetric Composite Laminates,” Journal of Composite Materials, Vol 11, 1977, pg. 92

[9] Rybicki, E.F., “Approximate Three-Dimensional Solutions for Symmetric Laminates Under In-plane Loading,” Journal of Composite Materials, Vol 5, 1971, pg. 354.

[10] Stanton, E.L., Crain, L.M.and Neu, T.F., “A Parametric Cubic Modeling for General Solids of Composite Materials,” Int. Journal. Num. Meth. Eng, Vol 11, 1977, pg. 653.

[11] Hwang, W.C. and Sun, C.T., “Analysis of Interlaminar Stresses Near Curved Free Edges of Laminated Composites using Iterative Finite Element Method,” Computers and Structures, Vol 28, 1988, pg. 461.

[12] Murphy, P.L.N. and Chamis, C.C., “Free Edge Delamination:Laminate width and loading conditions effects,” Journal of Composites Tech & Research, Vol 11, 1989, pg. 15.

[13] Yang, H. and He, C.C., “Three Dimensional Finite Element Analysis of the Free Edge Stresses of Composite Laminates,” Journal of Composite Materials, Vol 28, 1994, pg. 1394.

[14] Salpekar, S A and O'Brien, T K, "Combined Effect of Matrix Cracking and Free Edge on Delamination," Composttе Matertals Fattgue and Fracture (Thtrd Volume), ASTM STP 1110, T K O'Bnen, Ed, Amencan Society for Testing and Matenals, Phfladelphm, 1991, pp 287-311

[15] Fish, J. C., and T. K. O'Brien. "Three-Dimensional Finite Element Analysis of Delamination from Matrix Cracks in Glass-Epoxy Laminates." *Composite Materials: Testing and Design. 10th Volume, ASTM STP* 1120 (1992).

[16] O’Brien, T.K., 1982. Characterization of delamination onset and growth in a composite laminate. In: Reifsnider, K.L. (Ed.), Damage in Composite Materials, ASTM STP 775. ASTM, Philadelphia, PA.

[17] Kashtalyan, Maria, and Costas Soutis. "Analysis of local delaminations in composite laminates with angle-ply matrix cracks." *International Journal of Solids and Structures* 39.6 (2002): 1515-1537.

[18] Sun, Ch T., and C. J. Jih. "On strain energy release rates for interfacial cracks in bi-material media." Engineering Fracture Mechanics 28.1 (1987): 13-20.

[19] Krueger, Ronald. "Virtual crack closure technique: history, approach, and applications." Applied Mechanics Reviews 57.2 (2004): 109-143.

8. Fibre failure

8.1.Introduction

The breakage of fibres is the last stage of damage process, leading to the failure of fiber-reinforced composites.

When a unidirectional composite is loaded under tension in the direction parallel to the fibres, the single fibres may fail in correspondence of their weak points and stress between fibers and matrix is redistributed, affecting the fibers in the adjacencies of the broken fibers.

It is therefore evident that the fiber breakage is ruled by statistical law, due to the nonuniformity of fiber strength and the stress redistribution.

The statistical nature makes the ultimate tensile strength difficult to predict and this explains why the strength of unidirectional laminates has been widely studied in the literature.

Rosen [1] developed a model based on cumulative weakening. The unidirectional laminate was considered as a series of segments, characterized by a common length, equal to the fibre ineffective length. Fibres were assumed to progressively break, while the load was equally re-distributed to the remaining fibres. When one of the segments had many fibre breaks that could not support the load anymore, final failure occurred. However, the proposed model presents different limitations. It was found that the tensile strength predictions were too high for most materials and the implication of stable failure composite subject to increasing strain did not find a good correspondence with real failure of composites, mostly failing catastrophically.

These inconsistencies may be attributed to the effect of stress concentrations of fibre breaks, neglected by the author.

C. Zweben [2] modified the model proposed by Rosen, and included the effect of stress concentration induced by broken fibres to the adjacent remaining fibres.

Strength of the population was characterized by a cumulative distribution function F(σ), representing the probability that an element will break under a stress of σ.

The cumulative fracture propagation model allowed to calculate the expected number of single broken elements.

Later, Zweben and Rosen [3] furtherly improved the model, including considerations on the array of fibres based on a 3D representative volume element (constituted by a fibre embedded in a cylinder of matrix material).

The authors developed a method to calculate the expected number of fractures in the composite.

In the 1990s even Wisnom and Green [4] dealt with the problem of fibre breaks.

Tensile strength of unidirectional composites was predicted based on the linking of the fibre breaks, interacting only if the fibres were within a critical distance.

Probability of obtaining a given number of fibre breaks was estimated by scanning an array of fibres for clusters of broken fibres. Using an energy balance, it was shown that a bundle of failed fibres could lead to the catastrophic failure. In particular, the authors affirmed that if the energy released was larger than the energy required to pull out the bundle of fibres from the rest of the composite, the damage zone would have propagated, furtherly increasing the energy release rate and leading to catastrophic failure.

More recently, Pimenta and Pinho [5] presented an analytical model for taking into account the size effects on the strength of composite materials. Based on the Weibull distribution and a shear–lag model, they performed a probabilistic analysis of the failure process in hierarchical bundles.

Even the literature dedicated to the study of fatigue response of unidirectional composite laminates, with particular attention on the occurrence of fibre breakage, is particularly rich.

In particular, several authors investigated the damage evolution of laminae, suggesting different models to predict the final failure.

Subramanian, Reifsnider and Stinchcomb [6] developed a model inspired by the cumulative damage scheme proposed by Reifsnider and Stinchcomb [7]. Reduction in the strength of the 0° plies was estimated by means of the SN curve.

Shokrieh Lessard (1996) [8], [9] developed a generalized residual material property degradation model for simulating the fatigue behaviour of a unidirectional ply under multiaxial state of stress using the results of uniaxial fatigue experiments. The failure criterion that the authors adopted was similar to the Hashin-type.

Lee Fu and Yang (1996) [10] proposed a residual stiffness degradation model to assess the cumulative damage under spectrum loadings. The model was validated through comparison with results obtained from experimental tests conducted on [0°/90°/±45°]s laminates.

Further experimental tests were performed by Lee and Jen [11], who investigated the fatigue response of $[0/90]_{4s}$, $[0/45/90/-45]_{2s}$ and [±45]s glass/PEEK and proposed a nonlinear cumulative damage theory based on Marco-Starkey cumulative damage rule.

Gamstedt B. A. Sjogren [12] experimentally investigated the sequence effect of block amplitude loading on cross-ply laminate. The damage observed in cross-ply laminates (carbon/epoxy) tested to tension-tension fatigue loading consisted of the initial formation of transverse cracks, from which delaminations start to grow. Delaminations were observed to develop both symmetrically and unsymmetrically. During the growth process of delaminations, the peak stresses in the 0° plies were subdued and spread. 0° plies were therefore subjected to variable amplitude loading.

The fiber fractures were observed to initiate at the side of the fibers closest to the delamination.

Assuming that the load sequence effect in 0° laminas was negligible, fatigue life was assessed using the S-N data of pure 0° laminate.

Van Paepegem and J. Degrieck [13], after having underlined the inefficiencies of the Miner cumulative rule for describing fatigue damage and considering the load sequence effect, reviewed the present literature and concluded that there was not an agreement between which high-low and low high load sequence would be more detrimental.

The authors proposed a model based on the residual stiffness for assessing the damage growth and after having simulated different block loading sequence, they concluded that the most damaging effect consists of the transition from a low to a high stress level. Several other authors proposed in the literature models alternative to the Miner's law.

Chingshen, Ellyin and Wharmby [14] modelled laminae subjected to a local damage as an orthotropic medium with a local damage factor.

Since the damage process of cross-ply laminates is characterized by two damage mechanisms (transverse cracks and delamination formation), two meso-damage factors were defined.

The meso-factors chosen were respectively the reduction of the elastic modulus of transverse and longitudinal laminae.

The number of cycles at which crack density saturation state (CDS) was reached was estimated by using a modified SN curve of unidirectional laminae. Stage II (longitudinal cracking, delamination and fiber fracture) was predicted always by using a SN curve of unidirectional laminates.

However, the validation with experimental results is arguable, since fatigue tests have been not repeated and outliers have been excluded without any criterion.

Farahani, Haftchenari and Panbechi [15] proposed a criterion to predict fatigue life of unidirectional laminates.

Once individuated the three main damage mechanisms (matrix, matrix/fibres interface and fibres failures), for each an energy based damage parameter was expressed.

Kassapoglou [16] constructed the SN curve basing on the assumption that the cycles to failure were a function of the probability of failure. Probability of failure was assumed equal to the probability obtained from static test results.

Passipoularidis, Philippidis [17] compared different damage accumulation methods alternative to the Palmgren Miner (PM) rule.

H.S. Chen S.F. Hwang [18] developed an empirical fatigue damage model that considers the effects of frequency and load ratio.

The damage law they elaborated was the following:

$$D(n) = F_r\left(\frac{s}{\sigma_u}\right)F_f(f)F_R(R)\frac{1}{1+\frac{1}{ac}e^{-an}}$$

With F_r= function of the stress level, F_f= function of the frequency and F_R=function of the stress ratio

In this section, a model based on a probabilistic approach for the prediction of fibre failure of 0° laminae in cross ply laminates subjected to tensile tensile fatigue loading will be described.
Before the description of the model, a brief review of the statistical concepts used in the formulation is presented.

8.2 Statistical nature of brittle fracture

As reported in [19], the reasons for which brittle fracture phenomenon involves statistical concepts are three:

(a) The random distribution of flaws within the bulk of solids;

(b) The wide scatter in strength observed in mechanical tensile tests;

(c) The observation that the resistance of a solid to brittle fracture is essentially determined by the resistance of a small volume element surrounding the worst defect present.

The probability of occurrence of a critical defect in a solid of volume V was described by Weibull:

$$F(V) = 1 - \exp\left[-\left(\frac{V}{V_0}\right)\right] \quad (1)$$

Where V_0 is the mean volume per defect.

Equation (1) can be generalized when the final failure is due to the presence of n flaws in the volume V.

$$F(V) = 1 - [\Gamma(n+1) - \Gamma(V/V_0, n+1)]/\Gamma(n+1) \quad (2)$$

Imposing that the density if flaws V_0^{-1} is function of the applied stress σ and introducing two constants of the materials a and b, the two-parameter Weibull distribution function can be obtained:

$$V_0^{-1} = \left(\frac{\sigma}{a}\right)^b \quad (3)$$

The c) point states that failure occurs when the weakest link fails, and expresses the weakest link concept, frequently used in the literature. This implies that the fracture phenomenon can be assumed as the failure of a chain, in which failure occurs when one element of the chain fails. The chain can be viewed as a one-dimensional structure, or even a two-dimensional one.

The probability of failure of the chain is:

$$F_n(\sigma) = 1 - [1 - F(\sigma)]^n \quad (4)$$

With n indicating the number of elements of the chain.

Eq. 4 can be expanded and, taking into account only the dominant term, the probability of failure of the chain is simplified:

$$F_n(\sigma) \approx nF(\sigma) \tag{5}$$

The probability of failure is therefore:

$$F_n(\sigma) \approx 1 - \exp\left[-n\left(\frac{\sigma}{a}\right)^b\right] \tag{6}$$

The tensile failure of unidirectional composite is more complex from a statistical point of view, since it involves several modes of failures. A single fibre breaks does not lead to the failure of the structure, which means that the weakest link approach is not valid as it is. Nevertheless, if the unidirectional composite is divided into a series of bundles, each containing n fibre elements characterized by a common characteristic length (ineffective length), the composite can be viewed as a weakest link arrangement of its independent bundles.

8.3 Model of fibre failure

Consider a damaged cross ply, interested by transverse cracks in the 90° plies, uniformly distributed with a crack spacing of L, from the tips of which delaminations long 2ci are induced. A schematic is

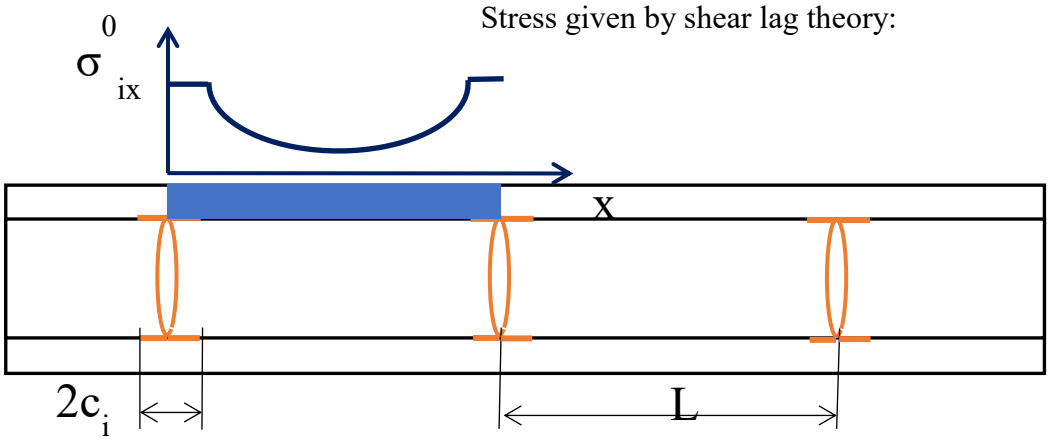

Figure 8.1 Schematic of the damaged cross-ply laminate

represented in Figure 8.1.

The entity of the stress in the 0° layer can be evaluated through a simplified shear lag model [20]. In the following equations, h_1 and h_2 indicate the thickness respectively of the 0° and 90° plies while E_1 and E_2 are the longitudinal and transverse Young's moduli of the lamina.

$$\sigma_{x1} = \frac{E_1}{E_0}\left\{1 + \frac{E_2 h_2 \cosh\left(\frac{\alpha l}{2} - \alpha x\right)}{E_1 h_1 \cosh\left(\frac{\alpha l}{2}\right)}\right\}\sigma_a \tag{7}$$

With

$$\alpha = \frac{(h_1 + h_2)E_0}{h_1 h_2 E_1 E_2} H \tag{8}$$

E_0 is the stiffness of the undamaged laminate and can be calculated as

$$E_0 = \frac{E_1 h_1 + E_2 h_2}{h_1 + h_2} \tag{9}$$

While H is a shear lag parameter, function of the shear moduli of the lamina and geometry of the specimen.

$$H = \frac{3G_{12}G_{23}}{h_1 G_{23} + h_2 G_{12}} \tag{10}$$

By plotting the eq (8), representing the tensile stress distribution between two neighboring transverse cracks, it can be easily seen that the stress is not uniform.

The presence of the delaminations can be taken into account by substituting the crack spacing L in eq (7) with an equivalent crack spacing, equal to the effective crack spacing at which delamination length is subtracted $L-2c_i$.

Then, the value obtained in correspondence of the tips of delamination is extended to all the delaminated volume of the 0° ply, i.e. the portion of the 0° ply included between the tip of the transverse crack and the tip of delamination.

The volume of the 0° ply included between two transverse cracks is subjected to inhomogeneous uniaxial stress state. It is useful therefore to recall the fracture probability valid for inhomogenous uniaxial stress state, which is:

$$Pf = 1 - \exp\left\{\left[-\frac{1}{V_0}\int_0^V \left(\frac{\sigma - \sigma_u}{\sigma_0}\right)^m dV\right\}\right. \tag{11}$$

Where V_0 and σ_0 are two normalization parameters and σ_u is the threshold stress below which the fracture probability is null.

In order to extend the fracture probability of eq (11), valid for quasi-static tensile tests, to fatigue tensile-tensile tests, let's define the fracture probability correspondent to cycle N_{fi} as:

$$Pf(N_{fi}) = 1 - \exp\left\{2n\left[-\frac{1}{L_0}\int_0^L \left(\frac{\sigma_i^0(x)}{K_0 N_{fi}^a}\right)^m dx\right]\right\} \tag{4}$$

With n=cracks number+1.

In this case, the normalization parameters are given by the SN curve of unidirectional 0° specimens (see Figure 8.2): K_0 is the slope of the curve, a is the exponent of the curve and L_0 represents the length of unidirectional 0° specimens.

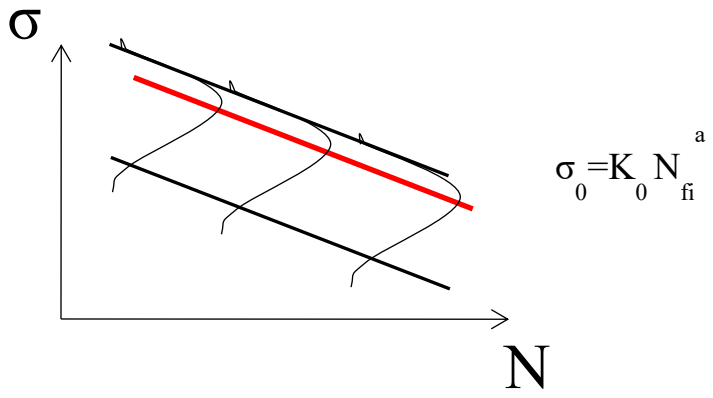

Figure 8.2 Typical SN curve of the 0° plies.

The $Pf(Nf_i)$ is usually represented by a curve similar to the one shown in Figure 8.3. It is possible to choose the target fracture probability $Pf^*(Nf)$, and calculate the correspondent number of cycles Nf at which the target fracture probability is reached.

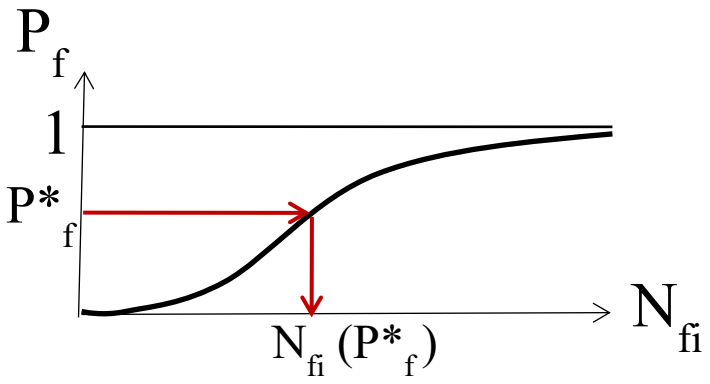

Figure 8.3 Typical curve of fracture probability

The damage correspondent to the ith step can be measured using the Miner's rule:

$$D_j = \frac{\Delta N_j}{Nf_j(P_f^*)} \tag{13}$$

Failure is assumed to occur when $D \geq 1$

$$D_i = \sum_{j=1}^{i} \frac{\Delta N_j}{Nf_j(P_f^*)} \tag{14}$$

As already presented in the literature review, the Miner's rule presents several limits, since gives unsatisfactory predictions for composite materials. One of the reason is that the development of damage is dependent on the order of the various stress levels, a high low amplitude order may be more detrimental than a low-high order.

Nevertheless, it was chosen to use the Miner's rule to describe the state of fatigue damage in the material, thanks to its simplicity of use.

The substitution of the law with other laws, for example with the Marco-Starkey model, does not alter the goodness of the approach proposed.

8.4 Flowchart

In this paragraph, the procedure adopted for determining the failure of 0° plies in cross-plies laminates will be described.

The input data, necessary to the execution of the flowchart, include the geometrical characteristic of the laminate, in particular the thickness of the 0°and 90° plies, and the crack density saturation cd_{sat}. In fact, since the failure of 0° fibres occurs in a late stage of fatigue life, it can be easily assumed that the formation of transverse cracks has already reached a saturation condition and that fibre failure will occur only after that. Then, in order to simulate the growth of delamination and predict the delamination length at a certain number of cycles, it is necessary to implement the Paris like curve describing the delamination growth process $dL_{del}/dN= D\ G_{II}(L_{del})^{n}$.

As regards the unidirectional laminates, from which the SN curve has been obtained, the input data are the slope K_0 and the exponent a of the curve, the length of the unidirectional specimens. The Weibull modulus m, exponent dependent on the material used, has to be determined and inserted as input.

Once inserted the input data, the algorithm begins calculating the delamination length c_i correspondent to a certain number of cycles N_i initially set. This value, which is an initial guess and can be imposed equal to the number of cycles for which crack density saturates, will be adjusted with the following iterations. The delamination length is estimated by integrating the Paris like curve. Then, by using the equations derived from the simplified shear lag theory, the average tensile stress in the 0° plies correspondent to the particular damage situation configuration delineated (crack density saturation and delamination length), is determined. Thus, the fracture probability Pf(N) can be calculated and, in particular, once individuated the target fracture probability P_f*, the number of cycles at which this is reached Nf* is calculated. Damage is then calculated by using the Miner's law. If the damage is equal or larger than 1, the failure occurs, and the Nf* represents the

number of cycles at which the 0° plies fail, otherwise the number of cycles Ni initially guessed is incremented and the procedure is iterated until the D is larger than 1.

It should be noticed that a cross ply laminate can fail in two ways: the failure occurs consequently to the breakage of 0° plies, or can be due to the achievement of a fully delaminated condition, which is reached when two adjacent delamination fronts join each other

It was therefore necessary to insert a further condition determining the exit from the flowchart, i.e. the procedure was performed while the delamination length was lower than the half crack spacing.

The flowchart is schematically represented in Figure 8.4.

Input:

- Geometrical characteristics of the laminate
- cd_{sat}, c_0
- Paris curve for delamination:
- Unidirectional laminates:

K_0 ,a ,L_0 , m and ΔN_i

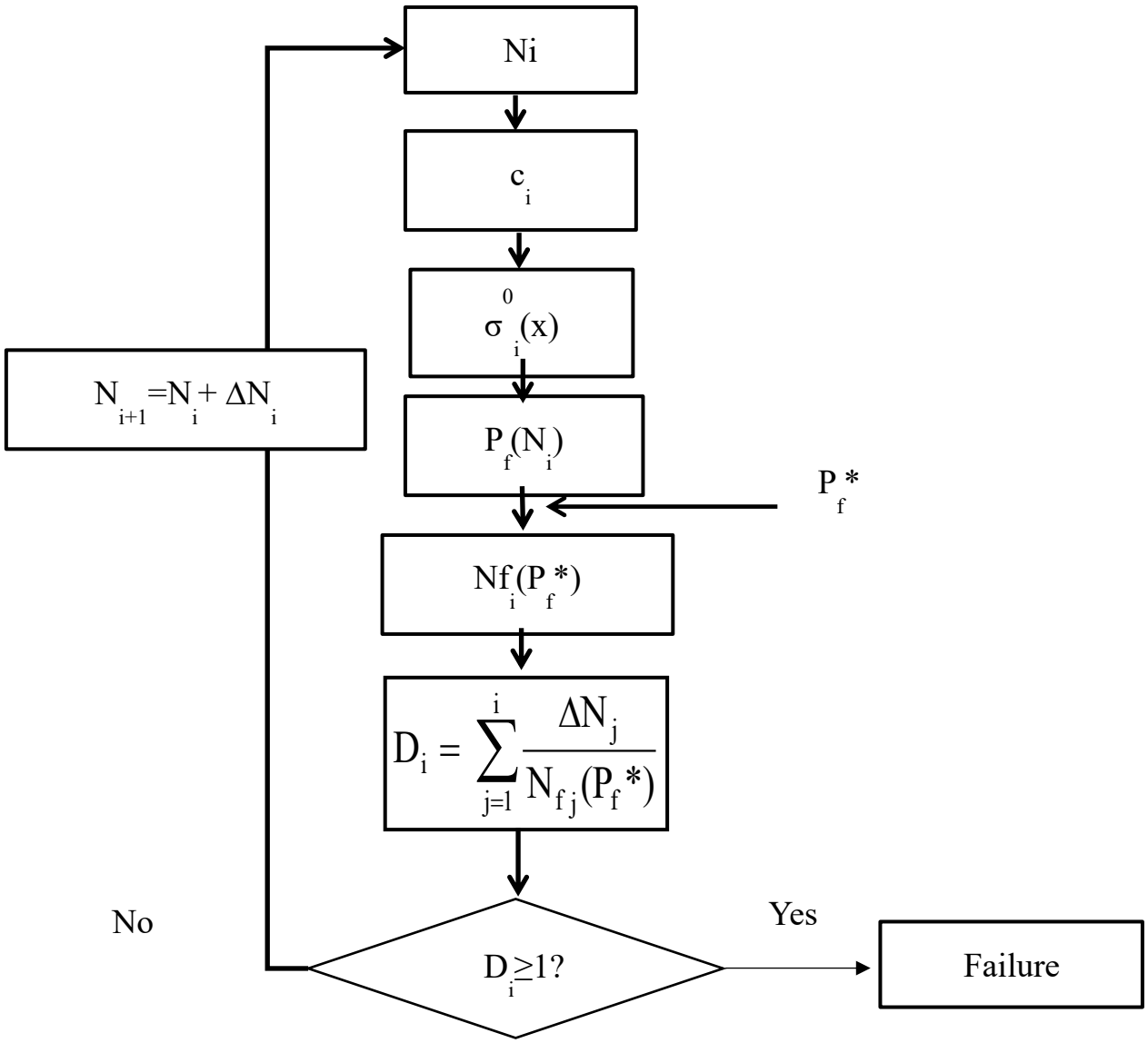

Figure 8.4 Flowchart of the procedure to assess the failure of 0° layers

8.5 Conclusions

In this chapter, a model for the prediction of the final failure of cross ply laminates subjected to tensile-tensile fatigue failure has been presented. The model is based on the statistical analysis of the failure process due to the breakage of fibres in the 0° plies in the volume included between two adjacent transverse cracks. Stress distribution was assessed through a simplified shear lag analysis.

References of chapter 8

[1] Rosen, B. Walter. "Tensile failure of fibrous composites." AIAA j 2.11 (1964): 1985-1991.

[2] Zweben, Carl. "Tensile failure of fiber composites." AIAA J 6.12 (1968): 2325-2331.

[3] Zweben, C., and B. Walter Rosen. "A statistical theory of material strength with application to composite materials." Journal of the Mechanics and Physics of Solids 18.3 (1970): 189-206.

[4] Wisnom, Michael R., and David Green. "Tensile failure due to interaction between fibre breaks." Composites 26.7 (1995): 499-508.

[5] Pimenta, Soraia, and Silvestre T. Pinho. "Hierarchical scaling law for the strength of composite fibre bundles." Journal of the Mechanics and Physics of Solids 61.6 (2013): 1337-1356.

[6] Subramanian, S., K. L. Reifsnider, and W. W. Stinchcomb. "A cumulative damage model to predict the fatigue life of composite laminates including the effect of a fibre-matrix interphase." International Journal of Fatigue 17.5 (1995): 343-351

[7] Reifsnider, K,L. and Stinchcomb, W.W. in 'Composite Materials: Fatigue and Fracture' (Ed. H,T. Hahn), ASTM STP 907, American Society for Testing and Materials, Philadelphia, 1986, pp. 298-303.

[8] Shokrieh, Mahmood M., and Larry B. Lessard. "Multiaxial fatigue behaviour of unidirectional plies based on uniaxial fatigue experiments—I. Modelling." International Journal of Fatigue 19.3 (1997): 201-207.

[9] Shokrieh, Mahmood M., and Larry B. Lessard. "Multiaxial fatigue behaviour of unidirectional plies based on uniaxial fatigue experiments—II. Experimental evaluation." International journal of fatigue 19.3 (1997): 209-217.

[10] Lee, L. J., K. E. Fu, and J. N. Yang. "Prediction of fatigue damage and life for composite laminates under service loading spectra." Composites science and technology 56.6 (1996): 635-648.

[11] Lee, C. H., and M. H. R. Jen. "Fatigue response and modelling of variable stress amplitude and frequency in AS-4/PEEK composite laminates, Part 1: Experiments." Journal of Composite Materials 34.11 (2000): 906-929.

[12] Gamstedt, E. Kristofer, and B. A. Sjögren. "An experimental investigation of the sequence effect in block amplitude loading of cross-ply composite laminates." International Journal of Fatigue 24.2 (2002): 437-446.

[13] Paepegem, W. Van, and Joris Degrieck. "Effects of load sequence and block loading on the fatigue response of fiber-reinforced composites." Mechanics of Advanced Materials and Structures 9.1 (2002): 19-35.

[14] Li, Chingshen, F. Ellyin, and A. Wharmby. "A damage meso-mechanical approach to fatigue failure prediction of cross-ply laminate composites." International journal of fatigue 24.2 (2002): 429-435.

[15] Varvani-Farahani, A., H. Haftchenari, and M. Panbechi. "A fatigue damage parameter for life assessment of off-axis unidirectional GRP composites." Journal of composite materials 40.18 (2006): 1659-1670.

[16] Kassapoglou, Christos. "Fatigue life prediction of composite structures under constant amplitude loading." Journal of Composite Materials 41.22 (2007): 2737-2754.

[17] Passipoularidis, V. A., and T. P. Philippidis. "A study of factors affecting life prediction of composites under spectrum loading." International Journal of Fatigue 31.3 (2009): 408-417.

[18] Chen, Hsing-Sung, and Shun-Fa Hwang. "A fatigue damage model for composite materials." *Polymer Composites* 30.3 (2009): 301-308.

[19] Wagner, H. Daniel. "Statistical concepts in the study of fracture properties of fibres and composites." Application of Fracture Mechanics to Composite Materials 6 (1989): 39-67.

[20] Lee, J-W., and I. M. Daniel. "Progressive transverse cracking of crossply composite laminates." Journal of Composite Materials 24.11 (1990): 1225-1243.

9. Concluding remarks

Laminated composites are becoming the preferred material system in different industrial applications, thanks to a plethora of advantages which differentiate these from conventional metallic materials. These include increased strength and stiffness for a given weight, toughness, mechanical damping, chemical and corrosion resistance together with the potential for structural tailoring.

Their enlarged use has underlined the necessity of better understanding their modes of failure and developing technologies to allow their performance to continuously improve.

Accordingly, extensive experimental investigations are needed, aimed at producing large databases and documenting damage mechanisms evolution leading these materials to failure.

Predictive models and criteria, in fact, should be able to take into account the real damage evolution of composites.

The principal mode of failure of layered composites is the separation along the interfaces of the layers, i.e. delamination, which is the main subject dealt with in the present thesis.

After a brief introduction (chapter 1), a model suitable for predicting the initiation of delamination from transverse cracks in cross-ply laminates under quasi-static loadings was proposed.

As a first step, a theoretical study was carried out, taking advantage of Lekhnitskii's complex potentials approach. Analytical expressions for the stress distributions were derived, the intensity of which is expressed as a function of a Generalized Stress Intensity Factor (GSIF). The analytical solution was validated through a bulk of finite element analyses, which allow also the effect of the ply thickness, elastic properties and crack density on the GSIF to be investigated.

Then, a criterion based on the GSIF was proposed to predict the initiation of a delamination from the transverse crack tips. The criterion was validated on experimental data taken from the literature and on those obtained from a new, ad hoc, experimental campaign carried out on glass/epoxy cross-

ply laminates. In particular, laminates with two different thickness values were tested under tensile static load and the evolution of damage was observed with the aid of a back-lighting system. The stress level required for the initiation of delamination was found to strictly depend on the transverse ply thickness, and it was proved that such a thickness effect can be quantified, theoretically, by using the GSIF-based criterion. The analytical solution for the description of the stress fields in the closeness of the matrix crack was developed and extended to be suitable to be used for laminates with generic orientation (Chapter 3).

In order to investigate delamination evolution for cross-ply laminates subjected to tensile-tensile fatigue loading, an experimental investigation was carried out on glass/epoxy cross ply laminates. Both phases of onset and delamination propagation were analyzed, and it was found that, when the focus was on the fatigue life, the onset phase could be considered negligible while the growth of delamination was the most fatigue life consuming mechanism (Chapter 4). Then, the characterization of delaminations areas extension with the cycles was performed. Delamination growth was described by means of a Paris-like curve, correlating the fatigue delamination growth rate with the ERR values. Since the experimental results elaborated in terms of the power law presented high scatter, an alternative model was proposed. This related the delamination growth rate with the average value of the principal stress, calculated within a process zone individuated in the closeness of the delamination tip. The second model was found to describe more effectively the delamination growth data (Chapter 5). Always in the same chapter, a model, based on a simplified shear lag analysis, to describe the stiffness loss associated with the presence of both transverse cracks and delaminations is presented. The validation with experimental results proved the soundness of the approach proposed.

The possibility that the process of delamination growth is affected by the friction sliding at the delaminated interface, between the 0° and 90° layers, was considered in the Appendix. FE analyses were carried out, modelling a representative part of the damaged laminate and using contact

elements at the interface of 0°/90° plies. Different conditions of damage were simulated, varying the coefficient of friction between the plies and the length of delaminations. The collected results showed that the friction did not significantly influence the ERR values.

Experimental investigations highlighted the existence of different preferential patterns for delamination growth. These started from the tips of the transverse cracks and developed either in both directions symmetrically to the transverse crack plane or asymmetrically, growing preferentially only in a direction.

The analysis of the fatigue data has been repeated simulating three different trends for the evolution of delaminations and the results are presented in the Appendix. The influence of these different morphological configurations on ERR values was investigated and the Paris-like curve was calculated for each case.

Then, the delamination evolution was studied also for laminates characterized by a different orientation.

To this aim, $[0/45_2/-45_2]_s$ laminates were manufactured and fatigue tested (R=0.05 and a frequency of 4 Hz). Photographs of the specimens and progressive micrographs of the edges allowed to reconstruct the damage process sequence.

However, with this layup, it was difficult to observe the evolution of delaminations occurring at the 0/45 interface, since it was hard to separate these from delaminations occurring from the 45/-45 interface. Therefore, specimens characterized by a different stacking sequence $[0/45_2]_s$ were produced and tested under tensile fatigue loading (Chapter 6).

The different phases characterizing the damage process for $[0/45_2]_s$ were documented by collecting a detailed series of images showing the accumulation of the observed failure modes. During the tests, Young's modulus and Poisson's ratio evolution stiffness loss were determined.

Following the approach used for cross-ply laminates, a Paris like curve was obtained for describing the delamination evolution, correlating the ERR values with the growth rate and separating the delaminations occurring from the edges to the delaminations growing within the central part of the specimens. However, the results obtained suggest that delamination propagation for this lay-up is not effectively described by a power law. This may be due to the fact that delamination areas for $[0/45_2]_s$ laminates are limited and that the Paris like curve is not able to describe such limited growth.

Additionally, Chapter 7 presents the results of a series of numerical investigations in response to the free edge delamination problem. FE analyses were carried out by simulating a damaged configuration of a $[0/45_2]_s$ laminate and the results obtained indicated that ERR values vary along the delamination profile. Hence, a procedure for describing the delamination evolution was defined, in order to take into account the influence of free edges.

Furthermore, a comparison between ERR values associated with the delamination growth for unbalanced and balanced laminates has been presented. The results obtained indicate that unbalanced laminates are more prone to this damage.

Finally, a model based on a probabilistic approach for describing the breakage of fibre in 0° layers is proposed in Chapter 8.

The model is referred to the case of cross ply laminates subjected to tensile-tensile fatigue failure, based on the statistical analysis of the failure process due to the breakage of fibres in the 0° plies in the volume included between two adjacent transverse cracks.